Humboldt-Universität zu Berlin

DISSERTATION

Ultrafast Vibrational Dynamics of Hydrogen-Bonded Base Pairs and Hydrated DNA

zur Erlangung des akademischen Grades
doctor rerum naturalium
(Dr. rer. nat.)

Mathematisch-Naturwissenschaftlichen Fakultät I

Łukasz Szyc, M.Sc.

Dekan: Prof. Dr. Andreas Herrmann

Gutachter/in: 1. Prof. Dr. Thomas Elsaesser

2. Prof. Dr. Jürgen P. Rabe

3. Prof. Dr. Wolfgang Zinth

Datum der Einreichung:01.06.2011

Datum der Promotion: 10.11.2011

Zusammenfassung

Diese Arbeit ermöglicht ein detailliertes Verständnis der Schwingungsdynamik und Kupplungen in einem Basenpaar-Modellsystem und in künstlichen DNA-Oligomeren bei verschiedenen Hydratationsgraden. Durch die Verwendung von nichtlinearer ultraschneller IR Pump-Probe Spektroskopie sind die Schwingungsbewegungen hydratisierter DNA und die schnellsten Veränderungen in den DNA-Wasser-Wechselwirkungen und Hydrationsgeometrien direkt zugänglich.

2-pyridone/2-hydroxypyridine ist ein Modellsystem für die gekoppelte intermolekularen Wasserstoffbrücken, deren Struktur der von DNA-Basenpaaren ähnelt. In Dichlormethan existiert das Molekül als ein zyklischer 2-Pyridon-Dimer, deren Vorkommern durch NMR-und 2D-FTIR Spektroskopie verifiziert wurde. Die beobachteten kohärente Oszillationen aufgrund niederfrequenter Wellenpaketbewegungen der Dimere können für die Dynamik und räumliche Geometrie der Basenpaare in den DNA-Molekül relevant sein.

Transiente Schwingungsspektren eines poly[d(A-T)]:poly[d(A-T)] Film erlauben die Zuordnung von verschiedenen NH-Streckbanden zu einer bestimmten Schwingung der Nukleinbasen und ermöglichen deren Abgrenzung zu den Beiträgen von OH-Streckschwingungen des umgebenden Wassers. Bei einem niedrigen Hydratisierungsgrad verändern die restlichen, an die Phosphatgruppen gebundenen Wassermoleküle, ihre Ausrichtung auf ultraschnellen Zeitskalen nicht. Im Fall vollständig hydratisierter DNA ist die Dynamik der Wasserhülle dem Verhalten des reinen Wassers ähnlicher und man beobachtet spektrale Diffusion der OH-Streckschwingung im Subpikosekundenbereich sowie einen Zerfall der Schwingungsanisotropie durch Molekülrotation und/oder Energietransfer. Die Wassermoleküle der Phosphat-Hydratationshülle dienen als effiziente Wärmesenke für Überschussenergie aus der DNA, wobei die Energietransferzeiten im Femtosekundenbereich liegen. Im Gegensatz dazu erfolgt Energietransport innerhalb der DNA auf einer langsameren Zeitskala von 20 ps.

Schlagwörter:

Energiedissipation, Femtosekunden-Schwingungsspektroskopie, Hydratisierte DNA, Wasserstoffbrücken

Abstract

This thesis provides a detailed understanding of vibrational dynamics and couplings in a base pair model system and artificial DNA oligomers at different levels of hydration. By using nonlinear ultrafast infrared pump-probe spectroscopy, the basic vibrational motions of hydrated DNA and the fastest changes in the DNA-water interactions and hydration geometries are directly accessed.

2-pyridone/2-hydroxypyridine is used as a model molecule for coupled intermolecular hydrogen bonds with a structure resembling a DNA base pair. In dichloromethane the molecule predominantly exists as a cyclic 2-pyridone dimer as determined using a combined NMR and 2D FTIR approach. The observed coherent oscillations due to low-frequency hydrogen bond wavepacket motions of the dimers are expected to be relevant for the dynamics and spatial geometry of base pairs in DNA molecule.

Transient vibrational spectra of a poly[d(A-T)]:poly[d(A-T)] film enabled the assignment of different NH stretching bands to particular nucleobase vibrations, also discerning them from the OH stretching contributions of the surrounding water. At a low hydration level, residual water molecules, bound to the phosphate groups, do not alter their orientation on ultrafast time scales. In the case of fully hydrated DNA, the dynamics of the water shell are closer to those of bulk liquid water with a sub-picosecond spectral diffusion and a loss of vibrational anisotropy as a result of molecular rotation and/or energy transfer. The water shell around the phosphates serves as a efficient heat sink accepting excess energy from DNA in a femtosecond time domain, whereas the energy transfer within DNA occurs on the time scale of 20 ps.

Keywords:

energy dissipation, femtosecond vibrational spectroscopy, hydrated DNA, hydrogen bonds

Inhaltsverzeichnis

1 Hydrogen bonding

1.1 The nature of the hydrogen bond

The hydrogen bond (H-bond) is a unique interaction, which can be described as relatively weak when comparing to covalent or ionic bonds. It typically has, however, order of magnitude higher dissociation energy than other type of intermolecular forces, like London (van der Waals) or dipole-dipole interactions. The history of the concept of the hydrogen bond has been described in many review publications and handbooks [1] [2].

According to the classical Pauling definition from 1928 [3], the term hydrogen bond describes an electrostatic in nature interaction between a proton donor X−H and proton acceptor Y in the same or different molecule: X−H···Y. Conventionally, the H atom is bonded to an electronegative atom such as N, O and F. Y can either be electronegative or have an electron excess [4]. However, the definition of hydrogen bond evolves in time [2]. Since mid-1980s, the existence of C−H···Y hydrogen bonds have been commonly accepted as well, although the C-atom in the proton donating group is not electronegative and thus these systems are not in line with the classical definition [5]. In the hydrogen bond, where the group C-H is involved, negatively charged π electrons can act as proton acceptors in the stabilization of weak H-bonding interactions in many chemical systems [6,7].

It is very useful for analytical purposes to introduce a classification of hydrogen bonds in terms of their physicochemical properties. Following the description of Jeffrey [4] one can distinguish three categories of hydrogen bond: weak, moderate and strong. Systems with strong and very strong hydrogen bonds are out of the scope of this thesis. Weak hydrogen bonds (like those existing in liquid water) have usually a binding energy not higher than 4 kcal/mol (~17 kJ/mol), which corresponds to the energy per molecule smaller than 3×10^{-20} J. Here, electrostatic and dispersive forces are the dominant interactions, whereas strong hydrogen bonds have mostly covalent character and their energies can be also relatively high, up to 40-50 kcal/mol (167-210 kJ/mol). The X···Y distance in weak hydrogen bonds is typically above 3.2 Å. However, other authors suggest the O···O distance in weak hydrogen bonds is comprised between 2.8 and 3.0 Å [13], which agrees with generally accepted average O···O distance in liquid water ≈ 2.84 Å. For strong hydrogen bonds, the X···Y length has the values between 2.2 and 2.5 Å. In contrary to the strong hydrogen bonds, the bond directionality in weak hydrogen bonds is minor and the bond angles can even approach 90 degrees. The hydrogen bonds of energy 15-40 kcal/mol (63-167 kJ/mol), moderate directionality and the hydrogen-bond length in the range 2.5-3.2 Å are called moderate, intermediate-strength hydrogen bonds [2]. Also for this class of hydrogen bonds the accepted X···Y distance adopts only approximate conventional values. For many medium-strong hydrogen bonds, this distance does not exceed 2.8 Å [13].

Hydrogen bonding leads to a distortion of potential energy surfaces that determine the nuclear positions and motions of the participating atoms. Characteristic for the vast majority of hydrogen bonds is an asymmetry of the position of the proton, which is not at half the distance between atoms X and Y. This asymmetry has also been found in dimers of carboxylic acids, e.g., in acetic acid dimer. Such dimers are stable even in the vapour through the pair of bonds, each of which has substantial energy [≈ 32 kJ/mol in $(CH_3COOH)_2$]. Potential energy curves of the asymmetric hydrogen bonding have two minima. In general, the proton is in a position corresponding to a deeper energy minimum. However, if the barrier is not too high, the proton transfer can occur between minima and the tautomeric equilibrium can be reached: $X - H \cdots Y \leftrightarrow X^{\delta-} \cdots H - Y^{\delta+}$. Such equilibria were monitored for acid-base complexes formed in non-aqueous solvents (e.g., in benzene) due to the formation of hydrogen bonds between donors of protons (phenols, carboxylic acids) and organic bases (amines, acridine derivatives, and others). Equilibrium constant depends both on the hydrogen bonding potential energy curve as well as the pK_a values of proton donor and acceptor [8].

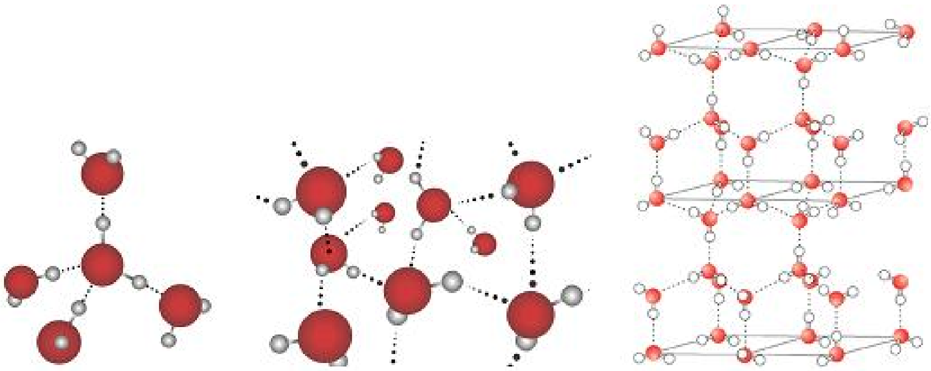

Figure 1.1: Tetrahedral arrangement of hydrogen bonds between molecules of water (left). Each water molecule participates in an average of 3.4-3.6 hydrogen bonds in a liquid at room temperature (in the middle). In the hexagonal crystalline structure of ice (right) each water molecule has four hydrogen bond neighbours.

Hydrogen bonds are ubiquitous in nature and play a fundamental role for structure and function of molecules. This attractive interaction is strong enough to be responsible for the structure of water and ice (Figure 1.1), but it also determines or stabilizes the structure of larger molecular systems such as proteins (Figure 1.2) and nucleic acids (Figure 6.1). On the other hand, the limited strength of hydrogen bonds allow for structural flexibility that is essential for the functionality of these systems. In liquid water, neighbouring water molecules form hydrogen bonds with each other, creating in this way a characteristic network (Figure 1.1). The existence of hydrogen bonds network has been used to explain the peculiar chemical and physical properties of water, such as relatively high boiling point when compared to other hydrides in Group 6 of the periodic table.

Apart from the abnormally high melting and boiling points of the solids and liquids with hydrogen bonding, existence of inter- and intramolecular hydrogen bonds influence also other physicochemical properties. Ammonia and water have the highest molar specific heat capacity of any known substance as well as high heat of vaporization[1]. Also the permittivities of liquids where the molecules are associated by hydrogen bonds (H_2O, lower aliphatic alcohols, liquid NH_3, HF, HCN an others) are very high, much higher than one could conclude from the dipole moments of the single molecules. Intramolecular hydrogen bonds in aromatic acids have a distinct influence on the acid dissociation constant. For example, 2-hydroxybenzoic acid (salicylic acid), where exists a strong intramolecular bond $O–H \cdots O$, is much stronger (pK_a = 3.0) than its isomers (pK_a = 4.08 and 4.58 for 3-hydroxybenzoic and 4-

---

[1] High molar specific heat capacity and heat of vaporization allow water to moderate Earth's climate by buffering large fluctuations in temperature.

hydroxybenzoic acid, respectively), where the relative position of –COOH and –OH functional groups exclude formation of such hydrogen bond bridges. The OH bond in carboxylic group is weakened in the 2-hydroxybenzoic acid by the hydrogen bond to the oxygen atom of hydroxyl group. Finally, hydrogen bonds between molecules that are building the molecular crystals influence the electrical conductivity of such crystals. In particular, conductivity of ice is attributed to the proton motions in O–H···O bridges [9,10].

Disordered extended networks of intermolecular hydrogen bonds in liquids such as water, hydrogen fluoride, ammonia or alcohols undergo pronounced structural fluctuations on a multitude of time scales. In contrast, well-defined molecular structures based on both intra- and intermolecular hydrogen bonds exist in polyatomic molecules, molecular dimers and – in particular – in macromolecules such as DNA and other biomolecular systems. In proteins, the two main types of secondary structures: α-helix and β-sheet are stabilized by hydrogen bonding between C=O and N–H groups of different amino acids. Both periodic structures, which determine the function of proteins in living organisms, are shown in Figure 1.2. The DNA double helix (Figure 6.1) has a rigid structure stabilized by hydrogen bonds (with the energy of approx. 4 to 21 kJ/mol) between complementary nucleic base pairs (two H-bonds for the AT and three for GC pairs) and by stacking interaction between adjacent bases [11]. During elementary genetic processes such as transcription or replication, these bands are temporarily cut and only a subtle interplay between enzyme activity and the hydrogen-bonded base pairs allows for functionality. In living organisms, genes are the DNA fragments. Base sequence in DNA molecules determines the order of amino acids in proteins synthesized in vivo. For this reason, it is said that DNA molecules contain the genetic code.

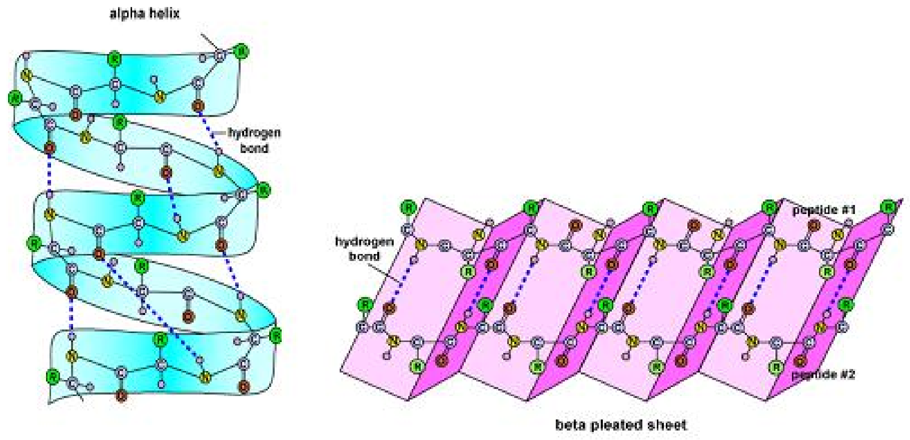

Figure 1.2: Two types of secondary structure in proteins: α-helix and β-sheet. Hydrogen bonds are presented by dotted line. (Reproduced with permission from Prof. G. Kaiser; *Website for microbiology course*: http://student.ccbcmd.edu/~gkaiser/biotutorials/proteins/, 20.05.2011).

Since eighty years, H-bonded systems have been investigated by large number of various theoretical and experimental methods. Historically, the largest amount of data on H-bonded system was obtained using infrared spectroscopy [12]. Recent progress is focused on ultrafast (throughout the thesis, by this term the time domain between 10^{-14} and 10^{-11} s will be understood) dynamics of hydrogen bonding (vibrational motions, proton transfer and breaking/formation of hydrogen bonds), where nonlinear vibrational spectroscopy plays a leading role [13,14].

1.2 Subject of the thesis

Understanding hydrogen bonded systems and their functionality requires both structural and dynamical information. Many processes, which are important in this context, such as energy relaxation and energy transfer, structural fluctuations, hydrogen bond breaking and (re)formation, occur on an extremely short time scale, down to the femtosecond (1 fs = 10^{-15} s) domain. The vibrational absorption spectra undergo characteristic and distinct changes upon hydrogen bond formation and thus, for many decades, infrared spectroscopy was a favourite tool for studying the systems with hydrogen bonds. However, linear spectroscopy does not allow for discerning the different microscopic interaction mechanisms that contribute to the shape of vibrational absorption band, because the result of measurement is averaged in time.

Recent progress in laser technology, in particular development of short laser pulses (picosecond and femtosecond) tunable in a broad frequency range, allows to study structural dynamics in real time. In this thesis, ultrafast vibrational pump-probe spectroscopy is used to investigate 2-pyridone, a model system for DNA base pairing, and finally to examine also DNA itself.

The thesis starts from a discussion of linear infrared spectroscopy in studying hydrogen-bonded systems (Chapter 2). In particular, the limitations of linear spectroscopy in understanding the mechanisms of vibrational dynamics and in reliable analysis of strongly overlapped bands are presented. At the end of the chapter, the theory of two-dimensional correlation spectroscopy, a powerful analytical technique will be provided. Though the 2D correlation spectroscopy is very useful to extract information from sets of measured steady-state spectra by enhancing the spectral resolution, it will still not provide an access to the fast dynamics of hydrogen-bonded systems simply because the linear vibrational spectroscopy offers only time-averaged picture. To overcome this problem, nonlinear time-resolved infrared spectroscopy is used. A short introduction to the theory of nonlinear spectroscopy is given in Chapter 3. The laser systems providing ultrashort pulses, which have been used for collecting the data presented throughout the thesis, together with a scheme of home-built frequency converters for infrared generation (optical parametric amplifier), are described in Chapter 4. Chapter 5 reports results on a model system for DNA base pairing – 2-pyridone/2-hydroxypyridine using various experimental techniques such as NMR spectroscopy, linear IR and nonlinear ultrafast IR spectroscopy supported by DFT calculations. The largest part of the thesis, Chapter 6, consists of extensive investigation of ultrafast dynamics of DNA-water system. The description of a novel method of producing thin, high optical quality DNA films is followed by a presentation of pump-probe results in a very wide frequency range, covering OH/NH stretching and phosphate stretching vibrations. Finally, the last Chapter summarizes this thesis.

2 One- and two-dimensional linear vibrational spectroscopy in studying hydrogen-bonded systems

2.1 Vibrational Hamiltonian of polyatomic molecule. Effects of anharmonicity

A molecule with N atoms has $3N$ degrees of motional freedom, of which three correspond to translation of the canter of mass, three to rotation of the whole molecule, and the remaining $3N - 6$ to internal vibrations that leave the centre of the mass stationary (since a linear molecule has only two rotational degrees of freedom, it has $3N - 5$ vibrational modes). Usually complex molecules are treated in the harmonic oscillator approximation, where only quadratic terms are included in the molecular potential energy function giving rise to independent vibrational *normal modes*. In this situation, it is possible to represent any vibrational motion as a superposition of normal modes. The vibrational energy of the molecule then can be written as the sum of the energies of the individual normal modes:

$$E_{vib}^{harm} = \sum_{i}^{3N-6} \left(n_i + \frac{1}{2} \right) h\omega_i \,, \tag{2.1}$$

where n_i is the vibrational quantum number (excitation level) of mode i ($n_i = 0, 1, 2, \ldots$) and ω_i is its harmonic frequency.

However, for hydrogen-bonded systems, the higher order terms of the molecular potential energy function in every single vibrational coordinate that leading to anharmonicity effects, cannot be neglected. Anharmonicity is typically treated as perturbation to the Hamiltonian in the eigenstate representation of the harmonic oscillator normal modes. The Schrödinger equation then no longer resolves into a number of independent equations for each normal mode. The total energy is no longer the sum of eigenvalues but it contains cross-terms involving two or even more normal vibrations and can be expressed as (without degenerate modes):

$$E_{vib}^{anharm} = \sum_{i}^{3N-6} \left(n_i + \frac{1}{2} \right) h\omega_i + \sum_{i \le j} \left(n_i + \frac{1}{2} \right) \left(n_j + \frac{1}{2} \right) hx_{ij} + \ldots \,, \tag{2.2}$$

where x_{ij} are the anharmonic coupling constants between modes i and j, which typically have negative values. They can be derived from the cubic and quartic (or even higher orders) force constants φ by expanding the potential energy V in a Taylor series in a normal coordinate (q) basis [15]

$$V = V_0 + \sum_{i}^{3N-6} \varphi_i q_i + \sum_{ij}^{3N-6} \varphi_{ij} q_i q_j + \sum_{ijk}^{3N-6} \varphi_{ijk} q_i q_j q_k + \sum_{ijkl}^{N} \varphi_{ijkl} q_i q_j q_k q_l + \ldots \,, \tag{2.3}$$

where the n^{th} order force constants are given by

$$\varphi_{ijk\ldots} = \frac{1}{n!} \left(\frac{\partial^n V}{\partial q_i \partial q_j \partial q_k \cdots} \right)_0 . \tag{2.4}$$

The potential can be defined such that $V_0 = 0$. First-order and harmonic second-order off-diagonal force constants vanish in the orthonormal basis of normal modes.

Electromagnetic radiation with an appropriate frequency in the IR region can excite the molecule from one nuclear state, n_i, to the next higher one, $n_i + 1$. If the frequencies of the normal modes do not change significantly when the molecule is excited, the excitation energy is $(n_i + 1 - n_i)h\omega_i$. In the cases where the potential energy curve displays a pronounced anharmonic shape, i.e., when exists a coupling between a given vibrational mode k and, for instance, bath of remaining modes $i \neq k$, its transition frequency is given by [16]:

$$\upsilon(n_k \to n_k + 1) = \upsilon_k + 2x_{kk}n_k + \sum_{i \neq k} x_{ik} n_i \tag{2.5}$$

where υ_k is the anharmonic correction of the $n_k = 0 \to 1$ transition when the other vibrational modes i are in their ground states, i.e., in the cold molecule:

$$\upsilon_k = \omega_k + 2x_{kk} + \frac{1}{2}\sum_{i \neq k} x_{ik} \; . \tag{2.6}$$

The second term in the Eq. (2.5) describes the "diagonal" anharmonic shift of an excited vibrational mode k. In transient vibrational spectra, diagonal anharmonicity manifests in the lower frequency of $\upsilon = 1 \to 2$ transition (called excited state absorption, see also Chapter 3) with respect to the $\upsilon = 0 \to 1$ fundamental one. In other words, the fact that the energy spacing between vibrational levels become smaller as the vibrational quantum number increases, makes possible to detect transient spectra of these transitions with time-resolved spectroscopy (for more details, see Chapter 3.10 about pump-probe spectroscopy).

The third term in the Eq. (2.5) reflects the "off-diagonal" anharmonicity, the situation when the vibrational energy of a molecule is redistributed over the low-frequency vibrational modes, in this way exciting them. When other modes i are highly excited, the marker mode k exhibits a red-shifted transition frequency, even for the fundamental $\upsilon_k = 0 \to 1$ transition. Anharmonic coupling to the examined mode affects not only its frequency, but also a lineshape, as it will be discussed in more detail in the sections 2.4.1-2.4.3.

The excitation of a vibrational mode requires

$$\vec{\mu} = \vec{\mu}_0 + \sum_{i}^{3N-6} \left(\frac{\partial \vec{\mu}}{\partial q_i} \right)_0 q_i + \sum_{ij}^{3N-6} \left(\frac{\partial \vec{\mu}}{\partial q_i q_j} \right)_0 q_i q_j + \ldots \tag{2.7}$$

to be nonzero (μ is the molecule's dipole moment including contributions from both electronic and nuclear charges, q is vibrational coordinate): the transition is allowed only if the vibration perturbs the equilibrium geometry in a way that changes the dipole moment of a molecule. In other words, IR transitions are forbidden (in a harmonic approximation) or only weakly allowed (in a case of anharmonic oscillator) for vibrations that are symmetric with respect to the molecular structure.

For anharmonic potentials, the higher terms of the potential energy according to Eq. 2.3 are not negligible; the *mechanical anharmonicity* gives rise to overtones: vibrations with the double, triple, or multiple frequencies of the fundamentals. Overtones may appear also as a result of *electrical anharmonicity* - the higher terms of the dipole moment according to Eq. 2.7. Since both equations may contain mixed terms, combinations of two or more normal vibrations, i.e., sums or differences, are produced. These appear in the spectra, but usually only with small intensity. Also Raman spectra show overtones and combinations due to mechanical and electrical anharmonicities [17].

Similar to IR spectroscopy, *Raman spectroscopy* reveals transitions between distinct vibrational states of molecule. However, the origin of Raman spectra is markedly different from that of IR spectra. In Raman spectroscopy the sample is irradiated by laser beams in the UV-VIS region (ν_0) and the two types of scattered light is observed. One, called *Rayleigh scattering* has the same frequency as the incident beam (ν_0) and the other, much weaker ($\sim 10^{-5}$ of the incident beam), is called *Raman scattering* and has frequencies ν_0 - ν_m (*Stokes* scattering) and $\nu_0 + \nu_m$ *(anti-Stokes* scattering), where ν_m is a vibrational frequency of a molecule. Raman spectra are typically observed for vibrational and rotational transitions, although it is possible to observe Raman spectra of electronic transitions between ground states and low-energy excited states [18]. The Raman excitation requires $(\partial \alpha / \partial q)_0$ to be nonzero, i.e., the vibration is Raman-active if the polarizability (α) of vibration with respect to the vibrational coordinate changes. In contrary to IR spectroscopy, the totally symmetric vibrations are always Raman-active. Hence, IR and Raman spectroscopy are often complementary spectroscopic techniques.

2.2 Vibrational spectra

Most analytical applications of IR spectroscopy are based on Bouguer- Lambert-Beer law, describing the transmission (absorption) of the flux of photons Φ_0 by a sample:

$$\Phi_{tr} = \Phi_0 \exp(-\varepsilon C l) = \Phi_0 10^{-\varepsilon C l} \equiv \Phi_0 10^{-A} \tag{2.8}$$

Here A is the *absorbance* or *optical density* of the sample, ε is called *molar extinction (absorption) coefficient*, customarily expressed in M^{-1} cm^{-1}, l is a cell thickness (in cm) and C is the concentration of the absorbers (in M).

The IR spectra typically display dependence of absorbance on the frequency of light by plotting A or ε as a function of the frequency (ν), the wavelength (λ) or the wavenumber ($\bar{\nu}$), where $\bar{\nu} = \frac{1}{\lambda} = \frac{\nu}{c}$ and has units of cm^{-1}.

If the set of spectra have been measured in function of some controlled change (perturbation), the mathematical correlation between the absorbance changes at different frequency position can be found and plotted as a two-dimensional contour map. This idea is essentially the fundament of two-dimensional correlation spectroscopy, developed by Isao Noda in the 1980s. The method will be introduced in the Section 2.5.

2.3 Vibrational spectroscopy of hydrogen-bonded systems

It is evident from the classical definition of hydrogen bonding that formation of X−H···Y bond is accompanied by a weakening of the covalent bond of the donor X–H group. As a consequence, the force constant of the stretching vibration is reduced, which leads to a red-shift of its frequency [6]. This effect is often accompanied by vibrational line broadening and reshaping (compare Figure 2.1) as well as substantial increase in intensity.

The substantial enhancement of the spectrally integrated absorption intensity is related to changes of the electronic structure. In contrast to the stretching mode, X−H in-plane bending modes (δ_{XH}) as well as out of plane bending modes (γ_{NH}), with transitions located in the fingerprint region of the vibrational spectrum (by the term fingerprint region of the infrared spectrum the frequency range between 500 and 1500 cm^{-1} will be understood throughout the thesis), undergo small shifts towards higher frequencies upon hydrogen bonding, but typically the line shape remains unaffected [12].

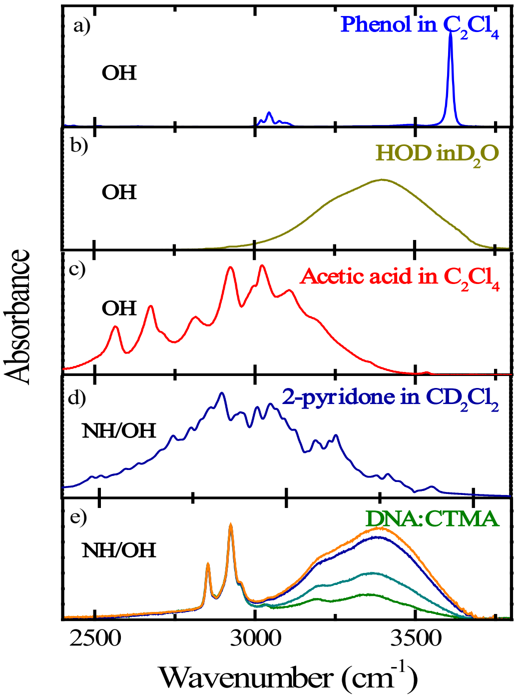

Figure 2.1 High frequency part of infrared absorption spectra of phenol in CCl_4 (a), HOD in D_2O (b), acetic acid in CCl_4 (c), 2-pyridone in CD_2Cl_2 (d) and DNA:CTMA complex for different hydration levels (e).

In Figure 2.1, the NH/OH stretching steady-state absorption spectra in different chemical environments are compared. Free (non-hydrogen-bonded) OH groups (Figure 2.1a), e.g., phenol dissolved in non-polar solvent give rise to a narrow (Full Width at Half Maximum, FWHM less than 20 cm^{-1}) absorption band with a maximum around 3600 cm^{-1}. A hydrogen-bonded OH or NH group displays a stretching frequency substantially lower than that of free OH/NH groups. In Figure 2.1b, the OH stretching band of HOD dissolved in D2O is shown. Such a system is classified as a weak hydrogen bond with an absorption band maximum of the OH stretching band at 3400 cm^{-1} and a bandwidth of 235 cm^{-1}. The cyclic acetic acid and 2-pyridone/2-hydroxypyridine dimers are examples of molecular systems that have been studied [19,20,21,22] because they represent valuable model systems of intermolecular hydrogen bonds that resemble the base pair of DNA. Their IR spectra in the frequency range 2300-3700

cm^{-1} are presented in Figure 2.1(c,d). In both cases, the OH/NH stretching band has a bandwidth exceeding several hundreds of wavenumbers with a band maximum strongly red-shifted compared to free or weakly hydrogen-bonded OH stretching vibrations. In addition, the IR vibrational bands of these systems display a fine spectral substructure, a characteristic feature of medium to medium-strong hydrogen bonds. In Figure 2.1e, the linear spectra of an artificial, short double-stranded DNA oligomer containing only adenine and thymine base pairs, is shown for different hydration levels.

The strong broadening of the fundamental OH/NH stretching transition upon hydrogen bonding has a non-trivial origin, which cannot be explained simply by faster dephasing times (T_2) due to solvent-solute interactions. The main factor, which must be taken into account for the detailed analysis of broad, and for medium-strong hydrogen bond also peculiar spectral envelope, is anharmonicity. Formation of a hydrogen bond enhances anharmonicity of potential energy surface of the OH/NH stretching coordinate, which leads to several consequences. The most obvious one is decreasing energy separation between the following vibrational states, υ, e.g. the $\upsilon = 1 \rightarrow 2$ transition with respect to $\upsilon = 0 \rightarrow 1$ ("diagonal" anharmonicity). According to a theoretical model proposed by Hadži and Bratos [12] anharmonicity of the potential energy surfaces results in a coupling of the X–H stretching (fast) mode to the low frequency modes (Figure 2.2), which modulates the hydrogen bond length (slow mode). The consequence of such coupling (also called in literature Frank-Condon progressions) is enhancement of spectral substructure of the X–H stretching band. Similar effects can be caused by Fermi resonances and excitonic/Davydov type of interaction (the latter for systems with several hydrogen bonds), all of them transforming the hydrogen stretching oscillator into a vibrational multilevel system with a numerous transition lines (the detailed discussion will be given in Sections 2.4.1-2.4.3). In addition, a fine substructure of the spectra is often washed out as a result of broadening of the vibrational transition lines and spectral diffusion induced by interactions with the liquid (see Section 2.4.4). As a consequence, the line shape analysis of vibrational spectra of hydrogen-bonded systems in the liquid phase (see also Section 3.8) has remained a very difficult scientific problem [23,24,25,26], almost unsolvable for linear spectroscopy.

The time scales of hydrogen bond dynamics is dictated by the relevant molecular vibrations:

- The hydrogen donor stretching vibration, X–H, displays a very short oscillation period, on the order of 10 to 15 fs (corresponding the frequency in the range of 3000 cm^{-1}) [27]. The strong OH stretching absorption band of neat water and the NH/OH stretching absorption of hydrated DNA (Figure 2.1e) extend over a broad frequency range between 3000 and 3700 cm^{-1}.

- Formation of intermolecular hydrogen-bonded dimers gives rise to new vibrational low-frequency modes, such as the dimer hydrogen bond stretching (ν_{dimer}) and bending (δ_{dimer}) modes. In hydrogen bond networks, e.g., in water, intermolecular modes often extend over several molecules and dominate the low-frequency vibrational spectrum. The small force constants and the large reduced mass of such hydrogen bond modes result in low-frequency modes typically located below 300 cm^{-1}. Thus, these hydrogen bond motions with vibrational periods of about 660 to 80 fs are clearly separated in time from high-frequency X−H stretching motions with much shorter vibrational periods.

- In intermolecular hydrogen bonds, molecular rotations hindered by hydrogen bonding and low-frequency translational modes are represented by *librational modes*. Librations and translations play a fundamental role for hydrogen bonds breaking and (re)formation [28] – processes which occur on a femtosecond to picosecond time scale.

Femtosecond spectroscopy allows for following the vibrational dynamics of hydrogen-bonded systems in real time. In addition, ultrafast vibrational spectroscopy provide specific information on the various coupling mechanisms (between different oscillators or between oscillators and their molecular bath) by separating them in the nonlinear time-resolved response [14,29].

2.4 Vibrational coupling mechanisms

In the section 3.2, the density matrix approach of statistical mechanics will be introduced. The density matrix, *ρ(t)*, can be calculated in a frame of perturbation theory, where interaction between the light field and the system is considered as a perturbation. Using this approach for describing the vibrational line shapes, the vibrational absorption coefficient for a $\upsilon = 0 \rightarrow 1$ transition is given by the Gordon formula [30]:

$$\alpha(\omega) = \frac{2\pi}{3c\hbar n(\omega)V}\,\omega\left[1-\exp\left(-\frac{\hbar\omega_0}{k_B T}\right)\right]\times\int_{-\infty}^{\infty} dt e^{-i(\omega-\omega_0)t}\left\langle \mathbf{M}(t)\mathbf{M}(0)\right\rangle \tag{2.9}$$

with

$$\left\langle \mathbf{M}(t)\mathbf{M}(0)\right\rangle = |\mu|^2\left\langle \exp[-i\int_0^t \delta\omega(\tau)]\right\rangle \approx \mu^2 \exp\left[-\frac{1}{2}\int_0^t\int_0^t \left\langle \delta\omega(\tau_1)\delta\omega(\tau_2)\right\rangle d\tau_1 d\tau_2\right] \tag{2.10}$$

where μ is the dipole moment of the vibrational frequency ω_0, V is the volume of the liquid sample and n is its refractive index. The Eq. (2.9) is fully quantum mechanical and is exact up to its first-order terms in perturbation energy. The core of Gordon expression is the *two-time dipole moment correlation function* $\left\langle \mathbf{M}(t)\mathbf{M}(0)\right\rangle$, which is characteristic in statistical mechanics for slightly perturbed systems, playing a similar role to two-time correlation functions (involving other dynamical variables) in other types of spectroscopy such as NMR, Raman and neutron scattering [13]. This approach is probably the most straightforward way to study band shape problems, since the vibrational line shape is determined by the Fourier transform of the dipole moment correlation function $\left\langle \mathbf{M}(t)\mathbf{M}(0)\right\rangle$ taken as an ensemble average of non-perturbed system. $\left\langle \mathbf{M}(t)\mathbf{M}(0)\right\rangle$ is related to the *transition frequency fluctuation correlation function* $C(t)$ = $\left\langle \delta\omega(\tau_1)\delta\omega(0)\right\rangle$ (Eq. 2.10), where $\delta\omega(\tau)$ represents the time-dependent fluctuation of the vibrational transition frequency ω_0.

To calculate vibrational absorption coefficient, the Hamiltonian including potential energy surface of hydrogen bonded molecules together with interactions with the bath must be known (Eq. 2.3) [24,25,26]. Therefore, different mechanisms of vibrational coupling need to be considered.

Hydrogen bonding increases the anharmonicity of the potential energy surface, which results in strong enhancement of mechanical coupling between the involved vibrations. Anharmonic mode coupling is responsible for broadening and reshaping of vibrational absorption band and is also crucial for hydrogen bond dynamics and vibrational energy transfer. In the vibrational spectra, anharmonic mode couplings are manifested by the appearance of over- and combination tones, band splitting and/or frequency shifts of harmonic transitions.

2.4.1 Anharmonic coupling with low-frequency hydrogen bond modes

The anharmonicity of the potential energy surfaces results in a coupling between the high-frequency X–H stretching mode and low-frequency hydrogen bond modes, which modulate the X–Y distance.

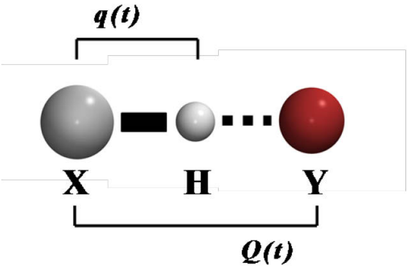

Figure 2.2: The graphic representation of a hydrogen bond where the high frequency X-H stretching mode (q) and the low frequency X-Y motion (Q) have been tagged.

The system Hamiltonian can be expressed as the sum of two harmonic oscillators (for a fast, q, and slow, Q, modes) coupled to the bath, x_n [12]:

$$H(q,Q)=\frac{p^2}{2m}+\frac{m\omega_{eff}^2(Q)\,q^2}{2}+\frac{P^2}{2M}+\frac{M\Omega^2(x)\,Q^2}{2}+\sum_n\frac{p_n^2}{2m_n}+\frac{m_n\omega_n^2x_n^2}{2} \tag{2.11}$$

with the reduced masses m, M and m_n, conjugate momenta p, P and p_n, and the corresponding eigenfrequencies ω, Ω and ω_n. An effective angular frequency ω_{eff} of the fast vibration is given by:

$$\omega_{eff}(Q)=\omega\sqrt{1+bq} \tag{2.12}$$

where b is a constant that quantifies the anharmonic coupling between the fast and the slow mode. In a given Hamiltonian, the fast mode is coupled to the slow mode, which in turn is coupled to the bath and hence, the effective eigenfrequencies of the fast mode ω_{eff} and slow mode Ω will depend on Q and x_n, respectively, regardless of the specific type of interaction between the coupled oscillators.

The square root in Eq. 2.12 can be expanded into a Taylor series to the first order of Q:

$$\omega_{eff}(Q)=\omega+bQ \tag{2.13}$$

This theoretical prediction stays in agreement with the experimental findings [31,32] that the spectral red shift of the X–H mode scales roughly linearly with the hydrogen bond length, Q.

The time scales between low- and high-frequency modes differ significantly and thus, similarly to the Born-Oppenheimer-like separation of electronic and nuclear degrees of freedom, the different states of the X−H stretching oscillator define adiabatic potential energy surfaces for the slow mode Q (Figure 2.3). Vibrational transitions from different levels of the low-frequency oscillator in the $\upsilon_{XH} = 0$ state to different low-frequency levels in the $\upsilon_{XH} = 1$ state leads to a progression of lines which, for moderate displacements, is centred at the pure X−H stretching transition and displays a mutual line separation by one quantum of the low-frequency mode, Ω. Excitation of anharmonically coupled oscillators with a broadband ultrashort laser pulse resonant to the X−H stretching band can create a phase-coherent superposition of several levels of the low-frequency mode making up a vibrational wave packet [27]. These vibrational wave packets can be observed by ultrafast nonlinear vibrational spectroscopy as coherent dynamics [22,33,34].

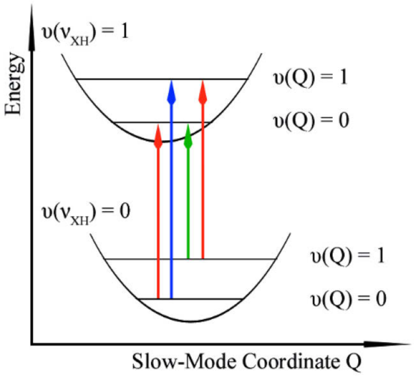

Figure 2.3: Potential energy surfaces for the hydrogen bond low-frequency mode in a single hydrogen bond, showing a displacement along the low-frequency (slow-mode) coordinate Q as function of the quantum state of the X−H high-frequency (fast-mode) stretching coordinate q (ν_{HX}).

2.4.2 Fermi resonances

If the two vibrational states of a molecule transform according to the same irreducible representation of the molecular point group and their transition energies (accidentally) are similar, the Fermi resonance[2] effect can occur. In the infrared or Raman spectrum, this phenomenon leads to two bands appearing close together when only one is expected.

Fermi resonances between the $\upsilon(\nu_{X-H}) = 0 \rightarrow 1$ stretching mode and overtones or combination bands of modes located in fingerprint range of vibrational spectrum lead to level splitting of the X–H stretching transition [25]. In this way, the weaker modes (over- and combination tones) gains intensity (becomes more allowed) and the more intense band decreases in cross

---

[2] The phenomenon was first discovered by the Italian physicist Enrico Fermi in 1931 for CO_2 molecule, where the bending overtone and the stretching fundamental frequency of the of C=O have almost identical energy. As a consequence, instead of expected one band in 1354 cm^{-1}, two bands were observed in the Raman spectrum of the CO_2 molecule with the frequencies 1285 cm^{-1} i 1388 cm^{-1}.

section. In the case when the stretching fundamental tone couples weakly to the bending overtone, the Fermi resonance facilitates an efficient vibrational energy redistribution channel (Figure 2.4, left scheme). When the Fermi resonance is strong, the resulting coupled states split, and coherent excitation of these split states will result in quantum beats of nonlinear signals. (Figure 2.4, right scheme) [27].

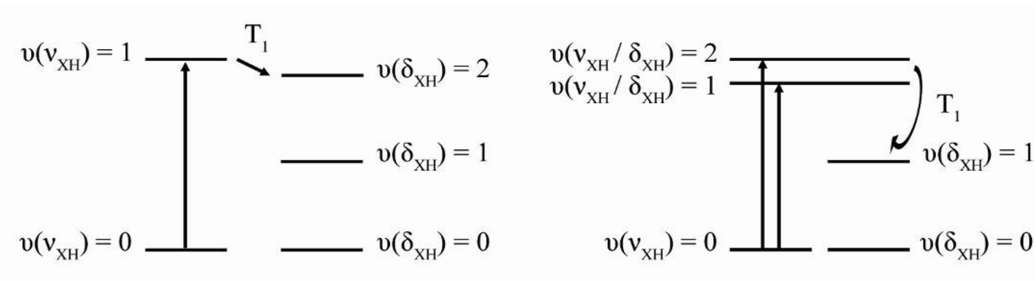

Figure 2.4: Fermi resonance scheme in the weak (left) and strong (right) coupling limits between the X−H stretching $\upsilon(\nu_{XH}) = 1$ and the $\upsilon(\delta_{XH}) = 2$ bending levels. In the weak Fermi resonance facilitates an efficient relaxation channel for energy redistribution, whereas in a strong coupling case explains the observation of additional transitions within the X−H stretching bands.

2.4.3 Davydov coupling between local X−H stretching oscillators

In systems where multiple hydrogen bonded oscillators exist in one molecular ensemble, for instance X–H stretching modes in 2-pyridone or acetic acid dimer, in *amide I* vibrations in peptides or in nucleic acid base pairs, an excitonic type of interaction (Davydov coupling) may occur between different resonant oscillators [24,35]. One can distinguish two limiting cases of weak and strong coupling, in similar fashion like it has been done for the Fermi resonance in the previous paragraph. Small couplings (Figure 2.5, left scheme) make the vibrational excitation energy transfer between the neighbouring oscillators possible, whereas strong coupling (Figure 2.5, right scheme), by creating the new combinations of quantum states, explains the energy delocalization and the line splitting [27].

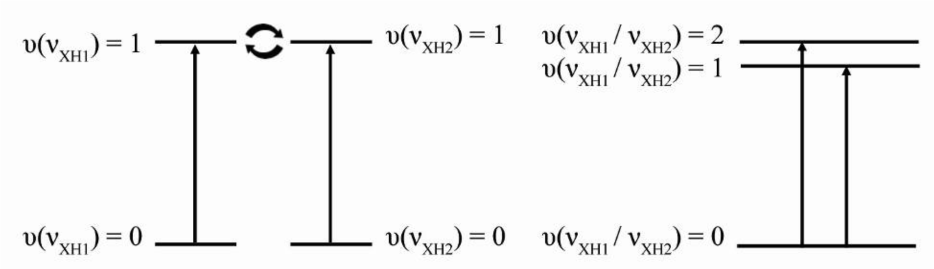

Figure 2.5: The Davydov coupling scheme in the weak (left) and strong (right) limits between $\upsilon(\nu_{XH}) = 1$ levels of different X−H oscillators explain the phenomenon of vibrational excitation energy transfer (left) and excitation delocalization (right).

2.4.4 Coupling with fluctuating solvent modes. Spectral diffusion

All the coupling mechanisms described in sections 2.4.1 - 2.4.3 occur simultaneously and, for the non-fluctuating systems like isolated cyclic acetic acid dimer or 2-pyridone/2-hydroxypyridine dimer, they are the main reason why the X–H stretching band displays many subcomponents [19,22].

In liquids such as water, hydrogen fluoride, ammonia or alcohols, intermolecular hydrogen bonds form extended networks, which structure undergo permanent distortion due to the (mainly electrostatic) interactions with the solvent bath. The long-range fluctuating Coulomb forces and hydrogen bond lengths lead to changes of transition frequencies and a decay of vibrational coherence (vibrational dephasing), both greatly contributing to the line shape [36,37,38,39,40,41]. The theoretical description of the vibrational relaxation phenomenon together with a brief discussion about the vibrational line shape problem will be given in Section 3.7.

The frequency of a particular transition (e.g., $\upsilon(\nu_{X-H}) = 0 \rightarrow 1$) in a disordered hydrogen-bond network depends on the local environment, resulting in a (inhomogeneous) frequency distribution within the absorption band. However, the structure of this network and – thus – local molecular environment fluctuate in time, changing the frequency of a considered oscillator. This (typically ultrafast) stochastic frequency shifts within the spectral envelope of a particular oscillator are called *spectral diffusion* [42].

Recently, spectral diffusion in H_2O has been observed directly with help of the two- and three-pulses photon echo experiments [41,43]. 2D spectra of the OH stretching mode have revealed that the configuration of water molecules interacting with an excited OH stretching oscillator changes within 50 fs significantly enough to destroy a major part of the correlation between the initial and final structural arrangement (ultrafast loss of structural memory).

Hydrated DNA combines quasi-static (N−H···N and N−H···O hydrogen bonds involved in the double helix) and fluctuating hydrogen-bond structures (water molecules beyond the first solvation shell). Understanding the ultrafast microscopic structural dynamics of hydrated DNA is the main goal of this thesis.

2.5 Two-dimensional correlation spectroscopy

In general, one of the most important difficulties in analysing the linear infrared spectra is existence of spectrally overlapping peaks. To overcome this problem, generalized 2D correlation analysis based on *Noda* concept [44] is frequently used. In this method, the congested spectra of perturbed sample consisting of many overlapped peaks can be simplified and the spectral resolution increased by spreading peaks over a second dimension. Further advantages are its ease of application and the possibility to make the distinction between band shifts and band overlap. Each type of spectral event, band shifting, overlapping bands of which the intensity changes in the opposite direction, band broadening, baseline change, etc. has a particular 2D pattern. Intriguing potential has the *heterospectral correlation*, where separate spectroscopic data obtained by means of two electromagnetic probes are combined using 2D correlation (heterospectral correlation analysis between completely different types of spectroscopic techniques such as IR and X-ray scattering or closely related spectroscopic measurements like IR/NIR, IR/Raman, UV-Vis/NIR, etc.).

In the following chapter, the theory of generalized two-dimensional spectroscopy together with a practical realisation will be briefly introduced.

The changes of the infrared band intensity, its shape and spectral position, induced by an external perturbation can be transformed into two-dimensional correlation spectra as described in the book of I. Noda and Y. Ozaki [45].

Temperature and concentration are the most commonly used static perturbations for generalized 2D spectroscopy. Among other experiments, the temperature-induced dissociation of hydrogen-bonded systems in alcohols [46,47,48,49,50,51] and amides [47,52,53], the denaturation of proteins [54,55], melting and premelting behaviour of polymers [56,57,58] should be noted. A number of experiments have been performed for concentration- or composition-dependent spectral modifications of simple molecules, proteins, polymers and multicomponent mixtures. Concentration changes often induce nonlinear structural perturbations for a variety of molecules. 2D correlation analysis is a potentially useful technique for finding such changes, because if the systems yield nonlinear responses of spectral intensities to concentration changes (i.e., apparent deviation from the classical Beer-Lambert law), some new features not readily analyzable by conventional techniques may be extracted [59].

The 2D correlation spectroscopy of the pressure or pH-dependent spectral variations has been used to investigate protein structural changes [60] and denaturation, or polymer deformations mechanisms [61]. 2D correlation spectroscopy has become very popular among optical spectroscopists, in particular for those who analyze IR or Raman spectra. In recent years, to investigate molecular orientation and structure of liquid crystals, 2D IR polarization angle-dependent spectroscopy has been used [62]. 2D IR maps can also be created for reaction-based spectral intensity changes, which make the technique very useful in studying complex reaction kinetics, in electrochemistry and photochemistry (Refs. in [45]). An example of chemical reactions studied by 2D correlation spectroscopy is an H/D exchange reaction to probe the secondary structure of protein [63,64,65].

Other stimuli that are frequently used for 2D correlation spectroscopy are mechanical deformation or an electric field. Recently the latter one has been particularly useful for exploring the mechanism of the reorientation of liquid crystals [66,67].

In the following section, based on several publications [45,68,69,70], the fundamental concept of perturbation-based 2D correlation spectroscopy will be provided. Discussion involves a formal mathematical as well as practical numerical computation procedure to generate 2D correlation spectra. Furthermore, basic properties of synchronous and asynchronous maps will be given and two scaling methods that enhance weak spectral contributions will be discussed.

An external perturbation θ, applied on the system during a fixed interval θ_{min} and θ_{max}, induce variations in the spectral intensity $y(v,t)$. Depending on the type of experiment, this external variable θ can be simply time or any other measure of physical quantity, such as temperature, concentration, pH, voltage, etc. The variable v can be any appropriate spectral index used in the field of spectroscopy (Raman shift, wavelength, scattering angle, etc.).

The response of the externally perturbed system leads to distinctive changes in the measured spectrum. This spectral variations induced by an external perturbation are referred to as a *dynamic spectrum* in 2D correlation, defined as:

$$\tilde{y}(\nu,\theta)=\begin{cases} y(\nu,\theta)-\bar{y}(\nu) & \text{for } \theta_{\min}\le\theta\le\theta_{\max} \\ 0 & \textit{otherwise} \end{cases} \tag{2.14}$$

where $\bar{y}(\nu)$ is the reference spectrum, which is not strictly specified, but in most cases the averaged spectrum is used, as:

$$\bar{y}(\nu) = \frac{1}{\theta_{\max} - \theta_{\min}} \int_{\theta_{\min}}^{\theta_{\max}} y(\nu,\theta)\, d\theta \qquad (2.15)$$

Depending on the experiment, it is sometimes better to select a different type of reference spectrum by choosing a spectrum observed at some fixed reference point: $\theta = \theta_{\mathrm{ref}}$, i.e., $\bar{y}(\nu) = y(\nu, \theta_{ref})$. However, without any prior knowledge about the specific physical origin of the dynamic spectrum, the reference spectrum as defined by Eq. (2.15) is recommended to be used for the correlation analysis.

The intensity of a 2D correlation spectrum, denoted as $X(\nu_1, \nu_2)$, is equal to the cross-correlation function designed to compare the dependence patterns on parameter θ of two chosen quantities $y(\nu_1, \theta)$ and $y(\nu_2, \theta)$ measured at two different spectral variables ν_1 and ν_2:

$$X(\nu_1,\nu_2) = \Phi((\nu_1,\nu_2) + i\Psi(\nu_1,\nu_2) = \frac{1}{\pi(\theta_{\max} - \theta_{\min})} \int_{0}^{\infty} Y_1(\Theta) \cdot Y_2(\Theta)\, d\Theta \qquad (2.16)$$

where $Y_1(\Theta)$ is the forward Fourier transform of the spectral variation $y(\nu_1, \theta)$ observed at a given spectral variable ν_1 with respect to the external variable θ

$$Y_1(\Theta) = \int_{-\infty}^{\infty} y(\nu_1,\theta) \cdot e^{-i\Theta\theta} d\theta \qquad (2.17)$$

and a similar expression holds for $y(\nu_2, \theta)$.

The intensity of a synchronous 2D correlation peak $\Phi(\nu_1, \nu_2)$ represents simultaneous or coincidental changes of two separate spectral intensity variations measured at ν_1 and ν_2 (cf. Figure 2.6). In contrast, the intensity of an asynchronous spectrum $\Psi(\nu_1, \nu_2)$ represents sequential or successive instead of coincidental changes of spectral intensities. The asynchronous spectrum has no diagonal peaks, and cross peaks appear only if the intensities of the two spectral changes are noncoincident. In addition, the sign of asynchronous peaks provides information on the sequential order of spectral changes (cf. Figure 2.7).

The basic concept of 2D correlation spectroscopy is closely related to the classical statistical theory of cross-correlation analysis.

One can express the *cross-correlation* function as:

$$C(\tau) = \frac{1}{\theta_{\max} - \theta_{\min}} \int_{\theta_{\min}}^{\theta_{\max}} \tilde{y}(\nu_1,\theta) \cdot \tilde{y}(\nu_2,\theta+\tau)\, d\theta, \qquad (2.18)$$

where τ is the correlation variable. The function compares the dependence (in function of perturbation parameter θ) of two separate functions (i.e., intensities of dynamic spectra measured at two different wavenumbers) shifted by a fixed constant τ. The corresponding cross spectrum $S(\omega)$, which is the Fourier transform of the cross-correlation function, is given by:

$$S(\omega) = \frac{\widetilde{Y}_1^*(\omega) \cdot \widetilde{Y}_1^*(\omega)}{\theta_{\max} - \theta_{\min}} = \phi_\omega(v_1, v_2) - i\psi_\omega(v_1, v_2). \tag{2.19}$$

It can be shown [45], that using the Wiener-Khintchine theorem (which establishes a convenient relationship between a cross-correlation of two functions and their Fourier transforms), the synchronous 2D correlation intensity $\Phi(v_1, v_2)$ can be directly calculated from the *cross-correlation* function with $\tau = 0$. It is important to note, that the determination of the cross-correlation function according to Eq. (2.18) does not require the use of the Fourier transformation of dynamic spectra and hence the synchronous 2D correlation spectra can be easily computed as:

$$\Phi(v_1, v_2) = \frac{1}{\theta_{\max} - \theta_{\min}} \int_{\theta_{\min}}^{\theta_{\max}} \widetilde{y}(v_1, \theta) \cdot \widetilde{y}(v_2, \theta)\, d\theta \tag{2.20}$$

To bypass Fourier transformation in calculating the asynchronous spectrum, the Hilbert transformation of dynamic spectra is utilized.

For a given analytic function *g(t)*, its *Hilbert transform h(t)* is defined by:

$$h(t) \equiv \frac{1}{\pi}\, {}_{pv}\!\int_{-\infty}^{\infty} \frac{g(\theta')}{\theta' - \theta} d\theta' \tag{2.21}$$

where the singularity at the point where $\theta' = \theta$ is excluded from the integration (Cauchy principal value). The functions *g(t)* and *h(t)* are *orthogonal* to each other with a relationship:

$$\int_{-\infty}^{\infty} g(t) \cdot h(t)\, dt = 0 \tag{2.22}$$

It can be presented [45] that the asynchronous 2D correlation spectrum can be computed directly from the dynamic spectrum and the orthogonal spectrum:

$$\Psi(v_1, v_2) = \frac{1}{\theta_{\max} - \theta_{\min}} \int_{\theta_{\min}}^{\theta_{\max}} \widetilde{y}(v_1, \theta) \cdot \widetilde{z}(v_2, \theta)\, d\theta \tag{2.23}$$

where the orthogonal spectrum $\widetilde{z}(v_2, \theta)$ is the Hilbert-transform of the dynamic spectrum $\widetilde{y}(v_2, \theta)$.

In a typical measurement, the spectral data are obtained in digitized discrete form rather than as continuous functions.

For a series of m sequentially collected spectral data $y_i(v)$ with a fixed increment along the external variable θ_j (between θ_{min} and θ_{max}), the dynamic spectra are defined as:

$$\tilde{y}_j(\nu) = \tilde{y}_j(\nu) - \bar{y}(\nu) \quad \mathrm{j} = 1, 2, \ldots, \mathrm{m} \tag{2.24}$$

If the average spectrum given by:

$$\bar{y}(\nu) = \frac{1}{m} \sum_{j=1}^{m} y_j(\nu) \tag{2.25}$$

is used for the reference, the dynamic spectra reduce to the *mean-centred* spectra.

It is possible to calculate standard intensity deviation of spectral intensity fluctuations observed at a selected wavenumber ν:

$$\sigma(\nu) = \sqrt{\sum_{j=1}^{m} \left[y_j(\nu) - \bar{y}(\nu) \right]^2} \tag{2.26}$$

The integral in Eq. (2.20) can be transformed to a discrete summation form and hence, the synchronous 2D correlation intensity may be directly calculated from the dynamic spectra:

$$\Phi(\nu_1, \nu_2) = \frac{1}{m-1} \sum_{j=1}^{m} \tilde{y}_j(\nu_1) \cdot \tilde{y}_j(\nu_2) \tag{2.27}$$

Similarly, by adopting Eq. (2.23) for a discrete set of dynamic spectra, one obtains the computational formula for an asynchronous spectrum:

$$\Psi(\nu_1, \nu_2) = \frac{1}{m-1} \sum_{j=1}^{m} \tilde{y}_j(\nu_1) \cdot \tilde{z}_j(\nu_2) \tag{2.28}$$

The discrete orthogonal spectra $\tilde{z}_j(\nu_2)$ can be directly obtained from the dynamic spectra $\tilde{y}_j(\nu_2)$ using a simple linear transformation:

$$\tilde{z}_j(\nu_2) = \sum_{k=1}^{m} N_{jk} \cdot \tilde{y}_k(\nu_2) \tag{2.29}$$

where

$$N_{jk} = \begin{cases} 0 & \text{for} \quad j = k \\ 1/\pi(k-j) & \qquad \textit{otherwise} \end{cases} \tag{2.30}$$

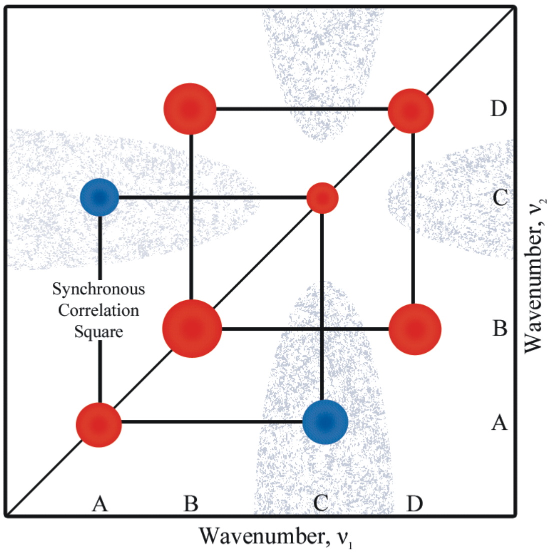

- *Autopeaks at diagonal positions represent the extent of perturbation - induced dynamic fluctuations of spectral signals.*
- *Cross peaks represent simultaneous changes of spectral signals at two different wavenumbers, suggesting a coupled or related origin of intensity variations.*
- *If the sign of a cross peak is positive, the intensities at corresponding wavenumbers are increasing (or decreasing) together. If the sign is negative, one is increasing, while the other is decreasing, i.e., changes in opposite directions.*

Figure 2.6: Schematic contour map of a synchronous ($\Phi(\nu_1, \nu_2)$ 2D correlation spectrum together with a brief summary of their interpretation rules. Shaded areas indicate negative correlation intensity.

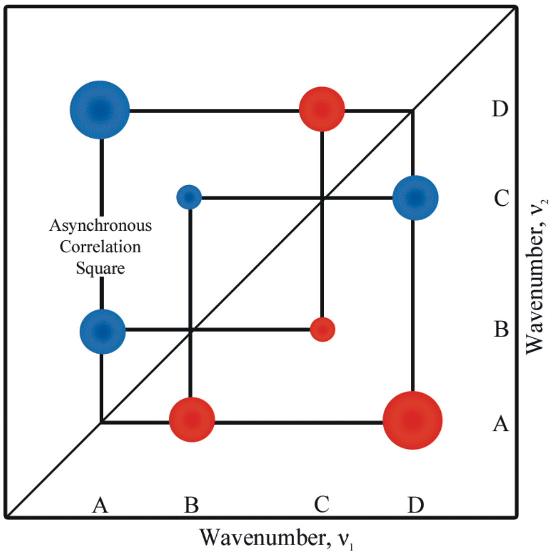

- *Cross peaks develop only if the intensities of two spectral features change out of phase with each other.*
- *The sign of a cross peak is positive if the intensity change at* ν_1 *occurs before* ν_2.
- *The sign of a cross peak is negative if the intensity change at* ν_1 *occurs after* ν_2.
- *The above sign rules are reversed if* $\Phi(\nu_1,\nu_2)<0$
- *The intensity changes at bands A and C occur after the changes at B and D.*

Figure 2.7: Schematic contour map of an asynchronous (Ψ (ν_1, ν_2)) 2D correlation spectrum together with a brief summary of their interpretation rules.

The synchronous and asynchronous 2D correlation maps presented in this thesis have been computed using home-made MATLAB script, where the set of dynamic spectra collected as a function of external perturbation have been composed in matrix form.

In such case, the spectral data matrix **Y** consist of *m* rows of dynamic spectra (each measured at a different perturbation variable $\theta = \theta_1, \theta_2, \ldots, \theta_m$) and *n* columns of spectral intensity variations along the external variable:

$$\mathbf{Y} = \begin{bmatrix} \tilde{y}(\nu_1,\theta_1) & \tilde{y}(\nu_2,\theta_1) & \cdots & \tilde{y}(\nu_n,\theta_1) \\ \tilde{y}(\nu_1,\theta_2) & \tilde{y}(\nu_2,\theta_2) & \cdots & \tilde{y}(\nu_n,\theta_2) \\ \vdots & \vdots & \cdots & \vdots \\ \tilde{y}(\nu_1,\theta_m) & \tilde{y}(\nu_2,\theta_m) & \cdots & \tilde{y}(\nu_n,\theta_m) \end{bmatrix} \tag{2.31}$$

It can be easily shown that synchronous spectrum may be related to the *covariance matrix* of the observed experimental result, if the sampling measurement is taken at fixed interval. Hence, a synchronous spectrum in matrix representation takes the form:

$$\Phi = \frac{1}{m-1}\mathbf{Y}^{\mathrm{T}}\mathbf{Y} \tag{2.32}$$

Similarly, the matrix form of an asynchronous spectrum is given by multiplying the data matrix **Y** and the orthogonal counterpart of **Y** obtained by the Hilbert transformation:

$$\Psi = \frac{1}{m-1}\mathbf{Y}^{\mathrm{T}}\mathrm{N}\,\mathbf{Y} \tag{2.33}$$

where **N** (*m* x *m*) is the *Hilbert-Noda transformation matrix*

$$\mathrm{N} = \frac{1}{\pi}\begin{bmatrix} 0 & 1 & \frac{1}{2} & \frac{1}{3} & \cdots \\ -1 & 0 & 1 & \frac{1}{2} & \cdots \\ -\frac{1}{2} & -1 & 0 & 1 & \cdots \\ -\frac{1}{3} & -\frac{1}{2} & -1 & 0 & \cdots \\ \vdots & \vdots & \vdots & \vdots & \ddots \end{bmatrix} \tag{2.34}$$

which by premultiplication provides the expression equivalent to a pertinent segment of the Hilbert transform of each column vector of **Y**.

Generalized 2D correlation spectra given by Eqs. (2.27) and (2.28) correspond to the real and imaginary part of complex cross-correlation function (Eq. 2.18). They contain both information about the magnitude and relative phase of intensity variations. Signal fluctuations with large amplitude tend to dominate the 2D correlation spectra, often obscuring the relatively small but important features [71]. This problem is especially serious for a synchronous peaks located close to the main diagonal, where they can be easily covered by overlapping strong autopeaks.

To enhance weak spectral contributions in 2D correlation spectra, various scaling methods have been proposed [70]. The technique called *unit-variance scaling* eliminates the effect of magnitude of intensity variations leaving only correlational information. Since the correlation intensity is all normalized to unity, no useful information can be extracted around the main diagonal of the synchronous map. Moreover, the method significantly amplifies the noise contributions. *Pareto scaling*[3], on the other hand, by using the square root of standard deviation as a scaling factor, circumvents the amplification of noise by retaining the small portion of magnitude information. Using the Eqs. (2.26-2.28), the *Pareto-scaled* 2D correlation spectra can be defined as:

$$\Phi(\nu_1,\nu_2)^{Pareto} = \frac{\Phi(\nu_1,\nu_2)}{\sqrt{\sigma(\nu_1)\cdot\sigma(\nu_2)}} \tag{2.35}$$

$$\Psi(\nu_1,\nu_2)^{Pareto} = \frac{\Psi(\nu_1,\nu_2)}{\sqrt{\sigma(\nu_1)\cdot\sigma(\nu_2)}} \tag{2.36}$$

In Pareto-scaled 2D spectra, minor peaks become much better visible and the autopeaks along the diagonal in the synchronous spectrum after scaling are still discernible.

All the two-dimensional spectra presented throughout this thesis, are generated using the algorithm based on Pareto-scaling method.

Infrared spectroscopy is widely used for structural analysis of polypeptides and proteins because many functional groups have characteristic vibrational frequencies. However, their spectra are affected by coupling of the vibrations of neighbouring peptide groups [72]. This coupling is analogous to exciton interactions of electronic transitions, and its results in similar splitting of the absorption bands (compare Section 2.4.3). In addition, the situation is complicated by coupling of the transitions through both covalent bonds and hydrogen bonds as well as through space. A linear infrared spectroscopy provides only time-averaged picture, having no possibility to diminish different microscopic interaction mechanisms.

As a consequence, combination of frequency and time-domain spectroscopic method, like (multidimensional) nuclear magnetic resonance and time-resolved optical spectroscopy, are required to investigate the dynamics of hydrogen-bonding systems. The fastest events that can be grasp by NMR spectroscopy have a time scale of milli- to microseconds. In contrary, with optical spectroscopy employing ultrashort laser pulses it is possible to study even the fastest dynamics occurring on a time scale of a few femtoseconds [13]. Time-resolved infrared spectroscopy, in particular two third-order nonlinear techniques: pump-probe (see Sections 3.10 and 4.4) and photon echo have been extensively applied in studying hydrogen-bonded systems. The introduction to nonlinear spectroscopy will be given in the next chapter.

---

[3] Vilfredo Pareto (1848-1923), Italian economist, well known from his famous Pareto principle, also known as the heuristic 80-20 rule.

3 Nonlinear spectroscopy

Nonlinear optical spectroscopy is a powerful tool to study the dynamics and interactions of condensed matter systems. Time-resolved vibrational experiments allow to extract spectroscopic information that is hidden in a conventional measurement of the infrared or Raman spectra.

3.1 Optical polarization

The light emitted from conventional light sources such as bulb or flash is neither monochromatic nor coherent and hence, the amplitude does not exceed the values 10^5 V/m, which correspond to several W/m^2. The radiation of such intensities interacting with matter (by absorption, light propagation, dispersion, reflection and refraction) does not change significantly its macroscopic and microscopic properties because it is several orders of magnitude smaller than the electric field in matter (about 10^{11} V/m) [73]. For a low intensity of light, the polarization, P induced in the material depends linearly on the electric field intensity E:

$$P_i = \chi^{(1)}_{ij} E_j \tag{3.1}$$

where the quantity $\chi(n)$ is the electric susceptibility tensor of order n and indices i and j denote the Cartesian components of the polarization and the incoming field, respectively. For higher light intensity, the functional dependence of P on E is unknown, but a common assumption is that polarization can be expanded in powers of electric field:

$$P_i = \chi^{(1)}_{ij} E_j + \chi^{(2)}_{ijk} E_j E_k + \chi^{(3)}_{ijkl} E_j E_k E_l + \ldots = P^{(1)}_i + P^{(2)}_i + P^{(3)}_i + \ldots \tag{3.2}$$

This situation can be easily achieved when matter interacts with focused laser pulses, where the light intensity can reach the values 10^{16} W/m^2 with a corresponding intensity of the electric field on the order of 10^9 V/m, comparable with electric fields existing between the charges, nuclei and electrons, constituting matter. Consequently, the progress and achievements of nonlinear optics that has been made in the last 50 years was strongly correlated with laser technology development, in particular with generating short and intense laser pulses. The relationship between the light intensity I and the electric field amplitude is:

$$I = 2n\sqrt{\frac{\varepsilon_0}{\mu_0}}\left|\vec{E}_0\right|^2 \tag{3.3}$$

where n, μ_0 and ε_0 are the refractive index of the material, vacuum permeability and permittivity, respectively.

Second order nonlinear phenomena are described by the second term of Eq. (3.2). If the material is irradiated with an optical field oscillating at two frequencies, ω_1 and ω_2:

$$P^{(2)}_i(\omega) = \chi^{(2)}_{ijk} E_j(\omega_1) \cdot E_k(\omega_2) \tag{3.4}$$

then the nonlinear polarization does not oscillate at ω_1 and ω_2 but rather at new frequencies: $\omega = 2\omega_1, 2\omega_2, \omega_1+\omega_2, |\omega_1-\omega_2|$, corresponding to the second harmonic generation (SHG), sum frequency generation (SFG), difference frequency mixing (DFM), and optical rectification (OR, $\omega = 0$).

The intensity, I_i, of the field generated by the polarization at a given frequency, ω_3, is [74]:

$$I_i(\omega_3) \propto \left|\chi^{(2)}_{ijk}\right|^2 I_j I_k L^2 \sin c^2\left(\frac{\Delta kL}{2}\right) \tag{3.5}$$

with $\mathrm{sinc}(x) = \sin(x)/x$, L is the optical path length and Δk is the wavevector (phase) mismatch:

$$\Delta k = \mathbf{k}_{out} - \sum \mathbf{k}_{in} \tag{3.6}$$

where $\mathbf{k}_{\mathrm{out}}$ is the wavevector of the new outgoing field and $\mathbf{k}_{\mathrm{in}}$ are the wavevectors of the incoming fields ($|\mathbf{k}| = k = n\omega / c$). The second-order polarization gives rise to a signal field with a significant intensity only if the phase-matching condition, $\Delta k = 0$, is satisfied. Since the wavevector $\mathbf{k}$ is related to the photon momentum $\boldsymbol{p}$ ($\mathbf{p} = \hbar\mathbf{k}$) this condition simply corresponds to momentum conservation law. For example for DFM, $\omega_3 = \omega_1 - \omega_2$ and momentum conservation (or phase-matching condition), $\Delta k = 0$, imposes that $\mathbf{k}_3 = \mathbf{k}_1 - \mathbf{k}_2$. An important consequence is that SHG, SFG and DFM cannot be realized simultaneously as their respective phase-matching conditions are different.

A closer look at second order effects will be presented in Chapter 4, where a frequency optical parametric converter (OPA), an important part of the experimental set-up, is described.

In isotropic media with inversion symmetry like liquid solutions, nonlinear effects that scale with even orders of the applied laser field, vanish. Therefore, the third order nonlinear susceptibility, $P_i^{(3)}$, is the lowest nonlinear response. In general, the third order polarization is given by:

$$P_i^{(3)}(\omega_4) = \chi^{(3)}_{ijkl} E_j(\omega_3) \cdot E_k(\omega_2) \cdot E_l(\omega_1) \tag{3.7}$$

The nonlinear polarization acts as a source of electromagnetic field with an intensity I_i and a frequency ω_4 of the signal, depending on the frequencies of the incoming fields and on the geometry of the experiment [74]:

$$I_i(\omega_4) \propto \left|\chi^{(3)}_{ijkl}\right|^2 I_j I_k I_l L^2 \sin c^2\left(\frac{\Delta kL}{2}\right) \tag{3.8}$$

Also in this case, the new field intensity is the largest when $\Delta k = 0$.

Third-order nonlinear spectroscopy involves the interaction of three electric fields in the material. However, this does not imply that one absolutely has to use three different laser beams. For example, as will be discussed in more detail in the Section 3.10, conventional transient absorption spectroscopy is a third-order nonlinear spectroscopy performed with two beams. The third-order polarization technique, pump-probe spectroscopy is an example of such approach.

3.2 The quantum mechanical polarization

In condensed phase systems, we are dealing with statistical ensembles rather than pure states. Therefore, the state of the system can be conveniently described by the density operator *ρ(t)*.

The time-dependent macroscopic polarization is given by the expectation value of the dipole operator μ_i [75]:

$$P_i(t) = \langle \mu_i \rho(t) \rangle \tag{3.9}$$

Let P_k be the probability of a system being in a pure state $|\psi_k(t)\rangle$. The density matrix is then defined as:

$$\rho = \sum_k P_k \cdot |\psi_k\rangle\langle\psi_k|, \tag{3.10}$$

with $P_k \geq 0$ and $\sum_k P_k = 1$ (normalization). If one expands $|\psi(t)\rangle$ in a basis set $\{|n\rangle\}$ so that $|\psi(t)\rangle = \sum_n c_n(t)|n\rangle$ and $\langle\psi(t)| = \sum_m c_m^*(t)\langle m|$ then ρ matrix has elements:

$$\rho_{nm} = \sum_k P_k \langle n|\psi_k\rangle\langle\psi_k|m\rangle. \tag{3.11}$$

In any representation, the diagonal elements of *ρ(t)* are nonnegative and thus, ρ_{nn} can be understood as the probability of the system to be found in the state $|n\rangle$ known as *populations*:

$$\rho_{nn} = \sum_k P_k \langle n|\psi_k\rangle\langle\psi_k|n\rangle = \sum_k P_k |\langle n|\psi_k\rangle|^2 \geq 0 \tag{3.12}$$

The off-diagonal elements, $\rho_{nm}(t)$ with $n \neq m$ are in general complex numbers and may contain a phase. These elements are denoted as *coherences*.

The quantum dynamics of a condensed phase system can be conveniently described by the Liouville-von Neumann equation which depicts the temporal evolution of the density matrix operator, *ρ(t)*:

$$i\hbar \frac{\partial}{\partial t}\rho(t) = \left[H, \rho(t)\right] \tag{3.13}$$

where [A, B] denotes a commutator ([A, B] = AB - BA) and *H*, being the sum of the system Hamiltonian *H0* and the electric field of a light pulse $E(t) \cdot \mu_i$, interacting with the system:

$$H(t) = H_0 + E(t) \cdot \mu_i \tag{3.14}$$

A non-linear optical experiment is now described with a system at $t = 0$ is at thermal equilibrium, expressed by a density matrix (with probabilities given by the Boltzmann distribution). The system propagates under its Hamiltonian during the periods between the interactions with the light field (e.g. three interactions in third-order nonlinear response). The polarization is then calculated by acting from the left with the dipole operator and taking the trace, which represents the average over the ensemble:

$$P_i(t) = Tr\left(\mu_i \rho(t)\right) \tag{3.15}$$

which is equivalent to the Eq. (3.9).

3.3 The nonlinear optical response functions

The interaction energy $E(t) \cdot \mu_i$ of the systems investigated here is small compared to the transition energies of the isolated molecules. Therefore, the interaction Hamiltonian can be treated as a perturbation assuming the stationary states of the molecule itself are known.

The dipole operator in the interaction picture is defined as:

$$\mu_i(t) = U_0^\dagger \mu U_0(t, t_0) \tag{3.16}$$

and the density matrix takes the form:

$$\rho_I(t) = U_0^\dagger \rho(t) U_0(t, t_0), \tag{3.17}$$

where $U_0(t,t_0)$ is the time evolution operator. Since H_0, the material Hamiltonian, is time independent and the time-dependent radiation-matter interaction is treated perturbatively, U_0 is simply given by:

$$U_0(t, t_0) = \exp\left[-\left(\frac{i}{\hbar}\right) H_0 \left(t - t_0\right)\right] \tag{3.18}$$

The Liouville-von Neumann equation (3.13) can be formally integrated and expanded in powers of the electric field. In the interaction picture, the perturbative expansion of the n^{th}-order density matrix $\rho(t) = \rho^{(0)}(t_0) + \sum_n \rho^{(n)}(t)$ yields [76]:

$$
\begin{aligned}
\rho^{n}(t) = \left(-\frac{i}{\hbar}\right)^{n} \int_{t_0}^{t} d\tau_n \int_{t_0}^{\tau_n} d\tau_{n-1} \ldots \int_{t_0}^{\tau_2} d\tau_1 E(\tau_n) \cdot E(\tau_{n-1}) \cdot \ldots \cdot E(\tau_1)\, U_0(t,t_0) \cdot \\
\cdot \left[\mu_i(\tau_n), \left[\mu_i(\tau_{n-1}), \ldots \left[\mu_i(\tau_1), \rho(t_0)\right] \ldots\right]\right] \cdot U_0^{\dagger}(t,t_0)
\end{aligned}
\tag{3.19}
$$

$\rho(t_0)$ is an equilibrium density matrix which does not evolve in time when subject of the system Hamiltonian H_0, and therefore $t_0 \rightarrow -\infty$.

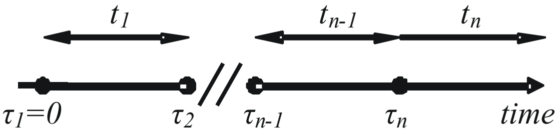

Figure 3.1: Time variables used in Eqs. (3.20) and (3.21). The time points when the interactions between the radiation field and matter takes place are denoted by τ and the time intervals between these interactions are represented by t.

By replacing the time variables according to the Figure 3.1 and then inserting Eq. (3.19) into (3.9), one obtains the expression for the n^{th}-order polarization:

$$
\begin{aligned}
P_i^{(n)}(t) = \int_{-\infty}^{\infty} dt_n \int_{-\infty}^{\infty} dt_{n-1} \ldots \int_{-\infty}^{\infty} dt_1\, S^{(n)}(t_n, t_{n-1}, \ldots, t_1) \times \\
\times E(t - t_n) \cdot E(t - t_n - t_{n-1}) \cdot \ldots \cdot E(t - t_n - t_{n-1} - \ldots - t_1
\end{aligned}
\tag{3.20}
$$

with

$$
\begin{aligned}
& S_i^{(n)}(t_n, t_{n-1}, \ldots, t_1) \equiv \\
& \equiv \left(-\frac{i}{\hbar}\right)^{n} \Theta(t_1)\Theta(t_2)\cdots\Theta(t_n) \times \\
& \times \left\langle \mu_i(t_n + \ldots + t_1)\left[\mu_i(t_{n-1} + \ldots + t_1), \ldots \left[\mu_i(0), \rho(-\infty)\right] \ldots\right]\right\rangle
\end{aligned}
\tag{3.21}
$$

The n^{th}-order nonlinear response function, $S^{(n)}$, carries the complete microscopic information necessary for the calculation of optical signals. The response function is defined for positive times t_j only, which is guaranteed by the Heaviside step function [Θ (t_j) = 1 for $t_j > 0$ and Θ (t_j) = 0 for $t_j < 0$]:

$$
S_i^{(n)}(t_n, t_{n-1}, \ldots, t_1) = 0 \tag{3.22}
$$

The reason for vanishing the response function, $S^{(n)}$ if any of its time arguments t_j become negative, reflects the principle of causality, which implies that the cause (here: electric field, *E*) must precede the effect (polarization, P_i).

The optical response function is a sum of *2^n* tensors (in practise only half of them are independent and need to be considered; the other half is the complex conjugate of the former), each consisting of *(n+1)* dipole correlation functions. These tensors, together with the possible field interactions represent the potential light matter interactions called Liouville space pathways. Graphic representation of these paths is provided by the double-sided Feynman diagrams, which will be introduced in the next section.

3.4 Feynman diagrams

The ensemble averaged part in the Eq. (3.21) for the third-order nonlinear response of a two-level system can be rewritten as a sum of eight terms:

$$\begin{aligned}
&\langle \mu(t_3+t_2+t_1)[\mu(t_2+t_1),[\mu(t_1)[\mu(0)],\rho(-\infty)]]\rangle = && \\
&= \langle \mu(t_3+t_2+t_1)\mu(t_2+t_1)\mu(t_1)\mu(0)\rho(-\infty)\rangle - && \Rightarrow R_4 \\
&- \langle \mu(t_3+t_2+t_1)\mu(t_2+t_1)\mu(t_1)\rho(-\infty)\mu(0)\rangle - && \Rightarrow R_1^* \\
&- \langle \mu(t_3+t_2+t_1)\mu(t_2+t_1)\mu(0)\rho(-\infty)\mu(t_1)\rangle + && \Rightarrow R_2^* \\
&+ \langle \mu(t_3+t_2+t_1)\mu(t_2+t_1)\rho(-\infty)\mu(0)\mu(t_1)\rangle - && \Rightarrow R_3 \\
&- \langle \mu(t_3+t_2+t_1)\mu(t_1)\mu(0)\rho(-\infty)\mu(t_2+t_1)\rangle + && \Rightarrow R_3^* \\
&+ \langle \mu(t_3+t_2+t_1)\mu(t_1)\rho(-\infty)\mu(0)\mu(t_2+t_1)\rangle + && \Rightarrow R_2 \\
&+ \langle \mu(t_3+t_2+t_1)\mu(0)\rho(-\infty)\mu(t_1)\mu(t_2+t_1)\rangle - && \Rightarrow R_1 \\
&- \langle \mu(t_3+t_2+t_1)\rho(-\infty)\mu(0)\mu(t_1)\mu(t_2+t_1)\rangle && \Rightarrow R_4^*
\end{aligned} \tag{3.23}$$

Since half of the terms in Eq. 3.23 are the complex conjugates of the other half, only four Feynman diagrams (four different Liouville space pathways) have to be considered here (Figure 3.2).

In these diagrams, the density operator is symbolized by two vertical lines: the time evolution of the ket is represented by the left line and the temporal evolution of bra – by right line, while time runs from the bottom to the top. Interactions with the light fields are represented by arrows: these pointing towards the diagram represent photon absorption, while the others, pointing away, symbolize photon emission. An arrow pointing to the right represents an electric field with a phase factor $e^{-i\omega t+i\mathbf{k}\mathbf{r}}$, while an arrow pointing to the left represents its complex conjugate. The central part of the diagram, between the pair of vertical lines, contains information on the density matrix ρ during the corresponding time interval (e.g. the density matrix for a two-level system has four elements $\rho = \begin{pmatrix} \rho_{gg} & \rho_{ge} \\ \rho_{eg} & \rho_{ee} \end{pmatrix}$, with subscripts *g* and *e* for the ground and excited states, respectively) [77]. Each diagram has an overall sign of *$(-1)^n$*, where *n* is the number of interactions from the right (acting with the dipole operator onto the bra). The last interaction (dashed arrow) is not part of the commutator, but originates from the trace in Eq. (3.9). It corresponds to the emission of light (an arrow pointing to the left) whose k-vector and frequency is determined by the preceding field interactions. The last interaction must lead to the system arriving in a population state.

In practice, the above described rules for constructing double-sided Feynman diagrams are frequently employed to establish the relevant terms of optical response functions. The rotating wave approximation (RWA) reduces the number of relevant interactions to resonant processes, which have a significant contribution to the signal. Some of the field interaction sequences can be excluded by the phase-matching condition due to the geometry of an experiment. Usually, only a few diagrams survive the RWA and the phase-matching condition.

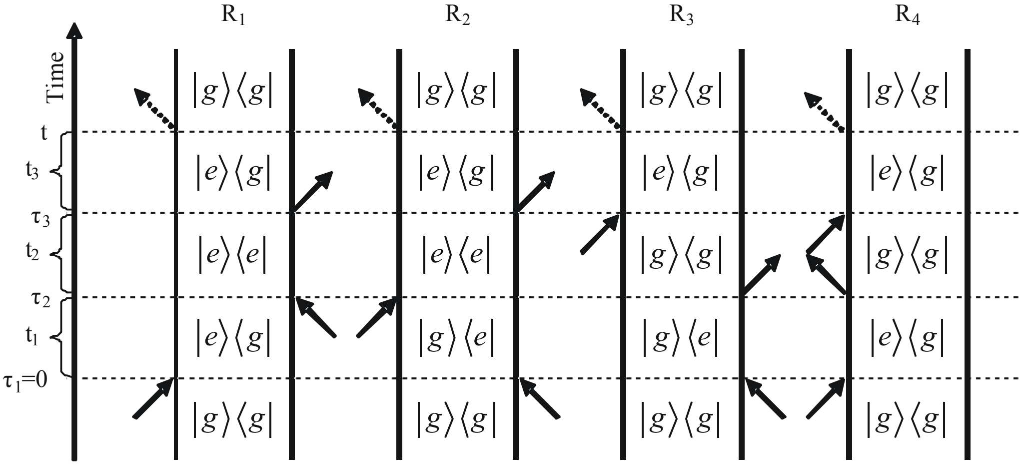

Figure 3.2: The third order response of a two-level system represented with double-sided Feynman diagrams.

3.5 The reduced density matrix and thermal averaging

The quantum dynamics of a condensed phase system which is in contact with a heath bath can be described in terms of density matrix *ρ(t)* which evolves according to the Eq. 3.13, now taking into account system-bath interaction in Hamiltonian governing the dynamics of the states:

$$i\hbar\frac{\partial}{\partial t}\rho(t)=\left[H_0+H_I(t)+H_{SB}(t),\rho(t)\right] \tag{3.24}$$

Here, H_0 is the Hamiltonian of unperturbed system and H_I describes the coupling between the system and applied electromagnetic field. The interaction between the system and the thermal bath is contained in H_{SB}. The random interactions $H_{SB}(t)$ have to be averaged over the statistical ensemble. It is often assumed that this always gives rise to the time-independent parameters in the Liouville - von Neumann equation of motion. The set of coupled differential equations called the optical Bloch equations, which describe the evolution of a two-level system interacting with a strong radiation field and with thermal bath, are the example of such approach. The effects of a bath are incorporated via relaxation parameters representing population relaxation (T_1) and coherence dephasing (T_2).

For large systems (such as investigated here molecules in condensed matter), with many degrees of freedom (in order of Avogadro's number) it is impossible to know the entire microscopic state. In such cases, a reduced description is needed, where one follows only the dynamics of a few selected and relevant molecules' degrees of freedom and the other degrees of freedom (e.g. surrounding solvent degrees of freedom) are treated as a thermal bath using methods of quantum statistical mechanics. Thus, instead of calculating the entire density matrix ρ as defined in Eq. 3.11, one need to know the density operator defined in the subspace of the system's degrees of freedom, called *reduced system density operator*, with the elements given by [76]:

$$\sigma_{nm}(t) = \sum_{\alpha} \langle n\alpha | \rho(t) | m\alpha \rangle = Tr_B \langle n | \rho(t) | m \rangle \tag{3.25}$$

where $|\alpha\rangle$ denotes the thermal bath eigenstates and Tr_B is a partial trace over the bath degrees of freedom. *Reduced description*, which offers the possibility to describe only the part of the system of interest, has a close analogy in the concept of entropy.

The entropy of any system represented by density operator ρ can be defined as [78]:

$$S = k_B \ln \Omega = -k_B Tr(\rho \ln \rho) \tag{3.26}$$

where Ω is the total number of accessible microstates of the system[4] and k is the Boltzmann constant. The entropy of a system described by the density operator ρ is time independent:

$$\dot{S} \equiv \frac{i}{\hbar} k_B Tr[H, \rho \ln \rho] = 0 \tag{3.27}$$

The entropy for a system described by reduced density operator σ is defined as:

$$S = k_B Tr_S(\sigma \ln \sigma) \tag{3.28}$$

and due to dephasing and relaxation processes induced by bath, does change in time. In a complete dynamic description of a system, the entropy does not need to be introduced. However, on the greatly reduced thermodynamic level, entropy is crucial for a proper description of the system, and the entropy of the subsystem reflects the loss of information about the system.

3.6 The role of dephasing processes

Physical observables are directly related to the density operator introduced in the section 3.2. In contrast to the wavefunction representation, every quantity appearing in the density operator description has a physical meaning and classical analogue. When an off-diagonal density operator element (coherence) evolves in time, it acquires a phase, which depends on the state of the environment (bath). Performing an ensemble average of the off-diagonal density operator elements over the distribution of the environment degrees of freedom results in a damping of these elements, called phase relaxation or simply dephasing. It is important to note, that

---

[4] The density operator represents an ensemble of systems through a mixed state. When Ω = 1, the ensemble is said to be a pure ensemble. The fact that the entropy vanishes for pure states is essentially the third law of thermodynamics.

describing the dephasing processes is possible only in the Liouville space with distinguishable diagonal and off-diagonal elements of the density operator matrix. If one would follow explicitly the dynamics of all degrees of freedom, the wavefunction description is correct and the concept of dephasing would be not necessary [76].

3.7 Vibrational relaxation

The vibrational energy relaxation in a condensed medium can be characterized, in the simplest approximation, by two processes: energy relaxation processes (population relaxation) defined as a lifetime in the excited vibrational level T_1 and the phase relaxation (dephasing time, T_2). From phenomenological point of view, the dephasing process is a quasi-elastic process in which the interactions with the environment destroy the phase coherence of the system, but do not remove the system from the quantum state of interest [79].

The limitations of the Bloch description of relaxation in terms of parameters T_1 and T_2 stem from the fact that this model requires a distinct time scale separation between the dynamics of the system and the bath motions. If the local environment fluctuates on a very fast time scale, its effect on the system can be averaged to constant parameters. In this *fast modulation* (*Markovian*) limit, the effects of the bath on the dynamics of the two-level system of Eq. 3.24 can be completely described by phenomenological relaxation parameter T_1, that affect the diagonal matrix elements of the density operator projected on the basis set of eingenfunctions of H_0 and parameter T_2, which governs the relaxation of the off-diagonal elements [80]. As a consequence, the optical transitions in the linear response regime are (homogenously) broadened. For a homogeneous line of width $1/(\pi T_2)$ the dephasing time T_2 is given by:

$$\frac{1}{T_2}=\frac{1}{T_2^*}+\frac{1}{2T_1} \tag{3.29}$$

where T_2^* is pure dephasing time, which describes the adiabatic modulation of the vibrational energy levels of a transition caused by fast fluctuations of its environment [81,82]. Thus, the measured vibrational linewidth may be dominated by population relaxation, dephasing or a combination of both. If the line is inhomogeneously broadened as a result of slow bath dynamics compared to that of the system, neither the dephasing time nor the population-decay time is directly related to the observed linewidth [79].

3.8 Line broadening mechanisms

The vibrational line shape of condensed matter systems contains detailed information about the interactions of system of interest (e.g. normal mode) with its environment (e.g. solvent molecules). Theories of spectral line shape analysis traditionally make a distinction between the different mechanisms responsible for the line broadening. Kubo [83] formulated the theory (originally developed for nuclear spin transitions) of linear response based on stochastic treatment of describing an oscillator whose frequency is modulated in a random way. In this approach, two limiting cases can be distinguished by the separation of time scales. In the slow modulation (static) limit, the correlation time of the bath dynamics is long compared to the dephasing process of the probed transition. Line broadening is *inhomogeneous* and the absorption (emission) profiles are Gaussians. The shape of the band reflecting such, essentially static distribution of transition frequencies carries no dynamic information. In the opposite case, if the motions of the solvent molecules are so fast that the radiation field observes averaged energy levels (fast modulation limit), one talk about *homogeneous* broadening and the absorption (emission) profiles are Lorentzians. For condensed matter at room temperature, the structural reorganization of the environment, which leads to inhomogeneous broadening, may occur on a time scale similar to the dynamic interactions responsible for the oscillator dephasing and homogeneous broadening of the absorption line. In such cases, the contribution of homogeneous broadening is masked within the inhomogeneous broadening and leads to the band narrowing (motional narrowing). When the two limiting cases are combined, the Bloch model is achieved [84] which implements an infinitely short homogeneous and infinitely long inhomogeneous contribution to the frequency correlation function (see Section 2.4 and Eq. 2.10):

$$C(t) = \frac{\delta(t)}{T_2^*} + \Delta^2, \tag{3.30}$$

where T_2^* is the pure dephasing time and Δ is the static inhomogeneity.

In a liquid, there is no static inhomogeneity. The decaying correlation function can be understood here as a description of the spectral inhomogeneity which is loosing over time because of the fast environment fluctuations.

Despite many attempts to estimate the contribution of inhomogeneous and homogeneous contributions to the total band broadening by analysing the band shape and characteristics of the correlation function, linear vibrational spectroscopy does not provide reliable results. Instead, the time-resolved spectroscopic techniques allow for determining vibrational dynamics, including the energy relaxation time T_1 and the phase relaxation time T_2. The excited state lifetime T_1 is typically obtained using the IR pump-probe method (see Section 3.10) and the dephasing time can be determined with coherent Raman scattering or vibrational echo spectroscopy.

Utilizing the Bloch approach to describe the relaxation of the complex systems such as liquids being examined with ultrafast laser pulses in terms of time-independent parameters is not always successful and does not provide much of physical insight. In the solution phase and, in particular, in protein and nucleic acid environments, fluctuations occur on many time scales from femtoseconds to seconds [85,86,87,88,89]. Thus, the dynamics cannot be simply characterized by a single T_2 parameter and the Bloch picture is completely inadequate to describe vibrational dephasing. If the distribution of frequencies homogenizes during the measurement (the process called *spectral diffusion*), a more sophisticated approach would have to be applied to investigate the dynamics of the system of interest. To resolve this *non-Markovian* dynamics of the inhomogeneous distribution, the three-pulse photon echo spectroscopy method is used [90]. Recently this coherent infrared experiment was used to investigate the ultrafast dynamics of neat water [41,43,91], DNA-model systems [92,93] G-C dimers in non-polar solvent [94] and hydrated A-T oligomers [95]

3.9 The dynamics of hydrogen-bonded systems

The molecular systems investigated in this thesis consist of the following hydrogen bonding combinations: N-H···O, N-H···N, O-H···O, O-H···PO_2 and thus, only the dynamics of hydrogen bonded NH and OH stretching oscillators will be discussed here. The NH/OH stretching vibrations undergo a pronounced spectral red-shift and band broadening upon hydrogen bonding. The strong broadening of the fundamental stretching transition together with the development of a peculiar spectral substructure, as one finds, e.g. in the spectra of carboxylic acid dimers and 2-pyridone/2-hydroxypyridine (Figure 2.1 c,d) represents a big challenge for line shape theory. Bratos, Witkowski and Maréchal [96,97,98] published numerous theoretical work that incorporates Fermi resonances in the lineshape function. Robertson and Yarwood [99,100] emphasized in their approach the coupling of the X–H mode to the anharmonic low frequency X–Y motion. In this semi-classical model (slow oscillator is treated classically), electric field fluctuations are not included and hence, it is better suited to the hydrogen bonds in non-polar solvents. Finally, Henri-Rousseau and co-workers proposed a fully quantum mechanical treatment of the slow mode that quantum state is changed by interaction with a solvent and then – through anharmonic coupling – it affects dephasing of the fast oscillator [26,101,102].

Similar strengths of the different interaction mechanisms that lead to the band broadening hamper quantitative and unambiguous theoretical calculation of infrared spectra. It is a big advantage of nonlinear vibrational spectroscopy in the ultrafast time domain to provide specific information on the different coupling mechanisms by separating them in the time-resolved response. In the following section, the theoretical description of the pump-probe technique, a widely applied method to study ultrafast vibrational dynamics, will be provided.

3.10 Theory of pump-probe spectroscopy

The pump-probe method is one of the most popular spectroscopic techniques to bypass the problem of insufficient time-resolution of available detectors. Here, the strong *pump* pulse creates a nonlinear vibrational excitation, i.e., a polarization on the vibrational transition and a population change of the optically coupled vibrational levels. The time evolution of the system response is monitored with a weaker *probe* pulse. By recording the intensity of the probe pulse transmitted through the sample as a function of pump-probe delay, one measures in fact the imaginary part of the third-order polarization, which is “self heterodyned” with the probe pulse (see Eq. 3.33). To control the timing of the two pulses, one of the pulses is sent over a path whose length is adjusted by moving a mirror on a translational stage (changing the path length by 1 cm corresponds to the temporal delay change by 33 ps). The transmitted probe pulse is usually dispersed by a monochromator onto an array of photodiodes, so that a full spectrum of the transient absorbance changes can be captured after each excitation. In practise, such measurements typically are averaged over many pairs of pump and probe pulses to increase signal-to-noise ratio (see also Chapter 4.4, where the experimental realisation of pump-probe experiment is discussed).

In a system with only two optically coupled states, the measured signal reflect either stimulated emission from the excited state or bleaching of the absorption band of the ground state and thus, four Feynman diagrams are sufficient for complete description of third-order nonlinear polarization of such system (compare Section 3.4 and Figure 3.2).

The spectrally broad short laser pulse has the potential to excite a collection of vibrational levels in a coherent superposition and to monitor in real-time the coherent nuclear motions [14]. In order to correctly interpret the observed nonlinear vibrational signals, the multilevel nature of the vibrational system has to be taken into account. In a three-state system, formation of the $\upsilon = 2$ state can be probed by excited state absorption (excitation from state $\upsilon = 1$ to $\upsilon = 2$) if the pump frequency is resonant for transitions between states $\upsilon = 0$ and $\upsilon = 1$, whereas the probe frequency is selective for transitions between states $\upsilon = 1$ and $\upsilon = 2$. The later transition is usually red-shifted with respect to the fundamental transition because of the anharmonicity of the potential. All the possible quantum pathways that contribute to the non-linear signal of a three-level system (including formation of hot ground states) are depicted as the Feynman diagrams in Figure 3.3.

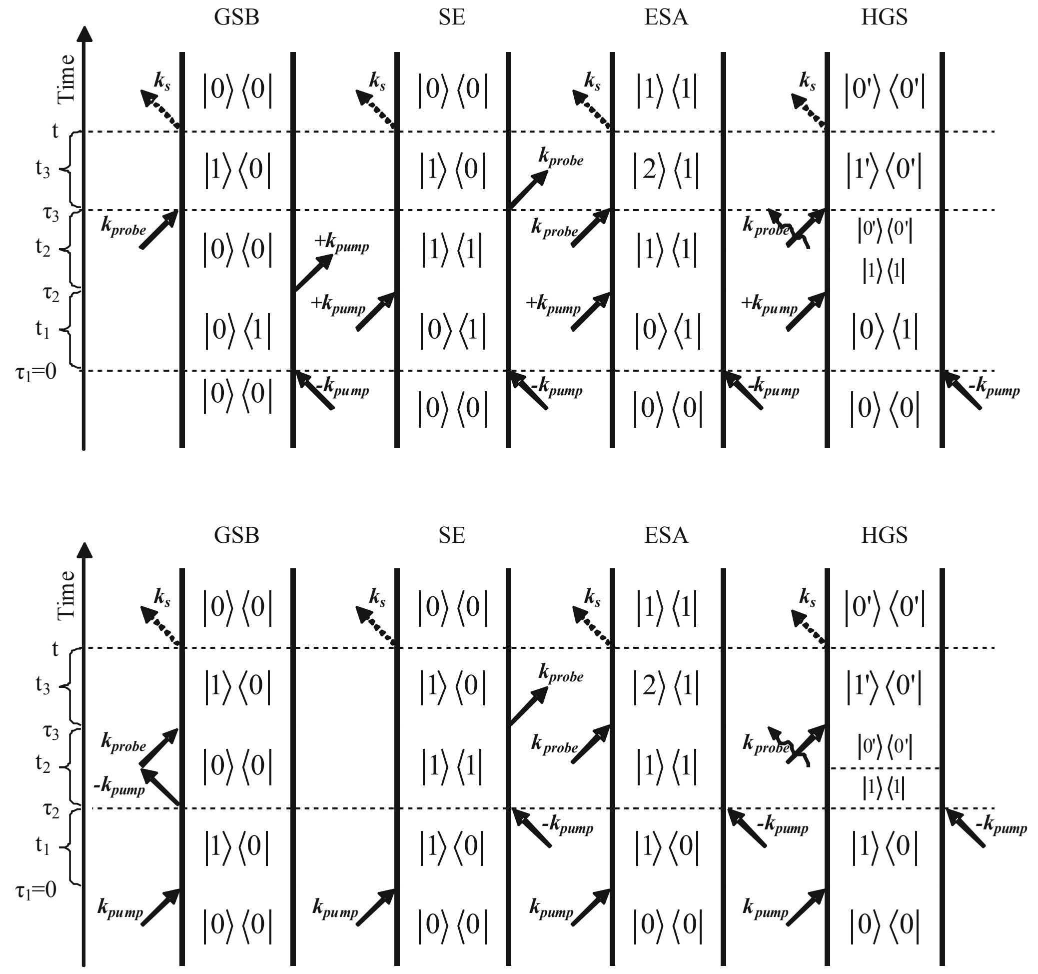

Figure 3.3: Double-sided Feynman diagrams that have to be considered in nonlinear infrared pump-probe experiment. They can be ordered in four pairs corresponding to ground state bleach (GSB), stimulated emission (SE), excited state absorption (ESA) and formation of hot ground state (HGS). This relaxation process ("vibrational cooling") is indicated by a horizontal line. For all eight diagrams it has been assumed that the pump pulse precedes the probe pulse.

In a pump-probe experiment, the generated third-order polarization is detected in exactly the same direction as the probe itself (Figure 3.4, $\mathbf{k}_{\text{signal}} = \mathbf{k}_{\text{probe}}$). The only way how this phase matching condition can be achieved for the chosen setup geometry is that pump pulse interacts twice with the sample with wave vectors $+\mathbf{k}_{\text{pump}}$ and $-\mathbf{k}_{\text{pump}}$. Since both interactions of the pump pulse come from the same field Epump, there is no possibility to distinguish in time between the two interactions. For eight Liouville space pathways that survive phase matching condition and rotating wave approximation, it has been assumed that the probe pulse is the last interaction (Figure 3.3).

In the case when the probe precedes the pump pulse (Figure 3.5), the signal generated at negative pulse delays in a frequency-resolved measurement stem from a *perturbed free induction decay* (PFID) [103]. This can be interpreted in terms of a perturbation of the probe-induced polarization by the pump pulse. When the pump and probe pulses overlap in time, coherent coupling effects related to the quantum pathways with a sequence $\mathbf{k}_{\mathrm{pump}} \rightarrow \mathbf{k}_{\mathrm{probe}} \rightarrow \mathbf{k}_{\mathrm{pump}}$ can make the interpretation of the measured signal more complex. The magnitude of some other unwanted contributions like cross-phase modulation (optical Kerr effect), can be remarkably reduced in practical applications.

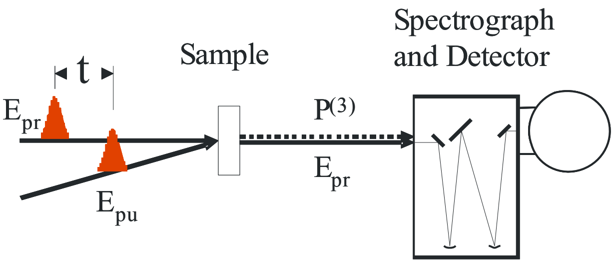

Figure 3.4: Experimental configuration of spectrally resolved pump-probe technique.

Assuming the simple situation, where a vibrationally hot ground state is not formed (processes with radiationless transitions to the hot ground state will be discussed at the end of this section), and neglecting the population relaxation, the third order response function of a homogenously broadened oscillator with a linewidth Γ is given by [75]:

$$S^{(3)}(\tau=0,T=0,t)=\sum_{i=1}^{6} S_i^{(3)}(\tau,T,t) \propto \frac{i}{\hbar^3}\left(4\mu_{10}^4 e^{-i\omega_{10}t}-2\mu_{10}^2\mu_{21}^2\right)e^{-\Gamma t}, \qquad (3.31)$$

with the transition dipole moments μ_{10} and μ_{21} and transition frequencies ω_{10} and ω_{21}.

In the semi-impulsive limit, i.e., when the laser pulses are short compared to the system response (lifetime and dephasing), the third order polarization equals nonlinear response function:

$$P^{(3)}(t)=S^{(3)}(t). \qquad (3.32)$$

The changes of absorbance can be measured by a slow detector directly or after transmitting the light through a spectrometer.

In the first case, the spectrally integrated absorption change measured by a probe pulse with centre frequency ω_{pr} is given by:

$$\Delta A(\omega_{pr})=-\log\left[\frac{I(\omega_{pr})}{I_0(\omega_{pr})}\right]=\frac{4\pi\omega_{pr}}{cn(\omega_{pr})}\frac{\mathrm{Im}\int_{-\infty}^{\infty} dt E_{pr}^*(t)P^{(3)}(t)}{\int_{-\infty}^{\infty} dt\left|E_{pr}(t)\right|^2} \qquad (3.33)$$

I and I_0 represent the transmission of the probe pulse with and without excitation (pump pulse either unblocked or blocked) when passing through the sample with refractive index n.

Here, the detector measures the time-integrated intensity. The pump-probe signal does not depend on the time separation between the laser pulses because no population relaxation, vibrational cooling or other dynamic processes except dephasing are included.

In the second case, the spectrometer performs the Fourier transform of the time-dependent probe field: $E_{pr}(\omega) = \int_{-\infty}^{\infty} dt \exp(i\omega t) E_{pr}(t)$. Then, for a spectrally resolved detection, the measured signal is given by:

$$\Delta A(\omega) = \frac{4\pi\omega_{pr}}{cn(\omega_{pr})} \frac{\left|E_{pr}(\omega)\right|^2 \operatorname{Im} \frac{P^{(3)}(\omega)}{E^*_{pr}(\omega)}}{\int_0^{\infty} d\omega \left|E_{pr}(\omega)\right|^2} \tag{3.34}$$

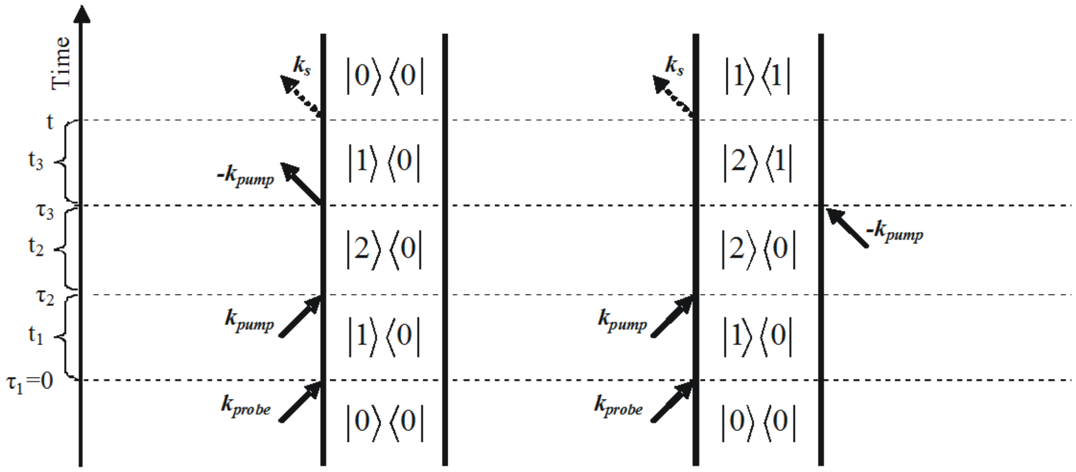

Figure 3.5: Two Feynman diagrams that have to be taken into account for the situation where the probe pulse precedes the pump pulse (perturbed free induction decay).

The third order polarization in the semi-impulsive limit is equal to the nonlinear response of the sample (Eq. 3.31) and hence, the obtained pump-probe spectrum is a superposition of two Lorentzian lines:

$$\Delta A(\omega) \propto -\frac{8\mu_{10}^4\Gamma}{(\omega_{10}-\omega)^2+\Gamma^2} + \frac{4\mu_{10}^2\mu_{21}^2\Gamma}{(\omega_{21}-\omega)^2+\Gamma^2} \tag{3.35}$$

The first (negative) term stem from ground state bleaching and stimulated emission (GSE and SE in Figure 3.3). Positive Lorentzian line will be observed at the frequency position of the 1→2 transition (excited state absorption, ESA in Figure 3.3). For a harmonic oscillator with $\omega_{21} = \omega_{10}$ and $\mu_{12} = \sqrt{2}\mu_{01}$, the ground state bleaching, stimulated and excited state absorption would cancel each other, i.e. $\Delta A(\omega) = 0$.

Stimulated emission and excited state absorption decay with the lifetime of excited state population. However, stimulated emission cannot be spectrally distinguished from ground state bleaching. The bleach recovery dynamics involve additional energy relaxation processes such as thermal relaxation in liquids and therefore, to estimate T_1 constant, excited state absorption signal is used.

In many cases (compare the results presented in section 6.5.7), the $\upsilon(\nu_{NH/OH}) = 1$ state does not decay directly back to the ground state upon population relaxation (T_1) by dissipating the energy excess to the surrounding (solvent) modes. Instead, a hot ground state $\upsilon(\nu_{NH/OH}) = 0'$ is formed in which the excess of vibrational energy is contained in other modes of the hydrogen-bonded system: OH/NH bending or low-frequency hydrogen bond vibrations.

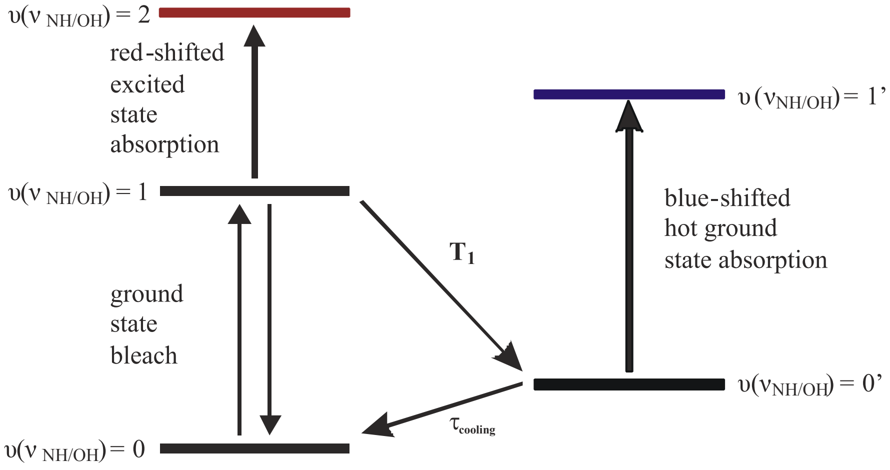

Figure 3.6: The NH/OH stretching three-level vibrational diagram including formation of hot molecule state.

Excited state stretching oscillator can be in Fermi resonance with combination tones or overtone states. In the case of weak Fermi resonance, the bend overtone $\delta_{N-H/O-H} = 0 \rightarrow 2$ is often assumed to be the major relaxation channel for the stretching mode $\nu_{N-H/O-H} = 1$ as it has been discussed in Section 2.4.2. Subsequently, energy dissipation to the solvent (vibrational cooling, τ) occurs on longer time scales on the order of picoseconds to hundreds of picoseconds. In this hot ground state configuration the OH/NH stretching mode is not excited, but its transition $\upsilon(\nu_{N-H/O-H}) = 0' \rightarrow 1'$ has higher frequency due to anharmonic coupling to the transiently highly populated hydrogen bond modes. In contrast, when OH/NH bending vibrations relax into the hot ground state upon intramolecular vibrational energy redistribution (IVR), red-shifting is observed, in accordance with more typically found negatively valued anharmonic couplings between intramolecular vibrational modes [27].

3.11 Polarization- resolved pump-probe spectroscopy

Vibrational anisotropy decay may in general be caused by rotational diffusion of the molecular system [104] or by excitation transfer between vibrational modes [41,43,105]. If one needs to find information about excitation transfer exclusively, the measurements has to be performed on a time scale that is fast compared to the rotational diffusion. For big molecular systems studied here, like the *AT oligomers*, the rotational diffusion occurs in the order of nano- to milliseconds. As a result, the subpicosecond temporal resolution of the experimental techniques presented here is definitely sufficient to obtain reliable data on the energy transfer between different vibrational transitions.

In polarization-sensitive IR-pump/IR-probe measurements, the measured signal depends in general on the transition dipole moment vectors μ_i and μ_j of the pump vibration *i* and the probed vibration *j*, the electrical field strengths E_i and E_j of the applied pump (tuned to the vibrational transition *i*) and probe (tuned to the vibrational transition *j*) pulses, and the nonlinear response function dependent on the coherence and population dynamics, as well as orientational factors. Assuming a sequential interaction with pump and probe pulses on a time scale longer that the vibrational dephasing times, excitation transfer is incoherent and the polarization-sensitive pump-probe signals are given by [79]:

$$S(t,\alpha) \propto \sum_{ij} \mu_i \mu_i^* \mu_j \mu_j^* E_i(0) E_i^*(0) E_j(t) E_j^*(t) R_{ij}(t) \Theta(t), \tag{3.36}$$

with, for parallel polarization of pump and probe pulses:

$$\Theta(t) = \frac{4}{15}\pi^2\left(2\cos^2\alpha + 1\right) \tag{3.37}$$

and, for perpendicular polarization between pump and probe pulses:

$$\Theta(t) = \frac{4}{15}\pi^2\left(\sin^2\alpha + 1\right) \tag{3.38}$$

Population dynamics including excitation transfer and population decay are described with *R(t)*, whereas polarization dependencies between the pump and probe pulses are contained in *Θ(α)*, where α is the angle between the pumped and the probed vibrational transitions.

In the case when all vibrations have infinite lifetimes and vibrational excitation transfer does not occur, the measured pump-probe anisotropy *r(α)* equals:

$$r(\alpha) = \frac{3\cos^2\alpha - 1}{5}, \tag{3.39}$$

which results, for instance, in r(0º) = 0.4, r(90º) = -0.2, r(45º) = 0.1.

It is frequently of interest to measure the pump-probe signal unaffected by orientational information. This can be done by performing experiments in which the probe is polarized at the *magic angle* (α = 54.74º; r(54.74º) = 0) to the pump-polarization direction.

IR pump – IR probe spectroscopy remains the most frequently used third-order nonlinear technique to study the ultrafast vibrational dynamics of hydrogen-bonded systems. This relatively simple method, in combination with vibrational (three-pulse) photon-echo spectroscopy permits for a detailed understanding of non-equilibrium properties of the system of interest, its transient structural changes, vibrational couplings, and complicated fast interactions with surrounding solvent molecules. Recent efforts focus on biologically-relevant molecules and their interactions with the aqueous environment.

4 Experimental techniques

4.1 Generation of mid-IR laser pulses

Molecular vibrations with eigenfrequencies in the range 1000-3600 cm^{-1} are the subject of interest in all experiments discussed in this thesis. The investigation of hydrogen-bond dynamics thus requires sufficiently short and intense laser pulses at mid-infrared wavelengths. Often their dynamics, including lifetimes, vibrational cooling, anharmonic coupling, spectral diffusion, energy transfer and anisotropy decay, occur in the subpicosecond time domain. Moreover, in the infrared range, the absorption cross sections for vibrational modes are usually small ($\sigma \cong$ 10-20 cm^2), making large pumping intensities on the order of $I_s \cong 10^{11} - 10^{12}\ \mathrm{W/cm^2}$ necessary to generate a nonlinear signal. Hence, the generation of femtosecond pulses tunable in the mid-IR regime, with energies of several microjoules is required.

Quantum cascade lasers represent a relatively recent development [106] in the area of semiconductor lasers. Whereas earlier mid-infrared semiconductor lasers were based on interband transitions, in which electromagnetic radiation is emitted through the recombination of electron–hole pairs across the material band gap, quantum cascade lasers utilize intersubband transitions. The photon energy (and thus the wavelength) of transitions can be varied in a wide range by engineering the details of the semiconductor layer structure. Even for a fixed design, some significant range for wavelength tuning (sometimes more than 10% of the centre wavelength) can be covered with external-cavity devices [107]. The generation of short pulses with durations in picosecond range is possible (the best performance is achieved when operating at low temperatures), although with fairly limited peak powers.

Before quantum cascade lasers were developed, large parts of the mid-infrared spectrum were accessed with various types of *lead salt lasers.* Lead salt lasers need to be operated at cryogenic temperatures and produce only low power levels (typically of the order of 1 mW).

The output power exceeding 10 W can be accomplished using newly developed chromium and iron doped semiconductor materials [108]. Cr^{2+}:ZnSe (chromium-doped zinc selenide) lasers can emit up to roughly 3.5 µm and Fe^{2+}:ZnSe lasers at 3.7–5.1 µm in doped insulator solid-state lasers.

Complex and expensive *free electron lasers* which fundamental lasing frequency can be tuned in the mid-IR range are currently less frequently used light source.

Another option for nonlinear frequency conversion is to start with a single near-infrared laser and pump an optical parametric oscillator (OPO), amplifier (OPA) or generator (OPG). The generated idler wave can then be in the mid-infrared spectral region.

A *mode-locked* picosecond Nd:YVO_4 laser at 1064 nm can be used for synchronous pumping of an OPO with a $LiNbO_3$ crystal, allowing idler outputs up to 4.5 µm, with the limit set by the increasing idler absorption at long wavelengths. The first femtosecond mid-IR pulses were generated with amplified pulses from a colliding-pulse mode-locked dye laser. Elsaesser and Nuss [109] describe a system capable of producing 400 fs pulses in the wavelength range near

5 µm in which amplified pulses from a CPM dye laser at 620 nm and the output of a femtosecond travelling-wave dye cell are mixed in a $LiIO_3$ crystal.

These solutions have later been superseded by Ti:Sapphire (Ti:Sa; $Ti^{3+}:Al_2O_3$) femtosecond *regenerative amplifiers* which utilizes the concept of chirped pulse amplification (CPA) [110]. Titanium doped sapphire lasers operate at 800 nm provide high energy (several mJ after amplification, peak power of terawatts), femtosecond pulses [110], which can then be converted to the ultraviolet, visible or infrared regime using optical parametric amplifiers (OPA) [111,112,113,114]. Generating µJ pulse energies that are needed for nonlinear vibrational spectroscopy usually involves more than one amplification stage (cascaded OPA, see next paragraph) and a difference frequency generation (DFG) step.

4.2 The laser system

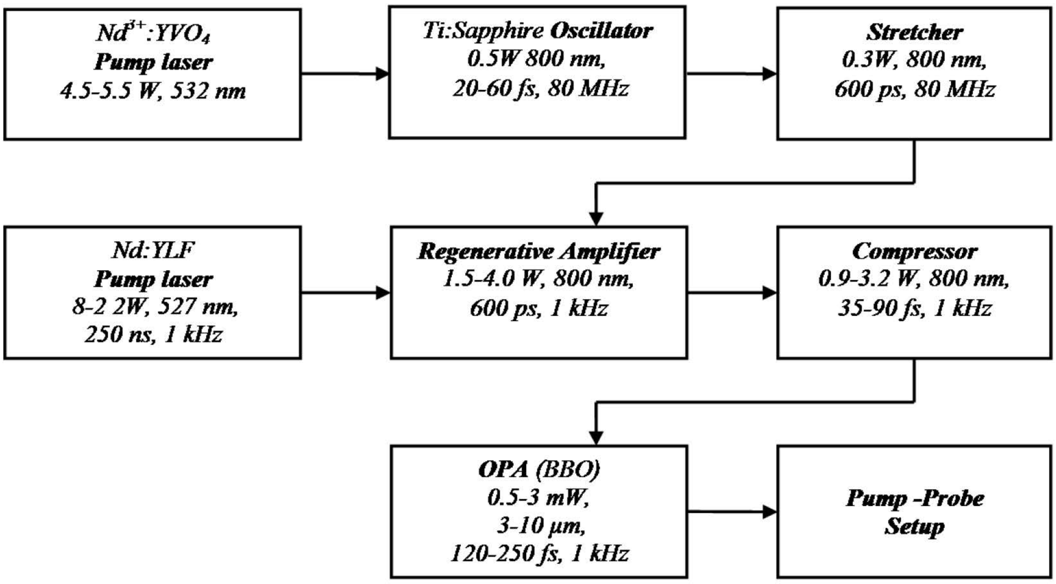

Figure 4.1: Scheme of the experimental laser system for nonlinear infrared experiment.

In Figure 4.1 the experimental setup is presented schematically. The system is composed of a commercial part, based on Ti:Sapphire lasers, a homebuilt optical parametric amplifier and a pump-probe setup. Experimental data discussed throughout this thesis were collected using two different laser systems, providing 800 nm pulses with similar parameters.

The second harmonic (λ = 532 nm) of an intra-cavity doubled solid-state $Nd^{3+}:YVO_4$ laser (Coherent Verdi; SP Millenia) is used as a pumping source for the Ti:Sapphire laser oscillator (Coherent Micra; SP Tsunami) working in the mode-locking regime (passive mode-locking due to Kerr-lensing, [115,116]). The Ti:Sapphire laser with a 100 nm bandwidth pulse (pulse duration: 20-60 fs) centred at 800 nm is used for further amplification. The oscillator's average output power is 400-500 mW. This corresponds to pulse energies of about 5-6 nJ for a repetition rate 80 MHz. The short but low-intensity laser pulses are injected into regenerative amplifier (Coherent Legend; SP Spitfire), where – to avoid too high peak intensities which could damage the gain medium or other optical elements – are first temporally stretched to a much longer duration by means of a strongly dispersive element (the *stretcher*, here: a grating pair). The gain medium (Ti:Sapphire crystal) of the amplifier is pumped with the second harmonic of the solid-state, Q-switched laser (Nd^{3+}:YLF, λ=527 nm) producing 250 ns long pulses with the repetition rate of 1 kHz (Coherent Evolution, SP Merlin). The regenerative amplifier selects an individual pulse from a train of modelocked pulses (called a *seed* pulse). The seed pulse is coupled into a cavity formed by two Pockels cells where it is amplified at each pass in the crystal. The pulse passes about 20-25 through the gain medium to reach the energy around 1.5 and 3.5 mJ (for SP and Coherent system, respectively). Finally, the amplified pulse is compressed using another grating pair (*compressor*). The parameters of the pulses generated in the above described commercial laser systems have been summarized in Table 4.1.

Tab. 4.1: Characteristics of amplified pulse.

	Coherent **Legend Elite**	Spectra Physics **Spitfire**
Centre wavelength	800 nm	
Repetition rate	1 kHz	
Pulse energy	3 mJ	1 mJ
Pulse duration	35 fs	90 fs
Output power	3 W	1 W

4.3 Optical frequency conversion and amplification

Accessing widely tunable, mid-infrared light pulses of microjoule energies requires optical parametric amplification (OPA) in combination with difference frequency generation stage (DFG). The conversion is achieved in birefringent crystals with large second-order nonlinear susceptibility [117].

The scheme of homebuilt cascaded optical parametric amplifier used to convert the 800 nm light into pulses in the wavelength range 3-10 μm is shown in Figure 4.2.

To pump the OPA, a fraction of RGA output is taken (400 μJ). This part is then divided into three separate pulses. The first pulse, the *seed*, has only 1% of the total energy and after changing its polarization by 90º is focused in 1 mm Sapphire plate to generate single-filament white light continuum (398-1000 nm) [118,119]. The *seed* pulse is re- focused and together with another 9% (*pre-amplifier pulse)* of the initial radiation are temporally and spatially overlapped in a nonlinear crystal, where the optical amplification takes place. Here, the 4 mm thick β-Barium Borate Type II crystal (BBO, negative uniaxial, point group *m3*, Θ=38º, φ=0º) is employed. Near-IR signal and idler beams are generated in a nonlinear crystal and afterwards they are separated from the fundamental beam by a dichroic mirror. Thereafter, the signal light is reflected by a polarizing beam splitter (transmitting the idler), collimated by a concave mirror and overlap in space and time with remaining fundamental, *pump*, pulse (90%) on the same BBO crystal. The *pump* beam diameter is adjusted with 4:1 telescope to match with the *seed* pulse and to avoid the white light generation on the BBO crystal. Obtained during the second amplification stage signal and idler pulses (1.2-2.5 μm) have together around 80 μJ. They are later separated from each other with the help of a dichroic mirror. The idler pulse additionally passes over a manual delay stage. In this way, the temporal delay between signal and idler can be controlled. Finally, both pulses generated in the second amplification, approach the difference frequency mixing crystal. Depending on the chosen wavelengths, $AgGaS_2$ [120] or GaSe [113] nonlinear crystal are used for frequency conversion due to their broad transparency range and relatively high nonlinearity.

By rotating the birefringent crystal, the phase-matching condition is changed. As a consequence, signal and idler frequency generated at the BBO crystal can be tuned. In combination with difference frequency generation in $AgGaS_2$ crystal, the broad wavelength range between 2.5 and 8 µm (4000-1250 cm^{-1}) is achieved. Using the GaSe crystal in the difference frequency generation stage makes the investigation of the infrared range between 3.5 and 10 µm (2850-1000 cm^{-1}) possible. Each nonlinear wavelength conversion step is about 10% efficient. To block the residual signal and idler components, long-wave pass filters (LWP) are used.

Amplification methods where the pre-amplification stage precedes larger power (pump) amplification, not only yield the intense signal and idler pulses, but also improve the signal to noise ratio. As a consequence, the mid-IR pulse stability of the above described OPA is very high, with a noise level better than 0.2% (rms) in the centre of the pulse spectrum. Depending on wavelength and thickness of used nonlinear crystal, typical pulse energy equals 1-2.5 µJ and the pulse duration 130-200 fs.

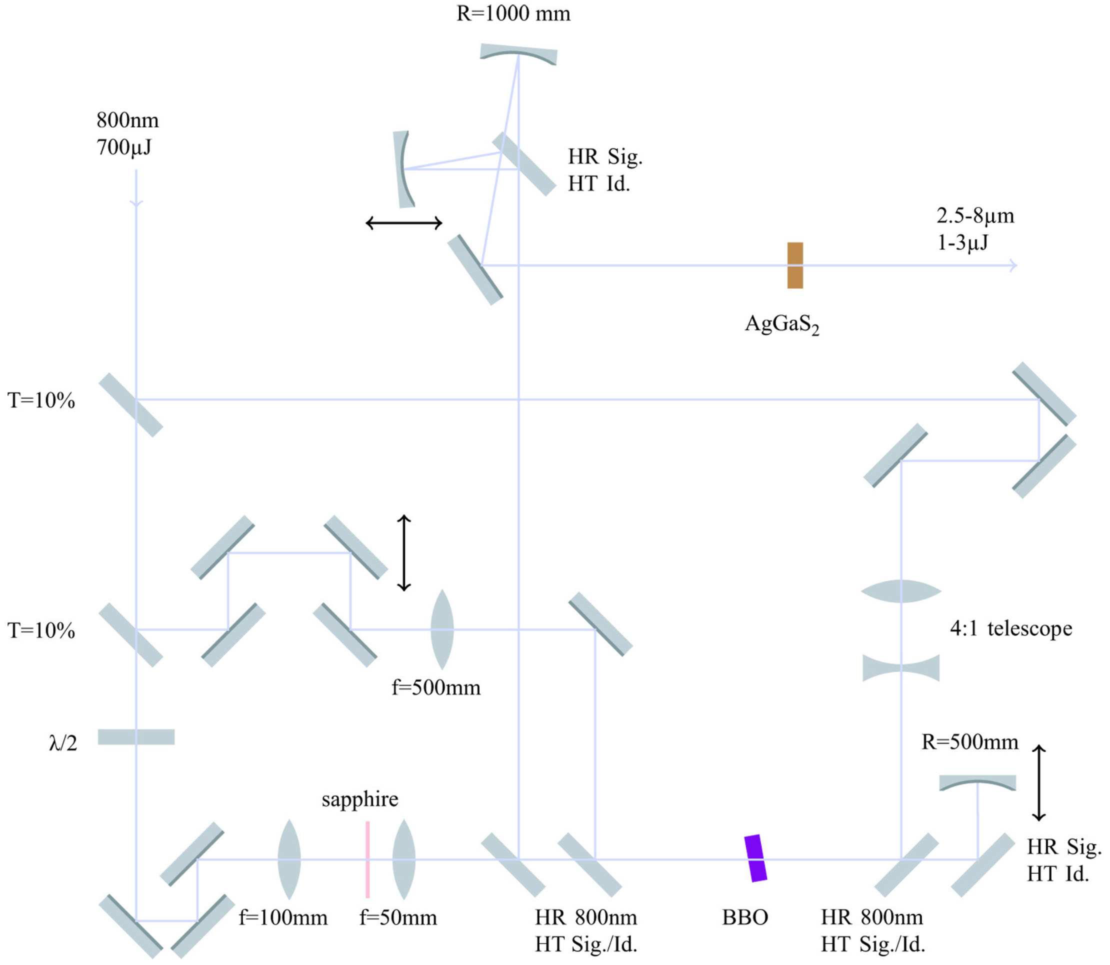

Figure 4.2: Design of the optical parametric amplifier. Mid-infrared is obtained by Difference Frequency Generation (in $AgGaS_2$) of two intense Signal and Idler pulses of two fold optical parametric amplification in a BBO crystal. HR/HT: high reflection/transmission, Sig.: signal, Id.: idler, λ/2: half waveplate.

In this work, two identical, independently tunable OPAs are used: one for probe and one for the pump pulse.

4.4 Pump-probe spectroscopy – experimental realisation

The pump-probe experiments were performed with the setup schematically presented in Figure 4.3. The pump pulse passes through an optical chopper, which is synchronized with the Q-switch of the RGA pump laser. The chopper runs at half the laser frequency (500 Hz) which means that it blocks every second pump pulse. Consequently, the sample transmission (absorption) changes with and without excitation is recorded. The pump pulse passes then a mechanical delay stage, where the optical path length with respect to the probe pulse can be changed with μm-precision, e.g., decreasing the path length of 3 μm of the pump pulse corresponds to an observation of the absorbance changes monitored by the probe pulse 10 fs after the excitation has taken place. The pump pulse is focused with a help of 30º off-axis parabolic mirror into the sample and there it is spatially overlapped with a pump pulse. Finding the best overlap between two infrared pulses is usually achieved using material with a high nonlinear response for a given spectral range such as Ge, InAs or InSb semiconductor. Typically the pump pulse diameter in focus (on the sample) equals 300 μm and is two times bigger than the probe beam to ensure probing of fairly homogeneous excited sample volume.

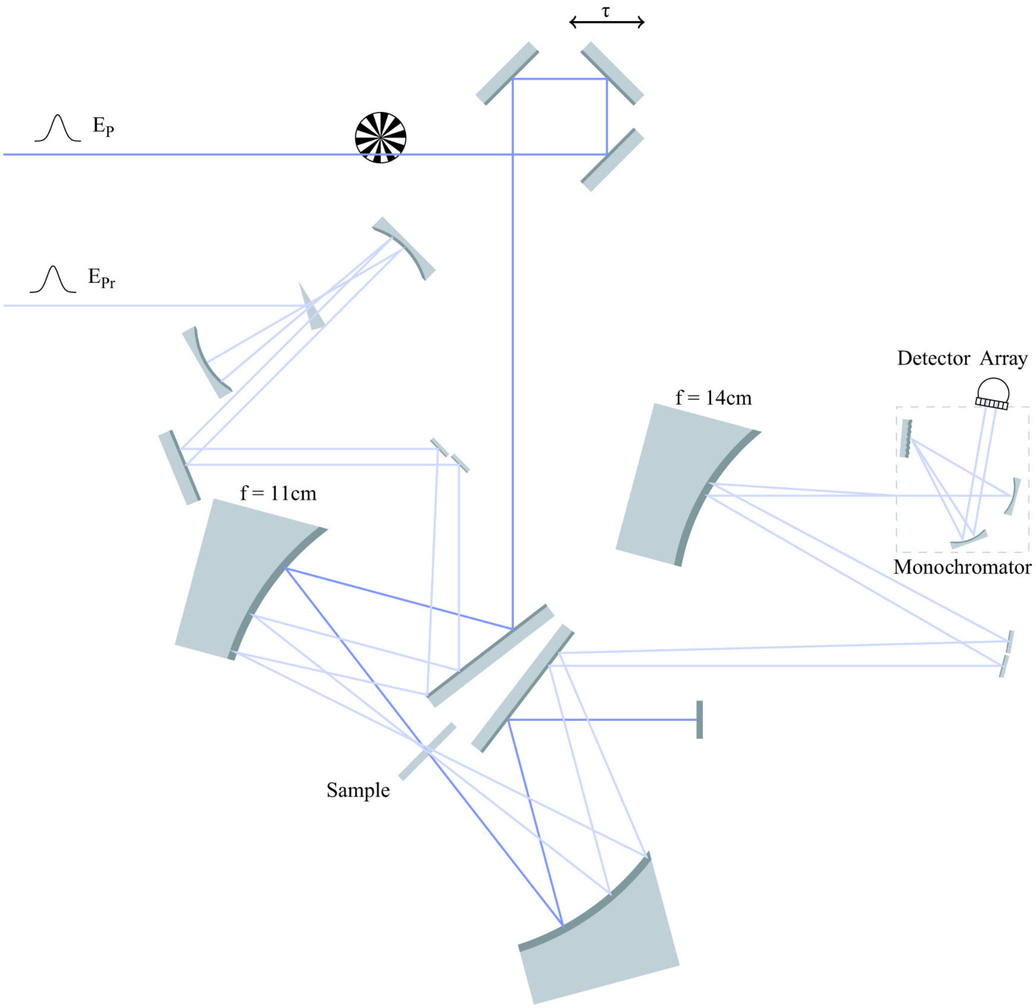

Figure 4.3: Design of pump-probe experiment. The generated third-order signal propagates collinear to the probe pulse. It has to be noted that the reference pulse is not parallel to the pump/probe pulse to avoid passage through the excited sample volume.

The probe pulse, after passing through a LWP filter, is then reflected by barium fluoride (BaF_2) wedge. The reflections from the front and back surface of BaF_2 are used as a probe and reference beams, respectively, both having energy of around 80 nJ (which is approximately a fraction of 4-5% of the pump pulse energy). The probe and the reference pulse are focused by a parabolic mirror into the sample with reference beam slightly displaced from the probe pulse focal region. The reference beam is introduced here to reduce signal fluctuations due to the sample inhomogeneity in the sample volume and shot-to-shot intensity variations of the probe pulse. After passing through the sample, all the three pulses are collimated by the next parabolic mirror. Then, the pump beam is blocked and remaining probe and reference pulses are spectrally dispersed in a grating spectrometer. The time integrated intensities are recorded as a function of wavelength using double array (2x16) MCT (HgCdTe) detector. The measured absorbance change, when including also the reference pulse is given by:

$$\Delta A(T,\omega) = -\log\left(\frac{I(T,\omega)}{I_0(\omega)} \cdot \frac{I_0^{(R)}(\omega)}{I^{(R)}(\omega)}\right) \tag{4.1}$$

$I_0^{(R)}(\omega)$ and $I^{(R)}(\omega)$ are the intensities of the reference beam when the pump pulse is blocked and unblocked, respectively. The sample transmission changes $\Delta T = I / I_0$ have been already defined in Chapter 3.10 (Eq. 3.33).

The experimental setup has been designed in a way that the very short laser pulses do not have to pass through the dispersive optical elements, which can cause pulse temporal profile distortion. Instead, only reflective optics is used, which additional advantage is making the pre-alignment procedure with HeNe laser very accurate.

When the mid-IR pulse is tuned to have the frequency, which overlaps with a water vapour or carbon dioxide absorption, the pump-probe experimental setup is closed in a box purged with nitrogen.

4.5 Characterisation of ultrashort pulses

To estimate the pulse duration, the concept of (intensity or interferometric) autocorrelation is commonly used. Autocorrelation involves splitting the pulse into two, spatially overlapping pulses replica in some instantaneously responding nonlinear-optical medium.

A complex electric field $E(t)$ corresponds to intensity $I(t) = |E(t)|^2$ and an intensity autocorrelation function defined by:

$$G(\tau) = \int_{-\infty}^{\infty} \left|E(t)E(t-\tau)\right|^2 dt = \int_{-\infty}^{\infty} I(t)I(t-\tau)\, dt\,, \tag{4.2}$$

where τ is the relative delay between the two pulses.

The autocorrelation signal is a convolution of functions, which describes the intensity profile of beam I (*I(t)*) and beam II (*I(t-τ)*). Knowing *G(τ)* from an experiment, the reverse procedure, deconvolution is used to derive the temporal impulse profile *I(t)*. It can be shown that the pulse duration can be calculated from the FWHM of the autocorrelation signal multiplied by some factor. This numerical factor, which depends on the shape of the pulse (0.707 for Gaussian and 0.648 for sech^2 function) is sometimes called the deconvolution factor. If this factor is known, or assumed, the time duration of a pulse can be measured using an intensity autocorrelation. However, the phase cannot be measured.

Instead of correlating the pulse *E(t)* with itself, it can be also correlated with other, reference pulse *E(t)*. This idea is called cross-correlation and the signal measured by the detector looks very similar to the autocorrelation signal (Eq. 4.2):

$$G_C(\tau) = \int_{-\infty}^{\infty} I(t) I_R(t-\tau)\, dt \tag{4.3}$$

The autocorrelation or cross-correlation signal is usually generated by the nonlinear processes such as second-harmonic generation or two-photon absorption.

The simultaneous absorption of two photons in a semiconductor occurs with some finite probability if the band gap of a semiconductor is larger than the photon energy and smaller than double of it, and there is a sufficiently high photon density. In this way, the absorption of the reference pulse changes as a function of time delay to the pulse τ to be characterized. As such, it is sufficient to measure only the time-integrated intensity of the reference pulse. If an optical chopper blocks every second pulse to be characterized, a comparison of the reference pulse with (I_R) or without ($I_{R,0}$) the interaction with this pulse is possible. The change of absorbance of the reference pulse is then given by:

$$A(\tau) = -\log\left(\frac{I_R(\tau)}{I_R}\right) \tag{4.4}$$

In this work, the mid-IR pulse temporal length was estimated using the pump-probe experimental setup, where the sample has been replaced by semiconductor in which the two-photon absorption occurs. The cross-correlation signal of the pump and the probe pulse was obtained in 50-70 µm thick plate of germanium, indium arsenide or indium antimonide, for spectral range 3, 6 and 8 µm, respectively.

The pump-induced absorbance change as a function of pump-probe delay (Eq. 4.4) is in first approximation proportional to the cross-correlation function described by Eq. (4.3). However, it is necessary to appropriate the attenuation of both beams in order to avoid the situation, where generated signal overlap with the two-photon absorption of only one of the involved pulses.

In pump-probe setup (Figure 4.3), the probe pulse before interacting with a sample (here: semiconductor) is reflected by the BaF_2 wedge. As a consequence, its energy in a focus corresponds to only 4% of the pump pulse energy. Then, to measure the cross-correlation function, only the pump pulse has to be attenuated. For this purpose, the fine copper grids are used; those not only reduce the probability of two-photon absorption from the only one pulse, but also suppress the generation of long-lived free charge carriers, without noticeable pulse elongation.

The typical measurement from which the temporal resolution of the experiment was derived is shown in Figure 4.4a for infrared pump and probe pulses centred at around 3250 cm^{-1} (Figure 4.4b,c).

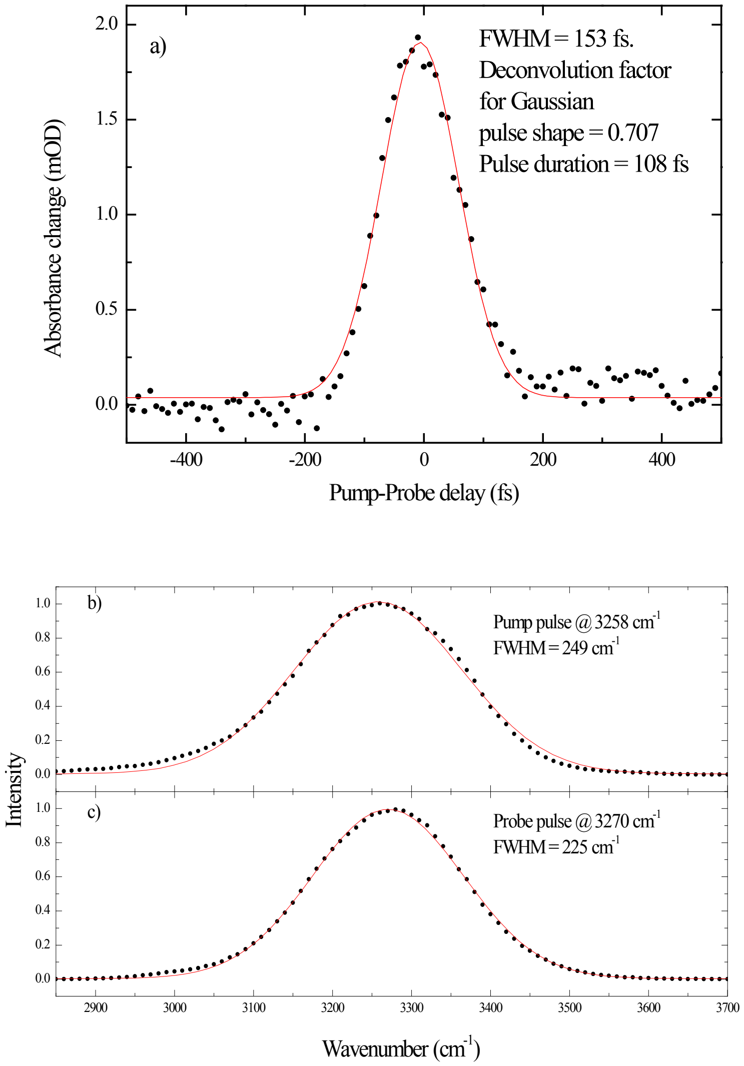

Figure 4.4: (a) Two-photon absorption in 50 µm Ge plate as a function of pump-probe delay. The Gauss-fit (red line) of the measured cross-correlation signal width equals 153 fs that leads to temporal resolution of an experiment of 108 fs. (b,c) Corresponding spectra of the mid-IR pump (b) and probe (c) pulses.

5 2-pyridone dimer: a DNA model system

To understand the functionality of deoxyribonucleic acid (DNA), its high replication ability and mutations mechanisms, hydrogen bonding between base pairs located on two, antiparallel strands and the proton transfer within a base pair have been the subject of numerous studies. Native DNA is a huge and complex macromolecule and therefore basic investigations focus on shorter oligomers containing only one type of complementary base pair (A-T or G-C) or even on single dimers in gas phase or in solution. Frequently, further simplification is made by replacing the DNA (or RNA) base pairs by model systems such as 7-azaindole or 2-pyridone/2-hydroxypyridine dimers. In this chapter, new results on the complex chemistry of 2-pyridone/2-hydroxypyridine in dichloromethane-d_2 (CD_2Cl_2) solution will be presented.

5.1 2-pyridone/2-hyroxypiridine tautomerism

2-pyridone (PD), an organic compound with the molecular formula $C_5H_4NH(O)$ is a popular model system for the pyrimidine nucleobases thymine and uracil [121,122]. The cyclic amide is subject to lactam-lactim tautomerism, whereby 2-hydroxypyridine (HP) is formed (Figure 5.1). In the gas phase both HP and PD have been investigated: as isolated molecule [123,124,125], in clusters with water or ammonia [126,127,128,129,130], sometimes also with larger hydrogen bonding agents [131,132]. In the solid state hydrogen-bonded puckered chains of PD with orthorhombic lattice type are predominant [133,134]. In a recent study an alternative monoclinic polymorph with cyclic dimer units has been reported [135]. In solution, due to the small energy difference, both tautomers can exist, with the equilibrium depending sensitively on solvent properties. As PD has a larger dipole moment than HP, PD is favoured in polar solvents, whereas HP is preferred in low-polarity solvents.

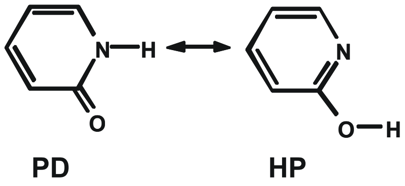

Figure 5.1: 2-Pyridone (lactam, cyclic amide) – 2-Hydroxypyridine (lactim, cyclic carboximidic acid) tautomerism.

Both tautomers can form three different cyclic dimers by hydrogen bond formation: two homodimers $(PD)_2$ and $(HP)_2$ and the cyclic mixed dimer PD-HP (reaction products in Figure 5.2b-d). Gas phase experiments allow for independent investigation of particular dimers [127,129,136,137,138,139]. In solution, however, all the three possible dimers have been suggested to appear simultaneously [140,141,142,143,144,145]. In hydrogen bonding solvents the two monomer tautomers can also form complexes with solvent molecules. In addition, the presence of chainlike dimeric species containing only a single hydrogen bond between the monomers should be taken into account.

As a result, a variety of solvent-dependent equilibria determines the relative concentrations of the different species. Their multitude makes it cumbersome to determine all equilibrium constants, which until now has mostly been attempted by means of UV [140,141,142,144,146,147,148], IR [143,144,149,150,151,152], and NMR spectroscopy [144,148,153] or by theoretical methods [145,151,153,154,155,156,157]. IR spectroscopy has been used to derive structural information on gas phase PD or HP monomer by looking at the free NH or OH stretching band [158] or at the full spectrum of PD using fluorescence dip spectroscopy [139] and on PD in solution by use of ^{15}N and ^{18}O isotope labelling [159]. $(PD)_2$ and PD-HP dimers in the gas phase have been explored with fluorescence dip spectroscopy [127,128,160,161]. In liquid solution fingerprint modes have been assigned to either PD monomer or cyclic $(PD)_2$ [147], and experimental low temperature matrix isolation spectroscopy of PD and HP has also been reported [149,150], as well as theoretical studies analyzing these results [151,162,163]. The low-frequency intermolecular modes of $(PD)_2$ have also been studied in detail in gas phase experiments, [136,137,138,164], in liquid solution [165], and with theoretical methods [166].

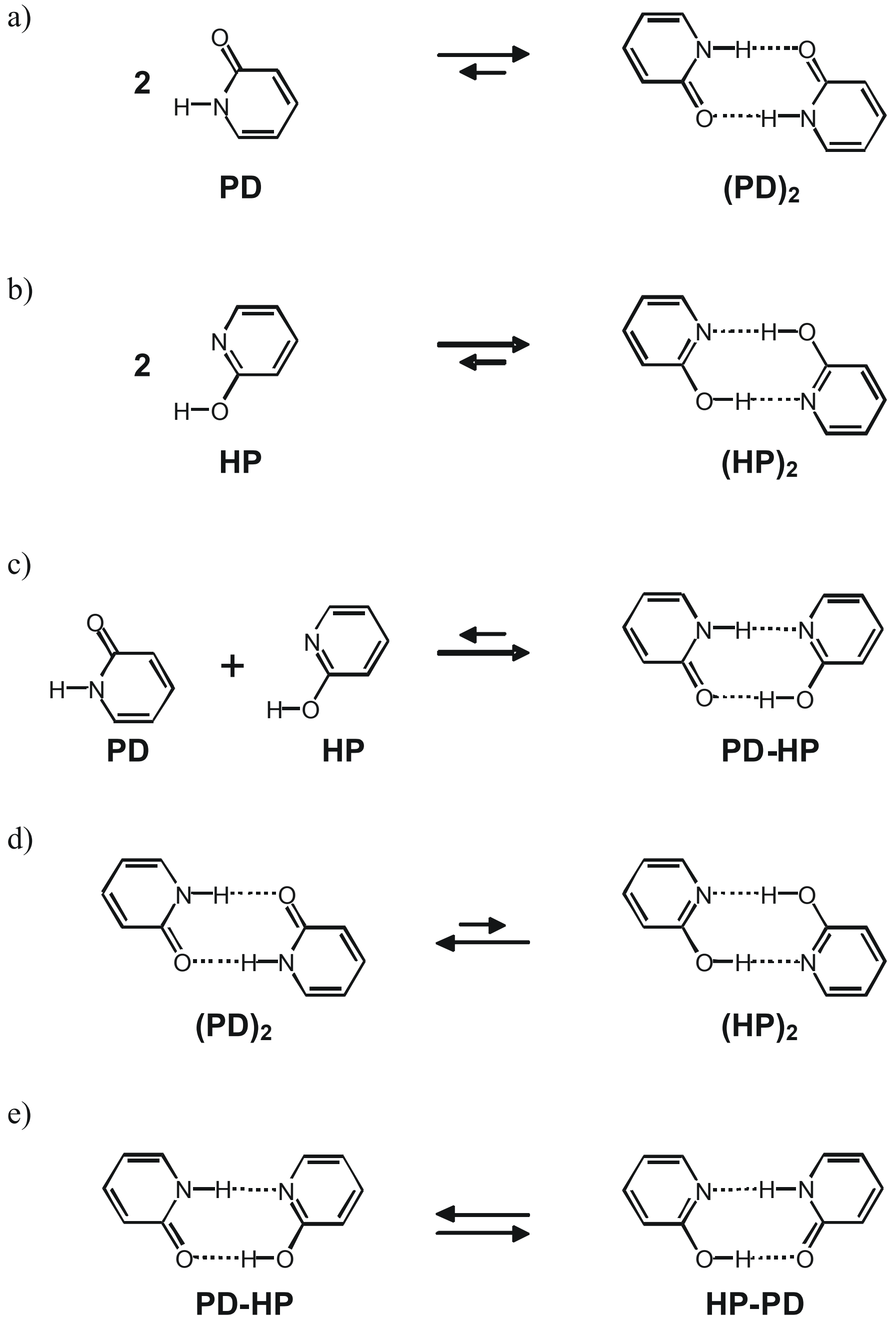

Figure 5.2: 2-Pyridone/2-Hydroxypyridine dimerization pathways (a-c) and double proton transfer mechanism, converting one cyclic dimer type to another (d,e).

In the complexation chemistry of PD/HP, hydrogen bonds play a central role. Proton transfer, necessary to convert PD into HP or vice versa, can be mediated by hydrogen bonds in protic solvents (Figure 5.2). In particular the two cyclic homodimers may exchange by a double proton transfer mechanism, converting $(PD)_2$ into $(HP)_2$, and vice versa, through the double hydrogen bond coordinate (Figure 5.2d). Proton transfer in the cyclic mixed dimer, changing PD-HP into HP-PD, has been investigated in context of possible proton transfer between DNA bases (Figure 5.2e) [167].

In the following sections, the results of IR spectroscopy and theoretical calculations combined NMR measurements will be presented that reveal the role of different tautomers in complexation chemistry of PD/HP in weakly polar solvent dichloromethane-d_2 [21,22].

In section 5.2, the results of temperature-dependent ^{1}H NMR experiment of ^{15}N-labeled 2-pyridone/2-hydroxypyridine will be discussed. Quantum chemical calculations (density functional theory) of vibrational spectra will be presented in section 5.3. In section 5.4, contributions of IR-active vibrations of different molecular species in the upper part of fingerprint range and NH/OH stretching mode region will be investigated. For detailed analysis of infrared linear spectra measured as a function of the total 2-pyridone/2-hydroxypyridine concentration and as a function of temperature (193-298 K), two-dimensional correlation spectroscopy is employed. The interpretation of synchronous and asynchronous correlation maps generated from experimental data will be given in section 5.5. Finally, femtosecond mid-IR pump-probe experiment on the NH/OH stretching band of 2-pyridone/2-hydroxypyridine in dichloromethane solution, followed by the analysis of the results in terms of contributions by vibrational population kinetics and by low-frequency wavepacket motions, is described in section 5.6. The chapter concludes with a summary in section 5.7.

The NMR measurements has been performed in collaboration with the research group of Prof. Hans-Heinrich Limbach from the Freie Universität Berlin, Institut für Chemie und Biochemie, and the temperature-dependent IR experiment as well as 2D correlation analysis has been accomplished together with Prof. Bogusława Czarnik-Matusewicz from the Faculty of Chemistry of Wrocław University.

5.2 Equilibrium composition of solutions – NMR spectroscopy

2-pyridone/2-hydroxypyridine labelled with ^{15}N was synthesized from coumalic acid methylester and a water solution of $^{15}NH_3$ as described in supplementary information for ref. [21]. The spectra were measured on a Bruker AMX-500 spectrometer, using CD_2Cl_2 as a solvent and 0.0002-0.02M of 2-pyridone/2-hydroxypyridine-^{15}N. Chemical shifts were measured using the solvent peak as internal standard and recalibrated into the conventional TMS scale.

5.2.1 Results and discussion

The NMR spectra were recorded as a function of temperature to investigate the possibility of slowing down proton transfer and molecular exchange processes between the different 2-pyridone/2-hydroxypyridine species and resolving their corresponding NMR signals.

At all temperatures only single NH signals are observed, which shifts to low field upon cooling. For all concentrations, the limiting value of the chemical shift, reached at the lowest temperature, is 14.2 ppm. This value has been confirmed by measuring ^{1}H spectra of 0.02 M solution of 2-pyridone/2-hydroxypyridine in CDF_3/CDF_2Cl mixtures at temperatures as low as 130 K (experimental technique is described in ref. [168]). Upon decrease of the temperature the signals decoalesce into doublets, characterized by a coupling constant of $^1J_{NH}$ = 89 Hz. The decoalescence temperature decreases from about 250 K for the 0.0002 M sample to 220 K for the 0.02 M sample. At the decoalescence temperature the inverse proton lifetime in pyridine is about 250 s^{-1}, as has been shown previously for related systems exhibiting intermolecular proton exchange from and to nitrogen [169,170]. The increase of the inverse lifetimes with concentration is a typical sign for a proton exchange mechanism involving 2-pyridone/2-hydroxypyridine self-associates. The low-field NH resonances arise exclusively from self-associates of 2-pyridone/2-hydroxypyridine since the exchange of the NH protons of 2-pyridone/2-hydroxypyridine with the OH protons of water is slow on the NMR time scale [171]. It follows that the shift of the NH signals to low field upon cooling indicates a fast molecular exchange between several 2-pyridone/2-hydroxypyridine species, with its equilibrium shifted to hydrogen-bonded associates upon cooling. The concentration dependence of the signals at given temperatures supports this conclusion. Experimental ^1H chemical shifts, δ(NH), are collected in Tab. 5.1.

At the lowest temperature, the δ(NH) chemical shift of 2-pyridone/2-hydroxypyridine approaches the value of 14.2 ppm in CD_2Cl_2 and also in CDF_3/CDF_2Cl mixture. This value is independent of concentration and remains the same in different polar solvents that are not hydrogen bond acceptors. Therefore, it has been assigned to the intrinsic value of the dominant dimer species. In addition to that, the large value of $^1J_{NH}$ = 89 Hz indicates that the PD dimer structure is predominant, whereas HP can be considered to be of minor relevance [159]. This value for the coupling constant is typical for hydrogen bonded NH···N or NH···O hydrogen bonds [172], where the value depends on the hydrogen bond strength [173]. Thus, the dominant complex at low temperatures is cyclic $(PD)_2$. Indeed, the cyclic heterodimer (PD-HP) would give rise to two different H-bonding proton signals in the slow exchange regime, whereas cyclic $(HP)_2$ would have a very small value of $^1J_{NH}$.

Tab. 5.1: Experimental 1H chemical shifts, $\delta N\underline{H}$ of the mobile proton of 2-pyridone/2-hydroxypyridine - ^{15}N, dissolved in CD_2Cl_2.

T [K]	δ(N<u>H</u>) [ppm] 0.0002 M	δ(N<u>H</u>) [ppm] 0.002 M	δ(N<u>H</u>) [ppm] 0.02 M
360	8.48	9.58	11.38
340	8.62	10.13	11.90
320	8.86	10.79	12.40
300	9.29	11.55	12.94
280	10.00	12.46	13.39
260	10.84	13.02	13.61
240	11.83	13.48	13.81
220	12.85	13.80	13.96
200	13.57	14.02	14.08
180	14.02	14.13	14.15

The NMR results show that the $(PD)_2$ dimer is the dominant species at low temperatures which exchanges with PD in monomeric form or complexed with the solvent. At temperatures above 240 K, a proton exchange mechanism sets in, leading to a collapse of the doublet of labelled 2-pyridone/2-hydroxypyridine. In Figure 5.2, a set of the reactions that are important for the discussion of the proton exchange mechanism are shown. Figure 5.2a-c shows the formation of cyclic dimers $(PD)_2$, $(HP)_2$, and (PD-HP) from the corresponding monomers. It will be shown in the Section 5.5.2 that breaking and formation of the cyclic dimers likely occur via the pathways involving chainlike open dimers, the latter may act as transient or a short-lived species, where short-lived species has a lifetime much shorter than the NMR time scale, estimated to be a millisecond in this case. However, the open-chain structures from Figure 5.2 were omitted for clarity purposes. Figure 5.2d shows the double proton transfer which converts $(PD)_2$ into $(HP)_2$. The direct intramolecular conversion of PD monomers into HP monomers is unlikely because of the high energy barrier for such a process [154]. The more probable conversion via the double proton transfer within the cyclic dimer is indirectly supported by the spectra of 2-pyridone/2-hydroxypyridine solutions in CD_2Cl_2 in the presence of $SbCl_5$. Figure 5.2e shows the degenerate double proton transfer reaction, which interconverts cyclic (PD-HP) and cyclic (HP-PD). The proton exchange mechanism consists of several steps and starts with the appropriate PD and HP monomers. At low concentration and high temperatures there is a significant fraction of 2-pyridone/2-hydroxypyridine monomers, while at lowest temperatures the formation of monomers would require breakage of a dimer. The dimers are mostly in the $(PD)_2$ form, so the HP monomers are created if the $(PD)_2$ converts into $(HP)_2$ by the double proton transfer prior to the breaking. The proton exchange proceeds when PD and HP monomers form a heterodimer (PD-HP), which converts into (HP-PD) by another double proton transfer. Eventually, the heterodimer breaks back into monomers, which can further participate in the formation of the dimers and continuation of the proton exchange.

5.3 Linear IR spectroscopy of 2-pyridone/2-hydroxypyridine in CD_2Cl_2

Two spectral regions provide insight into the chemical equilibria between the 2-pyridone/2-hydroxypyridine species. The upper part of the fingerprint region between 1600 and 1700 cm^{-1} involves C=O stretching vibrational modes indicative of PD species, either as monomer or as part of a complex. As has been discussed in the previous Section, no clear marker modes are available for the HP conformer (as monomer or as constituent of a complex). The strong absorption of the solvent C−D bending mode makes the spectral region of C−O stretching vibration inaccessible. In addition to that, the remaining part of the fingerprint region does not provide access to distinct vibrational marker modes of particular monomer or dimer species. In the NH/OH stretching region between 2400 and 3700 cm^{-1}, on the other hand, both PD and HP conformers can a priori contribute, as monomer and as constituent of complexes.

5.3.1 Experimental

Both 2-pyridone/2-hydroxypyridine (Fluka) and dichloromethane-d_2 solvent (Deutero GmbH) were used without further purification for IR measurements. A concentration-dependent series was measured with a Varian 640 FT-IR spectrometer (sample thickness 25 μm) in the range 0.05 – 0.35 M. A temperature-dependent measurement was obtained with a Nicolet Nexus FT-IR spectrometer, using a home-built 41 μm thick cell with KRS-5 windows, placed inside a temperature-controlled jacket (Specac).

5.3.2 Results and discussion

In Figure 5.3 the absorption spectra of 2-pyridone/2-hydroxypyridine dissolved in CD_2Cl_2, normalized to the total 2-pyridone/2-hydroxypyridine concentration, are shown. The concentration values ranging from 0.05 to 0.35 M indicate the total amount of 2-pyridone/2-

hydroxypyridine monomer dissolved. Absorbance changes after this normalization procedure reflect differences in relative spectral contributions, caused by an altered chemical composition as a function of total 2-pyridone/2-hydroxypyridine concentration.

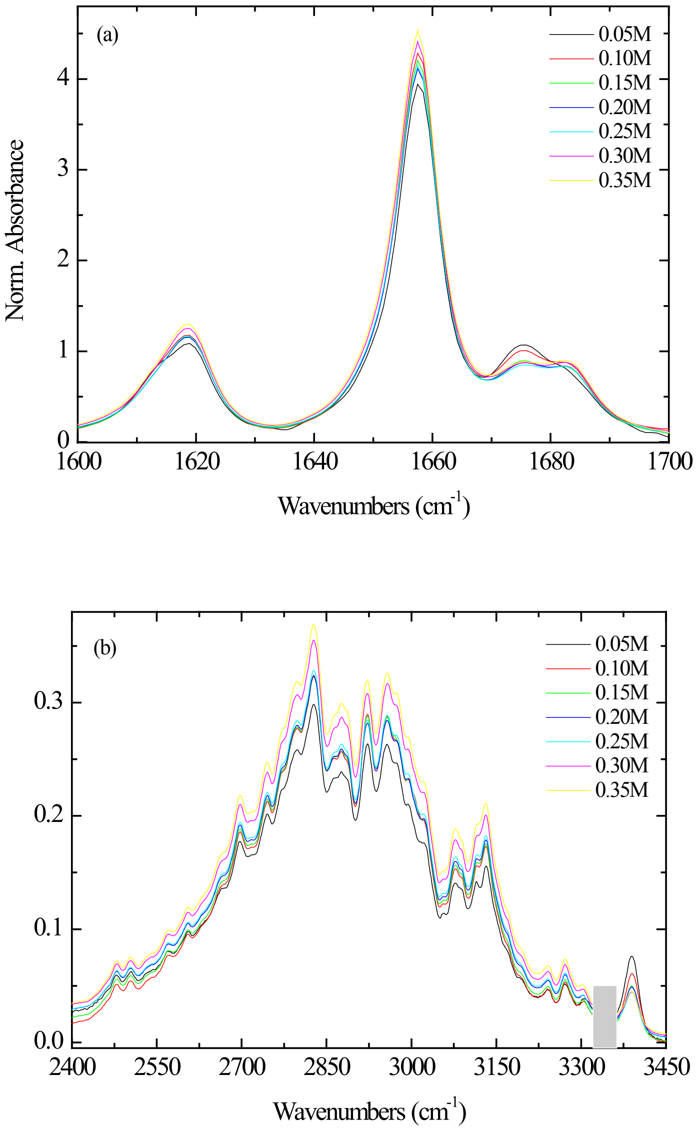

Figure 5.3: Concentration-dependent FT-IR spectra of PD/HP in CD_2Cl_2 after normalization to total 2-pyridone/2-hydroxypyridine concentration: (a) in the upper part of the fingerprint spectral region and (b) in the NH/OH stretching mode region. The gray bar around 3340 cm^{-1} indicates imperfect solvent subtraction.

The magnitude of the absorption peaks at 1618 and 1658 cm^{-1} increases continuously as a function of total 2-pyridone/2-hydroxypyridine concentration, whereas the absorption peak at 1675 cm^{-1} changes its magnitude significantly only for the two lowest 2-pyridone/2-hydroxypyridine concentration values. In the NH/OH stretching region a broad absorption band containing a detailed substructure covering the range from 2400 to 3350 cm^{-1} enlarges significantly upon concentration increase, whereas a narrow band at 3391 cm^{-1} changes its magnitude in the opposite direction. Decreasing the temperature of a 0.105 M 2-pyridone/2-hydroxypyridine solution from 298 to 193 K leads to a pronounced increase in magnitude of absorption bands at 1618 and 1658 cm^{-1}, where the latter shows a frequency-downshift of 2 cm^{-1}, accompanied by a band shape change (Figure 5.4a). In contrast, absorption bands at 1613 and 1675 cm^{-1} decrease in magnitude. The absorption band at 1675 cm^{-1} shows a frequency-downshift of 3 cm^{-1} and has fully disappeared at 193 K. The 1683 cm^{-1} band changes its magnitude to a lower value and its frequency position to a higher value (net frequency-upshift of 4 cm^{-1}). Upon temperature decrease, the NH/OH stretching region depicts a clear increase of the absorption manifold between 2400 and 3000 cm^{-1}, whereas the narrow transition at 3390 cm^{-1} exhibits a decrease (Figure 5.4b). Interestingly the spectral region between 3000 and 3350 cm^{-1} shows less profound absorption changes with alternating positive and negative signs.

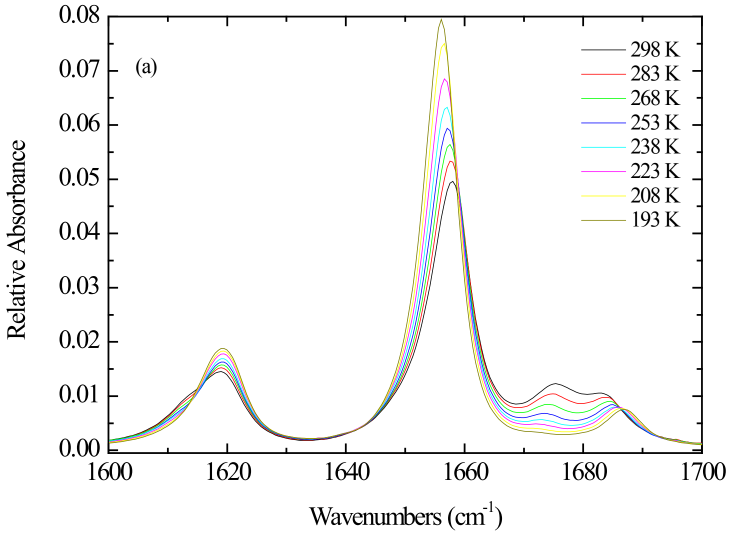

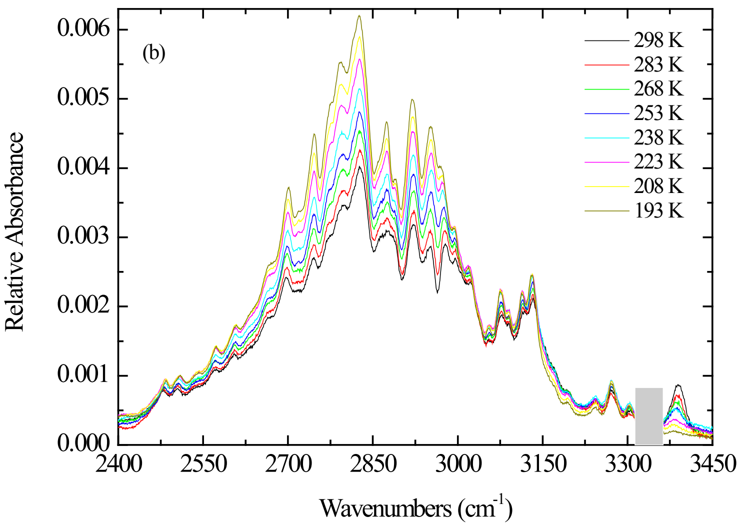

Figure 5.4: Temperature-dependent FT-IR spectra of PD/HP in CD_2Cl_2 after solution density correction: (a) in the upper part of the fingerprint spectral region and (b) in the NH/OH stretching mode region. The gray bar around 3340 cm^{-1} indicates imperfect solvent subtraction.

5.4 Quantum chemical calculations of vibrational spectra

Vibrational spectra have been calculated for various monomeric and dimeric species using density functional theory (B3LYP/6-311+G(d,p)) as implemented in Gaussian 03 [174]. Harmonic frequencies were obtained for optimized geometries and scaled by a factor of 0.965.

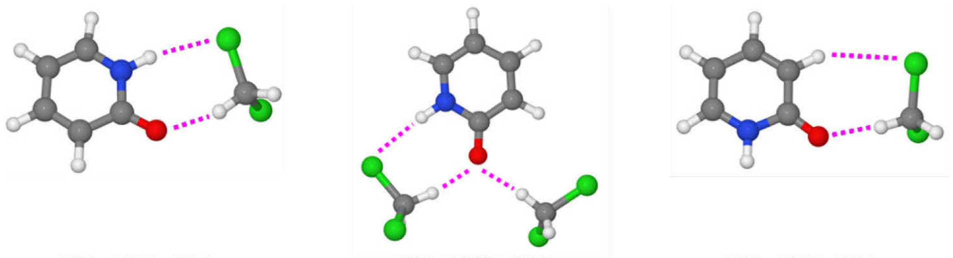

PD-$(CD_2Cl_2)_a$ **PD-$(CD_2Cl_2)_2$** **PD-$(CD_2Cl_2)_b$**

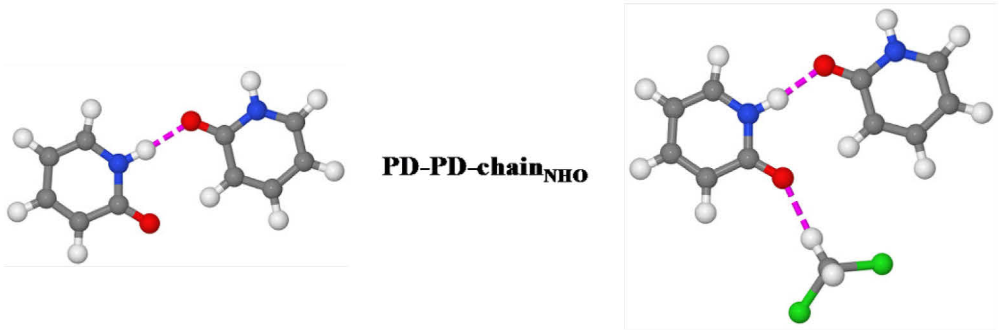

PD-PD-chain$_{NHO}$

PD-PD-chain$_{NHN}$

HP-PD-chain$_{OHO}$

$(PD)_4$ tetramer

Figure 5.5: Optimized structures of 2-pyridone monomer complexes with solvent molecule(s) (upper panel), single-hydrogen bonded complexes unsolvated (left) and with solvated carbonyl group (right) and $(PD)_4$ tetramer (bottom right).

In the gas phase, the PD conformer has been calculated to be the most stable among monomers and cyclic $(PD)_2$ among three possible dimers [21]. An open dimer, PD-PD, has been obtained from the cyclic double hydrogen-bonded dimer $(PD)_2$ by rotating one of the monomers around the C=O bond by 180° such that they are connected only by a single hydrogen bond (chain-like). Moreover, three different PD-solvent complexes have been explored, as well as the cyclic tetramer $(PD)_4$ (Figure 5.5). The carbonyl stretching mode ν(C=O) is relatively sensitive to the local environment and as such, it can serve as a specific marker mode capable of distinguishing different 2-pyridone/2-hydroxypyridine species.

In Figure 5.6a, the experimental IR steady-state absorption spectrum of 2-pyridone/2-hydroxypyridine dissolved in CD_2Cl_2 is decomposed into the individual bands of Voigt shape. The calculated peaks of different species that can potentially contribute to the equilibrium solution composition are shown in Figure 5.6b. The arrows denote the direction of normalized absorbance changes upon dilution. The absorption bands below 1630 cm^{-1} belong to NH or OH combination tones involving quanta of the bending modes and aromatic ring stretching motions). The bands between 1630 and 1700 cm^{-1} correspond to the absorption of the C=O stretching mode.

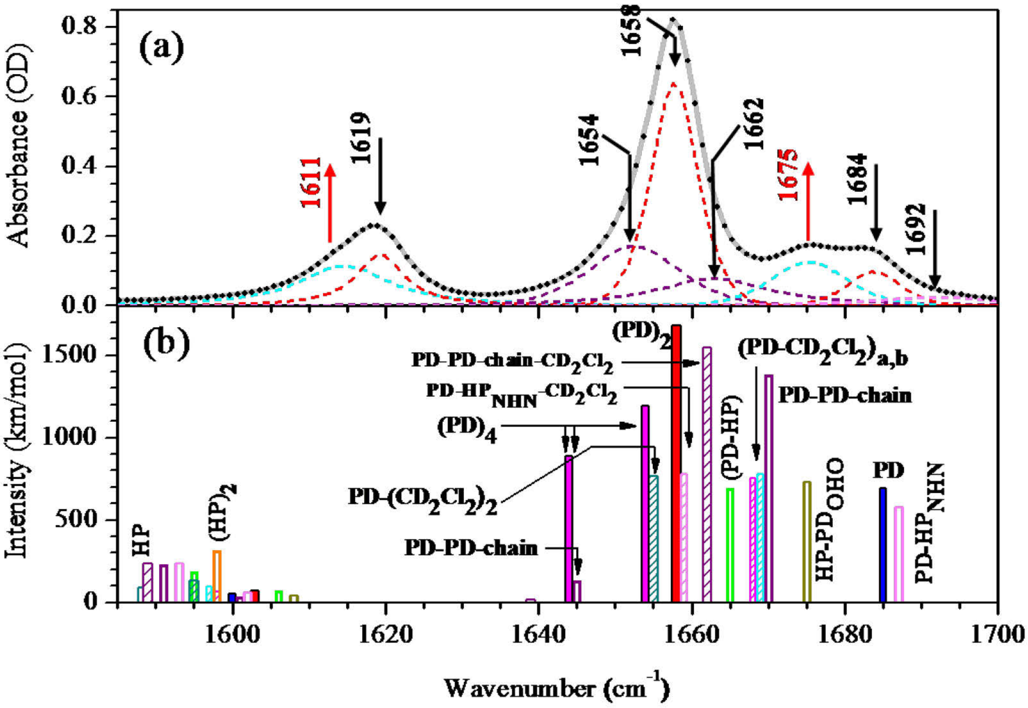

Figure 5.6: (a) IR absorption spectrum of 2-pyridone dissolved in CD_2Cl_2 (solid gray line) (c = 0.20 mol/L) together with a peak fitting decomposition (black dots; solid coloured lines depict different components) in the upper fingerprint spectral region; arrows indicate change of absorbance upon dilution. (b) Calculated peaks (B3LYP/6-311+G(d,p); scaled by 0.965) for different species (see Figure 5.2 and Figure 5.5): 1585-1630 cm^{-1}, NH/OH bending + aromatic ring stretching vibrations; 1630-1700 cm^{-1}, C=O stretching mode absorption.

In the fingerprint region, only those species that have C=O stretching marker modes, i.e., species that consist of at least one PD unit (PD monomer, PD-solvent complexes, cyclic $(PD)_2$, and cyclic (PD-HP) cyclic, and chainlike PD-PD, HD-PD, and PD-HP or even larger aggregations with at least one PD unit) can be identified. Calculated frequencies for the C=O stretching mode are summarized in Tab. 5.2. In contrast, HP monomer, HP-solvent complex, cyclic

$(HP)_2$ and chainlike HP-HP cannot be probed unequivocally in the fingerprint region, because OH bending motions are typically delocalized and mixed with unspecific aromatic stretching motions, which occur in all species. Experimentally observed frequencies in the range 1600-1700 cm^{-1} are compiled in Table 5.3 together with tentative assignments, which will be discussed in section 5.5.1.

Tab. 5.2: Calculated harmonic frequencies for ν(C=O) scaled by 0.965.

Species	Calculated frequency (cm^{-1})
PD	1685
$(PD)_2$	1658
PD-HP	1665
$(PD\text{-}CD_2Cl_2)_a$	1668
$(PD\text{-}CD_2Cl_2)_b$	1669
$(PD\text{-}CD_2Cl_2)_2$	1655
PD-PD $chain_{NHO}$	1670(s), 1645(w)
PD-PD $chain_{OHO}$	1675
PD-PD $chain_{NHN}$	1687

Experimental and calculated linear FT-IR spectra indicate the existence of several 2-pyridone/2-hydroxypyridine species, where, however, a straightforward interpretation is hampered by extensive spectral overlap of many vibrational transitions in both the fingerprint and the NH/OH stretching regions. To improve the spectral resolution, two-dimensional correlation spectroscopy [44,45] has been applied, which provides additional insight into the assignment of absorption bands to different species by analysis of concentration- and temperature-dependent spectral changes.

5.5 2D correlation analysis of IR experiment on 2-pyridone/2-hydroxypyridine

Due to the time averaging aspect of NMR spectroscopy, observing 2-pyridone/2-hydroxypyridine species with lifetimes clearly shorter than a millisecond is impossible. Instead, the analysis of the infrared results may provide access to short-lived species. Investigation of vibrational transitions of species-dependent marker modes in the fingerprint and in the NH/OH stretch spectral regions indicates the presence of these species in CD_2Cl_2 solution. Interpretation of the linear spectra - together with quantum chemical calculations - to derive the chemical speciation in CD_2Cl_2 solution involves many complications.

In the fingerprint spectral region it is not possible to identify a well-isolated marker mode for HP units as monomer or as part of dimers, neither for OH bending modes nor for C−O stretching vibrations. In the NH/OH stretching region only PD and HP units with their NH or OH groups not being part of a medium strong hydrogen bond (i.e., uncomplexed, or being part of a solute-solvent complex) are directly identifiable by their narrow NH or OH stretching bands. In contrast, hydrogen bond formation in dimers (in cyclic or chainlike conformations) leads to strongly broadened and red-shifted NH/OH stretching bands with pronounced substructures, revealing extensive anharmonic mode couplings of high-frequency NH/OH stretching modes with hydrogen bond low-frequency vibrations as well as fingerprint vibrations, the latter through Fermi resonance interactions with combination and overtone states. Similar characteristics have been observed in other medium-strong hydrogen-bonded molecular systems, such as formic acid dimer, acetic acid dimer, benzoic acid dimer, or 7-azaindole dimer [175,176,177,178,179,180,181,182].

In addition, a substantial spectral overlap both in the fingerprint region and in the NH/OH stretch region complicates the unique and unambiguous assignment of vibrational bands.

Two-dimensional correlation spectroscopy of spectrally overlapping vibrational transitions of 2-pyridone/2-hydroxypyridine, has the potential to lift some of the limitations of linear IR spectroscopy.

In the Section 2.5, the theory of two-dimensional correlation spectroscopy was introduced. Here, the external variable θ (perturbation parameter) is either the total concentration of 2-pyridone/2-hydroxypyridine in solution or the temperature of the solution. The perturbation shifts the equilibrium from dimeric species toward the increasingly favoured formation of monomeric species upon dilution or upon heating. 2D correlation spectroscopy allows for separating those different species by analyzing the synchronous and asynchronous maps simultaneously.

The resulting synchronous and asynchronous 2D IR correlation maps are presented in Figure 5.7 for the high-frequency part of the fingerprint spectral region, and in Figure 5.8 for the high-frequency NH/OH stretching mode region.

5.5.1 Analysis of FT-IR results of the high-frequency part of fingerprint region

Positive cross peaks in the synchronous correlation maps may develop if spectral changes for the two frequency positions are correlated (cf. Figure 2.6). To confirm this correlation, cross peaks at these positions should be absent in the asynchronous maps. The strong positive cross peak around $\Phi(1619, 1658)$ appearing in the synchronous maps of the temperature- and concentration-dependent experiments (Fig. 5.7, two top plots) together with the absence of a corresponding asynchronous peak (Fig. 5.7, two bottom plots) reveals that the spectral changes at the two frequency positions are correlated and develop in the same direction. There are two more positive synchronous cross peaks without counterpart in the asynchronous spectrum in the concentration-dependent experiment, namely, the weak peaks $\Phi(1619, 1684)$ and $\Phi(1658, 1684)$, which point to some slight correlation. A similar correlation is found in the temperature-dependent synchronous map at slightly different peak positions $\Phi(1619, 1688)$ and $\Phi(1656, 1688)$. Based on these observations, it can be concluded that the bands at 1619, 1658/1656, and 1684/1688 cm^{-1} are likely to originate from the same molecular species. The negative synchronous cross peaks $\Phi(1619, 1675)$, $\Phi(1658/ 1656, 1675)$, and $\Phi(1675, 1684/1688)$ indicate that the respective vibrational bands come from different species, because the spectral changes occur in opposite directions. A positive correlation between the 1612 and 1675 cm^{-1} bands in both experiments points to the fact that these originate from the same molecular species or associate. The concentration- and temperature- dependent synchronous maps are thus dominated by two molecular species, which are strongly negatively correlated to each other, i.e., a concentration increase or a temperature decrease leads to a rise of species I with bands at 1619, 1658/ 1656, and 1684/1688 cm^{-1} and a decline of species II with band at 1612 and 1675 cm^{-1}.

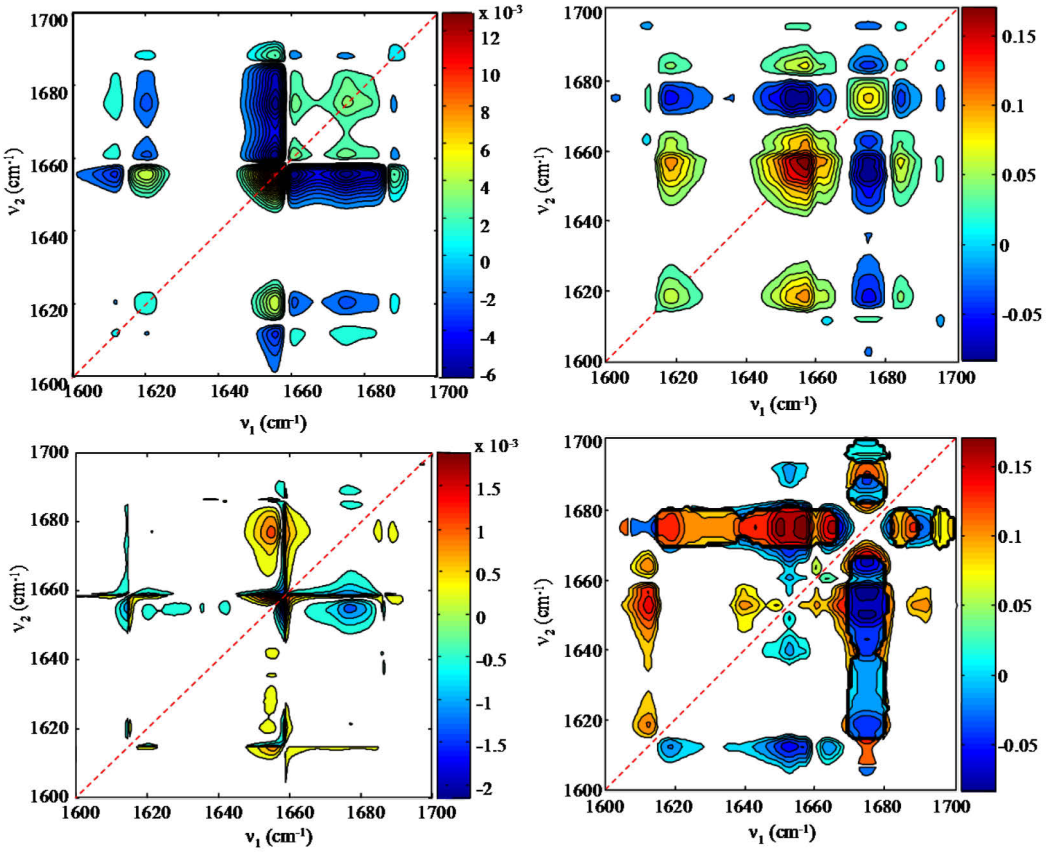

Figure 5.7: 2D IR correlation synchronous (top) and asynchronous (bottom) maps for temperature- (left) and concentration-dependent (right) spectra of 2-pyridone/2-hydroxypyridine in CD_2Cl_2 in the high-frequency part of fingerprint spectral region. The colour bars indicate the range of intensity values.

In the asynchronous spectrum of the concentration-dependent experiment (Fig. 5.7, right) cross peaks at Ψ(1675, 1687) and Ψ(1612, 1618) are observed between pairs of vibrational band assignable to different species. An even more pronounced example of improving spectral resolution is given by the temperature-dependent asynchronous map. Two strongly spectrally overlapping bands at 1654 and 1658 cm^{-1} can be distinguished by inspecting their asynchronous behaviour with respect to the 1677 cm^{-1} band. This is because the 1654 cm^{-1} transition has a strong asynchronous temperature dependence compared to the 1677 cm^{-1} band, whereas the 1658 cm^{-1} transition has not and, thus, is fully absent in the asynchronous map. The asynchronicity between the two closely located bands can be also observed directly in the asynchronous spectrum at Ψ(1654, 1658). This indicates, that the strongest band of the fingerprint region is actually composed of two overlapping vibrational transitions of two distinctly different structures, namely, molecular species I (located at 1658 cm^{-1}) and a molecular species III (located at 1654 cm^{-1}), which has not been reported on previously. The same conclusion can be drawn from the concentration-dependent asynchronous map.

The analysis of the sign of the asynchronous cross peaks multiplied by the sign of the corresponding synchronous cross peaks (on the basis of Noda's rules [44,45]) allows to derive the following sequence of the intensity variations upon temperature decrease can be deduced: 1653/1654 → 1612-1675 → 1619-1658/1656-1684/1688 cm^{-1}, i.e., spectral variation of molecular species III occur before those of species I and II, where those of I and II behave in a more synchronous, but in opposite direction. Such straightforward conclusion cannot be directly derived from the concentration-dependent data, which may hint at the fact that concentration variation and temperature change do not necessarily imply identical behaviour.

After having provided insight into synchronous and asynchronous correlations of different vibrational transitions, the assignments of the IR absorption bands (cf. Figure 5.6) based on the combined experimental and calculated results for the vibrational spectra is proposed. Such assignments are summarized in Table 5.3.

Tab. 5.3: Experimental frequencies observed in the fingerprint region with assignment (in cm^{-1}) and calculated counterparts.

Calculated frequency	2D spectra (varying T)	Fitting results	Assignment	Species
	1688(s)	1683.5	combination tone	$(PD)_2$
1668, 1669	1675(s)/1677 (a)	1674.9	ν(C=O)	$(PD\text{-}CD_2Cl_2)_{a,b}$
1670	1662(a)	1661.6	ν(C=O)	PD-PD chain ($C{=}O_{free}$)
1658	1656(s)/1658 (a)	1657.7	ν(C=O)	$(PD)_2$
1645	1654(a)	1654.0	ν(C=O)	PD-PD chain ($C{=}O_{HB}$)
1603	1619(s)	1618.7	δ(NH)/ν_{ring}	$(PD)_2$
	1612(s)	1610.9	δ(NH)/ν_{ring}	$(PD\text{-}CD_2Cl_2)_{a,b}$

Three transitions which from the 2D analysis have been shown to originate from the same molecular species I will be discussed first. The strong absorption band around 1658 cm^{-1}, which decreases upon dilution or heating, is assigned to absorption of the ν(C=O) mode in the cyclic homodimer $(PD)_2$, in agreement with previous assignments in the literature [143,152]. The 1619 cm^{-1} transition can be assigned to NH bending motions combined with aromatic ring stretching motions (δ(NH)/ν_{ring}) in $(PD)_2$. Because of its high transition frequency, the molecular transition located at 1684/1688 cm^{-1} cannot be due to a carbonyl stretching vibration. Instead, Fermi coupling of the carbonyl stretching vibration to either a combination tone from C-H wagging modes located around 776 and 940 cm^{-1} or a combination/overtone from a C-H wagging mode around 860 cm^{-1} and ring deformation modes around 847 cm^{-1} cause this transition. These frequencies have been derived from our own calculations. The previous results of the similar vibrational modes in PD monomers have been reported in Refs.[150,151,162,163].

Now molecular species II, which has vibrational transitions at 1612 and 1675 cm^{-1} will be assign. Upon diluting/heating, the peak at 1675 cm^{-1} increases, indicating that the absorption peak is due to a monomer species that is preferentially formed at lower concentrations/higher temperatures. The results of the calculations suggest that PD-CD_2Cl_2 complexes (see Figure 5.5 for the two forms *a* and *b*) are responsible for the 1675 cm^{-1} band, as their ν(C=O) modes absorb in this spectral range. The 1612 cm^{-1} mode is again due to NH bending motions combined with aromatic ring stretching motions (δ(NH)/ν_{ring}).

Molecular species III, which has a spectral signature at 1653/1654 cm^{-1}, must be different from previously assigned molecular structures. The temperature-dependent asynchronous map (Fig. 5.7) shows an extended peak Ψ(1654-1665, 1677), which is interrupted at 1658 cm^{-1}. This could mean that a single broad transition contributes to the observed peak or it could indicate the existence of two bands with maxima at 1654 and 1662 cm^{-1}. The hydrogen-bonded PD-PD chain associates (Figure 5.5) would fulfil these requirements. The peak at 1654 cm^{-1} could come from the hydrogen-bonded C=O group connecting the two PD units inside the chain dimer, whereas the peak at 1662 cm^{-1} could originate from the C=O group which likely interacts with CD_2Cl_2 solvent molecules.

On the basis of the 2D IR correlation analysis of the upper part of the fingerprint region, the molecular species I, II, and III can be assigned to cyclic homodimers $(PD)_2$, the monomer-solvent complex PD-CD_2Cl_2, and to the chainlike dimer-solvent complex PD-PD-CD_2Cl_2. Taking both number and position of peaks detected in the 2D synchronous and asynchronous spectra, a line shape fitting procedure using Voigt line shape functions was applied to the IR spectrum of the 0.20 M solution. A good match between experimental and calculated spectra (Figure 5.6) confirms the assignment of the different spectral features. Contributions of other molecular species, including free PD monomer, chainlike PD-HP, cyclic (PD-HP), or even larger constituents such as the symmetric cyclic tetramer $(PD)_4$ does not have to be included [165,183].

5.5.2 Analysis of FT-IR results of the NH/OH stretching region

The high-frequency IR spectrum in the range between 2400 and 3300 cm^{-1} is composed of many overlapping bands including CH stretching modes as well as overtone and combination bands of fingerprint modes. The absorbance in this spectral region is enhanced upon concentration increase, whereas the narrow band at 3390 cm^{-1} is decreased. Thus, the broad band can be assigned to dimer and the narrow band at higher frequency to monomer species.

Accordingly, 2D analysis of the synchronous spectrum (Figure 5.8, top right) shows that the spectral changes at 3390 cm^{-1} are negatively correlated with the broad absorption band expanding from 2400 and 3300 cm^{-1}. The synchronous map obtained in the temperature experiment (Figure 5.8, top left) shows the negative correlation of the 3390 cm^{-1} band with a somewhat smaller spectral range of 2650-3000 cm^{-1}. An additional peak at 3160 cm^{-1} shows a similar negative correlation with the 2650-3000 cm^{-1} manifold. The corresponding asynchronous map in the concentration-dependent study (Figure 5.8 bottom right) reveals a strong asynchronicity between the peaks at 3316 and 3390 cm^{-1}, respectively, and the entire range of the broad absorption. The peak at 3390 cm^{-1} is assigned to the absorption of free NH groups in agreement with computational results and earlier studies in the literature [127,143,150,151,152].

The weaker asynchronous peak observed at 3316 cm^{-1} is downshifted by 74 cm^{-1} compared to the absorption of free NH groups. According to our calculations such a red-shift accounts for NH groups hydrogen bonded to CD_2Cl_2 solvent molecules. From the sign of the peaks it can be deduced that the changes attributed to the free NH groups are ahead of all other changes. The 2D analysis does not allow, however, to distinguish changes, which could testify against different hydrogen-bonded dimers giving rise to the broad absorption band between 2400 and 3300 cm^{-1}. Therefore, to extract more detailed information, principal component analysis (PCA) is applied [184]. This technique reduces a multidimensional data set to a set of new orthogonal variables, which are called principal components. PCA decomposes the original data matrix, here the set of concentration-dependent spectra, as the sum of the outer product of vectors (scores) containing information on how the individual spectra relate to each other and a second set of vectors (loadings), which carry information on how the vibrational frequencies relate to each other plus a residual matrix. After smoothing the spectra with the Savitzky-Golay algorithm [185] (filter width 25 cm^{-1}, second-order polynomial) and mean centring, two components could be extracted, one accounting for 97.93% of the absorbance changes (PC1) and the second one accounting for 1.38% (PC2), which together capture 99.32% of absorbance changes.

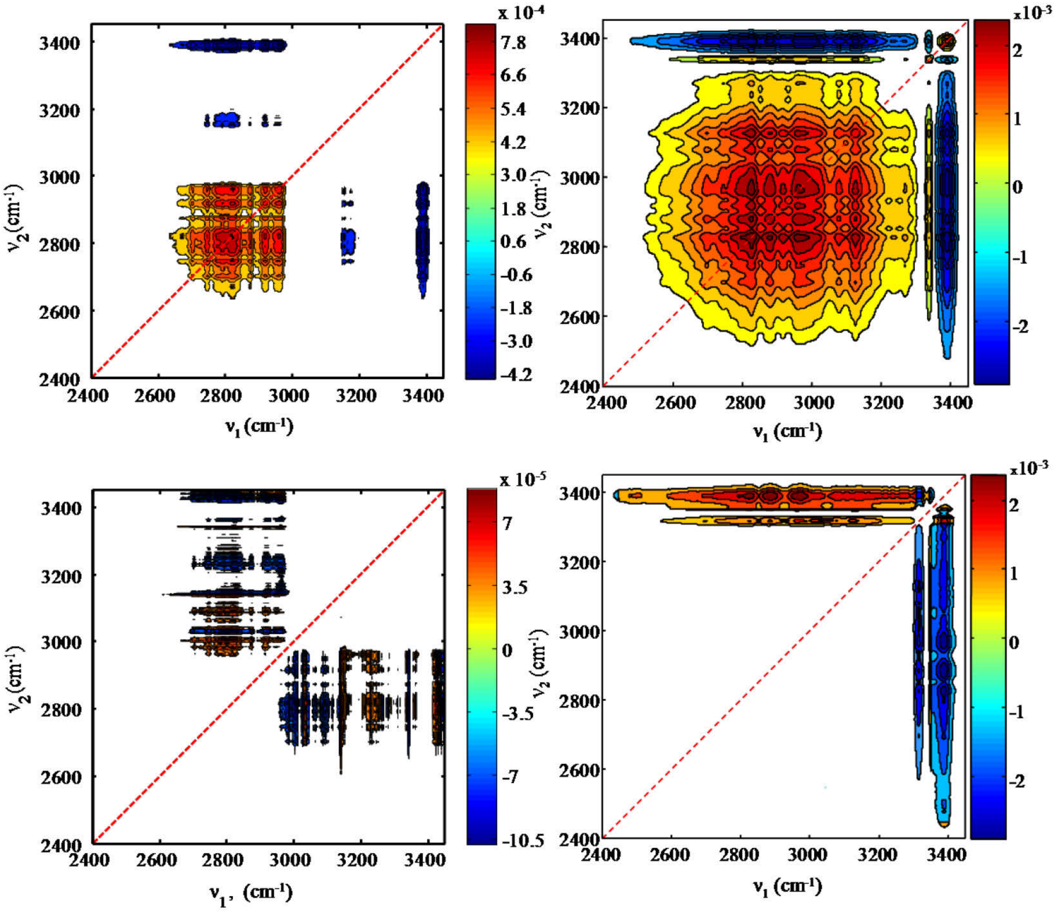

Figure 5.8: 2D IR correlation synchronous (top) and asynchronous (bottom) maps for temperature- (left) and concentration-dependent (right) spectra of 2-pyridone/2-hydroxypyridine in CD_2Cl_2 in the high-frequency spectral region. The colour bars indicate the range of intensity values.

The scores plot (Figure 5.9a) shows the relationship between the spectra for the different concentrations with respect to the principal component PC1 and the second component PC2. PC1 divides the spectra into two groups of low (0.05, 0.10 M) and high (0.30, 0.35 M) concentration, whereas spectra for intermediate concentrations are close to zero on the score plot and therefore less meaningful. PC2 on the other hand, divides the spectra into one group for low and high concentrations and a second group of intermediate concentrations (0.20, 0.25 M). The corresponding loadings plot (Figure 5.9b) shows that the vibrational frequencies can be associated with the two principal components. For PC1, two spectral regions can be distinguished, which reflect different directions of spectral changes. The two regions are discriminated by a sign change occurring around 3300 cm^{-1}. PC2 reveals an additional spectral distinction at about 2980 cm^{-1}, which splits the broad absorption between 2400 and 3300 cm^{-1} into two parts. To conclude this section, three spectral regions, which can be related to different concentration ranges, can be distinguished. Changes in the highest frequency range (above ~ 3300 cm^{-1}) occur mostly for the low concentration range, changes in the low frequency range (below ~ 2980 cm^{-1}) are associated with the two highest concentration values, whereas for concentrations with intermediate values spectral changes are linked to the frequency range 2980-3300 cm^{-1}.

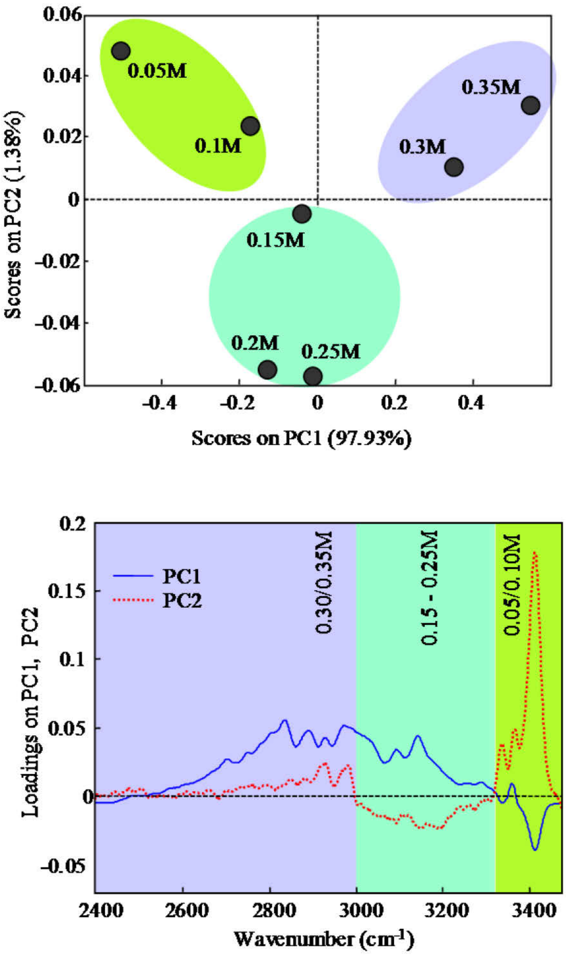

Figure 5.9: Principal component analysis: scores (a) and loadings (b) plot.

The results obtained by PCA allow for a more detailed analysis of the high-frequency region. The scores plot (Figure 5.9a) shows that the first principal component (PC1) of spectral variations reflects concentration-dependent absorbance changes. Dilute samples are characterized by negative scores over PC1, whereas the concentrated solutions have opposite values. From the loadings plot (Figure 5.9b) it is evident that the absorbance changes are related to the absorption of free NH groups at 3390 cm^{-1} and the broad absorption arises from dimers. Thus, PC1 is correlated with the association process as a function of concentration. As the concentration-dependent absorbance changes (PC1) dominate (97.93%) the high-frequency spectrum, any smaller spectral variations are difficult to observe without PCA. Here, a second component PC2, accounting for 1.38% of spectral variations has to be considered, which shows that the broad absorbance from 2400 to 3300 cm^{-1} arises from two differently associated species. From the simultaneous analysis of scores and loadings plots it can be concluded, that the high concentrations -where scores versus PC1 and PC2 are positive - have the biggest influence on spectral variations in the range from 2400 to 2980 cm^{-1}, where in addition the loadings against the two components are positive. Hence, the absorbance of the hydrogen-bonded NH stretching band of cyclic $(PD)_2$ must dominate this spectral region. The intermediate concentrations, instead, have the largest influence on the spectral variations in the range from 2980 to 3300 cm^{-1}. Therefore, absorptions in this range are attributed to species exhibiting weaker hydrogen bonds as compared to the cyclic dimer. For instance, single hydrogen-bonded chain dimers could account for absorption in this range. It should be noted that the relative contribution of principal components to the spectral changes does not allow forming a conclusion on the relative concentrations of different species in solution.

The PCA results are independently supported by analysis of the temperature-dependent linear spectra in the NH/OH stretching region (Figure 5.4b). In the range between 2400 and 3000 cm^{-1} the broad spectral manifold increases clearly in magnitude upon cooling, the transitions between 3000 and 3300 cm^{-1} show less change in absorbance, and the 3390 cm^{-1} band decreases in magnitude.

From the FT-IR measurements it can be concluded, that the marker bands of the fingerprint region provide evidence for the existence of cyclic $(PD)_2$ and PD-CD_2Cl_2 solute-solvent complexes, with an additional component assigned to chainlike PD-PD. The NH/OH stretching region shows vibrational marker bands that are assigned to uncomplexed NH groups (by PD monomers and/or PD units being part of chain-like dimers), and to PD-CD_2Cl_2 solute-solvent complexes. The uncomplexed OH stretching marker bands of the HP monomer and chainlike PD-HP and HP-HP was not observed. Extensive spectral overlap prevents from clear assignment of the broad spectral band between 2400 and 3300 cm^{-1} to a single hydrogen-bonded species. The 2D and PC analysis suggests strongly that this spectral region has three components, which would be in accordance with the assignment of the fingerprint region.

A detection of potentially existing short-lived transient species, which make possible routes for proton transfer between different PD units, is hampered in stationary FT-IR spectroscopy because of lack of distinct marker modes of $(HP)_2$.

In the next section, the first ultrafast infrared pump-probe experiments on the NH/OH stretching region of a 2-pyridone/2-hydroxypyridine solution in CD_2Cl_2 will be presented, which the possible contributions will be deduced through an analysis of vibrational population kinetics together with coherent low-frequency wavepacket motions.

5.6 Femtosecond mid-infrared Pump-Probe study

In the following sections, femtosecond IR pump-probe measurements on the NH/OH stretching band of 2-pyridone/2-hydroxypyridine in CD_2Cl_2 will be presented.

In the ultrafast experiments, a sample cell consisting of 1 mm thick BaF_2 windows separated by a Teflon spacer with a 100 μm thickness has been used. The sample solutions consisted of 0.2-0.35 M total concentration of 2-pyridone in CD_2Cl_2, resulting in a maximum absorbance at 2900 cm^{-1} of OD = 0.5.

5.6.1 Transient pump-probe spectra

Although in linear IR spectra measured in the NH/OH stretching region a narrow OH stretching band (the indicator of uncomplexed OH groups of HP monomers and/or HP units being part of chain-like dimers) was not observed, the possibility of spectral contributions of the cyclic and open chain-like dimers in the 2400-3300 cm^{-1} cannot be *a priori* excluded. In particular, the relative magnitudes of extinction coefficients of the NH/OH stretching transitions of cyclic $(PD)_2$, (PD-HP), and $(HP)_2$, and of the chain-like dimers PD-PD and HP-PD, are unknown. In addition, the absorption cross sections cannot easily be estimated by quantum chemical calculations, as the calculation of NH or OH stretching manifolds of medium strong hydrogen bonded dimers involves the inclusion of many anharmonic coupling constants of the NH or OH stretching modes with low-frequency hydrogen bond deformation modes and with fingerprint mode overtone/combination levels through Fermi resonances [181,182,186]. The 2D-IR correlation spectroscopic analysis presented in previous chapter does not warrant the conclusion that only one species contributes to the spectral manifold between 2400-3300 cm^{-1}, as a similar result would be obtained in the case of several species with similar concentration and temperature dependencies.

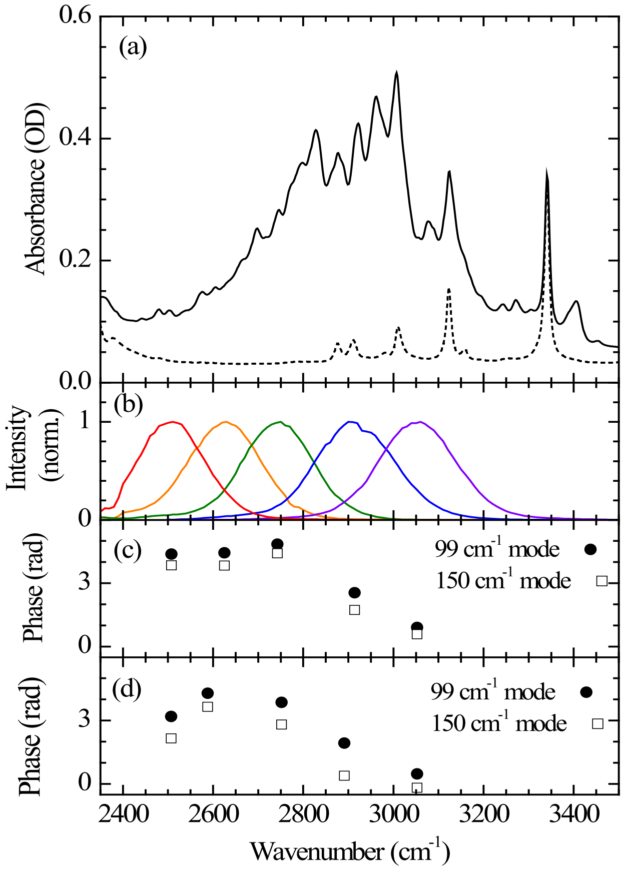

Figure 5.10: (a) Absorption spectrum of a solution of 0.3 M 2-pyridone in CD_2Cl_2 (solid line), and of the solvent only (dashed line). (b) Laser spectra of the pump pulses used in the experiment. Fitting results for pump pulses tuned at 2636 cm^{-1} (c) and 2926 cm^{-1} (d), derived from fitting the oscillatory components of Figure 5.12 obtained using Eq. (5.1), are shown as solid dots for the 99 cm^{-1} mode and as open squares for the 150 cm^{-1} mode.

Figure 5.10a and Figure 5.10b show the comparison of the linear IR absorption of the NH/OH stretching range of 2-pyridone/2-hydroxypyridine in CD_2Cl_2 and the spectral bandwidth of the femtosecond IR pump and probe pulses used in the experiments, respectively. The molecular response at 5 different spectral positions throughout the NH/OH stretching band for a given tuning of the pump pulse has been probed. The recorded spectrally integrated transient absorbance changes of the probe pulses as function of pulse delay with the IR pump pulses are shown in Figure 5.11. A direct comparison of the pump-probe transients reveals that the general features, increased absorption or bleach signals, as well as oscillatory components including their relative phase, appear to be independent of the tuning of the pump pulse. This observation strongly suggests that excitation and probing of the broad absorption band between 2400 and 3300 cm^{-1} is dominated by either one molecular species or by several molecular species with identical dynamical behaviour. Whereas formally the steady-state 2D-IR correlation spectroscopic analysis would not allow to determine whether the main spectral component is attributed to a single molecular species, or to several molecular complexes with similar complexation constants, the femtosecond pump-probe study now indicates that the broad spectral band in the NH/OH stretching region is a signature of a single molecular species. This statement could be made, because it is unlikely that several molecular species, with distinct different hydrogen bond characteristics, would behave in an identical fashion in vibrational population kinetics, as well as in coherent wavepacket motions, throughout the spectral range of the NH/OH stretching region.

The contributions from vibrational population kinetics in the pump-probe transients of Figure 5.10 will be analysed first. To do that, findings of previously studied hydrogen bonded complexes will be taken into account [34,187,188,189,190]. In particular, the vibrational level scheme to describe the population kinetics phenomena observed in the pump-probe data involves the $\upsilon = 0$, $\upsilon = 1$ and $\upsilon = 2$ levels of the hydrogen stretching oscillator of the molecular system under steady-state conditions, as well as the $\upsilon = 0'$ and $\upsilon = 1'$ levels of the same molecular system when being vibrationally "hot", i.e. having a substantial vibrational excitational degree of low-frequency modes of the molecular system (see also Sections 3.9 and 6.7.5). Due to anharmonic couplings between these low-frequency modes and the hydrogen stretching oscillator [16,191,192], the vibrational frequency of the hydrogen stretching oscillator is typically shifted to higher frequency when the low-frequency modes are highly excited. Because of the significantly different order of magnitude of the vibrational lifetimes of the hydrogen stretching oscillator (typically a few hundred of femtoseconds for medium strong hydrogen-bonded systems [16,191,192]), and of vibrational energy dissipation times to the surrounding solvent (with vibrational cooling time scales on the order of picoseconds to several tens of picoseconds, depending on the solvent mode density), such "hot" ground states of hydrogen stretching oscillators are observable.

The pump-probe data indicate that, upon vibrational excitation of the hydrogen stretching oscillator between 2400 and 3000 cm^{-1}, excited state absorption between the $\upsilon = 1$ and $\upsilon = 2$ levels dominate the signals at 2518 and 2613 cm^{-1}. The decay of the excited state absorption reveals that the hydrogen stretching oscillator has a rather short time constant of 150 ± 50 fs. Absorbance decrease dominates the signals probed at 2748 and 2908 cm^{-1}, where the steady state absorption also has the largest magnitude. The absorbance decrease recovery has two time constants, the first with a 150 ± 50 fs time constant reflecting the disappearance of $\upsilon = 1 \rightarrow \upsilon = 0$ excited state stimulated emission, and a second with effective time constants of 1 ps and 20 ps, due to ground state refilling dominated by $\upsilon = 0' \rightarrow \upsilon = 0$ vibrational cooling. Finally, the positive transient absorbance signals at 3053 cm^{-1} probed for pulse delays larger than 0.5 ps and decaying on picosecond time scales are indicative of hydrogen stretching oscillators of molecular complexes in a "hot" ground state.

5.6.2 Coherent dynamics

Superimposed on these transient absorbance signals oscillatory components occur with distinct initial phases. With the assignment of these oscillatory components to particular low-frequency wavepacket motions, the molecular species that leads to the vibrational absorption in the 2400 - 3000 cm^{-1} range can be identified. Using multi-exponential fitting of population kinetics (cf. Figure 5.11), such (incoherent) signal components is subtracted from the total absorbance changes to obtain the oscillatory contributions to the pump-probe signals. In Figure 5.12, the oscillatory components for different probe frequencies are shown for two particular pump frequencies (tuned at 2636 and 2926 cm^{-1}). It is obvious from the temporal envelope that a beating behaviour exists, indicating more than one molecular frequency contributing to the underdamped wavepacket motions. In addition, a phase flip of these low-frequency wavepacket motions can be found to occur between 2750 and 2900 cm^{-1}, near the maximum of the absorption band.

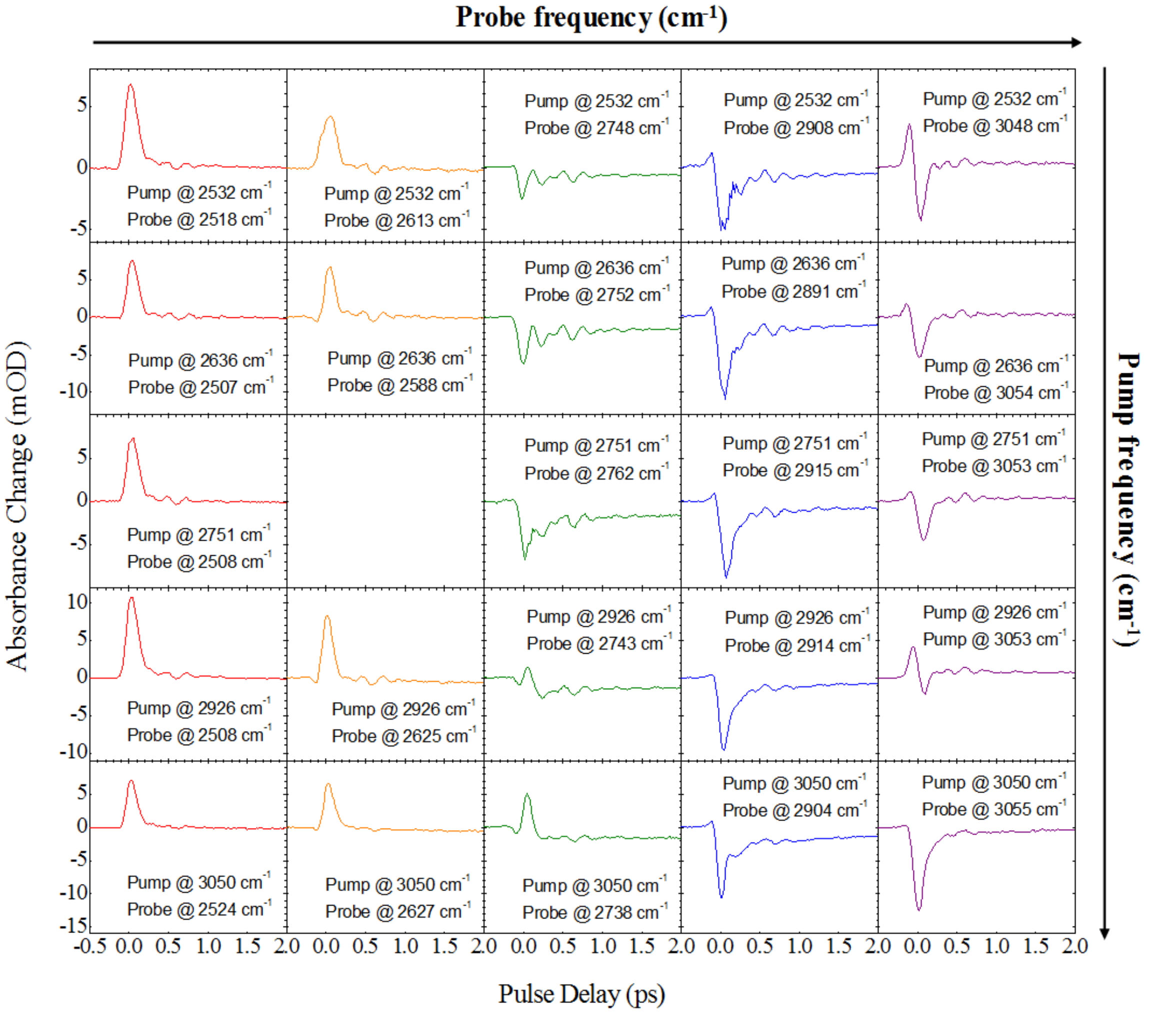

Figure 5.11: Transient IR pump-probe data recorded for different tuning of pump and probe pulses.

The oscillatory components have been analysed using Fourier transformation (Figure 5.13). Two major frequency components are found with maxima at 99 ± 30 and 150 ± 25 cm^{-1}. Even though the oscillatory components dephase with a time constant of around 0.75 ± 0.25 ps, and as such the Fourier-transformed signals may encompass several frequency components underneath the peaks at 99 and 150 cm^{-1}, it is apparent that the spectral density around 115-120 cm^{-1} has a magnitude which is small enough to exclude any significant molecular contributions in the latter frequency range.

The coherent oscillations are due to wavepacket motions along underdamped low-frequency coordinates of the dimers, similar to what has been observed in dimers containing medium strong hydrogen bonds [20,93,181,182,186,187,188,193,194,195,196,197,198,199]. Broadband femtosecond excitation of OH or NH stretching modes generates a quantum-coherent superposition of levels of low-frequency oscillators that anharmonically couple to the high-frequency stretching mode. In the OH and NH stretching υ = 1 state, such wavepackets are generated by direct dipole excitation whereas wavepackets in the υ = 0 state arise from a resonantly enhanced Raman process within the bandwidth of the pump pulse. The wavepacket motions modulate the infrared absorption of the high-frequency stretching modes, thus causing an oscillatory component in the pump-probe signals. Such phenomena are analogous to vibronic wavepackets generated upon electronic excitation of molecules [200].

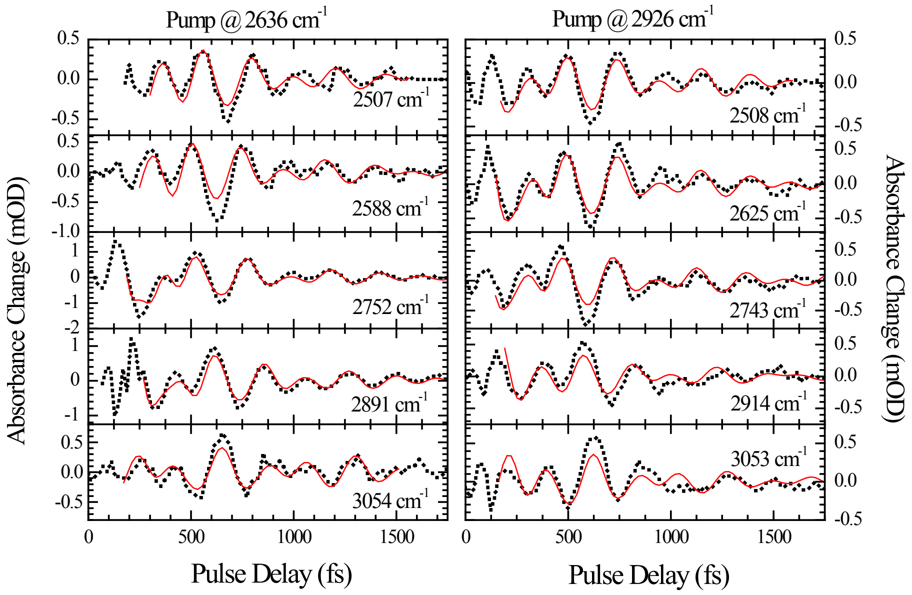

Figure 5.12: Oscillatory components extracted from the IR pump-probe data of Figure 5.11 for the pump pulse tuned at 2636 or at 2926 cm^{-1} (depicted as dots), for different probe frequencies, show clearly the beating between the 99 and 150 cm^{-1} modes, as well as the phase flip around 2800 cm^{-1}. The fitting results using Eq. 5.3 are shown as solid lines.

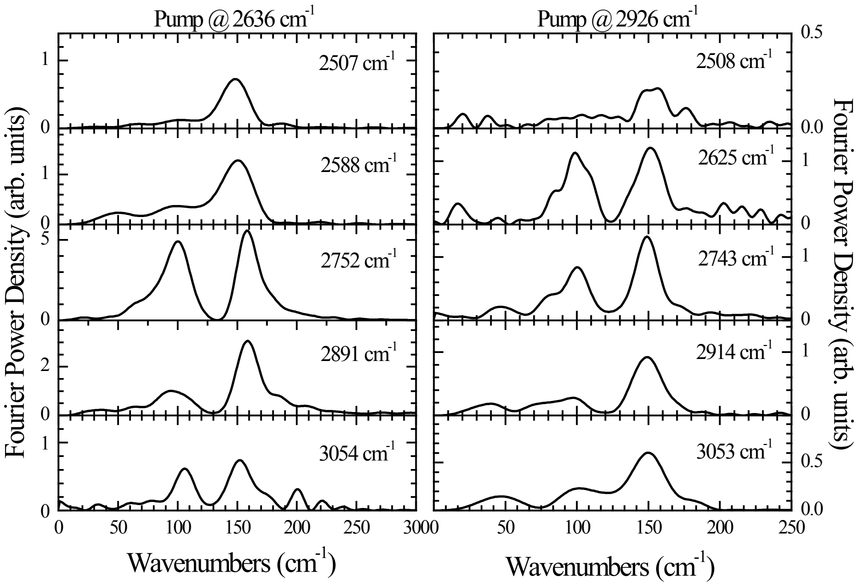

Figure 5.13: Frequency analysis of the oscillatory components of Figure 5.12 using Fourier transformation.

5.6.3 Theoretical modelling

The low-frequency modes can typically be identified by inspection of the nature of their motions: a large deformation of the hydrogen bond distance implies a large anharmonic coupling, as typified by the cubic coupling constant $\phi_{i}{}^{2}{}_{j}$. Corresponding quantum chemical calculations on $(PD)_2$, $(HP)_2$ and (PD-HP) have been presented and summarized in Tables 1-4 in Ref. [21]. For the cyclic homodimers $(PD)_2$ and $(HP)_2$ inversion symmetry exists, where only the totally symmetric Raman-active $\delta(a_g)$ in-plane (*ip*) bending (shearing) and $\nu(a_g)$ dimer stretching modes have significant cubic coupling constants with the IR-active NH or OH stretching modes, for $(PD)_2$ or $(HP)_2$ respectively. The asymmetric heterodimer (PD-HP) has three low-frequency modes with significant values for the cubic coupling constant with the NH/OH stretching modes, i.e. two $\delta(a')$ *ip* bending (shearing) modes and one $\nu(a')$ dimer stretching mode. All species have dimer stretching modes with frequencies ranging from 155 to 166 cm^{-1}, whereas $(PD)_2$ has an *ip* bending mode with a frequency of 99 cm^{-1}, $(HP)_2$ has an *ip* bending mode at 117 cm^{-1}, and (PD-HP) has two *ip* bending modes with frequencies at 85-88 and 116-123 cm^{-1}. Because both $(HP)_2$ and (PD-HP) have an *ip* bending mode around 115-120 cm^{-1} with significant anharmonic coupling to the OH or NH stretching vibrations, these cyclic dimers must play a negligible role in the coherent low-frequency wavepacket motions observed in the IR pump-probe data. In addition, the contribution to the coherent wavepacket motions of the linear PD-PD chain complex, where only one hydrogen bond connects two PD units, can be excluded. Apart from the fact that such a more floppy complex is expected to exhibit shorter dephasing times for low-frequency wavepacket motions, the δ *ip* bending and the ν dimer stretching modes have somewhat smaller frequency values, 78 and 115 cm^{-1}, respectively, reflecting the weaker hydrogen bond strength between the two PD units. Thus, experimentally observed oscillatory components originate solely from the $\delta(a_g)$ *ip* bending (shearing) and $\nu(a_g)$ dimer stretching modes of cyclic $(PD)_2$ (Figure 5.14). This finding strongly supports the idea that the vibrational manifold between 2400 and 3000 cm^{-1} in the IR spectrum is composed of the IR-active NH stretching vibration of cyclic $(PD)_2$ strongly coupled to these two low-frequency modes, as well as to combination states of fingerprint modes of this dimer.

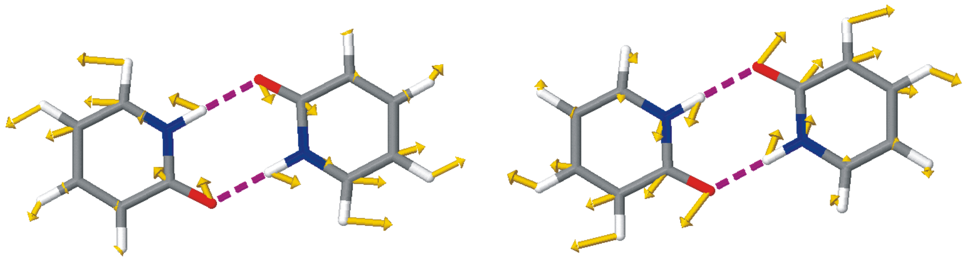

Figure 5.14: Graphical representation of the δ(a_g) *ip* bending (shearing) and ν(a_g) dimer stretching modes of $(PD)_2$, showing the displacement directions of these low-frequency modes.

The large anharmonic coupling of the δ(a_g) *ip* bending (shearing) and ν(a_g) dimer stretching modes with the IR-active NH stretching vibration of cyclic $(PD)_2$ gives rise to coherent superposition of these low-frequency modes upon femtosecond excitation of the NH stretching mode, in a similar fashion as wavepacket motions of Raman-active low-frequency modes are generated upon electronic excitation of molecular systems [200,201,202,203]. The wavepacket motion of these low-frequency modes in the υ = 1 excited state of the NH stretching mode, however, cannot be responsible for the oscillatory components observed for pulse delay times up to 2 ps, as the NH stretching υ = 1 lifetime is short (T_1 = 300 fs). The low-frequency mode wavepackets generated by a pump-induced stimulated Raman process, on the other hand, are not affected by NH stretching lifetime decay, as for this Liouville-space pathway the NH stretching mode is in its υ = 0 ground state. The oscillatory components were fitted as function of pulse delay time τ of Figure 5.12 using the following expression:

$$\begin{aligned} S(\tau) = {} & A_1\cos(\omega_1\tau+\varphi_1)\exp\left(-\frac{\tau}{T_2^1}\right)+A_2\cos(\omega_2\tau+\varphi_2)\exp\left(-\frac{\tau}{T_2^2}\right) \\ & +A_1A_2\cos(\omega_1\tau+\varphi_1)\cos(\omega_2\tau+\varphi_2)\exp\left(-\left[\frac{1}{T_2^1}+\frac{1}{T_2^2}\right]\tau\right) \end{aligned} \tag{5.1}$$

where the modulations induced by wavepacket motions of mode i are characterized by the frequency ω_i, phase φ_i and dephasing time T_2^i. Using the frequency values from Fourier transform result (Figure 5.13), the relative amplitudes and initial phases for these two low-frequency wavepackets have been derived (Figure 5.10c and Figure 5.10d). Despite the moderate signal-to-noise ratio of the oscillatory components in the pump-probe signal, a consistent frequency dependence of the initial phase of these oscillations occurs, that is very similar for both low-frequency modes. The values derived for the respective amplitudes of these two low-frequency modes show a slight variation that might be due to the variation in pump and probe intensities in the different pump-probe measurements. This is the first time when the amplitude and phase dependence of a molecular system with two low-frequency hydrogen bond deformation modes has been analyzed. It is evident that a nearly π phase flip occurs for both low-frequency modes around the maximum of the steady-state absorption band (2900 cm^{-1}). This shows again that the entire absorption band and the wavepacket motions arise from a single species. Contributions to the pump-probe signals by wavepacket motions driven by the intramolecular vibrational redistribution process where the υ = 1 NH stretching decays into the υ = 0' "hot" ground state can be excluded. First, the relative signal strength of transient "hot" ground state NH stretching absorption, in accordance to results obtained on 7-azaindole dimer [188], is significantly smaller than what have been observed with OH stretching modes of medium strong hydrogen-bonded molecular systems [33,34,204], including acetic acid dimer [187,194]. Secondly, the phase change of the oscillations is then expected to occur in the crossover region between transient bleach and "hot" ground state absorption, i.e. 3000 cm^{-1}.

5.7 Summary

Isomerization and association chemistry of 2-pyridone/2-hydroxypyridine involves a complex set of equilibria, including monomers, solute-solvent complexes, also cyclic and open chainlike dimers. In dichloromethane-d_2 solvent, the existence of PD-CD_2Cl_2 and cyclic $(PD)_2$ has been identified applying both NMR and FT-IR spectroscopy. The NMR results show that the cyclic dimer $(PD)_2$ is the dominant species at low temperatures (180 K), which exchanges with PD in monomer form or complexed with the solvent. At low temperature (193 K) the IR spectra support the NMR conclusions that the solution composition is dominated by cyclic $(PD)_2$. The 2D IR correlation spectra not only show the existence of PD-CD_2Cl_2 solute-solvent complexes, and of cyclic $(PD)_2$, but also hint at the presence of chainlike PD-PD. However, because of a lack of specific marker modes, a contribution of the cyclic dimer $(HP)_2$ to the NH/OH stretching absorption between 2400 and 3300 cm^{-1} could not be fully ruled out. $(HP)_2$ has not been detected with NMR, but it could exist as a short-lived transient species, making possible routes for proton transfer between different PD units.

To solve this problem, ultrafast infrared pump-probe experiment was performed of a solution of 2-pyridone (PD) in CD_2Cl_2 in the frequency range between 2400 - 3300 cm^{-1}, where NH or OH stretching resonances of medium-strong hydrogen-bonded dimers of PD and its tautomer 2-hydroxypyridone (HP) are expected to occur. Based on the experimental results, that regardless of pump frequency a similar temporal dependence, including the coherent low-frequency modulations was detected, for the transient absorbance throughout the NH/OH stretching region, it can be concluded, that a single species dominates the IR absorption in this spectral range. The Fourier analysis together with a fitting procedure of the coherent pump-probe modulations complemented by DFT calculations allow to assign these modulations to coherent wavepacket motions of low-frequency hydrogen bond deformation modes of $(PD)_2$ in CD_2Cl_2. The observed frequencies of these deformation modes, 99 and 150 cm^{-1}, are in full accordance with the in-plane deformation and stretching modes of the cyclic dimer $(PD)_2$. Contributions from $(HP)_2$ or even (HP-PD) or PD-PD to the ultrafast nonlinear response are negligible. The fact that consistent initial phase behaviour is observed for a molecular hydrogen-bonded system with multiple hydrogen bond deformation modes with large anharmonic couplings to the hydrogen stretching oscillator suggests a potential for mode-specific manipulation of these low-frequency wavepackets using appropriate amplitude and phase shaped mid-infrared pulses.

6 Ultrafast vibrational dynamics of hydrated DNA

6.1 Deoxyribonucleic acid

Deoxyribonucleic acid, DNA, is a linear, un-branched, long biopolymer consisting of repeating elementary units called nucleotides [205,206,207]. Nucleotides in DNA are composed of a nucleobase, a five-carbon sugar (2-deoxyribose), and a phosphate group. They are joined together by phosphate groups that form phosphodiester bonds between the hydroxyl group of the third carbon atom of one sugar molecule and hydroxyl group located at the last carbon atom of adjacent sugar ring. The first carbon atom in the sugar residue is linked through a N-glicosydic bond to one of the four types of nitrogen bases: the pyrimidines thymine, T and cytosine, C and the purines adenine, A and guanine, G (Figure 6.1, [208]).

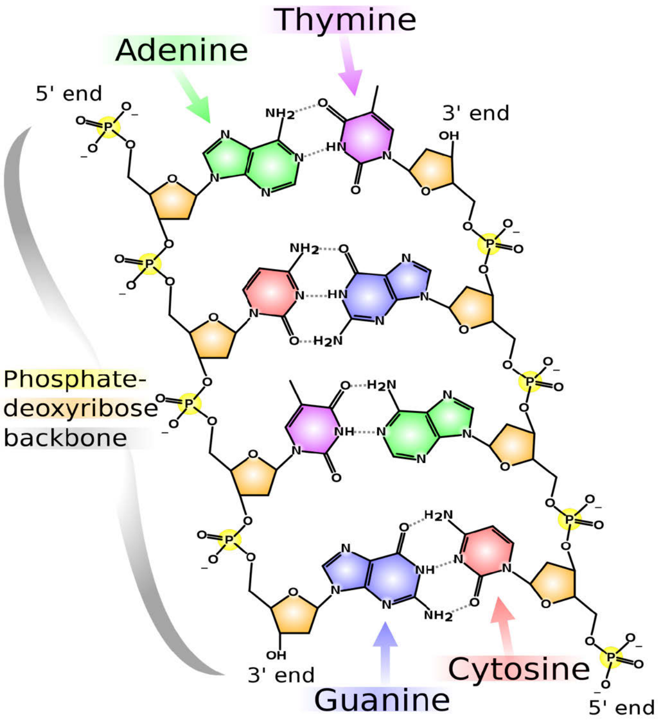

Figure 6.1: Chemical structure of DNA. Hydrogen bonds shown as dotted lines. The picture taken from: [208]

In living organisms, DNA does not usually exist as a single molecule, but instead as a pair of molecules that are held tightly together, forming two antiparallel strands that looks much like a twisted ladder (Figure 6.2) and named double-helix structure. The DNA double helix is stabilized by hydrogen bonds between the complementary bases attached to the two strands. In other words, each type of base on one strand forms a bond with just one type of base on the other strand: adenine is always paired with thymine and guanine always with cytosine. However, the sequence of bases along a poly-nucleotide chain is not restricted in any way. The precise sequence of nucleic acid bases along a strand carries the genetic information [209].

James Watson and Francis Crick by analysing X-ray diffraction patterns of DNA fibers [210] first suggested the double-helix structure of DNA (Figure 6.2, [211]).

The canonical A:T and G:C pairing geometries, typical for antiparallel DNA, is called Watson-Crick pairing. Despite the great importance of the standard Watson-Crick pairs, there exist more ways that bases can be assembled by hydrogen bonding. The alternative pairings occur mostly within other nucleic acid conformations: parallel-stranded DNA (reversed Watson-Crick), triplet helices (Hoogsteen and reversed Hoogsteen), loops, mispairs, RNA (Wobble) or chemically modified nucleic acids. In a condensed phase, most unusual schemes are less stable than the standard Watson-Crick pair [212,213]. In the gas phase, however, the canonical tautomers are not always the lowest energy forms.

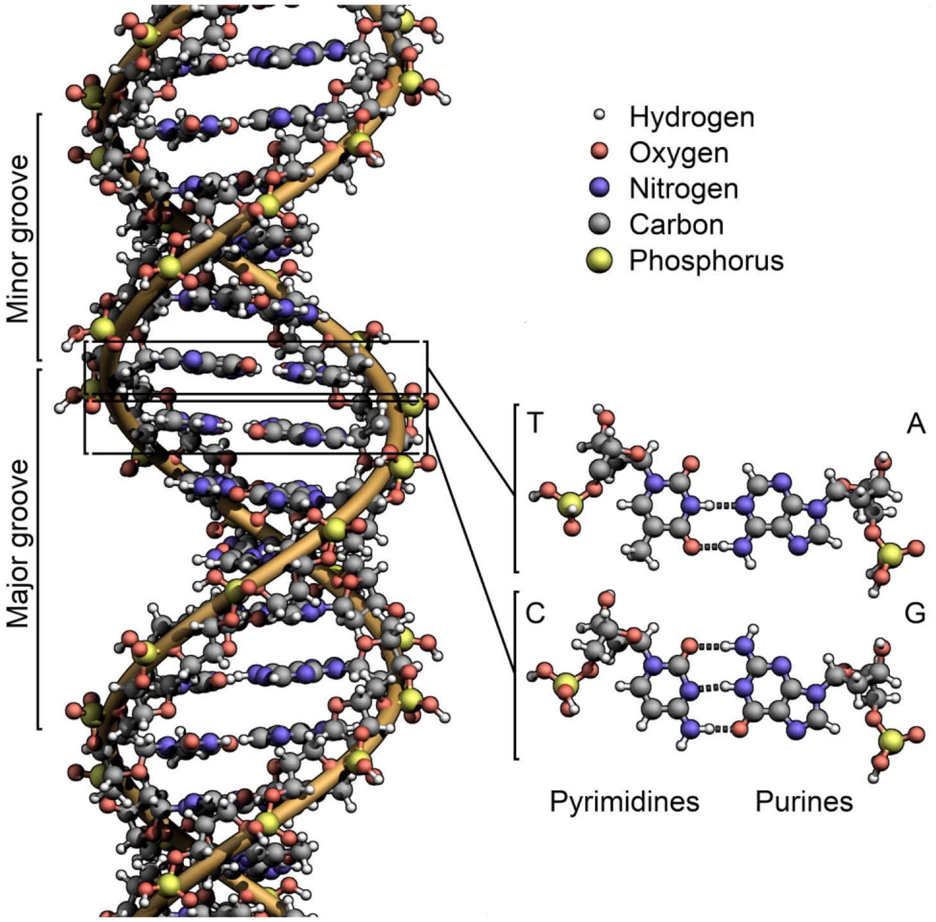

Figure 6.2: The structure of the DNA double helix. The atoms in the structure are colour coded by element, the spiralling backbone of the two strands is shown in orange and the detailed structure of two base pairs is shown in the bottom right. From: [211]

The sugar-phosphate backbones spiral around the outer part of DNA double helix. Closer look at the secondary structure of DNA exhibit that the double helix does not have smooth sides like a regular cylinder. Instead, two types of grooves in the "surface" of the DNA molecule between the phosphate groups can be distinguished. As the strands are not directly opposite to each other, the grooves are unequally sized. The major groove is 22 Å wide and has the nitrogen and oxygen atoms of the base pairs pointing inward toward the helical axis, whereas minor groove is 12 Å wide and the nitrogen and oxygen atoms point outwards [214]. Proteins that interact with DNA often make contact with the edges of the base pairs that protrude into the major groove [215]. Water molecules in the DNA grooves are critical for maintaining structural integrity, conformational changes, and molecular recognition. Since the minor groove is narrow and deep, water molecules in this groove are expected to be more ordered with longer residence times compared to the major groove [216].

The double-stranded DNA molecule has long been considered existing only in well-defined right-handed double helical conformations A (11 residues per turn) and B (10 residues per turn) [217]. The left-handed conformer has been crystallized later and due to its zigzag character of the backbone is called Z-DNA (12 residues per turn) [218]. However, in functional organisms, only B- DNA and Z-DNA have been observed [219].

The conformation that DNA adopts depends in general on the base sequence, environment and degree and direction of supercoiling stress [220]. It has been found that water molecules stabilize the DNA double-helical structure [221,222] and the degree of the DNA hydration determines its conformation. The water molecules surrounding DNA are typically described in terms of a primary hydration shell consisting of molecules directly adjacent to the DNA helix and a secondary hydration shell made of water molecules beyond the primary shell. As has been established by X-ray diffraction studies, regardless of origin and base composition, fully hydrated DNA has the B configuration [223,224]. A-DNA double-helix can be formed, e.g. by the dehydratation of B-DNA. Humidity-driven conformational transitions of DNA have been the subject of intensive studies, where IR spectroscopy (in particular infrared linear dichroism) played a leading role [225,226]

6.2 Static and dynamic hydration scheme of DNA

Falk et al. [227] studied the IR active modes of various molecular subgroups in NaDNA as a function of relative humidity (r.h.). Important conclusions about the sequence in which different molecular sites become hydrated have been drawn from the shifts and relative absorption changes of the vibrational mode frequencies:

- $PO_2^-Na^+$ groups located on the DNA backbone are primary adsorption sites for water molecules,
- the P-O-C and C-O-C oxygen atoms became also hydrated below 65%,
- the C=O groups and ring nitrogen atoms of the purine and pyrimidine bases become hydrated above 65%,
- between 75 and 80 % r.h. the water molecules continue to fill the groves of the DNA helix and the further hydration of DNA is accompanied by swelling.

Falk's conclusion that at lower relative humidity water molecules are located mostly around phosphate groups and do not diffuse freely has been later confirmed with help of resonant microwave absorption and phosphorescence spectra [228,229]. The fact that water is first removed from grooves indicates a weaker hydrogen bonding by bases than by phosphates. Similar observations have been reported using neutron quasielastic scattering technique to study hydration of NaDNA [230].

It is important to distinguish changes in the spectra due to the direct effect of hydration from the humidity-driven changes in the DNA structure and interhelical interactions. In DNA without surfactant counterions, changes of relative humidity induce macroscopic changes in the helix conformation, as proved by X-ray diffraction analysis [231]. DNA oligomers with alternating A-T pairs have been shown to exist in the D conformation at r.h. between 40 and 70% and in the B conformation at higher humidity levels [205 ,231]. Also at 0% r.h., DNA adopts a well-defined helix structure as has been concluded from the X-ray diffraction studies on thin films [232] and infrared spectroscopy on DNA-surfactant films, where a band characteristic of base pairing (the band is not observed in the case of denaturated DNA), involving the in-plane C=O and C=N stretching vibrations, is observed at 1698 cm^{-1} (1715 cm^{-1} for 92% r.h.) [233]. X-ray diffraction has also been used to confirm that the replacement of the metal cation with a long-chain surfactant does not hinder the ability of the DNA-surfactant complex to undergo these water-content-driven changes in its helix conformation [232,234,235]. For DNA-CTMA films any drastic deviations from the almost linear dependence between the frequency shift of an asymmetric phosphate stretching band and the relative humidity have not been observed, which suggests that conformational transformations of the double-helical structure of short DNA-CTMA oligomers have a minor influence on the spectral frequency shift of an $\nu_{as}(PO_2)^-$ oscillator. Hence, it seems to be reasonable to choose the phosphate asymmetric $\nu_{as}(PO_2)^-$ stretching vibration as a specific probe of the hydration level of DNA-CTMA films. In contrary, in oriented films of eukaryotic NaDNA some authors [236] observed a steep slope of the frequency of $\nu_{as}(PO_2)^-$ vs. r.h. curve with maximum at approximately 80-85%. In such films, the steep slope indicates a rearrangement of the $(PO_2)^-$ of DNA during the A – B transition rather than electronic effects exerted by water molecules on the P–O bonds [237].

X-ray diffraction and neutron scattering results suggest that six water molecules interact with the two free oxygen atoms in the fully hydrated B conformer of DNA [238]. Each phosphate group is surrounded by its own hydration shell (Figure 6.22). The water shells of neighbouring phosphate groups are spatially separated and thus, the interaction strength between them is limited. In an aqueous environment, the first hydration shell (water interacting directly with DNA functional groups through, for example, hydrogen bonds) is complemented by water molecules at larger distances that interact through long-range Coulomb interactions [205]. Differentiation between the various water species has remained unsolved beyond the qualitative concept of hydration shells and most of the results discussed so far characterize the steady-state behaviour of DNA close to the thermal equilibrium.

The gravimetric data obtained by Falk et al. [227] give directly the number of molecules of water bound to DNA as a function of r.h. The experimentally observed adsorption of water by NaDNA was compared with values calculated from the BET equation (adsorption equation introduced by Brunauer, Emmett and Teller and given in a statistical mechanical foundation by Hill, [239,240]). In the humidity range between 0 and 80%, the authors reached an excellent fit of the data with theory. Above 80% however, the data show a sudden negative deviation from the BET equation. It has been concluded that at 80% r.h. the minor and major grooves are fully hydrated and further hydration requires energy for pushing the DNA molecules apart (swelling). It has been found that the equatorial X-ray diffraction spacing begins to increase very sharply between 80 and 85% r.h., which seems to support the conclusion about the expansion caused by water molecules.

The experiments presented in this thesis focus on fully-hydrated DNA (92% r.h.) films and on samples where only residual, strongly bounded water molecules remain (0% r.h.), which corresponds to more than 20 and ≈ 2 water molecules per DNA base pair, respectively. Our own gravimetric studies confirmed that drying (using the P_2O_5 agent) the highly hydrated (92% r.h.) DNA-surfactant film leads to removing of around 18.5 molecules per base pair. The water concentration in the film samples is approximately $c \approx 0.57$ M for 0% r.h. and $c \geq 5.7$ M for 92% r.h.

Under equilibrium conditions, the residence time of individual water molecules at DNA hydration sites spans over the range from 10 ps up to nanoseconds as has been predicted theoretically (mostly MD simulations) and confirmed experimentally (mainly NMR) [216,241,242,243,244,245]. Liepinsh et al. [216] studied the residence time of water molecules in the major and minor grooves of DNA by nuclear Overhauser effect (NOE). These authors have found that the average residence time of water molecules in minor groove is noticeably longer than those in the major groove. They also observed that even these "slow" water molecules on DNA surface are accessible to the bulk solvent, unlike interior water molecules in protein structures. The NMR studies of Sunnerhagen et al. [246] complemented by molecular dynamic simulation [241] have provided very different residence times of water in the hydration layer. The residence times reported there are short not only for water molecules in the major groove but also in the minor groove where longer residence times could be expected. The average residence time of the hydrogen bonded water molecules was 11 (±11) ps with a maximum of 223 ps. When all water molecules within the distance (0.35 nm) of non-exchangeable protons were considered, the average residence times increased to an average of 100 (±4) ps and a maximum of 608 ps. More recent MD simulations [244] have investigated microscopic aspects of hydration dynamics in terms of the hydrogen bond lifetime correlation functions. The authors concluded that the average hydrogen bond lifetime is longer in the minor groove than that in the major groove by almost a factor of 2. Further analysis showed that water hydrogen bonds with phosphate oxygen have substantially shorter lifetimes than those with the groove atoms. Pal et al. [247] studied the hydration dynamics at DNA interfaces by measuring time-resolved fluorescence spectra of 2-aminopurine as the intrinsic fluorescence probe. The time scale of hydration dynamics observed in the modified DNA duplex and the DNA–drug complex (10–12 ps) is similar to molecular dynamics simulations of ultrafast hydration in 16-mer duplex DNA [241].

The long residence time of water molecules detected by NMR is more important for maintaining the structural integrity (structural water), whereas the dynamically ordered water is of more significance to recognition processes [247] such as those involved in ligand [248] or protein [249] binding.

The breaking and (re)formation of DNA-water and water-water hydrogen bonds and the reorientation of water molecules occur however on even shorter time scale: from pico- down to femtoseconds [241,250]. The high photostability of DNA is commonly attributed to efficient radiationless electronic and vibrational relaxation processes, in which the key step in accommodating the large excess of energy is fast, nonequilibrium energy exchange between DNA and its environment [251,252,253].

In many cases the equilibrium fluctuations around the time-averaged structure are essential for the functionality of biomolecules. A prominent example is myoglobin, whose binding site would never be reached by oxygen or iron atoms if the structure of this protein were static, as obtained from X-ray spectroscopy [90]. Molecular dynamics simulations suggest however, that ultrafast fluctuations of the peptide backbone and side chains make the binding site transiently open (*instant binding tenacity*) [254,255]. It has been shown theoretically that selectivity of some enzymes is determined by their conformational fluctuations [256]. MD simulations reported also the important role of fast structural fluctuations in protein folding mechanisms [257,258,259]. Most of the knowledge on protein dynamics originates from computer simulations with rather indirect or no experimental verification.

As has been already discussed in the previous Chapter, the main reason why there is only very limited number of experiments dealing with a direct investigation of dynamics of biomolecules is scarcity of appropriate spectroscopic techniques. For example, the time scale which can be grasped by NMR spectroscopy is in order of milliseconds, whereas the dominating part of the fluctuation correlation function responsible for dephasing processes, decays on the pico- and femtosecond time scale. Any detailed information on fast protein-water or DNA-water dynamics is inaccessible and only very slow processes, such as hydrogen exchange, can be observed directly. X-ray spectroscopy on the other hand, provides no information on the time scale of structural rearrangements. Collective protein motions after fast optical triggers have been studied with help of pulsed synchrotron radiation with nanosecond temporal resolution [260,261].

Nonlinear vibrational spectroscopy with a femtosecond time resolution is a promising technique for investigating structural dynamics of (bio)molecules and ultrafast energy exchange [14,29]. Particularly interesting is also the water dynamics in the hydration layer around proteins or nucleic acids that control the structure, function and reactivity of many natural and biological systems. The shell of water around DNA is essential for replication and transcription [262].

6.3 Ultrafast vibrational and structural dynamics of bulk water

Femtosecond photon-echo and pump-probe experiments supported by MD calculations have provided detailed insight into the microscopic dynamics of neat (H2O) and isotopically substituted (HOD in H_2O or D_2O) water, both in the bulk and in confined environments [36,38,39,41,105,263,264,265,266,267,268,269,270,271]. The experiments have shown that fluctuating Coulomb forces exerted on the anharmonic OH stretching oscillators in the hydrogen-bonded network of water molecules lead to a pronounced spectral diffusion, the situation in which the transition frequency of OH stretching oscillator undergoes fast, stochastic shifts within the spectral envelope. This frequency modulation results in dephasing: the loss of quantum coherence of the optically coupled states in the anharmonic oscillator. In the linear spectrum such phenomena show up as a vibrational band broadening giving no information about the underlying time scales. Time-resolved nonlinear experiments, in particular two-dimensional spectra of OH stretching mode of H_2O have shown that the fastest components of the fluctuating force in the sub-50 fs time range are related to high-frequency hindered rotations (librational motions) of water molecules [41,43]. The energy transfer of OH stretching excitations between neighbouring water molecules with slightly different fundamental transition frequencies occurs on 100 fs time scale [41,43,105] and also contributes to spectral diffusion. These observations are in agreement with recent theoretical work based on MD simulations of water dynamics [38,40,264,265,267,272,273]. The lifetime of the $\upsilon = 1$ state of the OH stretching and OH bending mode is 200 fs and 170 fs, respectively [41,43,263,266,274]. Vibrational energy relaxation of the $\upsilon = 1$ OH stretching mode occurs via the off-diagonal anharmonic coupling with the $\upsilon = 2$ OH bending mode (both states are in Fermi resonance). Femtosecond pump-probe experiments have demonstrated the cascaded decay of the OH stretching vibration via the overtone and fundamental tone of OH bending mode and concomitant distribution of vibrational energy excess into intermolecular modes (such as librations) of the hydrogen-bonded network [91]. As a consequence, hydrogen bonds are locally weakened around the excited molecules and the energy delocalization within a molecular network is completed within several ps after excitation [91] (the average lifetime of water-water hydrogen bonds is of the order of 1 ps). The latter processes establish a macroscopically heated ground state of the network, characterized by an enhanced fraction of broken hydrogen bonds.

6.4 DNA thin-film samples

To work with a well-defined molecular configuration, thin films of artificial DNA oligomer duplexes containing 23 alternating adenine-thymine (A-T) pairs in Watson-Crick geometry were studied. In order to generate films of high optical quality, the sodium counterions of the DNA oligomers are replaced by a cationic amphiphile, hexadecyl-trimethylammonium chloride (CTMA) [232,234,235]. The oligomers are cast into thin films on 500 nm thick Si_3N_4 windows and held in a cell where the relative humidity (r.h.) can be controlled, that determines the water concentration in the film.

6.4.1 Preparation of high optical quality DNA:CTMA films

An aqueous solution (1mL) of sodium salt of double-stranded adenine-thymine (A-T) oligomers composed of 5'-T$(TA)_{10}$-TT-3' (Thermo Scientific) and an aqueous solution of the molar equivalent of CTMA chloride are mixed together at room temperature. The water-insoluble DNA-surfactant complex is formed spontaneously upon dropwise addition of the cationic surfactant to the DNA and is gathered by repeated centrifugation. The precipitate is rinsed with distilled water several times in order to purify it from replaced sodium ions from DNA salt and chloride ions from surfactant. The DNA-surfactant complex is then dissolved in ethanol and cast on a Teflon plate. The solvent is slowly evaporated at room temperature. The dry DNA-CTMA complex is finally dissolved in *tert*-butanol and drop-cast onto Si_3N_4 or BaF_2 (for Raman measurements) substrate. The solvent is evaporated under the saturated vapour at room temperature. The obtained film is physically stable, transparent and gives only minor scattering during the linear and nonlinear infrared spectroscopic measurements.

To control the water content in a film, samples are placed in a home-built stainless steel humidity cell. The cell is designed in a way that a channel connects the sample chamber with a special reservoir where various agents can be placed to control the chamber atmosphere. To maintain the relative humidity (r.h.) inside the chamber at constant 0% value, the sample is held in a cell with phosphorus pentoxide, P_2O_5 in the reservoir. To hydrate the sample to a well-defined level, pertinent saturated salt solutions are used such as $NaBrO_3$ (92% r.h.), $NaClO_3$ (75% r.h.) and other, as described in [227]. Equilibration to the new r.h. occurs typically within two days in each case.

6.4.2 Stationary vibrational spectra of hydrated DNA films

The linear infrared and Raman spectra of DNA and their change upon hydration have been the subject of extensive experimental studies and theoretical calculations [275,276,277,278,279,280,281,282,283]. The linear vibrational spectrum of condensed-phase DNA is very congested, with many overlapping bands, in particular in the frequency range between 800 and 1800 cm^{-1}. Above 3000 cm^{-1}, the assignment of different bands to NH and NH_2 stretching vibrations of base pairs as well as their reliable separation from water OH stretching vibration has remained controversial [279,282,283,284].

In Figure 6.3, infrared spectra of DNA-CTMA film are plotted for 0, 33, 75 and 92 percent of relative humidity, corresponding to ≈ 2, ≈ 6, ≈ 12 and more than 20 water molecules per base pair in the DNA structure. With increasing hydration level, the spectra show a strong absorption enhancement between 3000 and 3700 cm^{-1}. Concomitantly, the libration-bend combination tone of water around 2150 cm^{-1} becomes stronger. In the frequency range above 3000 cm^{-1}, the sample at 0% r.h. displays a broad absorption with some substructure. Increasing the water content enhances and reshapes this absorption band substantially, mainly due to the enhanced absorption of OH stretching vibration at higher water concentration. However, the change of absorbance amplitude at 3400 cm^{-1} from 0 to 92% r.h. is much less than expected from the ratio of the water concentration, which suggests that the band observed at 0% r.h. contains not only contributions from OH stretching vibration from residual water molecules but contains also NH stretching vibrations from DNA base pairs.

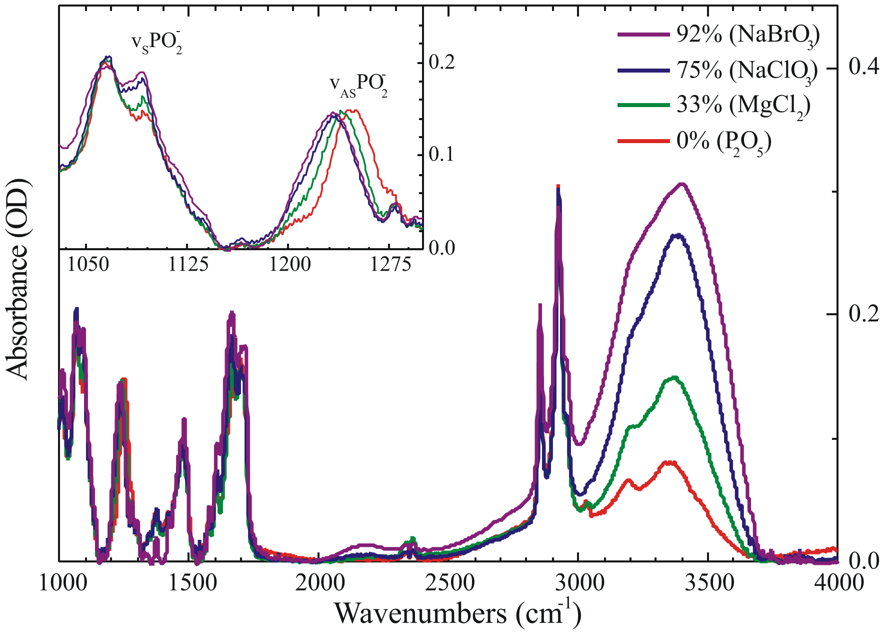

Figure 6.3: Infrared linear absorption spectra of DNA oligomers containing 23 alternating adenine-thymine base pairs. The thin film sample on Si_3N_4 windows is held at hydration levels 0, 33, 75 and 92 % r.h. Inset: Infrared absorption in the frequency range of symmetric and asymmetric stretching vibrations of the phosphate groups located in the DNA backbone.

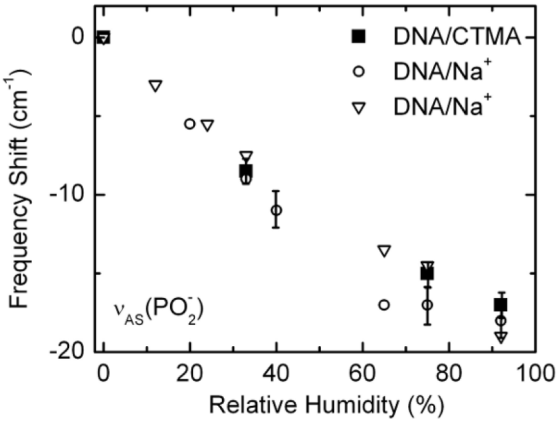

Figure 6.4: Frequency shift of the asymmetric $\nu_{as}(PO_2)^-$ stretching vibration as a function of the relative humidity (r.h.) in the sample. Data for the DNA/CTMA complexes studied here are compared to results for DNA with Na$^+$ counter ions (see text).

The inset of Figure 6.3 shows the changes in the $(PO_2)^-$ stretching absorption bands of the DNA backbone for the four hydration levels. The observed reshaping of the $\nu_s(PO_2)^-$ envelope and the dehydration-induced blue shift of the $\nu_{as}(PO_2)^-$ are very close to the behaviour of DNA with sodium counterions [277,285] as shown in Figure 6.4. The slightly different frequency positions of the $\nu_{as}(PO_2)^-$ stem from not identical polarity of cations used, but the observed shifts upon hydration level changes are identical [286]. This vibrational mode will be used as a sensitive probe of hydration dynamics of DNA in the time-resolved experiments (see Section 6.8) in order to extract specific information on microscopic dynamics of DNA-water interactions and on the role of the relevant coupling mechanisms.

6.5 Deuterium exchange effects on IR absorption spectrum of DNA

Hydrogen isotopic exchange of deoxyribonucleic acid has been studied by infrared spectroscopy [287,288]. Polynucleotide films can be deuterated almost completely through vapour-phase exchange except for the hydrogen atoms of the CH bonds [288]. The exchangeable hydrogens in DNA can be divided into three categories, related to the rate of deuteration [289]:

(i) The fastest exchange is expected to occur for those OH and NH hydrogens that are not involved in the interstrand base pairing by hydrogen bonding (this “instantaneous” exchange is completed in a fraction of a second).

(ii) Interaction with solvent molecules of those hydrogens of base moieties that are involved in interstrand base pairing is limited. Exchange is “fast”, i.e., half of H atom fraction is replaced by D atoms within 3 hours.

(iii) “Slow exchange” corresponds to a half-time of hours or days; often observable only at elevated temperatures. The hydrogens attached to C-8 of purine base moieties as well as hydrogens on C-4 and/or C-5 in pyrimidines belong to this group.

On deuteration, the frequency $\nu_{X\text{-}H}$, the intensity A and the half width $\Delta\nu_{1/2}$ of X–H stretching bands decrease. For a harmonic oscillator, all the spectral features mentioned above scale by factor of $\sqrt{2}$. This ratio is a good approximation also for weakly hydrogen-bonded X–H vibrations. For medium-strong hydrogen bonds, the D-substitution results in a spectral red-shift and intensity variations that do not follow harmonic rules. The corresponding factors are on the order of 1.3 for $\nu_{X\text{-}H} / \nu_{X\text{-}D}$ and 2 for $A_{X\text{-}H} / A_{X\text{-}D}$ [13].

The frequency shift induced by deuteration is the most important spectral change for analytical purposes. As the spectral shift can reach a couple hundreds of wavenumbers, it often allows for separating different spectral contributions. However, in the case of hydrated DNA both hydrogens of residual water molecules as well as hydrogens of the base pair moieties are expected to exchange on similar time scales and as a consequence, ND stretching absorptions are overlapped with a strong OD stretching mode similarly to the case before deuteration where the NH contributions were masked by a strong and spectrally broad water band. To bypass these problems, a novel approach discussed below is proposed.

6.5.1 Experimental results

The dry DNA-CTMA film (1-2 residual water molecules per nucleotide) is held in a sealed cell and a liquid D_2O is placed at the bottom of the cell. After a certain time, all hydrogen atoms in the film except those of the CH bonds have been replaced by deuterium atoms. Simultaneously, a DNA double-helix is expected to be hydrated with heavy water. The deuteration process is followed by measuring a set of linear FTIR spectra with a fixed time interval (for clarity only three representative spectra are shown in Figure 6.5).

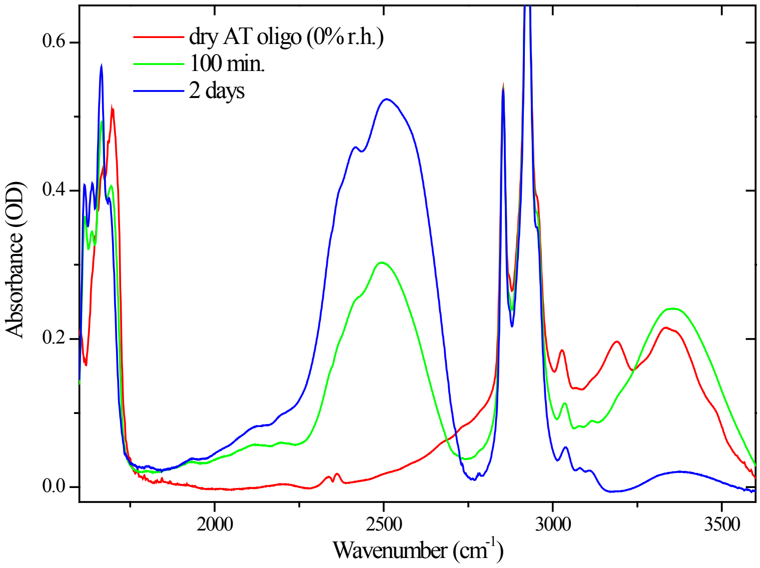

Figure 6.5: FTIR spectrum of 0% r.h. AT oligomer (black line). Exposing the film onto the D_2O vapour results in deuteration and hydration of the sample (red line). These processes are completed after two days (green line).

The most pronounced spectral changes upon deuteration and hydration occur in the frequency range between 1700 and 3600 cm^{-1}. As the sample is exposed to D_2O vapour, the intensity of the band with maximum at 2505 cm^{-1} increases continuously, whereas the broad absorption between 3335 and 3375 cm^{-1} slightly enhances within the first hour and later monotonically decreases. The intensity of the band at 3200 cm^{-1} decreases as function of time. Also the very broad absorption starting at around 2400 cm^{-1} and extending the high frequency tail probably up to 3100-3200 cm^{-1} (partially covered by very strong aliphatic C-H stretching bands of the surfactant molecules, 2853 and 2924 cm^{-1}, as well as by other vibrations at higher frequencies) decreases in intensity. On the other hand, the existence of a broad absorption extending between 1750 cm^{-1} and at least 2300 cm^{-1} is observed which intensity increases monotonically as the H/D exchange progresses.

After the deuteration and hydration processed have been completed, i.e., when no spectral changes are further observed as function of time, the D_2O solution in a cell reservoir is replaced with a P_2O_5 powder to reduce the water content in the sample film. The resulting spectral changes are again monitored with a linear spectrometer as a function of time until the equilibrium is reached. The last spectrum corresponds to the 0% r.h. film, with residual D_2O and/or HOD absorptions (Figure 6.6).

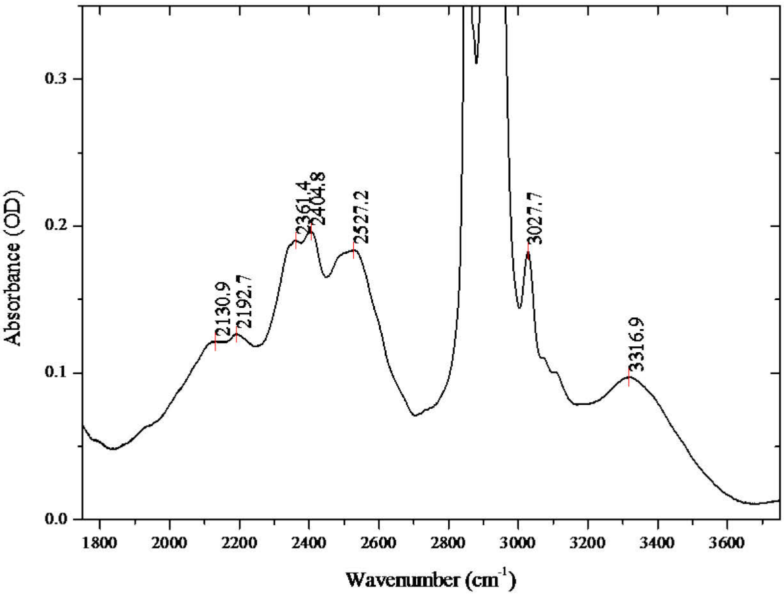

Figure 6.6: FTIR spectrum of deuterated AT oligomer film after two days of dehydratation with P_2O_5 powder.

The straightforward interpretation of the collected linear spectra is hampered by the fact that simultaneously to the isotopic exchange, the hydration of the film occurs. The reliable separation of these two processes is extremely difficult as the relevant spectral bands are spectrally broad and strongly overlap. However, the rates of the H/D exchange of the OH stretching vibration of water and different NH oscillators of base pairs are unlikely to be identical. Hence, it is possible to treat the time when the DNA film is exposed to heavy water vapour as an external perturbation to the system, and analyze the correlations between the spectral changes at different frequencies in function of such perturbation parameter θ using Noda's two-dimensional correlation spectroscopy as described in Section 2.5. This analytical tool has been applied in the evaluation of the spectra of 2-pyridone/2-hydroxypyridine as described in Section 5.5, albeit with different external variables (concentration and temperature).

The synchronous and asynchronous contour plots were generated for two time ranges:

- the time-window I: 0-80 minutes (measured with 10 minutes steps) after placing the D_2O into the sample cell, where the H/D exchange is expected to dominate the observed spectral variations (Figure 6.7),
- the time-window II: 0-800 minutes (80 min. steps), where the hydration process strongly contributes to the observed spectral changes (Figure 6.8).

In the synchronous spectrum (period I, Figure 6.7 left), the autopeaks are located at 2113 (w), 2188 (w), 2485 (vs), 3021 (m), 3289 (sh), 3432 (vs) and 3505 (sh) cm^{-1}. The strongest positive cross-peak peak is observed at Φ(2485, 3432) with a shoulder at Φ(2485, 3289). The negative off-diagonal peaks develop at Φ(2485, 3021) and Φ(2485, 2792). Because of the very strong absorption of amphiphile CTMA molecule at this region, it is not clear whether the strong negative correlation between the broad contour between 1800 and 2600 cm^{-1} (with maximum at 2485 cm^{-1}) is synchronous with the two distinct peaks with maxima at around 3021 and 2760 cm^{-1} or to the one broad band extending from approximately 2700 to 3100 cm^{-}

[1]. This spectral region (one broad or two separate peaks) is also negatively correlated with the broad absorption with an intensity maximum located at 3432 cm^{-1}.

In the asynchronous spectrum (period I, Figure 6.7 right) the strongest peak is located at Ψ(3382, 2537). This peak is spectrally broad and has a second maximum at around Ψ(3200, 2505). Both peaks are positive, but the sign of the latter changes at the low-frequency side (~3160 cm^{-1}) suggesting that in this range (3160-3200 cm^{-1}) the absorbance changes may originate from two distinct peaks which behave differently with respect to the broad absorption with a intensity maximum located at 2505 cm^{-1}. Another negative asynchronous peak is located at Ψ(3432, 3169).

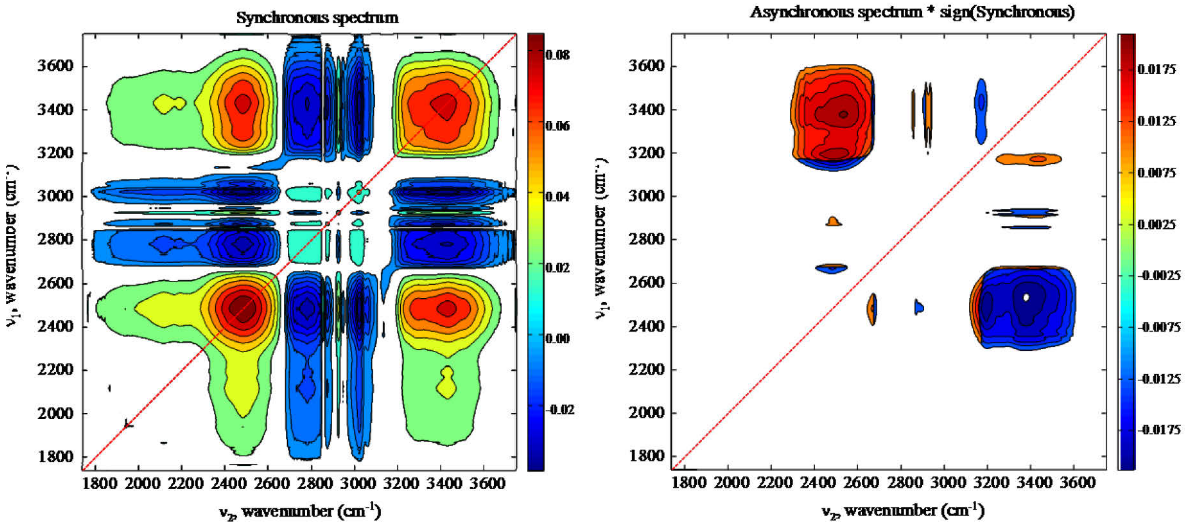

Figure 6.7: 2D correlation spectra generated from the set of nine (0-80 minutes; 10 min. interval) linear FTIR spectra measured as function of time when the DNA sample was exposed onto the D$_2$O vapour.

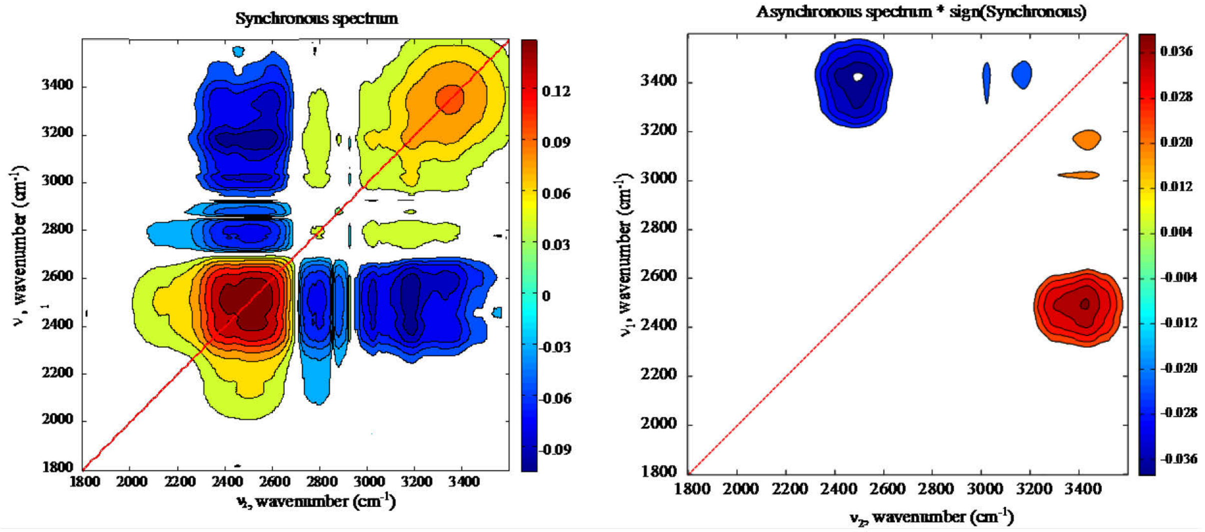

Figure 6.8: 2D correlation spectra generated from the set of eleven (0-800 minutes; 80 min. interval) linear FTIR spectra measured as function of time when the DNA sample was exposed onto the D$_2$O vapour.

The second set of data analysed with the help of two-dimensional correlation spectroscopy (period II) involve eleven infrared spectra starting from the one measured immediately after replacing the drying agent with D_2O. The last spectrum has been collected 800 minutes after exposure the DNA film on heavy water vapour.

There are several peaks at the diagonal of the synchronous spectrum (Figure 6.8, left) with maxima located at 2125 (w), 2416 (s), 2505 (vs), 3022(m), 3195 (s) and 3335 (s) cm^{-1}. In contrary to the synchronous spectra of the data measured in the time period between 0 and 80 minutes, all the off-diagonal peaks here have a negative sign. Strong peaks are observed at $\Phi(3185, 2410)$, $\Phi(3185, 2535)$ and $\Phi(3335, 2580)$. In addition, a weaker negative peak with a maximum at 2505 cm^{-1} is synchronous to the broad absorption extending from 2700 to 3100 cm^{-1} and similarly to the synchronous spectrum of period I, it is unclear if the observed band is in fact composed of one or two peaks.

The asynchronous spectrum (Figure 6.8, right) is dominated by the peak at 3429 cm^{-1}, which is asynchronous strongly with an absorption centred at around 2492 cm^{-1} and weakly with a peaks located at 3024, 3176 and 3335 cm^{-1}.

6.5.2 Discussion and conclusions

The synchronous spectra for the time period I and II differ substantially. In the period I, no peaks are observed with maxima corresponding to the peaks of the linear spectrum of a dry DNA film (3200, 3335 cm^{-1}, cf. red lines in Figure 6.3 and in Figure 6.5). Instead, a strong positive peak at $\Phi(2485, 3432)$ develops, which reveals the correlation between the OD stretching absorption from D_2O (the literature value for the maximum of the bulk D_2O is 2495 cm^{-1}) and the OH stretching absorption of HOD. The band at 2485 cm^{-1} is negatively synchronous with a broad absorption extending from 2700 to 3100 cm^{-1}. The latter is then negatively correlated with the band at 3432 cm^{-1}. In other words, the broad absorption which in the linear spectrum partially overlaps with strong CH stretching bands of the CTMA molecules decreases with concomitant intensity enhancement of OD stretching absorption of heavy water and the OH stretching bands of HOD molecules.

As such, the synchronous spectrum (period I) is dominated by the OH/OD rather than NH/ND exchange. These results suggest that a broad absorption between the 2700 and 3100 cm^{-1} may originate from the OH stretching vibrations (see also Section 6.7.5).

The asynchronous spectrum of period I suggest the existence of two overlapping peaks at around 3169 and 3200 cm^{-1}, which in addition behave differently with respect to the water (3382 cm^{-1})/heavy water (2505 cm^{-1}) absorption. From the sign of an asynchronous spectrum, the following sequential order of the spectral changes can be derived: 3200 → 2505 → 3169 (cm^{-1}). From the order of spectral changes it can be concluded that the H/D exchange of the NH group absorbing at 3200 cm^{-1} occurs faster than the deuteration of the NH stretching oscillator at 3169 cm^{-1}. With help of the ultrafast infrared pump-probe experiments on the hydrated DNA oligomers it is possible to assign the bands around 3200 and 3350 cm^{-1} to the different NH stretching vibrations of the adenine and thymine base pairs. A detailed discussion about the assignment of the NH and OH vibrations of the hydrated DNA will be given in the Section 6.7.3.

The synchronous spectrum of period II is dominated by the NH/ND exchange as the strongest cross-peaks develop at the frequency positions where the contribution of NH and ND stretching absorption is expected. By drying the deuterated sample with P_2O_5 it is possible to reveal the ND stretching vibrations by decreasing the intensity of the strong OD absorption (with maximum at around 2505 cm^{-1} and a shoulder at 2418 cm^{-1}). The corresponding FTIR spectrum is shown in Figure 6.6 (with marked peaks maxima).

The asynchronous spectrum (period II) reveals the non-correlated intensity changes that originate from OH stretching vibration from HOD and the OD mode of D_2O as well as NH/ND absorptions of base pairs.

Most of the hydrogens in the double-helix DNA oligomer are replaced by deuterium atoms on a time scale of several hours. Using two-dimensional correlation spectroscopy, the different exchange rates have been derived. In addition, the deuteration process has been spectrally separated from the hydration of the adenine-thymine oligomer. These results will give additional insight to the discussion about the assignment of different NH and OH vibrational modes based on the gas-phase calculations and the time-resolved experiments (Section 6.7.3).

6.6 Ultrafast pump-probe spectroscopy: Experimental

For all time-resolved experiments, the DNA oligomers duplexes were prepared as described in the section 6.4.1.

Femtosecond infrared pulses were generated in two independently tunable optical parametric amplifiers driven by 800 nm pulses of a repetition rate of 1 kHz from a Ti: sapphire laser as described in the Section 4.3 and depicted in Figure 4.3. In the frequency converters, a $AgGaS_2$ (0.5 mm thick for probe and 0.75 mm for pump) different frequency (DFG) crystal was used to generate infrared pulses at the frequency of the OH/NH stretching vibrations, and with help of a GaSe (0.5 mm thick for probe and 1 mm for pump) DFG crystal, the 8 μm pulses in the range of the phosphate vibrations were prepared. In polarization-resolved measurements, the infrared probe pulse passes additionally a 1 mm thick half-waveplate to change polarization of the probe with respect to the pump pulse.

The 500 nm thick silicon nitride and 1mm thick BaF_2 substrates were used to construct the humidity cell. The sample was placed on the thinner window which makes a negligible contribution to the detected nonlinear pump-probe signal as was confirmed in measurements with uncoated substrates [41]. After interaction with a DNA sample, the pump pulses were removed by a dichroic mirror and the probe pulse were dispersed in a monochromator and detected with 16-element MCT (HgCdTe) detector array (resolution 8 and 2 cm^{-1} for wavelength ~3 and ~8 μm, respectively).

The energy of the pump pulses was around 1.5-2μJ, the temporal width of the cross-correlation with the probe pulses was in the range between 130-160 fs (for both pulses tuned to similar frequency) and 200 fs (for cross correlation with 3500 cm^{-1} pump and 1230 cm^{-1} probe pulses). The fraction of the OH/NH stretching oscillators excited by the pump pulses at 3500 cm^{-1} was less than 3% and the pump pulses centred at 1220 cm^{-1} excite around 5% of phosphate stretching oscillators. Thus, multi-photon excitations and, in particular, multiple vibrational excitations on a single base pair can be ruled out.

6.7 Ultrafast vibrational dynamics of NH and OH excitations in hydrated DNA

In contrast to the relatively large amount of publications dealing with the ultrafast dynamics of water (summarized in section 6.3), femtosecond studies of DNA vibrations or model systems mimicking base pair geometries have remained limited. Coupling schemes of DNA carbonyl and other fingerprint modes have been studied using nonlinear 2D spectroscopy [290,291], and the relevant vibrational lifetimes have been determined in pump-probe experiments [190,282]. Biologically relevant water dynamics and solvation processes around chemically modified DNA (chromophores incorporated into the structure) have been studied by fluorescence methods with femtosecond time resolution supported by molecular dynamics simulations [247,292,293].

In this section, the first experimental results providing a detailed picture of the hydrogen-bonding vibrational dynamics and couplings of DNA oligomers at different levels of hydration will be presented. Femtosecond vibrational spectroscopy is applied to measure transient vibrational spectra, population kinetics and pump-probe anisotropies in the spectral range from 3000 to 3600 cm^{-1}.

6.7.1 Transient vibrational spectra of 0% r.h. DNA film

In Figure 6.9a, the linear absorption spectrum of the A-T oligomer at 0% r.h. is shown for the frequency range between 3000 and 3600 cm^{-1} (red line) together with the spectral profile of excitation pulses (grey lines) centred at three frequency positions: 3150, 3250 and 3550 cm^{-1}. In the steady-state infrared spectrum, the absorption around 3050 cm^{-1} is due to the C-H stretching vibrations. The different maxima and shoulders above 3100 cm^{-1} reflect both NH stretching modes of the base pairs and the OH stretching absorption of residual water molecules. In Figure 6.9b-d, transient spectra for different excitation conditions are displayed. The change of absorbance ΔA is plotted as a function of frequency of the probe pulse, which was delayed with respect to the pump pulse by 100, 200, 500 and 1000 fs. At low probe frequencies, transient spectra display a spectrally broad enhanced absorption ($\Delta A > 0$) that stems from the $\upsilon = 1 \rightarrow 2$ transition of the excited NH and/or OH stretching oscillator. At higher frequencies, the transient spectra show a decrease of absorption ($\Delta A < 0$) with the spectral envelope depending on the pump frequency. The observed negative signal originates from bleaching of the ground state $\upsilon = 0$ and stimulated emission from the first excited state $\upsilon = 1$. The corresponding Feynman diagrams of all three contributions have been shown in Figure 3.3. For excitation at 3150 cm^{-1} and 3250 cm^{-1}, a strong negative component at 3200 cm^{-1} is complemented by weaker contributions with maxima at around 3350 and 3480 cm^{-1}. The latter peak becomes stronger when exciting at E_{ex} = 3550 cm^{-1}. The relative amplitude of the different components of the transient spectra agrees with the peaks of the linear spectrum. Their width and position are roughly constant up to the measured delays of 10 ps (not shown). In other words, nonlinear spectra of low-hydration DNA films display a negligible spectral diffusion (being less than the individual line widths), in contrast to the disordered fluctuating hydrogen-bonded system such as bulk liquid water.

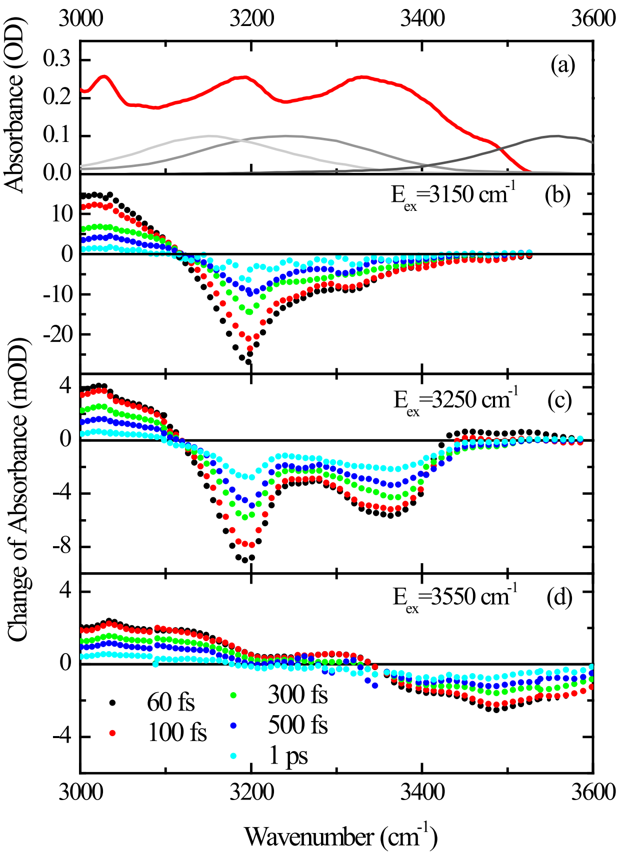

Figure 6.9: (a) FTIR absorption spectrum of a DNA-CTMA film in the range of the NH and OH stretching absorption for 0% r.h. (red line). Grey solid lines: spectral profiles of femtosecond pump pulses for three centre frequencies: 3150, 3250 and 3550 cm^{-1}. (b) Transient vibrational spectra measured with pump pulses centred at E_{ex}= 3150 cm^{-1}. The absorbance change $\Delta A = -\log(T/T_0)$ is plotted as a function of probe frequency for delay times of 60, 100, 300, 500 and 1000 fs (coloured symbols, T_0, T – sample transmission before and after excitation). (c,d) Transient spectra measured with pump pulses centred at E_{ex} = 3250 cm^{-1} and 3550 cm^{-1} for the probe pulse delays identical to those in (b).

In general, spectral diffusion originates from the modulation of the vibrational transition energy by structural fluctuations of the hydrogen-bond geometries or by fluctuating forces exerted by the bath. The DNA backbone structure enforces a well-defined structure of the A-T pairs, i.e., hydrogen bond geometry fluctuations are drastically suppressed, similar to other dimer systems such as cyclic carboxylic acid dimers in the gas phase or in a non-polar solvent [179,193].

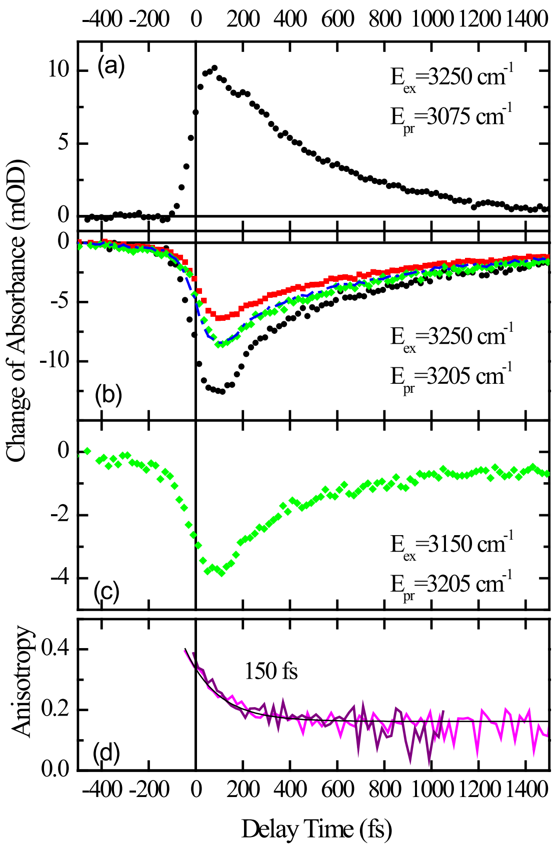

Figure 6.10: (a,b) Pump-probe transients measured at probe frequencies E_{pr} = 3075 cm^{-1} and E_{pr} = 3205 cm^{-1} with pump pulse tuned at E_{ex} = 3250 cm^{-1}. The change of absorbance is plotted as a function of pump-probe delay for parallel (black dots) and perpendicular (red squares) linear polarization of pump and probe pulses, as well as polarization for magic angle (green diamonds). The dashed blue line in (b) is a calculated magic angle signal $\Delta A_{\circ} = (\Delta A_{\parallel} + 2\,\Delta A_{\perp})/3$ (c) Magic angle transient spectrum (isotropic) measured with E_{ex} = 3150 cm^{-1} and E_{pr} = 3205 cm^{-1}. (d) Time-dependent anisotropy $r(t) = (\Delta A_{\parallel} - \Delta A_{\perp})/(\Delta A_{\parallel} + 2\,\Delta A_{\perp})$ derived from the data with probing and excitation condition as in (b) (solid magenta line) and (c) (violet solid line) together with a single-exponential fit.

On the other hand, the DNA molecule contains also polar groups, such as phosphate groups located on the double-helix backbone. Such groups undergo fluctuating thermal motions, which result in a fluctuating long-range Coulomb interaction with the vibrational transition dipoles. Negligible spectral diffusion found here may arise from the very low (< 20 cm^{-1}) frequency of the DNA backbone motions [294] and the inhibition of such motions in the DNA-surfactant film sample [232,235]. In addition, the comparably large distance between the polar groups located on the outside and the A-T base pairs in the inner part of the DNA structure limits the interaction strength. The time evolution of the absorbance difference for pump pulses centred at E_{ex} = 3150 cm^{-1} and E_{ex} = 3250 cm^{-1} and three different probe frequencies E_{pr} = 3075 cm^{-1}, E_{pr} = 3205 cm^{-1} and E_{pr} = 3335 cm^{-1} are presented in Figure 6.10 and Figure 6.11.

The transient $\upsilon = 1 \rightarrow 2$ absorption at E_{pr} = 3075 cm^{-1} (Figure 6.10a) decays with a time constant of approx. 508 fs, similar to the recovery time of the bleaching signal at 3205 cm^{-1}. Its decay was analyzed by fitting an instantaneous rise at zero delay and exponential decay convoluted with cross-correlation function of pump and probe pulse to the transient in Figure 6.10b.

The long-lived residual bleaching found in Figure 6.10b,c and Figure 6.11a reflects the formation of a hot ground state, i.e. the υ = 0’ → 1’ transition of NH/OH oscillators that have relaxed to the ground state and have passed the excess of vibrational energy to the neighbouring environment. This relaxation pathway is quite common in other hydrogen-bonded systems [14] and is described in the Section 3.10 and illustrated by the Feynman diagrams in Figure 3.3.

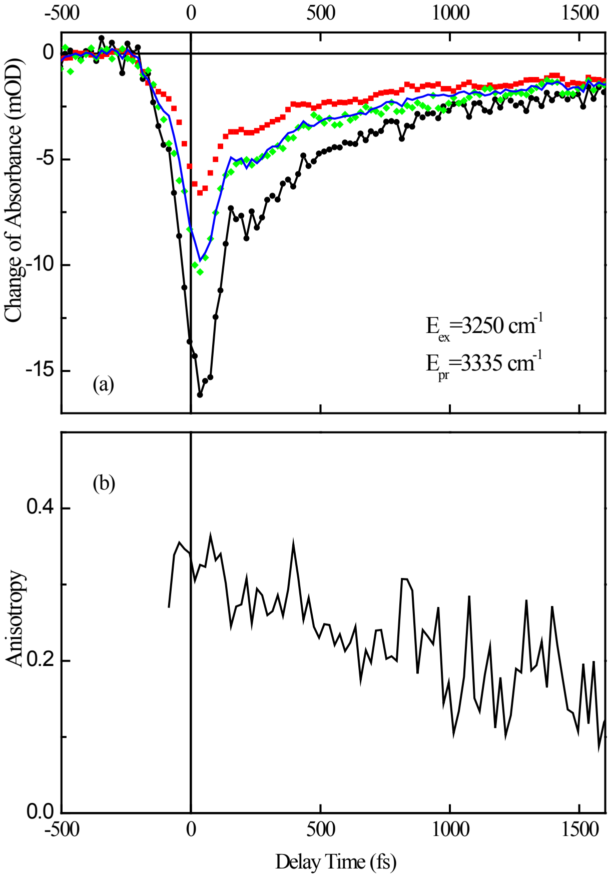

Figure 6.11: Transient spectra measured with E_{ex} = 3250 cm^{-1} and E_{pr} = 3335 cm^{-1} for parallel (black dots) perpendicular (red squares) and magic angle (green diamonds) linear polarization of pump and probe pulses, The blue line is a calculated magic angle signal as in Figure 6.3. (b) Anisotropy decay reaching for longer delay time (above 1 ps), a non-zero constant value.

It is frequently of interest to measure the signal uncontaminated by orientational information. This can be done by performing experiments in which the probe is polarized at the magic angle (54.74°) to the pump-polarization direction. The isotropic signal $\Delta A_{\circ}$ can be also calculated from the parallel and parallel and perpendicular signals using the equation: $\Delta A_{\circ} = (\Delta A_{\|} + 2\,\Delta A_{\perp})/3$. Such time-traces can be then compared to the measured magic angle transient. For all pump-probe time-traces presented here, calculated isotropic signals (blue lines in Figure 6.10 and Figure 6.11) agree very well with the experimental data recorded at the magic angle (green symbols in Figure 6.10 and Figure 6.11). The time-dependent anisotropy (magenta solid line in Figure 6.10d), derived from the data presented in Figure 6.10b using formula $r(t) = (\Delta A_{\|} - \Delta A_{\perp})/(\Delta A_{\|} + 2\,\Delta A_{\perp})$ exhibit an initial femtosecond delay from its initial value of r = 0.4 to a constant residual value of r ≈ 0.18. A similar behaviour is found for excitation frequencies at E_{ex} = 3150 cm^{-1} (dashed cyan line).

The transients measured with excitation at E_{ex} = 3250 cm^{-1} and probing the second pronounced bleaching (E_{pr} = 3335 cm^{-1}) of the spectra in Figure 6.11a show slightly different time evolutions of the absorbance change. Biexponentials have been fitted to the data with time constants of approximately 200 and 500 fs. The anisotropy decays on a 1 ps time scale (Figure 6.11b), slower than the 144 fs time constant found for the bleach signal with a maximum frequency at around 3205 cm^{-1} (Figure 6.10d). In both cases, however, the decay is not completed on a several picosecond time scale.

After excitation at high frequencies (E_{ex} = 3550 cm^{-1}), the $\upsilon = 1 \rightarrow 2$ absorption decays on a 1 ps time scale, similar to what is found after excitation at E_{ex} = 3250 cm^{-1}. The bleach recovery showed in Figure 6.12a displays a long-lived thermal signal, similar to these observed already in previously discussed transient spectra. In contrast to the data in Figure 6.10d and Figure 6.11b, the anisotropy derived from the data presented in Figure 6.12a does not decay and has a constant value r = 0.4.

A detailed discussion of the results will be given in Section 6.7.3, where the data from low- and high-humidity DNA will be merged together in order to extract reliable conclusions about contributions of NH and OH stretching modes to the vibrational spectrum of hydrated DNA, and about vibrational coupling between different NH stretching oscillators.

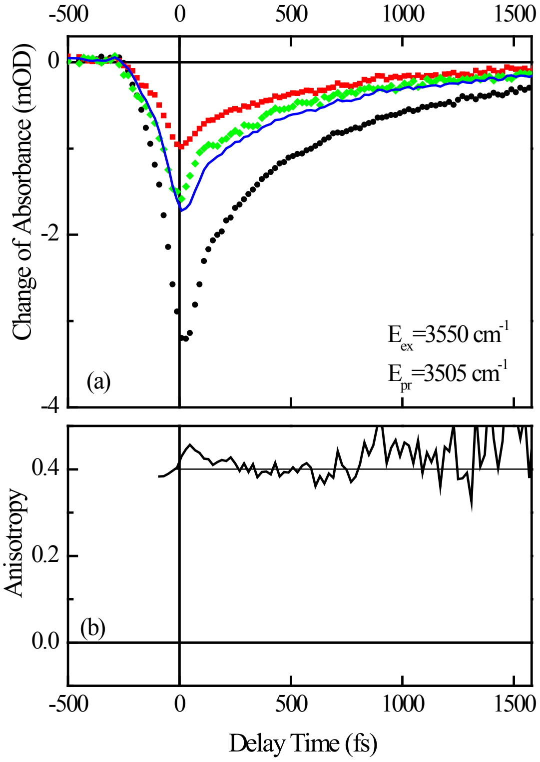

Figure 6.12: (a) Transient spectra measured with E_{ex} = 3550 cm^{-1} and E_{pr} = 3505 cm^{-1} for parallel (black dots) perpendicular (red squares) and magic angle (green diamonds) linear polarization of pump and probe pulses. The blue line is a calculated magic angle signal as in Figure 6.3. (b) Anisotropy has a constant value of 0.4 for all positive delays.

6.7.2 Transient vibrational spectra of 92% r.h. DNA film

In Figure 6.13, the transient spectra for a DNA film at 92% r.h. (more than 20 water molecules per base pair) are shown. They have been measured with similar excitation conditions as the spectra for 0% r.h. sample. Nevertheless, a comparison of the absolute amplitudes of the spectral features in Figure 6.9 and Figure 6.13 is difficult since spatial pump-probe overlap or other experimental conditions may vary slightly in independent measurements. For this reason, the absorbance changes ΔA for both humidity cases was normalized to their respective maximum change and calculated the difference: $\delta A(E_{pr}, t_d) = A_{norm}(E_{pr}, t_d, 92\%\ \text{r.h.}) - A_{norm}(E_{pr}, t_d, 0\%\ \text{r.h.})$. Difference spectra obtained in this way are plotted for two excitation conditions $E_{ex} = 3250\ \text{cm}^{-1}$ and $E_{ex} = 3560\ \text{cm}^{-1}$ and two delay times $t_d = 300$ fs and $t_d = 1$ ps in Figure 6.14.

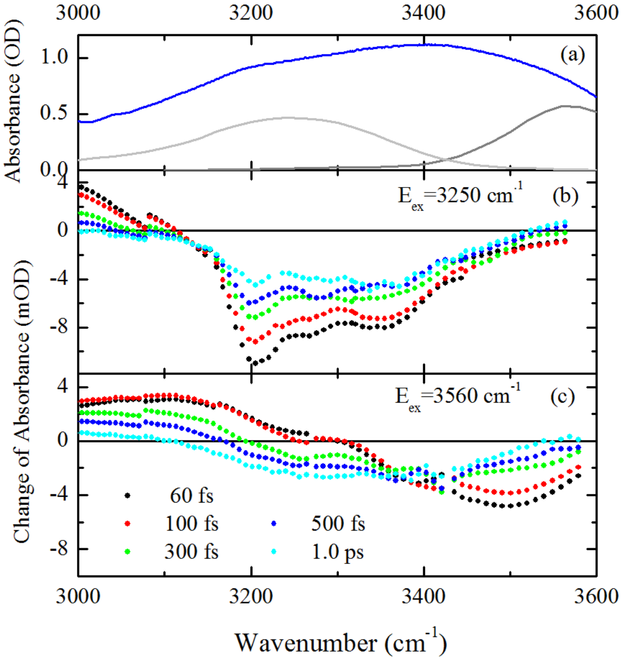

Figure 6.13: FTIR absorption spectrum of a DNA-CTMA film in the range of the NH and OH stretching absorption for 92% r.h. (blue line). Grey solid lines: spectral profiles of excitation pulses centred at 3250 and 3560 cm^{-1}. (b) Transient vibrational spectra measured with pump pulses centred at $E_{ex} = 3250\ \text{cm}^{-1}$. The absorbance change $\Delta A = -\log(T/T_0)$ is plotted as a function of probe frequency for delay times of 60, 100, 300, 500 and 1000 fs (coloured symbols, T_0, T – sample transmission before and after excitation). (c) Transient spectra measured with pump pulses centred at $E_{ex} = 3560\ \text{cm}^{-1}$ for the probe pulse delays identical to those in (b).

The transient spectra for 92% r.h. displays three negative components at frequency position very similar to the low-humidity case, namely at around 3200, 3350 and 3500 cm^{-1}. In addition, the bleaching between the first two negative components is enhanced when comparing to the 0% r.h. sample, a situation, which is clearly visible in the difference spectrum (Figure 6.14a). Excitation with pump pulses centred at $E_{ex} = 3560\ \text{cm}^{-1}$ results in a bleaching with a maximum at around 3500 cm^{-1} (Figure 6.13c). As time evolves, the bleaching feature exhibits a transient shift towards smaller frequencies, demonstrating spectral diffusion on a time scale of hundreds of femtoseconds.

The differential absorbance change on the 3350 cm^{-1} peak is close to zero. This is an important observation in context of discerning the NH from OH stretching contributions in the vibrational spectra of hydrated DNA system, as will be discussed in the next Section.

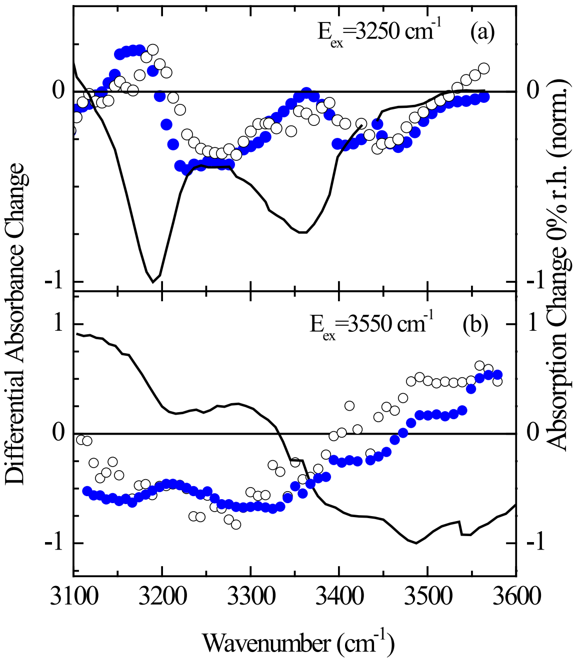

Figure 6.14: Transient difference spectra of 0 and 92% r.h. DNA film after pumping at E_{ex} = 3250 cm^{-1} (a) and E_{ex} = 3550 cm^{-1} (b). The normalized transient spectra measured for 0% r.h. were subtracted from the normalized spectra measured for 92% r.h. for delay times of 300 fs (blue dots) and 1 ps (open circles). Solid lines: normalized transient spectra measured at 0% r.h. (t_d = 300 fs).

The pump-probe time-traces measured with the sample at 92% r.h. for the same combinations of pump and probe as for the low-hydrated sample spectral positions are presented in Figure 6.15 and Figure 6.16. The excited state absorption (Figure 6.15a) decays much faster (< 200 fs) than for 0% r.h. sample and is followed by a negative signal that builds up on a time scale of several hundreds of femtoseconds. The bleach recovery can be characterized by two time constants: fast partial recovery (~ 500 fs) on a time scale similar to the enhanced absorption is followed by a slower (several picoseconds) contribution. The anisotropy presented in Figure 6.15c decreases from its initial value r(t) = 0.3 within less than 700 fs to zero, in a sharp contrast to the behaviour at 0% r.h (compare Figure 6.10d). The transients recorded with a pump pulse centred at E_{ex} = 3560 cm^{-1} (Figure 6.16) does not differ significantly from those collected for low-humidity sample shown in Figure 6.12. However, in contrast to the 0% r.h. data, where anisotropy has a constant value, for 92% r.h. sample the decay of anisotropy is observed, and decay from an initial value of approximately r(t) = 0.3 to the value below r(t) = 0.1 occur within the first picosecond after excitation.

The polarization-resolved measurements presented in this section reveal the different behaviour of anisotropy for low and high r.h. sample, and for different pumping and probing conditions. It will be presented in the next section, how important such information is for reliable separation different NH and OH stretching contributions to the vibrational spectra of DNA.

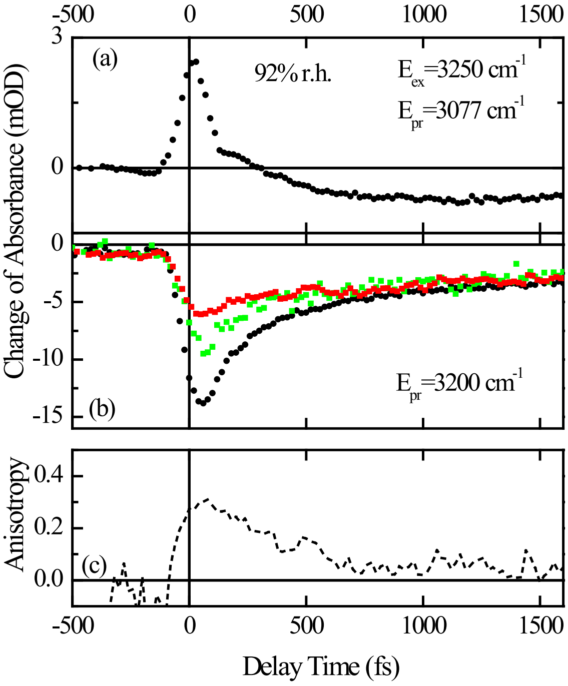

Figure 6.15: (a,b) Pump-probe transients measured with the 92% r.h. sample for two probing frequencies after excitation tuned to E_{ex} = 3250 cm^{-1} for parallel (black dots) perpendicular (red squares) and magic angle (green diamonds) linear polarization of pump and probe pulses. (c) Time-dependent anisotropy derived from the data in (b) decays to the value close to zero.

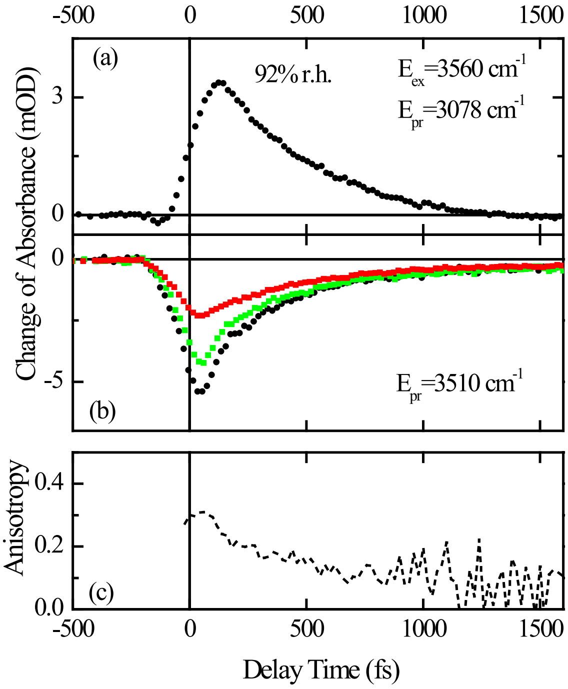

Figure 6.16: Pump-probe transients measured with the 92% r.h. sample after excitation centred at E_{ex} = 3560 cm^{-1} for parallel (black dots) perpendicular (red squares) and magic angle (green diamonds) linear polarization of pump and probe pulses for E_{pr} = 3075 cm^{-1} (a) and E_{pr} = 3510 cm^{-1}. (c) Time-dependent anisotropy derived from the data in (b) decays to the value close to zero.

6.7.3 The assignment of different transitions to particular NH stretching modes

As has already been pointed out in the Section 6.4.2, the unambiguous assignment of different NH stretching vibrations of the A-T oligomers and separating them from OH stretching modes of water based on stationary infrared spectra has remained difficult. In the A-T base pairs (Figure 6.17), two NH stretching oscillators are located on the adenine NH_2 group and one on the thymine NH group.

In a recent evaluation of isolated A-T pairs in the gas-phase, IR-UV double-resonance spectra were compared with *ab initio* calculated vibrational spectra of A-T isomers and base pairs [279]. The IR-UV spectrum of A-T fits two cluster structures with HNH···O=C/N···HN hydrogen bonding, based on comparison with the IR spectra of A and T monomers and with ab initio calculated vibrational spectra of the most stable A-T isomers. The dominant geometries found are different from Watson-Crick pairs, displaying however similar strength of hydrogen bonds.

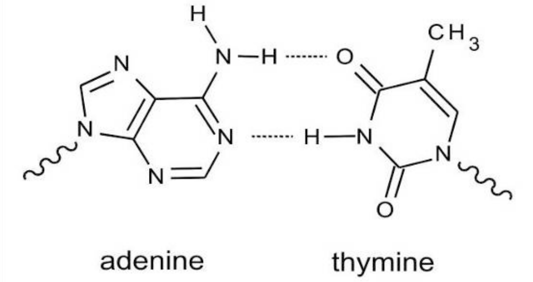

Figure 6.17: Molecular structure of the adenine-thymine base pair in Watson-Crick geometry.

In this gas phase study, the NH_2 vibrations of an isolated adenine molecule have been described in terms of a symmetric and asymmetric stretching mode with a measured frequency splitting $\Delta\nu_{NH} = \nu_{as} - \nu_s \approx 3569 - 3451 \approx 120\ \mathrm{cm}^{-1}$ [279,295]. This splitting corresponds to a coupling of $\Delta\nu_{NH}/2 = 60\ \mathrm{cm}^{-1}$ between the two local NH oscillators, each having a frequency of approximately $\nu_0 = 3510\ \mathrm{cm}^{-1}$. The stretching band of the single N9H group of adenine is located at 3508 cm^{-1}. More recent DFT calculations on the amino group in adenine suggest similar anharmonic frequencies: $\nu_{as} = 3539\ \mathrm{cm}^{-1}$, $\nu_s = 3432\ \mathrm{cm}^{-1}$ and $\nu_{N9H} = 3497\ \mathrm{cm}^{-1}$ [296].

Upon formation of the A-T pair, the hydrogen bond to the thymine carbonyl group distorts the symmetry of the NH_2 group of adenine. As a consequence, it is not obvious a priori whether the two NH_2 modes should be considered as symmetric and asymmetric or as individual stretching modes of the two local oscillators: one hydrogen-bonded and the other free.

The gas-phase spectra of isolated A-T base pairs display two stretching bands of the adenine NH_2 group at 3326 and 3530 cm^{-1} ($\Delta\nu_{NH} \approx 200\ \mathrm{cm}^{-1}$) and the stretching band of the free N9H group at 3507 cm^{-1} [279]. A similar spectral pattern has been observed in the IR-UV spectrum of isolated 9H-adenine. The stretching frequency of 3530 cm^{-1} in the A-T pairs is more than 20 cm^{-1} higher than ν_0, the frequency an uncoupled local NH oscillator would display. Moreover, the spectral red-shifts caused by hydrogen bonding are of the same order of magnitude as $\Delta\nu_{NH}$ and theoretical models suggest coupling between the adenine and thymine NH stretching vibrations much smaller than $\Delta\nu_{NH}/2$ [297]. The question whether the local or symmetric description of the NH_2 modes is more appropriate remains open. However, the experimental data (both linear and time-resolved IR spectra) presented in the previous chapter do not hint for presence of a free (non-hydrogen bonded) NH_2 group of adenine. In pump-probe experiments, two strong bleaching signals at around 3200 and 3350 are observed that frequencies are independent on humidity level of the sample. The minor changes in shape and absolute amplitudes of the 3200 and 3350 cm^{-1} bleaching components upon increasing the hydration level from 0 to 92% r.h. strongly suggest that such bands originate from the NH stretching modes of the A-T base pairs in the DNA oligomers rather then from the OH stretching from water. Moreover, even for the long pump probe delays (above 1 ps) these negative transient components do not show the spectral diffusion – a characteristic feature for the OH stretching modes in liquid water. The bands at 3200 and 3350 are thus assigned to the NH vibrations from base pairs. The frequency mismatch is similar to the observed in the gas-phase spectra and calculated for the A-T base pairs adenine NH_2 symmetric and asymmetric stretching vibrations. The strong red-shift of both vibrations observed in the A-T oligomers with respect to the gas-phase studies and their description in terms of symmetric and asymmetric modes can be additionally justified when assuming the hydrogen bonding interaction between water molecule(s) and the NH oscillator of the amino group of adenine. In other words, the symmetry distortion of the amino group caused by hydrogen bonding of one of its NH oscillators to the thymine base upon formation of a double-helix can be suppressed by hydrogen bonding of the second one to the water molecule. Therefore, the bands observed at 3200 and 3350 have been assigned to the symmetric and asymmetric stretching modes of adenine amino group in the A-T oligomers.

Isolated thymine molecules in the gas phase display stretching frequencies of 3435 cm^{-1} (N3H) and 3482 cm^{-1} (N1H) group [279,298]. Upon formation of A-T pairs, the frequency of the hydrogen bonded NH group of thymine shift to 3295 cm^{-1}, a value close to the frequency of the symmetric NH_2 stretching vibration of adenine in base pair (3326 cm^{-1}). Different experiments preformed at the DNA oligomers and described in previous sections (linear spectra measured in function of humidity, H/D exchange experiments and ultrafast pump-probe spectroscopy) suggest the lowest energy NH vibration is located at 3200 cm^{-1}. Hence, the band at around 3200 cm^{-1} is tentatively assigned to the superposition of the adenine NH symmetric mode and thymine NH vibration.

Pump-probe anisotropy measurements give independent arguments for an unambiguous assignment of different NH stretching oscillators of A-T base pairs. In Section 3.11, the polarization-sensitive pump-probe experiment has been introduced and the vibrational anisotropy decay phenomenon has been discussed. In the case of large molecular system, the anisotropy decay observed on the femtosecond time scale may be caused only by vibrational excitation transfer. Such energy redistribution can be accomplished when two or more vibrational modes couple to each other through-bond or through-space (dipole-dipole). In a double-helix structure of the A-T oligomer, the vertical distance between the base pairs is too large (beyond 0.3 nm) for effective vibrational coupling via though-space mechanism between NH groups located on different base pairs. As a result of relatively small pump fluences in all pump-probe experiments presented here, not more than one NH stretching oscillator per base pair is excited.

In adenine-thymine base pairs, the three NH stretching vibrations have similar extinction coefficients [279,299,300,301]. Accordingly, the effects of vibrational excitation transfer translate into population transfer to a quasi-equilibrium situation between these three oscillators. The excitation transfer between modes with similar eigenfrequencies is expected to be the most probable and hence, the transfer of the vibrational energy between the symmetric NH_2 stretching vibration of adenine and NH stretching mode of thymine should be reflected in fast anisotropy decay. The energy mismatch between these two vibrational modes and the asymmetric stretching mode of adenine is about 150 cm^{-1} and thus, excitation transfer rates are expected to be substantially smaller and the contributions to anisotropy decay – slower.

For excitation centred at E_{ex} = 3250 cm^{-1}, the anisotropy of the bleach signal with maximum at around 3205 cm^{-1} does not decay to zero for the 0% r.h. A-T film, even at long delays between pump and probe pulses (Figure 6.10d), but it stays on the constant level of approximately r = 0.18. The explanation of such finding is following:

- For vibrational excitation transfer rates higher than the population decay rates of the NH stretching oscillators, a full equilibration of population between the NH stretching modes will occur. Initial anisotropy, dictated by the vibrations excited by the pump pulse, will then change into fully equilibrated anisotropy values. The measured anisotropy decay (Figure 6.10d) is faster than the population decays (Figure 6.10a) and thus the anisotropy is equilibrated.

- Linearly polarized pump pulse centred at E_{ex} = 3250 cm^{-1} creates with equal magnitude excited state population of the symmetric NH_2 stretching mode of adenine and NH stretching mode of thymine.

- Before the excitation transfer takes place ($t_d = 0$), both excited oscillators contribute linearly to the pump-probe signal, and the initial anisotropy value, calculated from the Eq. 3.36, is equal $r(\alpha) = 0.4$, because the probed vibration equals pump vibration, $\alpha = 0$ for all systems in an ensemble.

- In a double-helix DNA structure, the dipole moment of the symmetric and asymmetric stretching NH_2 mode of adenine and NH stretching mode of thymine have a well-defined orientation with respect to each other: the angle between the dipole moments of the symmetric NH_2 stretching mode of adenine and NH stretching oscillator of thymine is 60°.

- For long delay times ($t_d = \infty$) a half of the initially excited population of the symmetric NH_2 stretching mode of adenine has transferred the excitation to the NH stretching mode of thymine, and vice versa (population equilibration).

- The anisotropy at long times ($t_d = \infty$) then approaches a value equal to $r = \frac{1}{2}(\alpha = 0°) + \frac{1}{2}(\alpha = 60°) = \frac{1}{2} \times 0.4 + \frac{1}{2} \times (-0.05) = 0.175$.

- The calculated anisotropy matches very well with the experimentally observed value and thus, an additional channel of vibrational excitation transfer to the asymmetric NH_2 stretching vibration of adenine is less important up to the delay times of 1.5 ps (which agrees with the intuitive picture that energetically uphill pathways are in general less probable).

The time scale of anisotropy decay allows for an estimate a vibrational coupling strength between the symmetric NH_2 stretching mode of adenine and NH stretching oscillator of thymine. The black solid line in Figure 6.10 agrees very well with the experimental data was calculated with a rate of 1/150 $fs^{-1} = 6.67 \times 10^{12}\ s^{-1}$ for the incoherent population transfer between the oscillators. Using standard Fermi golden rule approach, the value of 15 cm^{-1} was derived assuming both oscillators have the same $\upsilon = 0 \rightarrow 1$ absorption strength. It is interesting to compare this number with the interaction strength estimated for a through-space dipole–dipole coupling, taking into account the NH transition dipole strength, the distance between and the angular orientation of the two dipoles. Based on the Förster expression for point-like dipoles [302], one estimates a coupling of 4 (+5/-2) cm^{-1}, a fraction of the interaction strength derived from the experiment. The assumption of point-like vibrational dipoles in this model represents however a very crude approximation, very often insufficient for the accurate theoretical modelling of dipole–dipole and through-bond couplings.

In conclusion, the IR pump – IR probe results presented here suggest an assignment of the spectral component around 3350 cm^{-1} to the asymmetric stretching mode of adenine and the component with maximum around 3200 cm^{-1} to a superposition of symmetric NH_2 stretching vibration of adenine and the NH stretching mode of thymine.

The deuteration experiment presented in Section 6.5 reveals dissimilar exchange rates of different NH stretching modes of two overlapping bands absorbing at 3169 cm^{-1} and 3200 cm^{-1}. Theoretical calculations suggest the thymine NH stretching vibration has the lowest frequency. Thus, from the order of spectral changes derived from two-dimensional asynchronous spectra can be concluded that the slowest exchange occurs for the thymine NH oscillator (3169 cm^{-1}).

The transient anisotropy decay discussed above give an independent confirmation of the assignment of the absorption band at 3200 cm^{-1} to two different spectral components. The suggested NH stretching spectral pattern is in line with gas phase investigations introduced at the beginning of this Section.

6.7.4 Ultrafast redistribution of vibrational energy after excitation of NH stretching modes

The femtosecond two-colour IR pump – IR probe experiments presented so far allow the different NH stretching bands of the A-T base pairs and the mutual couplings of the different oscillators to be identified. For the sample at 0% r.h., the time evolution of enhanced absorption ($\upsilon = 1 \rightarrow 2$ transition) and bleaching ($\upsilon = 0 \rightarrow 1$ transition) shown in Figure 6.10a,b reveals a relaxation with the lifetime of the excited $\upsilon = 1$ states of approximately 0.5 ps.

In this section, the pathways of NH stretching relaxation and the concomitant redistribution of vibrational energy will be explored, and the modes accepting the excess energy from initially excited NH stretching levels will be identified using time-resolved IR pump / anti-Stokes Raman probe spectroscopy.

In this technique, infrared-pump pulses excite a distinct vibration, whereas probe pulses in the visible or ultraviolet range generate anti-Stokes Raman spectra indicating the transient population distributions of the excited vibrational levels. Because of the small Raman cross-sections, however, the sensitivity of this method is not sufficient for most solutes that cannot be studied at very high concentrations (e.g. because of their limited solubility or to avoid formation of molecular aggregates). Sensitivity can be considerably enhanced under electronic resonance conditions that results in increasing of scattering efficiency. This approach has been applied for studying vibrational populations after photochemical reactions [303,304] or to selectively monitor population kinetics of modes coupling to the electronic transition [305,306].

Mid-infrared pulses for vibrational excitation and UV pulses for anti-Stokes resonance Raman probing were generated in two independent optical parametric sources driven by amplified 800 nm pulses from Ti:Sapphire laser system as described in Ref. [307]. The subpicosecond infrared (3000 – 3600 cm^{-1}) pulse has a spectral width of about 40 cm^{-1}, and energy per pulse of ~10 μJ. Excitation pulses tuned in the spectral range between 266 and 306 nm had an energy of about 0.7 μJ and a spectral width of ~30 cm^{-1}. The 1 ps temporal resolution of the experiment has been determined from the cross-correlation function of the pump and probe pulses.

The infrared pulses that generate vibrational excitations in DNA sample were tuned to three frequency positions: 3200, 3350 and 3550 cm^{-1}. Following the assignment from the section 6.7.3, the peak at 3200 cm^{-1} represents a superposition of the symmetric NH_2 stretching vibration of adenine and the hydrogen-bonded NH stretching mode of thymine, whereas the peak at 3350 cm^{-1} reflects the absorption of the asymmetric stretching vibration of adenine. At 0% r.h., the OH stretching mode of the residual water molecules, contributes to the absorption band above 3500 cm^{-1}. Transient anti-Stokes resonance Raman spectra were recorded with subpicosecond UV pulse centred at λ = 306 nm, i.e., outside of electronic absorption band of DNA-CTMA film, in order to avoid a resonant electronic excitation of the sample.

In Figure 6.18, the spectra collected at a delay time of 800 fs after excitation at 3200, 3350 and 3550 cm^{-1} are shown. With infrared excitation at 3200 cm^{-1} (blue triangles), the pronounced Raman peaks of similar intensity at about 1660, 1590, 1490 and 1330 cm^{-1} are observed. These vibrational bands are also present in the resonance Stokes Raman spectra of pure adenine and pure thymine solutions in water [307]. For excitation at 3350 cm^{-1} (red dots), mainly the peak at 1660 cm^{-1} with a shoulder at 1590 cm^{-1} is observed, whereas for excitation at 3550 cm^{-1} (black squares), only the peak at 1660 cm^{-1} is present. Excess populations of the different fingerprint modes of adenine and thymine generated for different infrared excitation frequencies clearly shows that the NH stretching modes of base pairs strongly contribute to the infrared absorption at such position, as it has also been concluded from infrared pump-infrared probe experiments [233,308] described in previous sections.

The analysis of the population kinetics presented in Figure 6.19 of the modes at 1660, 1590 and 1490 cm^{-1} reveals two time constants: $\tau_1 = 0.6 \pm 0.3$ ps and $\tau_2 = 1.5 \pm 0.4$ ps, where the constant τ_1 describes the (rise) time in which the initially excited vibrations populate the excited states of the fingerprint modes, and τ_2 decay corresponds to the relaxation time of the fingerprint modes to other vibrations [307]. The mode at 1330 cm^{-1} exhibit slower kinetics with rise time $\tau_1 = 1.4 \pm 0.4$ ps and $\tau_2 = 2.0 \pm 0.5$ ps. The population rise times of the anti-Stokes Raman intensities at 1660, 1590 and 1490 cm^{-1} are in accordance with the population decay of the initially excited NH stretching modes, all showing the decay times of the order of 0.5 ps, as discussed in section 6.5.2. This indicates direct population of these fingerprint modes from the NH stretching vibrations. In contrast, the population rise time of the band at 1330 cm^{-1} is substantially slower, suggesting an indirect population of this mode via vibrational energy redistribution. As its rice time ($\tau_1 = 1.4 \pm 0.4$) is comparable to the decay time of the three other fingerprint modes ($\tau_2 = 1.5 \pm 0.4$ ps), it is probable that excess population in the mode at 1330 cm^{-1} originates from these three modes.

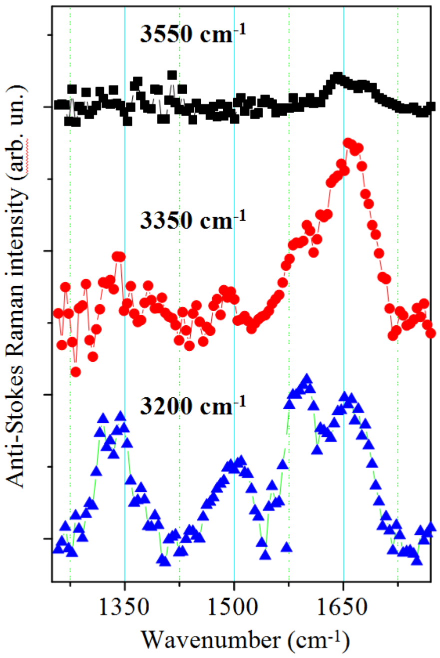

Figure 6.18: Infrared-pump/anti-Stokes resonance Raman-probe spectra of DNA-CTMA complexes recorded with a delay time of 0.8 ps after infrared excitation and with a probing wavelength of 306 nm. Spectra were recorded after infrared excitation at 3200, 3350 and 3550 cm^{-1}, respectively. Intensities are corrected for equal pump and probe intensities.

Although for excitation with infrared pulse tuned to 3350 cm^{-1}, the asymmetric NH_2 stretching mode of adenine is expected to be populated, the transient Raman spectra exhibit pronounced excess populations of the thymine fingerprint mode at 1660 cm^{-1}. This colourable discrepancy is in fact a confirmation of discussed in section 6.5.5 femtosecond excitation transfer between adenine and thymine NH stretching modes founded with help of polarization-resolved IR pump – IR probe spectroscopy.

The rate of population transfer from initially excited NH stretching vibrations into the individual fingerprint modes is determined by their respective energy mismatch. Hydrogen bonding is responsible for the lowering the energy of the NH stretching $\upsilon = 1$ state and in this way bringing them energetically closer to over- and/or combination tones. It has been shown [307] that the strongest anharmonic coupling, and thus, the most effective relaxation channel for the initially excited NH stretching modes exist for those overtones and combination bands which have a strong NH bending contribution [282,305,306].

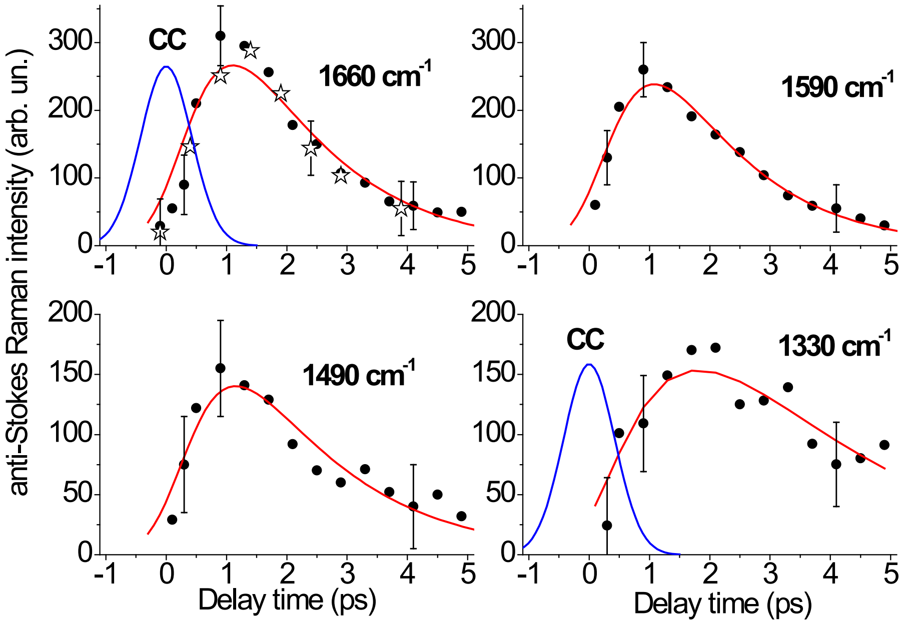

Figure 6.19: Circles: Anti-Stokes resonance Raman intensities of the vibrational bands at 1660, 1590, 1490 and 1330 cm^{-1} depending on delay time after infrared excitation at 3200 cm^{-1}. Stars: Normalized anti-Stokes Raman intensities at 1660 cm^{-1} for infrared excitation at 3350 cm^{-1}. Anti-Stokes resonance Raman spectra were probed at 306 nm. Solid lines: Approximation of the population kinetics by a three level model. The modes at 1660, 1590 and 1490 cm^{-1} are all fitted with a rise time $\tau_1 = 0.6 \pm 0.3$ ps and a decay time $\tau_2 = 1.5 \pm 0.4$ ps, whereas the kinetics of the mode at 1330 cm^{-1} is approximated with $\tau_1 = 1.4 \pm 0.4$ ps and $\tau_2 = 2 \pm 0.5$ ps. CC: Cross correlation function of the infrared pump and ultraviolet probe pulses ($\Delta\tau = 1$ ps, FWHM).

6.7.5 OH stretching dynamics of water interacting with DNA. Formation of a hot ground state

The so far presented results for the DNA sample at different hydration levels clearly show that NH stretching bands give a prominent contribution to the steady-state infrared absorption in the range of 3000 to 3700 cm^{-1}. For an assignment of the different absorption bands to particular NH and/or OH stretching vibrations of the adenine-thymine base pairs in the DNA oligomers and water, the changes of the transient spectra upon increasing of the water concentration in the DNA films have been analyzed. The difference spectra (Figure 6.14) for excitation at E_{ex} = 3250 cm^{-1} show that additional water molecules cause two more bleaching components around 3250 cm^{-1} and 3450 cm^{-1}. In contrast, the transient negative bands at 3200 cm^{-1} and 3350 cm^{-1} remain unchanged. Hence, the additional components present at high hydration level are assigned to water.

Deuteration experiment presented in Section 6.5 suggests that a broad absorption between 2700 and 3100 cm^{-1} may originate from the OH stretching vibrations of strongly hydrogen-bonded water molecules.

For DNA-CTMA film at 0% r.h., the vibrational couplings have been derived from the IR probe-IR pump anisotropy measurements and sub-picosecond Raman experiment have shown that NH excitations decay predominantly into fingerprint modes in the frequency range of the NH bending vibrations.

At 0% r.h., individual water molecules (~ 2 per base pair) are likely to be located closely to the negatively charged phosphate groups of the DNA backbone (see discussion about hydration DNA scheme in Section 6.2). This type of local interaction is similar to that of water molecules interacting with the polar heads of small reversed micelles [269,270,309]. The dynamics of water molecules in the hydration shell around protein or micelle is partly determined by and reflected in the hydrogen bond lifetime kinetics, which in turn depends on the structure of the layer induced by the macromolecular surface [262]. In geometries restricted to the nanometre length scale, like micelles or reversed micelles, the OH stretching band is narrower than in bulk water, with maximum at frequencies around 3500 cm^{-1} and above, depending on the micelle size [269]. Moreover, the $\upsilon = 1$ lifetime of OH stretching oscillator observed in reversed micelles and in the DNA film (500 fs, [308]) is longer than in bulk water (200 fs, [41,91,263]). The increase of vibrational lifetime is probably due to the bigger energy mismatch between the $\upsilon = 1$ state of OH stretching mode and the $\upsilon = 2$ state of OH bending vibration, which is located at around 3200 cm^{-1} and plays an important role in vibrational relaxation process [91].

At 0% r.h., the pump-probe anisotropy measured for $E_{ex} = 3550\ cm^{-1}$ and $E_{pr} = 3505\ cm^{-1}$ has a time-independent value of $r = 0.4$ (Figure 6.12b) rather than the 100 fs decay observed in bulk water [41,43,310]. This fact demonstrates that for water molecules strongly interacting with the ionic phosphate groups, rotational diffusion is suppressed and the vibrational excitation transfer to other OH stretching oscillators is of minor importance for such low water concentration. In contrast, a decay of anisotropy is observed for fully hydrated A-T oligomer (Figure 6.6), suggesting that both rotational reorientation and resonant energy transfer occur in the hydration shell of DNA. Again, this decay is substantially slower than in bulk water.

In order to understand the water dynamics in the vicinity of the DNA double helix, the results presented in the section 6.7.2 for 92% r.h. will be discussed now in more detail.

The transient pump-probe spectra of the sample at 92% r.h. (Figure 6.13c) exhibit a pronounced spectral diffusion, a characteristic feature for a disordered network of hydrogen bonds in aqueous systems. The bleaching signal with a maximum initially located around 3500 cm^{-1} shifts towards smaller frequencies (by ~100 cm^{-1}) on a sub-picosecond time scale. Hence, this broad essentially structureless spectral envelope is assigned to the OH stretching mode of water molecules.

In addition to water molecules directly interacting with DNA double-helix through local hydrogen bonds, a second hydration shell should be formed when increasing the film relative humidity to 92%. The experimental results presented in Figure 6.15 and Figure 6.20 indeed give evidence for a second subset of water molecules that is absent in low-hydrated A-T oligomers.

After pumping at $E_{ex} = 3250\ cm^{-1}$, the OH stretching response have properties which are much closer to the bulk water than when exciting at $E_{ex} = 3500 - 3560\ cm^{-1}$.

The arguments are given below:

- for excitation frequencies centred at $E_{ex} = 3250\ cm^{-1}$, an initial recovery with a time constant of 200 fs is found (Figure 6.20a), which agrees with the fast decay of the excited state absorption presented in the Figure 6.15a, and is close to the lifetime of $\upsilon = 1$ of OH stretching vibration in water.

- At 92% r.h., the pump pulse centred at $E_{ex} = 3250$ cm^{-1} excites both NH and OH stretching vibrations and thus, a separation of contributions of these individual modes to the observed transient spectra is impossible. However, the fast decay (within 250 fs) of the enhanced absorption (Figure 6.15a) sets an upper limit to the lifetime of $\upsilon = 1$ of OH stretching oscillator, which is then substantially shorter than the corresponding transient for 0% r.h. (Figure 6.10a) and the $\upsilon = 1$ lifetime of the OH stretching mode observed when pumping at $E_{ex} = 3560$ cm^{-1} (Figure 6.16a).

- At probing position (Epr = 3500 cm^{-1}) well above the excitation frequency ($E_{ex} = 3250$ cm^{-1}), the 500 fs build-up of a long-lived transient absorption is observed (Figure 6.20a, cyan diamonds). This behaviour reflects the formation of hot ground state in the water shell and it is very similar to bulk water transient measured with the same pumping/probing conditions (Figure 6.20a, blue solid line, data taken from [263]).

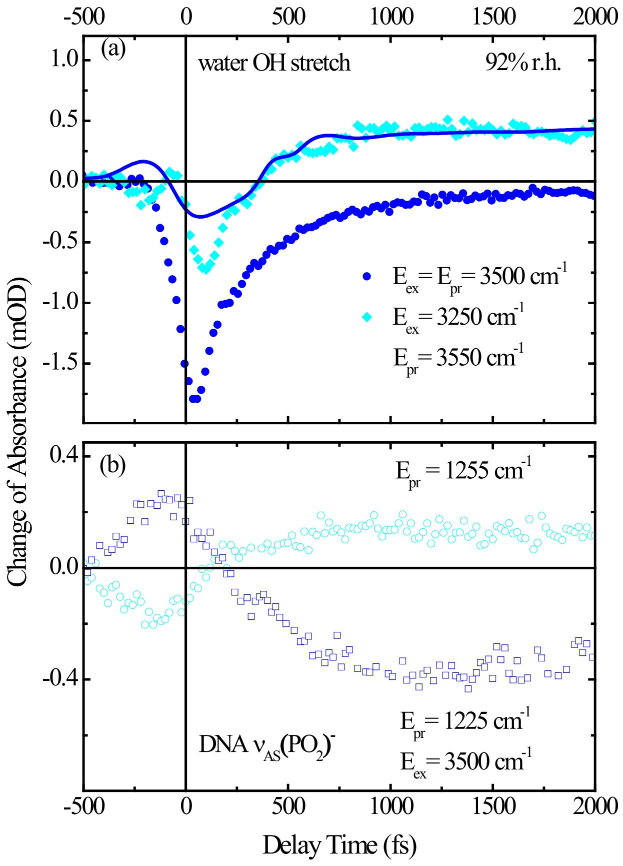

Figure 6.20: (a) Pump-probe transients (parallel polarization) recorded with $E_{ex} = 3500$ cm^{-1} and $E_{pr} = 3500$ cm^{-1} (blue dots) and $E_{ex} = 3250$ cm^{-1} and $E_{pr} = 3550$ cm^{-1} (cyan diamonds). The enhanced absorption at longer delays is due to the formation of hot ground state of water, similar to pure H_2O (solid line, data take from Ref. 263). (b) Time-resolved change of $\nu_{as}(PO_2)^-$ absorption for two fixed probe positions after excitation of the OH stretching mode of surrounding water ($E_{ex} = 3500$ cm^{-1}).

The positive signal in Figure 6.15a is followed by a long-lived absorption decrease, which is absent in corresponding transient spectra measured for 0% r.h. sample (Figure 6.10a), where mostly an ultrafast response of excited NH stretching vibrations of A-T base pairs are probed. This negative component is attributed to a reshaping of the transient OH stretching absorption originating from the quick repopulation of the OH stretching oscillator's ground state.

Formation of vibrational hot ground state has been schematically presented in Figure 6.21, and such relaxation pathway has been described by Feynman diagram in Figure 3.3. Here, the energy excess originating from the decay of the OH stretching excitation is transferred to intermolecular degrees of freedom and delocalized in the hydrogen-bond network. This result in an increase of vibrational temperature of 3-5 K for the IR pump-IR probe experiments presented here. In the heated water network (in the hot ground state of the water shell), the fraction of weakened or even broken hydrogen bonds is larger. As such, the number of free (not hydrogen-bonded) OH stretching oscillator statistically increases, resulting in enhanced absorption at the high-frequency edge of OH stretching band.

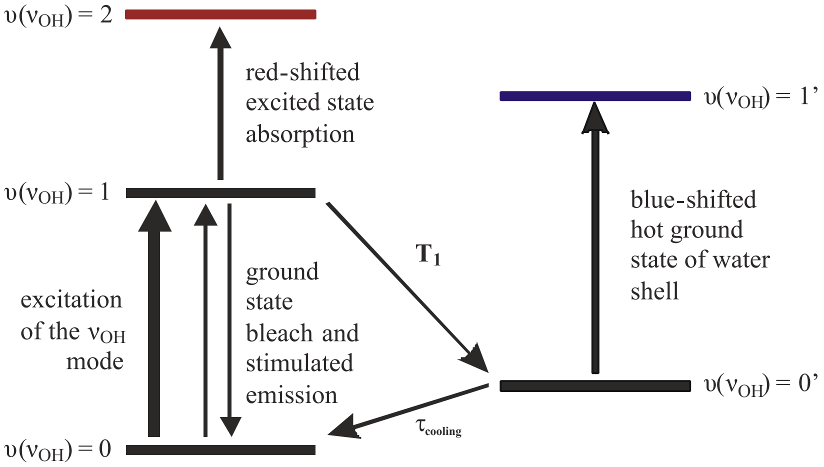

Figure 6.21: Formation of vibrational hot ground state of water. In the heated water network, the fraction of broken hydrogen bonds increases. As a consequence, the shift of the OH stretching mode towards higher frequencies is observed.

In the hot ground state of the hydration shell, also the number of hydrogen bonds between the water molecules and the charged phosphate groups located at the double-helix backbone decreases. Excitation of OH stretching vibration of water molecules result in a strong reshaping of the $\nu_{as}(PO_2)^-$ absorption spectrum. The transient $\nu_{as}(PO_2)^-$ spectra after excitation at E_{ex} = 3500 cm^{-1} demonstrate that this modified spectral envelope builds up on the same time scale as the hot ground state of the surrounding water (Figure 6.20a).

More detailed understanding of changes in the water-phosphate interaction pattern induced by excitation of hydration shell as well as the non-equilibrium energy redistribution in DNA double-helix after vibrational excitation of asymmetric $(PO_2)^-$ stretching of DNA or OH stretching band of water, will be the subject of the next section.

6.8 Non-equilibrium energy dissipation via water-phosphate interactions

The static equilibrium picture of the DNA hydration has been presented in Section 6.2. It has been shown that vibrations of the ionic phosphate groups located at the double-helix backbone are a sensitive probe of DNA-water interactions. In particular, the asymmetric stretching vibration $\nu_{as}(PO_2)^-$ undergoes characteristic frequency shifts when the hydration level of the DNA film changes (inset Figure 6.3). In the following, the first study of the dynamics of this mode will be presented, where the femtosecond infrared pulse excites the asymmetric stretching vibration $\nu_{as}(PO_2)^-$ and the second pulse probes its time evolution in interaction with the hydration shell. In a second series of measurements, the hydration shell itself is vibrationally excited and the response of the phosphate oscillator is measured. Such investigations are complemented by ultrafast experiments on the low-hydrated DNA samples, where statistically only 1-2 water molecules directly interact with the phosphate groups. In fully hydrated A-T oligomer, each phosphate moiety is surrounded by its own hydration shell, interacting only weakly with other hydration shells (Figure 6.22).

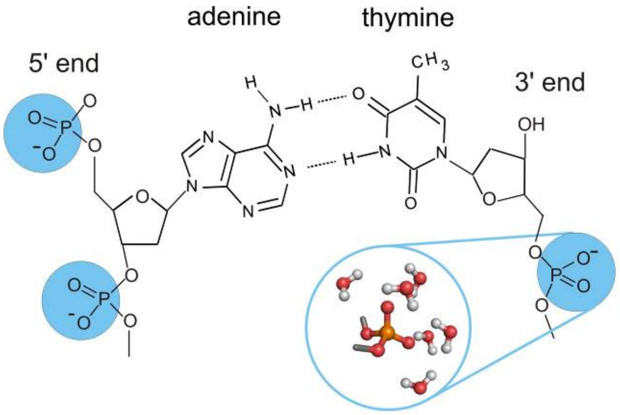

Figure 6.22: Molecular structure of nucleotide containing adenine-thymine base pair in Watson-Crick geometry. The shaded areas indicate hydration sites on phosphate groups. Inset: Scheme of a fully-hydrated phosphate group with arbitrary angular orientations of water molecules.

6.8.1 Ultrafast response of the resonantly excited phosphate asymmetric stretching $\nu_{as}(PO_2)^-$ vibration

The time evolution of the $\nu_{as}(PO_2)^-$ absorption of DNA at 0% r.h. (Figure 6.23a) and 92% r.h. (Figure 6.23b) was measured after excitation pulses centred at $E_{ex} = 1230\ cm^{-1}$. The spectra display an enhanced, red-shifted absorption on the $\upsilon = 1 \rightarrow 2$ transition and transient absorption decrease in the fundamental $\upsilon = 0 \rightarrow 1$ transition. Both components decay without changing their shapes and spectral position within the first picosecond after excitation, demonstrating minor spectral diffusion.

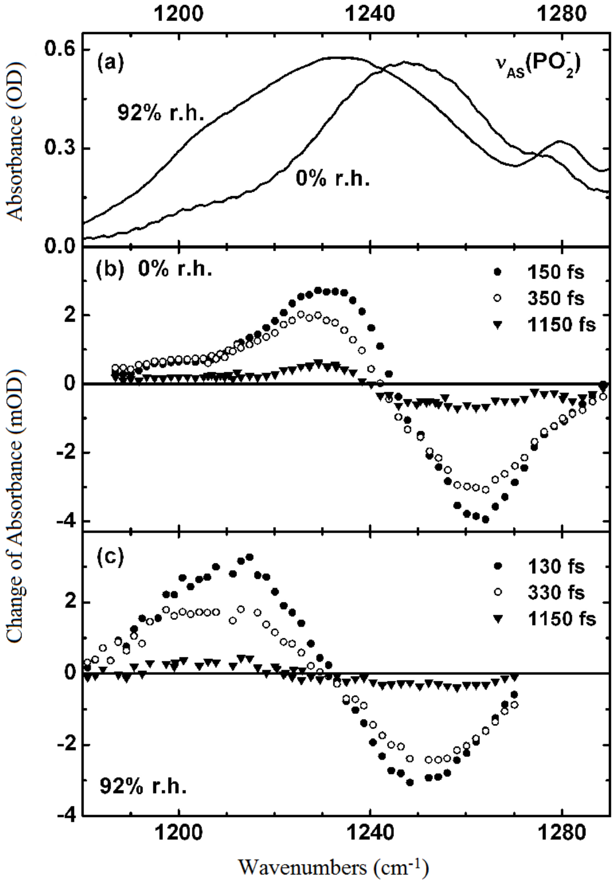

Figure 6.23: (a) Linear infrared absorption of the asymmetric $\nu_{as}(PO_2)^-$ vibration of the DNA oligomers at 0% and 92% r.h. (b) Transient spectra of the $\nu_{as}(PO_2)^-$ vibration after femtosecond excitation by pulses centred at E_{ex} = 1230 cm^{-1}. The change of absorbance is plotted as a function of probe frequency for different pump-.probe delays. The spectra display the enhanced $\upsilon = 1$ to 2 absorption at low frequencies and the decrease of $\upsilon = 0$ to 1 absorption at high frequencies. (c) Same for DNA oligomers at 92% r.h. Inset of (b): the spectra reflects the enhanced $\upsilon = 1 \rightarrow 2$ absorption at low frequencies and the decrease in the $\upsilon = 0 \rightarrow 1$ absorption at high frequencies (left); schematic representation of the $\upsilon = 0 \rightarrow 1$ absorption after relaxation of the $\upsilon = 1$ state.

The spectral shift of the enhanced $\upsilon = 1 \rightarrow 2$ absorption relative to the decrease of the $\upsilon = 0 \rightarrow 1$ absorption is a measure for the (diagonal) anharmonicity $\Delta\nu = \nu(\upsilon_{21}) - \nu(\upsilon_{10})$ of the $\nu_{as}(PO_2)^-$ oscillator which can be extracted by a line shape analysis (Figure 6.24).

As the lineshape of the linear absorption spectrum is not understood in detail, two limiting cases are considered:

- For a homogeneously broadened phosphate absorption band, the bleaching spectrum of the 0-1 transition is given by the (inverted) linear absorption band (blue lines in Figure 6.24b,c). Adjusting the amplitude of this band to and subtracting it from the transient spectra (symbols in Figure 6.24b,c), one derives the 1-2 absorption spectra of the oscillator (blue lines). The shift of the maxima of the respective 1-2 band relative to the 0-1 band is taken as a measure of the anharmonicity $\Delta\nu$.

- For an inhomogeneously broadened phosphate absorption band, the bleaching spectrum of the 0-1 transition is given by the convolution of the (inverted) linear absorption band with the pump spectrum (dash-dotted line in Figure 6.24a). Following the same subtraction algorithm, one derives the corresponding 1-2 spectra (red dash-dotted lines) and the anharmonicities.

Both models give very similar anharmonicity values of $\Delta\nu = -12 \pm 2$ cm^{-1} at 0% r.h. and $\Delta\nu = -18 \pm 2$ cm^{-1} at 92% r.h.

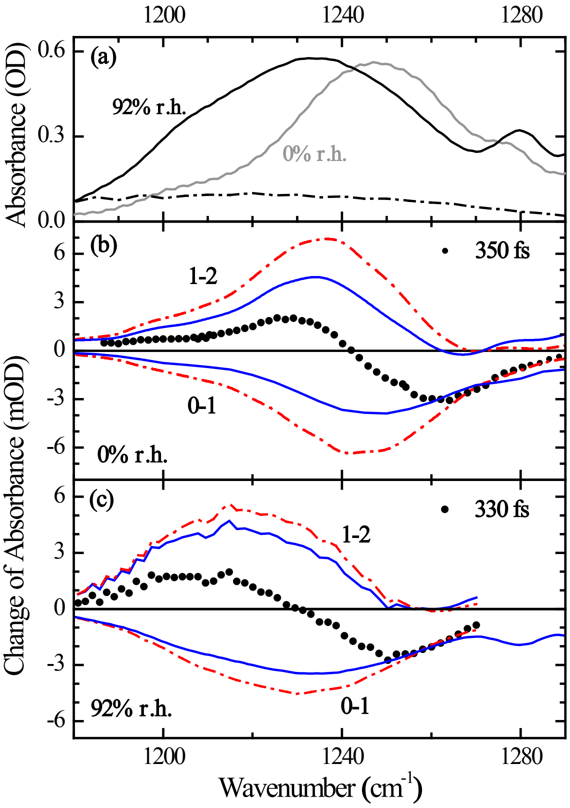

Figure 6.24: (a) Linear absorption spectrum of DNA in the range of the antisymmetric phosphate stretching vibration $\nu_{as}(PO_2)^-$ for 0% r.h. and 92 % r.h. (solid lines). Dash-dotted line: Spectrum of the femtosecond pump pulse. (b) Transient spectrum of the $\nu_{as}(PO_2)^-$ vibration at a delay time of 350 fs (symbols). Black solid lines: Inverted linear absorption spectrum (0-1 transition, lower part) and calculated 1-2 absorption (upper part). Red solid lines: Inverted linear absorption spectrum convoluted with the pump spectrum (0-1 transition, lower part) and calculated 1-2 absorption (upper part). (c) Same for a sample at 92% r.h.

The red-shift of the fundamental transition of the $\nu_{as}(PO_2)^-$ absorption band as observed in the stationary infrared spectrum (Figure 6.3) upon increasing the hydration level, together with a transient shift towards small frequencies of $\nu_{as}(PO_2)^-$ excited state absorption and diagonal anharmonicity increment from 12 to 18 cm^{-1} are all due to the hydration level increase of the phosphate groups. At 92% r.h., in addition to a larger number of hydrogen bonds between the phosphate groups and water molecules, the relocation of electronic charge in the $(PO_2)^-$ groups polarized by interaction with surrounding water dipoles could potentially plays an important role [311]. The constant pump-probe anisotropies (Figure 6.25b,d) derived from data in Figure 6.25a,c suggests a minor role of a resonant energy transfer between different $\nu_{as}(PO_2)^-$ oscillators.

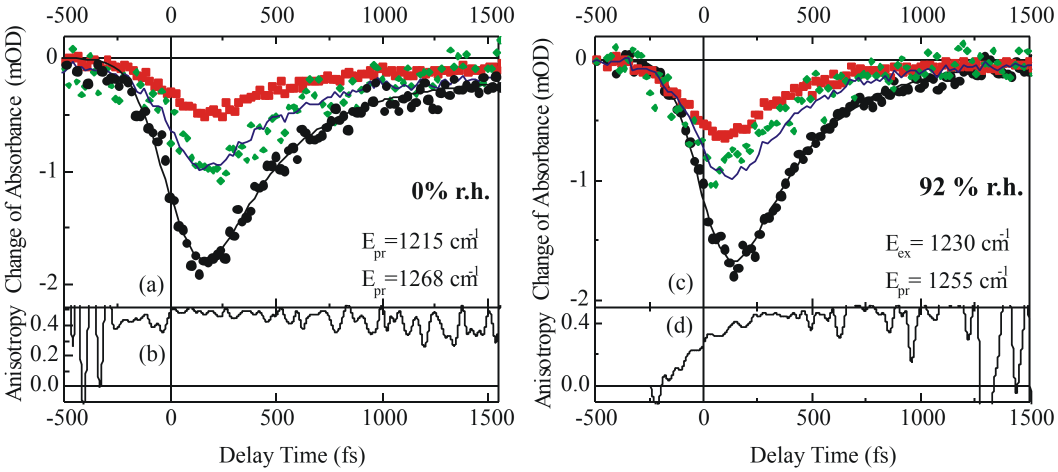

Figure 6.25: (a,c) Transient spectra of $\nu_{as}(PO_2)^-$ excitation at 0 and 92% r.h. measured for parallel (black dots), perpendicular (red squares) and magic angle (green diamonds) linear polarization of pump and probe pulses. The blue lines are the calculated magic angle signals. (b,d) Anisotropy has a constant value around 0.4 for all positive delays.

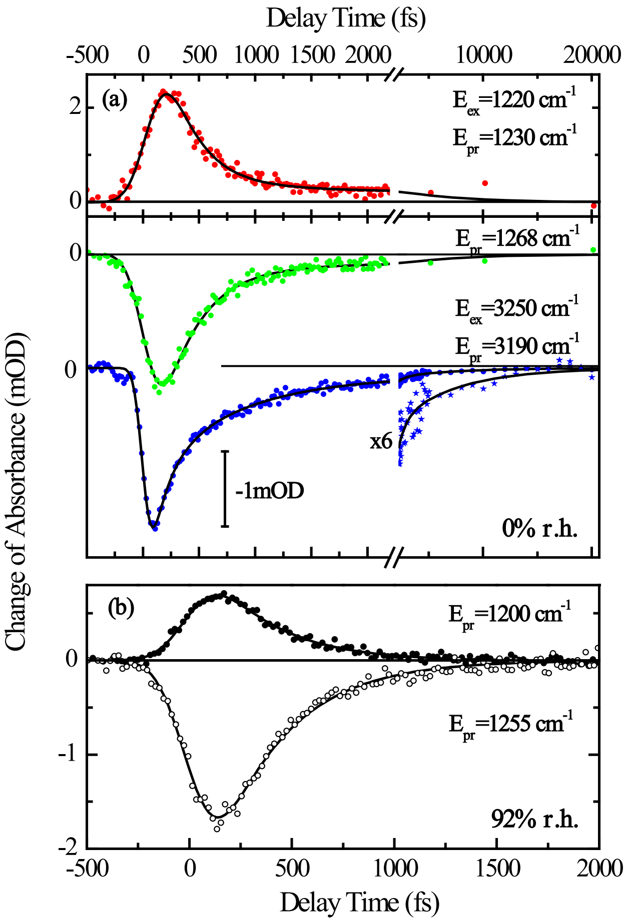

Figure 6.26: Time-resolved changes of the $\nu_{as}(PO_2)^-$ absorption at fixed probe frequencies for DNA oligomers at (a) 0% r.h. and (b) 92% r.h. (symbols). The initial 340 fs decay is independent of the hydration level (solid lines: rate equation fits) and represents the $\upsilon = 1$ population relaxation. At 0% r.h., this component is followed by a slow residual signal. This component is also observed in the NH stretching kinetics (bottom transient in (a)) and decays with a 5.5 ps time constant (solid line). At 92% r.h., any slow signal is absent.

In Figure 6.26, the kinetics of absorption changes at fixed spectral positions are shown. At both hydration levels, the enhanced absorption and the absorption decrease show a fast decay with a time constant of 340 fs (solid line: numerical fit), the lifetime of the $\upsilon = 1$ state of the $\nu_{as}(PO_2)^-$ oscillators. The fact that the depopulation of $\upsilon = 1$ level is independent of the hydration level indicate, that the relaxation pathway of the $\nu_{as}(PO_2)^-$ involves DNA vibrations at lower frequencies rather than couplings to the water vibrations. The symmetric phosphate stretching vibration, $\nu_{as}(PO_2)^-$, and/or the combination band involving the diester-phosphate stretching and $(PO_2)^-$ twisting modes may serve as initial energy acceptors [280,312,313].

After this initial decay, a small longer-lived absorption change is found at 0% r.h., which decays completely within 20 ps. A similar component is present in the NH stretching kinetics shown (Figure 6.26a, blue dots). The high accuracy of the latter measurement allows for deriving a decay time of 5.5 ps. It is important to note that this slow component is absent at 92% r.h. (Figure 6.26b). These observations points to a very important phenomenon, namely dissipation of the excess of vibrational energy to the DNA and / or water modes and will be discussed separately in the next section.

6.8.2 Non-equilibrium energy delocalization in hydrated DNA

In this section, the scenario of ultrafast redistribution of excess energy after vibrational excitation of PO_2^- mode of DNA will be discussed.

At 0% r.h., the transient absorbance changes of $\nu_{as}(PO_2)^-$ vibration at 1268 cm^{-1} and (Figure 6.26a) display – after the decay of $\upsilon = 1$ state – long-lived residual component that decay completely within 20 ps. The population relaxation of $\nu_{as}(PO_2)^-$ oscillator establishes excess energy in other, mainly low-frequency modes. Some of these modes couple anharmonically to the $\nu_{as}(PO_2)^-$ vibration, being now in its ground states. This coupling gives rise to a spectral reshaping of the $\nu_{as}(PO_2)^-$ $\upsilon = 0 \rightarrow 1$ absorption band (hot ground state) and, thus, to the signal in the picosecond range. Cooling the low-frequency modes by transferring the energy to other DNA vibrations and to the water environment, i.e., delocalizing the excess energy into a heated macroscopic volume, is mapped by the decay of this slow, “thermal” component. A similar scenario of ultrafast energy flow has been observed in the azobenzene molecule. The vibrational cooling of this polyatomic molecule after ultrafast photoisomerisation was investigated by time resolved IR spectroscopy with femtosecond time resolution [191]. There, after an initial ultrafast intramolecular energy redistribution process, the intermolecular energy transfer to the solvent occurs on a time scale of ca. 20 ps.

At 0% r.h., only single water molecules are located near phosphate groups of DNA. As a consequence, the potential role of accepting the vibrational energy by H_2O modes is strongly suppressed for such low water concentration. Thus, DNA with its large manifold of low-frequency vibrations represents the main heat sink, and the time constant of 5.5 ps, obtained from numerical fitting of the transient spectra (Figure 6.26a), reflects the time scale of energy transport within and along DNA (see energy relaxation scheme of $\nu_{as}(PO_2)^-$ for 0% r.h. in Figure 6.27, left).

For fully hydrated DNA at 92% r.h., no slow kinetics in the $\nu_{as}(PO_2)^-$ response is present. This fact suggests that excess energy released on the decay of asymmetric phosphate stretching vibration is mainly transferred to the surrounding hydration shell and redistributed in the aqueous bath. The initial energy transfer to the hydration shell is faster than observed 340 fs lifetime of $\nu_{as}(PO_2)^-$ excited state. Clearly, water molecules with a broad range of librational excitations serves as a very efficient heat sink preventing from energy accumulation in the DNA phosphate group (Figure 6.27, right).

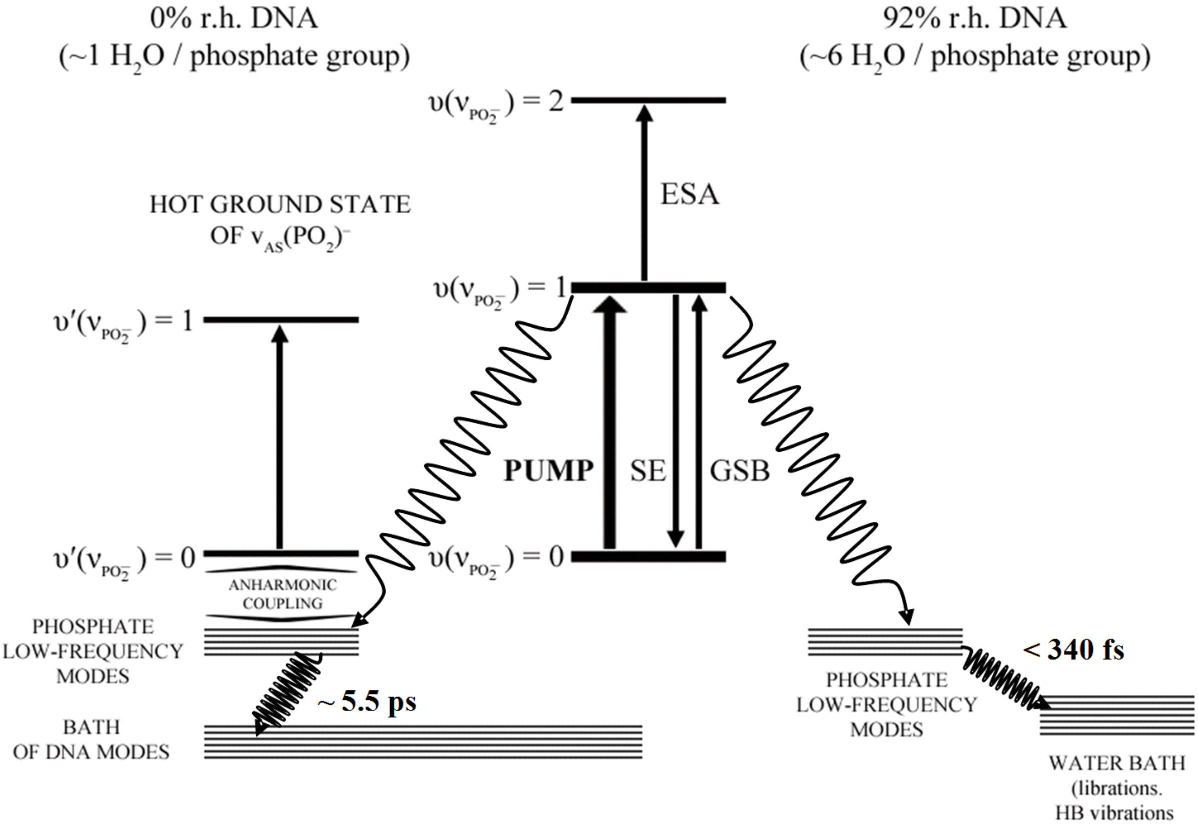

Figure 6.27: A schematic energy level diagram showing the possible energy relaxation pathways of asymmetric phosphate stretching excitation. For 0% r.h. sample (left side of the scheme), $\upsilon = 1$ decay brings the excited $\nu_{as}(PO_2)^-$ vibration back to its ground state and establishes excess energy in its low-frequency modes. Cooling these vibrations by transferring the energy to other DNA vibrations is mapped by the slow (~ 5.5 ps), thermal component. For fully hydrated DNA (right side) water molecules with a broad range of librational excitation act as a very efficient energy accepting manifold into which the energy is quickly transferred.

6.8.3 Response of the $\nu_{as}(PO_2)^-$ vibration to OH stretching excitations of water

To understand the interaction between the phosphate groups and their water shells in more detail, a series of experiments was performed in which the water shell is excited via the OH stretching band and the response of the $\nu_{as}(PO_2)^-$ vibration is monitored in a spectrally and temporally resolved way.

In Figure 6.28, transient $\nu_{as}(PO_2)^-$ spectra are plotted for different delay times after excitation at $E_{ex} = 3500$ cm^{-1}. Before delay zero (probe precedes pump), an enhanced absorption at low frequencies and a decrease of absorption at high frequencies is observed. As time evolves, the transient spectra undergo a strong reshaping, now developing a pronounced absorption decrease at low frequencies and an enhanced absorption at high frequencies, both persisting for delay times longer than 10 ps. In Figure 6.20b, time dependent absorption changes are shown for fixed probe frequencies. The transients demonstrate that the modified spectral envelope builds up on a time scale of approximately 1 ps, following a kinetics very similar to the formation of the hot water ground state as discussed already in section 6.7.5 and depicted in Figure 6.20a. The ultrafast response of the $\nu_{as}(PO_2)^-$ mode to an OH stretching excitation of the hydration shell gives independent evidence of the strong water-phosphate coupling at 92% r.h. The decay of the OH stretching excitation on a subpicosecond time scale (cf. Figure 6.20b) transfers the excess energy into low-frequency modes of water, forming a hot water ground state within 1 to 2 ps, very similar to the behaviour of bulk water. During and after this process, the $\nu_{as}(PO_2)^-$ oscillator remains in its $\upsilon = 0$ state and the interaction with the excited hydration shell modifies its $\upsilon = 0$ to 1 absorption.

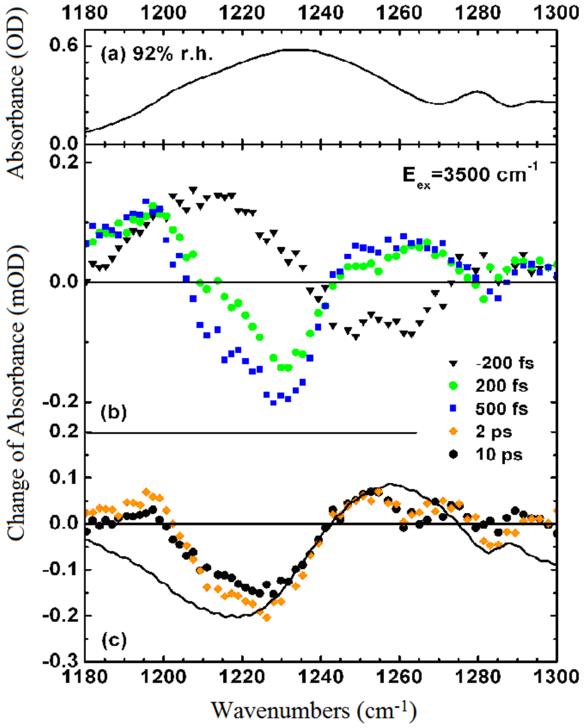

Figure 6.28: (a) Transient spectra (symbols) of the $\nu_{as}(PO_2)^-$ mode after excitation (E_{ex} = 3500 cm^{-1}) of the OH stretching mode of the water molecules in the DNA sample at high humidity (92% r.h.). Spectra are shown for two different pump-probe delays (parallel linear polarizations of pump and probe). (c) Transient spectra at delay times of 2 and 10 ps (symbols). Solid line: Difference $\Delta A = A(0\%) - A(92\%)$ of the linear absorption spectra for 0% and 92% r.h. scaled for the fraction of excited water molecules.

The transient spectra of Figure 6.28 reflect changes in the local interaction pattern of phosphate and water. Heating the hydration shell introduces defects in the hydrogen bond pattern, i.e., the fraction of geometrically distorted and/or broken hydrogen bonds increases, a mechanism also affecting the phosphate-water hydrogen bonds.

The shape of the transient spectra in Figure 6.28b (symbols) resembles the absorbance difference (solid line) $\Delta A = A(0\%) - A(92\%)$ of the linear absorption spectra for 0% and 92% r.h. (cf. Figure 6.3). This finding demonstrates that the average number of hydrogen bonds between the phosphate group and its hydration shell is reduced in the hot ground state. It has to be noted however, that the mechanisms that lead to the observed decrease of the average number of hydrogen bonds in transient and linear spectra are different. Subtracting the linear absorption spectra reflects the situation where the number hydrogen bonds decreases as a result of removing the water molecules from the DNA sample using the drying agent, in contrast to the transient thermal breaking of hydrogen bonds observed in the pump-probe spectra.

The hot ground state exists much longer than the 20 picosecond time interval of intra-DNA energy delocalization observed at 0% r.h. This observation suggests a very limited energy flow from the water shell back into DNA, potentially due to the reduced number of water-phosphate hydrogen bonds in the hot hydration shell and the limited number of low-frequency phosphate vibration that can serve as energy acceptors.

6.8.4 Response of the $\nu_{as}(PO_2)^-$ vibration at 0% r.h. after excitation at 3250 and 3500 cm^{-1}

In an additional series of measurements, the response of the $\nu_{as}(PO_2)^-$ vibration to excitation in the 3000 to 3500 cm^{-1} range for 0% r.h. has been studied. Transient spectra and time traces are presented in Figure 6.29 and Figure 6.30. At 0% r.h., pump pulses centred at 3500 cm^{-1} excite the OH stretching mode of the residual water molecules whereas pump pulses centred at 3250 cm^{-1} excite the NH stretching vibrations of adenine and thymine and eventually OH stretching from the residual water molecules. The spectra in Figure 6.29 display a similar shape and time evolution for both excitation conditions that is markedly different from the behaviour at 92% r.h. shown in Figure 6.28. The data for 0% r.h. reflect vibrational couplings between the OH stretching modes and the $\nu_{as}(PO_2)^-$. The characteristic transient reshaping of the asymmetric phosphate stretching band has been also observed in phospholipid reversed micelles (dioleyolphosphatidylcholine, DOPC) for low-hydration level ($w_0 = 0$, where $w_0 = [H_2O]/[\text{amphiphile}]$) [314]. In self-assembled phospholipids, the interaction of (confined) water molecules with ionic phosphate groups resembles water-phosphate coupling in hydrated biological membranes and in RNA or DNA.

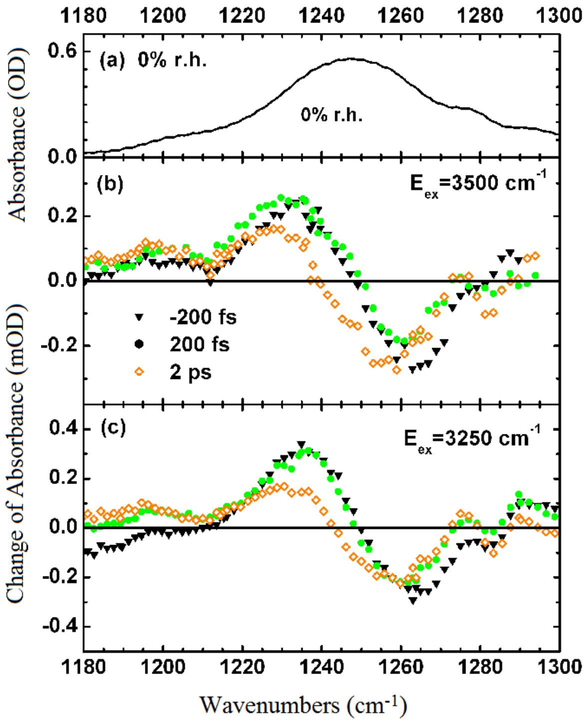

Figure 6.29: (a) Linear absorption spectrum of DNA in the range of the antisymmetric phosphate stretching vibration $\nu_{as}(PO_2)^-$ for 0% r.h. (solid line). (b,c) Transient spectra (symbols) of the $\nu_{as}(PO_2)^-$ mode after excitation at (b) E_{ex}=3500 cm^{-1} and (c) E_{ex}=3250 cm^{-1}. Spectra are shown for 3 different pump-probe delays (parallel linear polarizations of pump and probe).

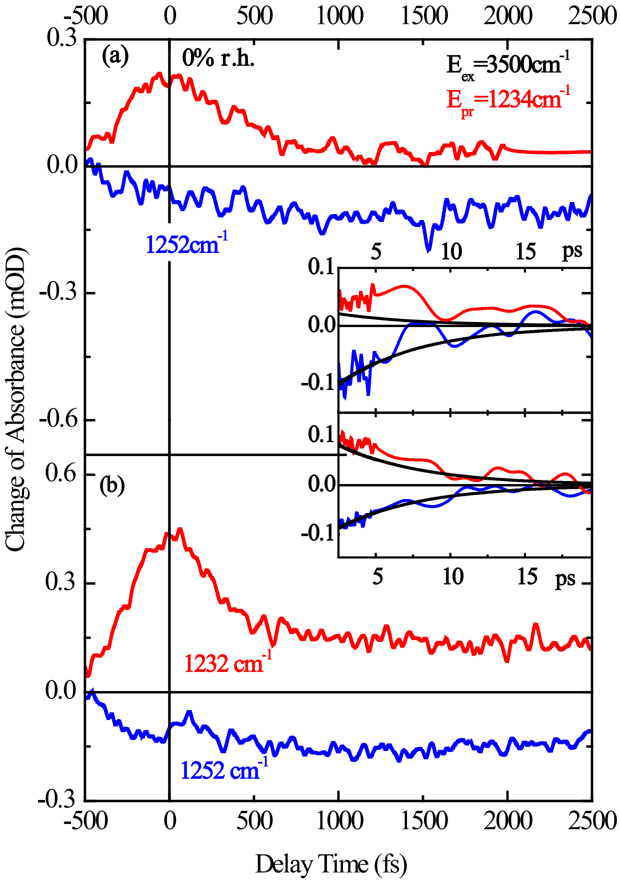

Figure 6.30: Time-resolved change of the $\nu_{as}(PO_2)^-$ absorption at fixed frequency positions E_{pr} of the probe after excitation at (a) E_{ex}=3500 cm^{-1} and (b) E_{ex}=3250 cm^{-1} (coloured lines, parallel linear polarization of pump and probe). The insets give the time evolution up to 20 ps delay. Black solid lines in the insets: Numerically calculated signal decay with a time constant of 5.5 ps.

It should be noted that the long-term signal of the transients in Figure 6.30 again shows the 5.5 ps kinetics (black lines) of vibrational energy transfer within DNA.

6.9 Conclusions and outlook

A comprehensive study of the DNA-CTMA films at different hydration level has been presented in this chapter. The results demonstrate the potential of nonlinear infrared pump-probe spectroscopy to discern and assign DNA and water vibrations, to determine their couplings, and to explore microscopic interaction mechanisms governing the dynamics of hydration shell. By measuring the anisotropy decay, the mutual couplings of the different NH stretching modes of the adenine-thymine base pairs in the DNA oligomers have been documented. The pronounced example is the coupling between the NH stretching vibration of thymine and the symmetric NH_2 stretching mode of adenine, calculated to have strength of the order of 15 cm^{-1}.

Vibrational energy transfer from the excited NH stretching modes to fingerprint vibrations has been observed in real-time using subpicosecond infrared pump/anti-Stokes Raman-probe spectroscopy. The decay of different NH stretching vibrations populates distinct accepting modes in the NH bending range with a rise time of 0.6 ps that is close to the NH stretching decay times. Excitation of the accepting modes in the fingerprint region relaxes on a time scale of several picoseconds.

At low hydration level, single water molecules interacts with a phosphate groups in the DNA backbone, thereby forming a rigid geometry in which rotation of the water molecules is inhibited. At 92 % r.h., i.e., in the case when DNA oligomer is considered as a fully hydrated, the dynamics of the water shell is more complex. Two types of water species with markedly different properties have been found. In addition to the OH stretching band around 3500 cm^{-1}, which has been assigned to the water molecules that interacts strongly with DNA backbone (similarly to the low-humidity case), second type of OH excitation has been observed. Its dynamical properties are closer to those of bulk liquid water with a pronounced spectral diffusion that is loss of structural memory on a time scale of several hundreds of femtoseconds. The OH stretching excitation of water molecules that weakly interact with DNA oligomer exhibit a lifetime of about 200 fs, a loss of vibrational anisotropy due to molecular rotations and/or energy transfer, very broad absorption and vibrationally hot ground state formed by disposal of excess energy.

The interaction of the DNA backbone with water has been probed via the asymmetric $\nu_{as}(PO_2)^-$ vibration. The ultrafast time scales of nonequilibrium energy dissipation have been established and the concomitant changes of the water-phosphate hydrogen bond pattern have been characterized. While the transfer of excess energy from DNA into the hydration shell occurs on a femtosecond time scale, energy delocalization within DNA is a slower picosecond event. The phosphate hydration shells represent a highly efficient heat sink with an intrinsic dynamic behaviour close to bulk water and negligible energy back-transfer into DNA.

Since more then 140 years, when the Swiss physician Friedrich Miescher first isolated deoxyribonucleic acid, this fascinating molecule has continuously inspired scientist. The ultrafast pump-probe experiments on DNA oligomers at controlled humidity level would be not possible without developing a method of preparation high optical quality thin films. The results presented in this chapter have contributed to elucidate microscopic dynamics of adenine-thymine base pairs in hydrated DNA oligomers. A very recent femtosecond two-dimensional (coherent) infrared spectroscopy on this system continues the efforts to understand complicated vibrational relaxation processes, in particular, vibrational coupling mechanisms and water dynamics in DNA hydration shell [95].

In the two-dimensional spectroscopy, a sequence of three pulses of femtosecond duration interacts with the molecular sample and induces a coherent vibrational response which is readout via photon-echo signal [315,316,317]. The time interval between pulse 1 and 2 is called coherence time τ, and the time interval between pulse 2 and 3 – population (waiting) time, T. The photon echo signal is often detected in a phase-resolved way by mixing it with the electric field of a fourth, reference pulse, the local oscillator (heterodyne detection). The heterodyned signal is then measured as a function of the time delay t between the echo signal and the local oscillator. Fourier transforming these signals with respect to τ and t produces a complex 2D spectrum with the excitation and detection frequencies (ν_1 and ν_3, respectively). The shapes and spectral positions of the peaks contain information about the couplings in the sample, spectral diffusion as well as the degree of homogeneous and inhomogeneous broadening that is present in the system of interest.

In an inhomogeneously broadened ensemble of oscillators, a correlation between the excitation and detection frequencies is found at early times after excitation, resulting in peaks elongated along the diagonal $\nu_1 = \nu_3$ as shown in Figure 6.31 for hydrated DNA and bulk water.

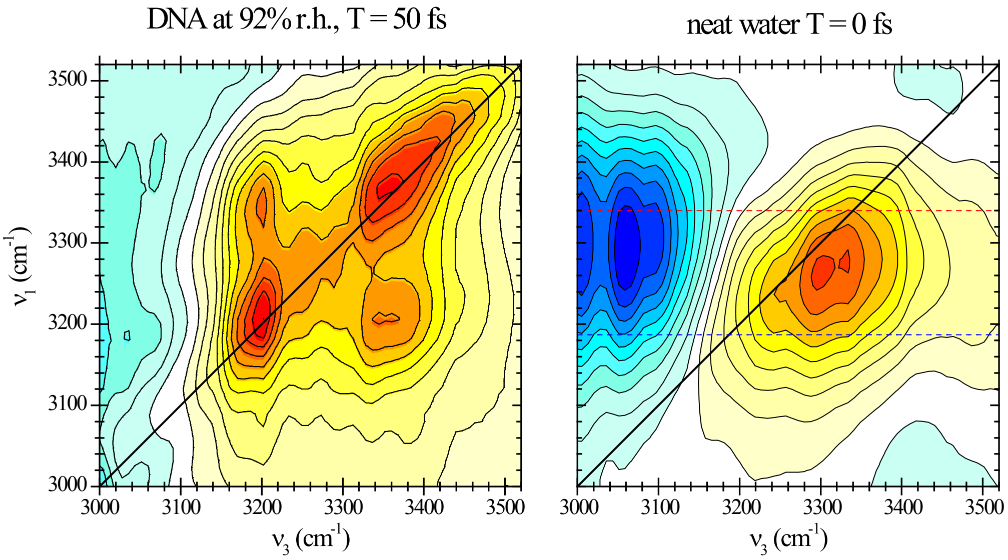

Figure 6.31: 2D vibrational spectra of hydrated DNA at 92% r.h. (left) and bulk water (right, taken from Ref. [41]) for early population times. The signal in the yellow-red areas correspond to the $\upsilon = 0 \rightarrow 1$ transition, whereas the blue areas give the $\upsilon = 1 \rightarrow 2$ signals.

Spectral diffusion destroys this correlation and the 2D spectrum become rounder and rounder as the population time (*T*) increases. Such reshaping has been observed for bulk water and recently for hydrated DNA (Figure 6.32).

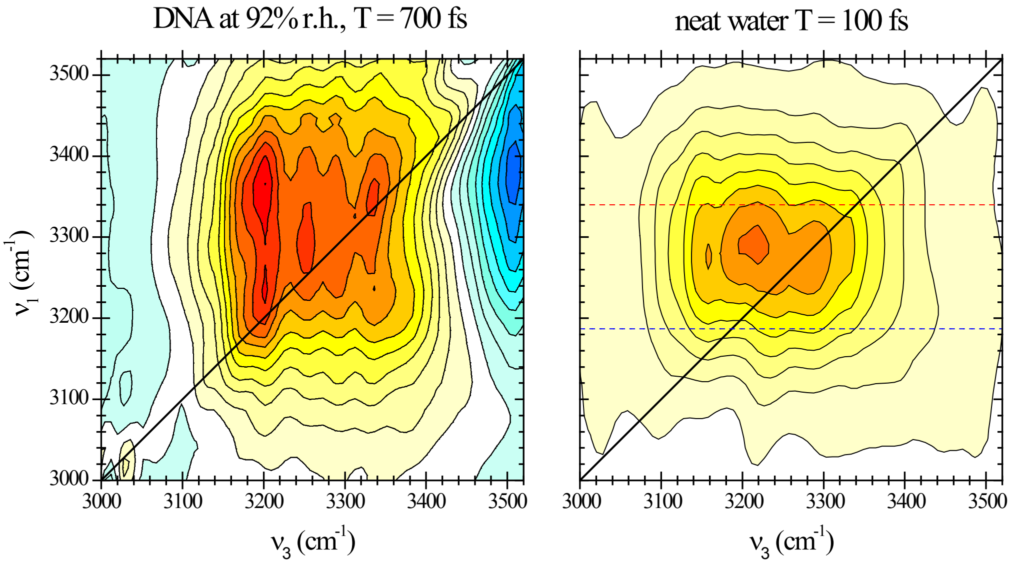

Figure 6.32: 2D vibrational spectra of hydrated DNA at 92% r.h. (left) and bulk water (right, taken from Ref. [41]) for population times 700 and 100 fs, respectively, reflecting ultrafast spectral diffusion. The signal in the yellow-red areas correspond to the $\upsilon = 0 \rightarrow 1$ transition, whereas the blue areas at lower frequencies give the $\upsilon = 1 \rightarrow 2$ signals. The blue areas at higher frequencies correspond to the hot ground state formation.

The extremely fast spectral diffusion (~ 50 fs) observed in pure water is due to fluctuating forces originating from the fastest librational motions in the hydrogen-bonded network as has been discussed in detail in Refs. [41,43]. At T = 50 fs the DNA/water system exhibits a pronounced signal on the diagonal, which involve the NH stretching peaks of base pairs and the broad OH stretching contribution of water. Two off-diagonal peaks at frequency position of $(\nu_1,\nu_3) = (3200\ \mathrm{cm}^{-1}, 3330\ \mathrm{cm}^{-1})$ and $(\nu_1,\nu_3) = (3330\ \mathrm{cm}^{-1}, 3200\ \mathrm{cm}^{-1})$ result from coupling between the NH stretching modes absorbing at 3200 cm^{-1} and the asymmetric stretching mode of adenine at 3330 cm^{-1}. At T = 700 fs, the NH stretching peaks are still at their original positions. In other words, the spectral diffusion is minor, as it has been already concluded from presented in the Section 6.7.2 pump-probe results. On the other hand, the OH stretching component exhibits now an essentially round shape. The change in the OH stretching contribution is qualitatively similar to neat H_2O, occurring however on somewhat slower timescale.

Future work will address vibrational couplings and energy-transfer processes by measuring two-colour 2D spectra to elucidate couplings between modes of distinctly different frequencies. Supported by theoretical calculations, such data should enable the quantitative analysis of the complicated coupling schemes. Another direction is to study the energy dissipation induced by radiationless decay of electronically excited states of DNA. Femtosecond spectroscopy is a promising tool to understand in detail microscopic mechanisms that are responsible for the high photostability of DNA.

7 Summary

Hydrogen bonding is a relatively weak molecular interaction but its relevance in nature is prodigious. Indeed, in living organisms biochemical processes occur mainly in an aqueous environment where interactions with water greatly modulate the structure and function of biomolecules.

The multitude of hydrogen bonds existing between nucleobases as well as the interaction of DNA with surrounding water molecules strongly influence the spatial arrangement and couplings of functional units of the macromolecular structure of the double helix. Water molecules also stabilize the helical structure by partly shielding electrostatic interactions between charged or polar groups such as the phosphate groups in the DNA backbone.

The fastest changes of the DNA hydration shell geometries occur in the time domain below 1 picosecond (1 ps = 10^{-12} s). It is thus only with the advent of ultrafast vibrational spectroscopy that examining such processes in real-time has become possible.

The motivation of this thesis was to gain a deeper understanding of vibrational dynamics and couplings in DNA oligomers at different levels of hydration. The coupling of DNA to the aqueous environment allows for energy exchange and, is thus expected to play a key role for non-equilibrium processes such as the dissipation of excess energy originating from the decay of electronic and/or vibrational excitations in DNA.

Native DNA is a very large and complex macromolecule (the largest human chromosome is approximately 220 million base pairs long). Initial studies have focused on shorter oligomers containing only one type of complementary base pair (Adenine-Thymine or Guanine-Cytosine) or even on single dimers in the gas phase or in solution. Often, further simplification is achieved by replacing the nucleic acid base pairs by model systems. An example of this is 2-pyridone/2-hydroxypyridine in dichloromethane, which forms cyclic dimers that serve as a model system for coupled intermolecular hydrogen bonds, with a structure resembling a DNA base pair. However, the isomerisation and association chemistry of 2-pyridone/2-hydroxypyridine involves a complex set of equilibria. These include monomers, solute-solvent complexes, and cyclic and open chainlike dimers, whose presence was confirmed using NMR and IR spectroscopy. By analysing the set of stationary infrared spectra recorded as a function of temperature and concentration using Noda's two-dimensional correlation spectroscopy supported by chemometric techniques, we were able to associate these perturbation induced spectral variations to the particular molecular species.

The OH/NH stretching vibrations in these dimers display a broad and very complex absorption band, caused by different coupling mechanisms. Of which are distinguishes notably Fermi resonances of the fundamental OH/NH stretching transition with combination- or overtones of other vibrational modes and anharmonic coupling between the OH/NH stretching modes and low-frequency hydrogen bond modes. Ultrafast infrared pump-probe experiment of 2-pyridone/2-hydroxypyridine in CD_2Cl_2 unambiguously confirmed that only a single dimer species dominates the IR absorption in the frequency range between 2400 and 3300 cm^{-1}. Comparing the observed low-frequency wavepacket motions of 99 and 150 cm^{-1} wavenumbers with literature values as well as our quantum chemical calculations we were able to conclude, that this single molecular species is cyclic 2-pyridone dimer, (PD)2. The observed coherent oscillations due to wavepacket motions along underdamped low-frequency coordinates of the dimers and its dephasing on a timescale of 750 fs suggest that such low-frequency motions might potentially be relevant for the dynamics and spatial geometry of base pairs in DNA molecule.

In contrast to the 2-pyridone/2-hyroxypyridine model system, the artificial 23-base pair DNA oligomer, which we then studied, has a well-defined double-helix structure, with adenine-thymine base pairs in Watson-Crick geometry. The high optical quality film was cast onto a 500 nm thick Si_3N_4 membrane, whose contribution to the measured pump-probe signal is negligible. Exact control of the water content in the DNA sample was achieved by placing the DNA oligomer sample into a specially designed humidity cell.

Transient vibrational spectra, both spectrally and polarization-resolved, allow us to assign the different NH stretching bands to the particular adenine-thymine base pairs vibrations and to discern them from the OH stretching contributions of the surrounding water.

At 0% relative humidity (r.h.), residual water molecules are expected to hydrate ionic phosphate groups located on the DNA backbone. The observed OH stretching frequency of about 3500 cm^{-1} and a constant anisotropy of 0.4 suggest that these water molecules maintain a rigid geometry to the phosphate groups.

At high humidity levels, the NH stretching transient absorption pattern remains unaffected, whereas changes in the OH stretching absorbance suggest the presence of two water species with distinct environments: one, which we associate with water strongly bound to the DNA backbone (similar to the low-humidity case, ~3500 cm^{-1}), and a second, which acts more like a bulk water. The second type of OH stretching excitation displays a relatively short lifetime of ~200 fs, a very broad absorption, and the formation of a vibrational hot ground state observed when probing (E_{pr} = 3500 cm^{-1}) well above the excitation frequency (E_{ex} = 3250 cm^{-1}). The 500 fs build-up of a long-lived transient absorption is very similar to the bulk water transient measured with the same pump/probe conditions. In addition, in the case of fully hydrated DNA, we observed a sub-picosecond spectral diffusion of the OH stretching vibration and ultrafast loss of vibrational anisotropy as a result of molecular rotations and/or energy transfer. In contrast, the NH stretching vibrations display negligible spectral diffusion at all measured humidity levels. The coupling strength between the symmetric NH_2 stretching of adenine and the NH stretching mode of thymine of approximately 15 cm^{-1} is derived from time-dependent anisotropy measurements.

The ionic phosphate groups in the DNA backbone are important sites of DNA hydration and their vibrations are sensitive probes of DNA-water interactions. The femtosecond dynamics of this mode has been investigated with ultrafast pump-probe spectroscopy. The measured 340 fs lifetime of the $\nu_{as}(PO_2)^-$ $\upsilon = 1$ state is independent of the sample hydration level, which indicates that its relaxation pathway includes low-frequency phosphate vibrations rather than water modes. Cooling these low-frequency modes by redistributing the excess energy to other DNA vibrations and to the water shell is mapped by the slower, thermal component of the pump-probe signal. The experimental results clearly show, that the water shell around the phosphates serves as a primary heat sink accepting vibrational excess energy from DNA on a femtosecond time scale. In contrast, energy transfer within DNA occurs in the 20 ps time domain.

The structural dynamics of hydration shells induced by the dissipation of excess energy from vibrational or electronic DNA excitations are key processes for the stability of the DNA structure. To understand the interaction between the phosphate groups and their water shells in more detail, we performed a series of experiments in which the water shell at 92% r.h. was excited through the OH stretching band and the response of the $\nu_{as}(PO_2)^-$ vibration monitored in a spectrally and temporally resolved way. The hydrogen bond pattern of a heated hydration shell undergoes subpicosecond rearrangements, reducing the average number of phosphate-water hydrogen bonds. In other words, the coupling between the DNA and water modes is reduced in the heated sample. Consequently, the energy flow from the hot water shell into DNA may be very inefficient. On the contrary, water molecules in the phosphate hydration shell couple strongly to the water in its surrounding. The very long lifetime of the hot water ground state substantially exceeds the 20 ps time interval over which the intra-DNA energy transport occurs.

Vibrational coherence experiments such as vibrational photon echo examine the time evolution of the phase relationship among vibrations. Future work will aim at measuring two-dimensional infrared spectra of DNA (or smaller model systems), including two-colour studies, to elucidate couplings between the relevant modes which absorb at different frequencies (e.g., between OH and $(PO_2)^-$stretching oscillators). In combination with theoretical calculations, this will allow for a more detailed and quantitative understanding of vibrational couplings and energy-transfer processes.

Bibliography

[1] Gilli, Gastone, Gilli, P. (2009): The Nature of the Hydrogen Bond, IUCr Monographs on Crystallography 23, Oxford University Press.

[2] Steiner, Thomas (2002): The Hydrogen Bond in the Solid State, Angew. Chem. Int. Ed. 41 [1], pp. 48-76.

[3] Pauling, L. (1928): The shared-electron chemical bond, Proceedings of the National Academy of Sciences of the United States of America 14, p. 359.

[4] Jeffrey, G. A. (1997): Introduction to hydrogen bonding, Oxford University Press, Oxford.

[5] Grabowski, S. (2006): Hydrogen Bonding - New Insights, Leszczynski, J., Challenges and Advances in Computational Chemistry and Physics 3 pp. v-vi, Springer, Dordrecht.

[6] Desiraju, G. R. and Steiner, T. (1999): The Weak Hydrogen Bond in Structural Chemistry and Biology Press, Oxford University, Ed, Oxford.

[7] Scheiner, Steve (1997): Hydrogen bonding: A theoretical perspective, Oxford University Press, Oxford.

[8] Pigoń, Krzysztof and Ruziewicz, Zdzisław (2005): Chemia fizyczna 2, 5. ed., PWN, Warszawa.

[9] Antonchenko, V. Ya; Davydov, A. S. and Zolotariuk, A. V. (1983): Solitons and proton motion in ice-like structures, physica status solidi (b) 115 [2], pp. 631-640.

[10] Pang, X. F. (2006): The conductivity properties of protons in ice and mechanism of magnetization of liquid water, The European Physical Journal B 49, pp. 5-23.

[11] Yakovchuk, Peter; Protozanova, Ekaterina and Frank-Kamenetskii, Maxim D. (2006): Base-stacking and base-pairing contributions into thermal stability of the DNA double helix, Nucleic Acids Research 34 [2], pp. 564-574.

[12] Hadži, D. and Bratos, S. (1976): Vibrational spectroscopy of the hydrogen bond, Schuster, P.; Zundel, G. and Sandorfy, C., The hydrogen bond: Recent developments in theory and experiments II. Structure and Spectroscopy pp. 565-611, North Holland, Amsterdam, the Netherlands.

[13] Bratos, S.; Leicknam, J.-Cl.; Gallot, G. and Ratajczak, H. (2002): Infra-red spectra of hydrogen bonded systems: Theory and experiment, Elsaesser, T. and Bakker, H. J., Ultrafast hydrogen bonding dynamics and proton transfer processes in the condensed phase 23 pp. 5-30, Kluwer Academic Publishers, Dordrecht.

[14] Nibbering, E. T. J. and Elsaesser, T. (2004): Ultrafast vibrational dynamics of hydrogen bonds in the condensed phase, Chemical Reviews 104 [4], pp. 1887 -1914.

[15] Nielsen, Harald H. (1951): The Vibration-Rotation Energies of Molecules, Reviews of Modern Physics 23 [2], p. 90.

[16] Herzberg, G. (1945): Molecular spectra and molecular structure. II.Infrared and Raman spectra of polyatomic molecules, D. Van Nostrand Co. Inc, New York.

[17] (1995): Infrared and Raman spectroscopy. Methods and applications., Schrader, Bernhard, Ed, VCH.

[18] Ferraro, John R.; Nakamoto, Kazuo and Brown, Chris W. (2003): Introductory Raman Spectroscopy, 2. ed., Elsevier.

[19] Heyne, K.; Huse, N.; Nibbering, E. T. J. and Elsaesser, T. (2003): Ultrafast relaxation and anharmonic coupling of O-H stretching and bending excitations in cyclic acetic acid dimers, Chemical Physics Letters 382 [1-2], pp. 19-25.

[20] Elsaesser, T.; Huse, N.; Dreyer, J.; Dwyer, J. R.; Heyne, K. and Nibbering, E. T. J. (2007): Ultrafast vibrational dynamics and anharmonic couplings of hydrogen-bonded dimers in solution, Chemical Physics 341 [1-3], pp. 175-188.

[21] Szyc, Łukasz; Guo, Jing; Yang, Ming; Dreyer, Jens; Tolstoy, Peter M.; Nibbering, Erik T. J.; Czarnik-Matusewicz, Bogusława; Elsaesser, Thomas and Limbach, Hans-Heinrich (2010): The Hydrogen-Bonded 2-Pyridone Dimer Model System. 1. Combined NMR and FT-IR Spectroscopy Study, The Journal of Physical Chemistry A 114 [29], pp. 7749-7760.

[22] Yang, Ming; Szyc, Łukasz; Dreyer, Jens; Nibbering, Erik T. J. and Elsaesser, Thomas (2010): The Hydrogen-Bonded 2-Pyridone Dimer Model System. 2. Femtosecond Mid-Infrared Pump-Probe Study., Journal of Physcial Chemistry A 114 [46], pp. 12195–12201.

[23] Stepanov, B. I. (1946): Interpretation of the regularities in the spectra of molecules forming the intermolecular hydrogen bond by the predissociation effect, Nature 157 [3998], p. 808.

[24] Marechal, Y. and Witkowski, A. (1968): Infrared spectra of H-bonded systems, Journal of Chemical Physics 48 [8], pp. 3697-3705.

[25] Maréchal, Y. (1987): IR spectra of carboxylic acids in the gas phase: A quantitative reinvestigation, Journal of Chemical Physics 87 [11], pp. 6344-6353.

[26] Henri-Rousseau, O.; Blaise, P. and Chamma, D. (2002): Infrared lineshapes of weak hydrogen bonds: Recent quantum developments, Advances in Chemical Physics 121, pp. 241-309.

[27] Nibbering, Erik T. J.; Dreyer, Jens; Kühn, Oliver; Bredenbeck, Jens; Hamm, Peter and Elsaesser, Thomas (2007): Vibrational dynamics of hydrogen bonds, Analysis and Control of Ultrafast Photoinduced Reactions 87 pp. 619-687, Springer Berlin Heidelberg.

[28] Elsaesser, Thomas (2009): Ultrafast memory loss and relaxation processes in hydrogen-bonded systems., Biol. Chem. 390, pp. 1125-1132.

[29] Fayer, M. D. (2001): Ultrafast infrared and Raman spectroscopy [Practical Spectroscopy Series Vol. 26], Fayer, M. D., Ed, Practical Spectroscopy Series Vol. 26, Marcel Dekker, Inc., New York.

[30] Gordon, R. G. (1968): Correlation functions for molecular motion, Advances in Magnetic Resonance 3, pp. 1-42.

[31] Novak, A. (1974): Hydrogen bonding in solids. Correlation of spectroscopic and crystallographic data, Structure and Bonding (Berlin) 18, pp. 177-216.

[32] Pimentel, George C. and McClellan, Aubrey L. (1960): The hydrogen bond, Pauling, Linus, Ed, W. H. Freeman and Co., San Francisco.

[33] Stenger, J.; Madsen, D.; Dreyer, J.; Nibbering, E. T. J.; Hamm, P. and Elsaesser, T. (2001): Coherent response of hydrogen bonds in liquids probed by ultrafast vibrational spectroscopy, Journal of Physical Chemistry A 105 [13], pp. 2929-2932.

[34] Madsen, D.; Stenger, J.; Dreyer, J.; Nibbering, E. T. J.; Hamm, P. and Elsaesser, T. (2001): Coherent vibrational ground state dynamics of an intramolecular hydrogen bond., Chemical Physics Letters 341 [1-2], pp. 56-62.

[35] Lim, M. and Hochstrasser, R. M. (2001): Unusual vibrational dynamics of the acetic acid dimer, Journal of Chemical Physics 115 [16], pp. 7629-7643.

[36] Gale, G. M.; Gallot, G.; Hache, F.; Lascoux, N.; Bratos, S. and Leicknam, J. Cl (1999): Femtosecond dynamics of hydrogen bonds in liquid water: a real time study, Physical Review Letters 82 [5], pp. 1068-1071.

[37] Woutersen, S. and Bakker, H. J. (1999): Hydrogen bond in liquid water as a Brownian oscillator, Physical Review Letters 83 [10], pp. 2077-2080.

[38] Rey, R.; Møller, K. B. and Hynes, J. T. (2002): Hydrogen bond dynamics in water and ultrafast infrared spectroscopy, Journal of Physical Chemistry A 106 [50], pp. 11993-11996.

[39] Stenger, J.; Madsen, D.; Hamm, P.; Nibbering, E. T. J. and Elsaesser, T. (2002): A photon echo peak shift study of liquid water, Journal of Physical Chemistry A 106 [10], pp. 2341-2350.

[40] Piryatinski, A.; Lawrence, C. P. and Skinner, J. L. (2003): Vibrational spectroscopy of HOD in liquid D2O. V. Infrared three-pulse photon echoes, Journal of Chemical Physics 118 [21], pp. 9672-9679.

[41] Cowan, M. L.; Bruner, B. D.; Huse, N.; Dwyer, J. R.; Chugh, B.; Nibbering, E. T. J.; Elsaesser, T. and Miller, R. J. D. (2005): Ultrafast memory loss and energy redistribution in the hydrogen bond network of liquid H2O, Nature 434 [7030], pp. 199-202.

[42] Oxtoby, D. W. (1979): Dephasing of molecular vibrations in liquids, Advances in Chemical Physics 40, pp. 1-48.

[43] Kraemer, D.; Cowan, M. L.; Paarmann, A.; Huse, N.; Nibbering, E. T. J.; Elsaesser, T. and Miller, R. J. Dwayne (2008): Temperature dependence of the two-dimensional infrared spectrum of liquid H2O, Proceedings of the National Academy of Sciences 105 [2], pp. 437-442.

[44] Noda, I. (1993): Generalized 2-Dimensional Correlation Method Applicable to Infrared, Raman, and Other Types of Spectroscopy, Applied Spectroscopy 47 [9], pp. 1329-1336.

[45] Noda, Isao and Ozaki, Yukihiro (2004): Two-Dimensional Correlation Spectroscopy, John Wiley & Sons, Chicester.

[46] Noda, Isao; Liu, Yongliang; Ozaki, Yukihiro and Czarnecki, Miroslaw A. (1995): Two-Dimensional Fourier Transform Near-Infrared Correlation Spectroscopy Studies of Temperature-Dependent Spectral Variations of Oleyl Alcohol, The Journal of Physical Chemistry 99 [10], pp. 3068-3073.

[47] Ozaki, Yukihiro; Liu, Yongliang and Noda, Isao (1997): Two-Dimensional Infrared and Near-Infrared Correlation Spectroscopy: Applications to Studies of Temperature-Dependent Spectral Variations of Self-Associated Molecules, Appl. Spectrosc. 51 [4], pp. 526-535.

[48] Czarnecki, Miroslaw A.; Maeda, Hisashi; Ozaki, Yukihiro; Suzuki, Masao and Iwahashi, Makio (1998): Resolution Enhancement and Band Assignments for the First Overtone of OH Stretching Modes of Butanols by Two-Dimensional Near-Infrared Correlation Spectroscopy. 2. Thermal Dynamics of Hydrogen Bonding in n- and tert-

Butyl Alcohol in the Pure Liquid States, The Journal of Physical Chemistry A 102 [46], pp. 9117-9123.

[49] Sasic, Slobodan; Muszynski, Andrzej and Ozaki, Yukihiro (2000): A New Possibility of the Generalized Two-Dimensional Correlation Spectroscopy. 2. Sample-Sample and Wavenumber-Wavenumber Correlations of Temperature-Dependent Near-Infrared Spectra of Oleic Acid in the Pure Liquid State, The Journal of Physical Chemistry A 104 [27], pp. 6388-6394.

[50] Czarnecki, Mirosław A. and Wojtków, Dagmara (2004): Two-Dimensional FT-NIR Correlation Study of Hydrogen Bonding in the Butan-1-ol/ Water System, The Journal of Physical Chemistry A 108 [13], pp. 2411-2417.

[51] Wojtków, Dagmara and Czarnecki, Mirosław A. (2006): Effect of Temperature and Concentration on the Structure of sec-Butyl Alcohol and Isobutyl Alcohol/Water Mixtures: Near-Infrared Spectroscopic Study, The Journal of Physical Chemistry A 110 [36], pp. 10552-10557.

[52] Noda, Isao; Liu, Yongliang and Ozaki, Yukihiro (1996): Two-Dimensional Correlation Spectroscopy Study of Temperature-Dependent Spectral Variations of N-Methylacetamide in the Pure Liquid State. 2. Two-Dimensional Raman and Infrared-Raman Heterospectral Analysis, The Journal of Physical Chemistry 100 [21], pp. 8674-8680.

[53] Czarnecki, Mirosław A. and Haufa, Krzysztof Z. (2005): Effect of Temperature and Concentration on the Structure of N-Methylacetamide-Water Complexes: Near-Infrared Spectroscopic Study, The Journal of Physical Chemistry A 109 [6], pp. 1015-1021.

[54] Fabian, Heinz; Mantsch, Henry H. and Schultz, Christian P. (1999): Two-dimensional IR correlation spectroscopy: Sequential events in the unfolding process of the λ Cro-V55C repressor protein, Proceedings of the National Academy of Sciences of the United States of America 96 [23], pp. 13153-13158.

[55] Ismoyo, Fenny; Wang, Yan and Ismail, Ashraf A. (2000): Examination of the Effect of Heating on the Secondary Structure of Avidin and Avidin-Biotin Complex by Resolution-Enhanced Two-Dimensional Infrared Correlation Spectroscopy, Appl. Spectrosc. 54 [7], pp. 939-947.

[56] Tian, Ge; Wu, Qiong; Sun, Suqin; Noda, Isao and Chen, Guo-Qiang (2001): Study of Thermal Melting Behavior of Microbial Polyhydroxyalkanoate Using Two-Dimensional Fourier Transform Infrared Correlation Spectroscopy, Appl. Spectrosc. 55 [7], pp. 888-893.

[57] Ozaki, Yukihiro; Liu, Yongliang and Noda, Isao (1997): Two-Dimensional Near-Infrared Correlation Spectroscopy Study of Premelting Behavior of Nylon 12, Macromolecules 30 [8], pp. 2391-2399.

[58] Zhang, Jianming; Sato, Harumi; Noda, Isao and Ozaki, Yukihiro (2005): Conformation Rearrangement and Molecular Dynamics of Poly(3-hydroxybutyrate) during the Melt-Crystallization Process Investigated by Infrared and Two-Dimensional Infrared Correlation Spectroscopy, Macromolecules 38 [10], pp. 4274-4281.

[59] Marcott, Curtis; Noda, Isao and Dowrey, Anthony E. (1991): Enhancing the information content of vibrational spectra through sample perturbation, Analytica Chimica Acta 250, pp. 131-143.

[60] Murayama, Koichi; Wu, Yuqing; Czarnik-Matusewicz, BogusĹ‚awa and Ozaki, Yukihiro (2001): Two-Dimensional/Attenuated Total Reflection Infrared Correlation Spectroscopy Studies on Secondary Structural Changes in Human Serum Albumin in Aqueous Solutions: pH-Dependent Structural Changes in the Secondary Structures and in the Hydrogen Bondings of Side Chains, The Journal of Physical Chemistry B 105 [20], pp. 4763-4769.

[61] Noda, Isao; Story, Gloria M. and Marcott, Curtis (1999): Pressure-induced transitions of polyethylene studied by two-dimensional infrared correlation spectroscopy, Vibrational Spectroscopy 19 [2], pp. 461-465.

[62] Nagasaki, Yoshihisa; Yoshihara, Toshiaki and Ozaki, Yukihiro (2000): Polarized Infrared Spectroscopic Study on Hindered Rotation around the Molecular Axis in the Smectic-C* Phase of a Ferroelectric Liquid Crystal with a Naphthalene Ring. Application of Two-Dimensional Correlation Spectroscopy to Polarization Angle-Dependent Spectral Variations, The Journal of Physical Chemistry B 104 [13], pp. 2846-2852.

[63] Dzwolak, Wojciech; Kato, Minoru; Shimizu, Akio and Taniguchi, Yoshihiro (2000): Comparative Two-Dimensional Fourier Transform Infrared Correlation Spectroscopic Study on the Spontaneous, Pressure-, and Temperature-Enhanced H/D Exchange in α-Lactalbumin, Appl. Spectrosc. 54 [7], pp. 963-967.

[64] Nabet, Anne and Pezolet, Michel (1997): Two-Dimensional FT-IR Spectroscopy: A Powerful Method to Study the Secondary Structure of Proteins Using H-D Exchange, Appl. Spectrosc. 51 [4], pp. 466-469.

[65] Wu, Yuqing; Murayama, Koichi and Ozaki, Yukihiro (2001): Two-Dimensional Infrared Spectroscopy and Principle Component Analysis Studies of the Secondary Structure and Kinetics of Hydrogen-Deuterium Exchange of Human Serum Albumin, The Journal of Physical Chemistry B 105 [26], pp. 6251-6259.

[66] Czarnecki, M. A.; Jordanov, B.; Okretic, S. and Siesler, H. W. (1997): Two-dimensional correlation analysis of time-resolved step-scan FT-IR spectra of a liquid crystalline guest-host system in an electric field, Applied Spectroscopy 51 [11], pp. 1698-1702.

[67] Czarnecki, M. A.; Okretic, S. and Siesler, H. W. (1997): Reorientation of nematic liquid-crystals and liquid-crystalline polymers in an electric field studied by FT-IR time-resolved spectroscopy and 2D-correlation analysis, Journal of Physical Chemistry B 101 [3], pp. 374-380.

[68] Noda, I. (2000): Determination of Two-Dimensional Correlation Spectra Using the Hilbert Transform, Appl. Spectrosc. 54 [7], pp. 994-999.

[69] Noda, I.; Dowrey, A. E.; Marcoli, C.; Story, G. M. and Ozaki, Y. (2000): Generalized Two-Dimensional Correlation Spectroscopy, Appl. Spectrosc. 54 [7], pp. 236A-248A.

[70] Noda, Isao (2008): Scaling techniques to enhance two-dimensional correlation spectra, Journal of Molecular Structure 883-884, pp. 216-227.

[71] Morita, Shin-Ichi; Ozaki, Yukihiro and Noda, Isao (2001): Global Phase Angle Description of Generalized Two-Dimensional Correlation Spectroscopy: 1. Theory and its Simulation for Practical Use, Appl. Spectrosc. 55 [12], pp. 1618-1621.

[72] Parson, William W. (2009): Modern Optical Spectroscopy: With Exercises and Examples from Biophysics and Biochemistry (Student Edition), Springer.

[73] Abramczyk, Halina (2005): Introduction to Laser Spectroscopy, Elsevier, Amsterdam.

[74] Vauthey, Eric (2010): Introduction to nonlinear optical spectroscopic techniques investigating ultrafast processes, Lectures of Virtual European University on Lasers, Marie Curie Chair Virtual University on Laser Science: Lectures, 2010-08-06

[75] Hamm, Peter (2005): Principles of Nonlinear Optical Spectroscopy: A Practical Approach, Lectures of Virtual European University on Lasers, Marie Curie Chair Virtual University on Laser Science: Lectures, 2010-08-06

[76] Mukamel, Shaul (1995): Principles of nonlinear optical spectroscopy 6, Lapp, Marshall; Nishizawa, Jun-Ichi; Snavely, Benjamin B.; Stark, Henry; Tam, Andrew C. and Wilson, Tony, Eds, Oxford Series in Optical and Imaging Sciences, Oxford University Press, Oxford, ISBN: 0-19-509278-3.

[77] Fleming, G. Nonlinear Optical Methods to Study Condensed Phase Chemical and Biological Dynamics Lectures of Virtual European University on Lasers, Marie Curie Chair Virtual University on Laser Science: Lectures, 2010-08-06

[78] Huang, Kerson (1987): Statistical Mechanics, Second Edition. ed., Wiley.

[79] Fleming, Graham R. (1986): Chemical Applications of Ultrafast Spectrosopy 13, The International series of monographs on chemistry., Oxford University Press, New York.

[80] Nibbering, Erik T.J. (1993): Femtosecond Optical Dynamics in Liquids Rijksuniversiteit Groningen.

[81] Oxtoby, D W (1981): Vibrational Relaxation in Liquids, Annual Review of Physical Chemistry 32 [1], pp. 77-101.

[82] Schweizer, Kenneth S. and Chandler, David (1982): Vibrational dephasing and frequency shifts of polyatomic molecules in solution, The Journal of Chemical Physics 76 [5], pp. 2296-2314.

[83] Kubo, R. (1962): A Stochastic Theory of Line-Shape and Relaxation, Haar, D. ter, Fluctuation, Relaxation and Resonance in Magnetic Systems pp. 23-68, Oliver and Boyd, Edinburgh.

[84] Bloch, F. (1946): Nuclear induction, Phys. Rev. 70.

[85] Homoelle, Bradley J.; Edington, Maurice D.; Diffey, William M. and Beck, Warren F. (1998): Stimulated Photon-Echo and Transient-Grating Studies of Protein-Matrix Solvation Dynamics and Interexciton-State Radiationless Decay in Î± Phycocyanin and Allophycocyanin, The Journal of Physical Chemistry B 102 [16], pp. 3044-3052.

[86] Jimenez, Ralph; van Mourik, Frank; Yu, Jae Young and Fleming, Graham R. (1997): Three-Pulse Photon Echo Measurements on LH1 and LH2 Complexes of Rhodobacter sphaeroides: A Nonlinear Spectroscopic Probe of Energy Transfer, The Journal of Physical Chemistry B 101 [37], pp. 7350-7359.

[87] Groot, Marie-Louise; Yu, Jae-Young; Agarwal, Ritesh; Norris, James R. and Fleming, Graham R. (1998): Three-Pulse Photon Echo Measurements on the Accessory Pigments in the Reaction Center of Rhodobacter sphaeroides, The Journal of Physical Chemistry B 102 [30], pp. 5923-5931.

[88] Thorn Leeson, Daan; Wiersma, Douwe A.; Fritsch, Klaus and Friedrich, Josef (1997): The Energy Landscape of Myoglobin: An Optical Study, The Journal of Physical Chemistry B 101 [33], pp. 6331-6340.

[89] Johnson, J. B.; Lamb, D. C.; Frauenfelder, H.; Müller, J. D.; McMahon, B.; Nienhaus, G. U. and Young, R. D. (1996): Ligand binding to heme proteins. VI. Interconversion

of taxonomic substates in carbonmonoxymyoglobin, Biophysical journal 71 [3], pp. 1563-1573.

[90] Hamm, P. and Hochstrasser, R. M. (2001): Structure and dynamics of proteins and peptides: Femtosecond two-dimensional infrared spectroscopy, Fayer, M. D., Ultrafast infrared and Raman spectroscopy [Practical Spectroscopy Series Vol. 26] pp. 273-347, Marcel Dekker, Inc., New York.

[91] Ashihara, Satoshi; Huse, Nils; Espagne, Agathe; Nibbering, Erik T. J. and Elsaesser, Thomas (2007): Ultrafast Structural Dynamics of Water Induced by Dissipation of Vibrational Energy, The Journal of Physical Chemistry A 111 [5], pp. 743-746.

[92] Heyne, K., Nils Huse, Erik T J Nibbering and Thomas Elsaesser (2003): Coherent vibrational dynamics of intermolecular hydrogen bonds in acetic acid dimers studied by ultrafast mid-infrared spectroscopy, J. Phys.: Condens. Matter 15, pp. 129-136.

[93] Huse, N.; Bruner, B. D.; Cowan, M. L.; Dreyer, J.; Nibbering, E. T. J.; Miller, R. J. D. and Elsaesser, T. (2005): Anharmonic Couplings Underlying the Ultrafast Vibrational Dynamics of Hydrogen Bonds in Liquids, Physical Review Letters 95 [14], p. 147402.

[94] Yang, Ming; Szyc, Łukasz; Röttger, Katharina; Fidder, Henk; Nibbering, Erik T. J.; Elsaesser, Thomas and Temps, Friedrich (2011): Dynamics and Couplings of N-H Stretching Excitations of Guanosine-Cytidine Base Pairs in Solution, The Journal of Physical Chemistry B, pp. 5484-5492.

[95] Yang, Ming; Szyc, Łukasz and Elsaesser, Thomas (2011): Femtosecond Two-Dimensional Infrared Spectroscopy of Adenine-Thymine Base Pairs in DNA Oligomers, The Journal of Physical Chemistry B 115 [5], pp. 1262-1267.

[96] Bratos, S. (1975): Profiles of hydrogen stretching ir bands of molecules with hydrogen bonds: A stochastic theory. I. Weak and medium strength hydrogen bonds, Journal of Chemical Physics 63 [8], pp. 3499-3509.

[97] Witkowski, Andrzej and Wójcik, Marek (1973): Infrared spectra of hydrogen bond a general theoretical model, Chemical Physics 1 [1], pp. 9-16.

[98] Marechal, Y (1973): Hydrogen dynamics in the hydrogen bonds of acetic acid dimers, Journal of Physics B: Atomic and Molecular Physics 6 [7], p. L188.

[99] Robertson, G. N. and Yarwood, J. (1978): Vibrational relaxation of hydrogen-bonded species in solution. I. Theory, Chemical Physics 32 [2], pp. 267-282.

[100] Yarwood, J.; Ackroyd, R. and Robertson, G. N. (1978): Vibrational relaxation of hydrogen-bonded species in solution. II. Analysis of nu s(XH) absorption bands, Chemical Physics 32 [2], pp. 283-299.

[101] Chamma, D. and Henri-Rousseau, O. (1999): IR theory of weak H-bonds: Davydov coupling, Fermi resonances and direct relaxations. I. Basis equations within the linear response theory, Chemical Physics 248 [1], pp. 53-70.

[102] Chamma, D. and Henri-Rousseau, O. (1999): IR theory of weak H-bonds: Davydov coupling, Fermi resonances and direct relaxations. II. General trends, from numerical experiments, Chemical Physics 248 [1], pp. 71-89.

[103] Hamm, P. (1995): Coherent effects in femtosecond infrared spectroscopy, Chemical Physics 200 [3], pp. 415-429.

[104] Woutersen, S.; Emmerichs, U. and Bakker, H. J. (1997): Femtosecond mid-IR pump-probe spectroscopy of liquid water: Evidence for a two-component structure, Science 278 [5338], pp. 658-660.

[105] Woutersen, S. and Bakker, H. J. (1999): Resonant intermolecular transfer of vibrational energy in liquid water, Nature 402 [6761], pp. 507-509.

[106] Faist, Jerome; Capasso, Federico; Sivco, Deborah L.; Sirtori, Carlo; Hutchinson, Albert L. and Cho, Alfred Y. (1994): Quantum Cascade Laser, Science 264 [5158], pp. 553-556.

[107] Paschotta, Rüdiger (2008): Encyclopedia of Laser Physics and Technology, Wiley-VCH, Berlin.

[108] Mirov, S.; Fedorov, V.; Moskalev, I.; Martyshkin, D. and Kim, C. (2010): Progress in Cr2+ and Fe2+ doped mid-IR laser materials, Laser & Photonics Reviews 4 [1], pp. 21-41.

[109] Elsaesser, Thomas and Nuss, Martin C. (1991): Femtosecond pulses in the mid-infrared generated by downconversion of a traveling-wave dye laser, Opt. Lett. 16 [6], pp. 411-413.

[110] Strickland, D. and Mourou, G. (1985): Compression of amplified chirped optical pulses, Opics Communications 56, pp. 219-221.

[111] Di Trapani, P.; Andreoni, A.; Banfi, G. P.; Solcia, C.; Danielius, R.; Piskarskas, A.; Foggi, P.; Monguzzi, M. and Sozzi, C. (1995): Group-velocity self-matching of femtosecond pulses in noncollinear parametric generation, Physical Review A 51 [4], p. 3164.

[112] Wilhelm, T.; Piel, J. and Riedle, E. (1997): Sub-20-fs pulses tunable across the visible from a blue-pumped single-pass noncollinear parametric converter, Optics Letters 22 [19], pp. 1494-1946.

[113] Kaindl, R. A.; Wurm, M.; Reimann, K.; Hamm, P.; Weiner, A. M. and Woerner, M. (2000): Generation, shaping, and characterization of intense femtosecond pulses tunable from 3 to 20 mu m, Journal of the Optical Society of America B 17 [12], pp. 2086-94.

[114] Baum, Peter; Lochbrunner, Stefan and Riedle, Eberhard (2004): Tunable sub-10-fs ultraviolet pulses generated by achromatic frequencydoubling, Opt. Lett. 29 [14], pp. 1686-1688.

[115] Spence, D. E.; Kean, P. N. and Sibbett, W. (1991): 60-fsec pulse generation from a self-mode-locked Ti:sapphire laser, Opt. Lett. 16 [1], pp. 42-44.

[116] Proctor, Bob; Westwig, Erik and Wise, Frank (1993): Characterization of a Kerr-lens mode-locked Ti:sapphire laser with positive group-velocity dispersion, Opt. Lett. 18 [19], pp. 1654-1656.

[117] Dmitriev, V.G.; Gurzadyan, G.G. and Nikogosyan, D.N. (1997): Handbook of Nonlinear Optical Crystals, 2. ed., Springer-Verlag, Berlin & Heidelberg.

[118] Alfano, R. R. and Shapiro, S. L. (1970): Observation of Self-Phase Modulation and Small-Scale Filaments in Crystals and Glasses, Physical Review Letters 24 [11], p. 592.

[119] Brodeur, A. and Chin, S. L. (1999): Ultrafast white-light continuum generation and self-focusing in transparent condensed media, J. Opt. Soc. Am. B 16 [4], pp. 637-650.

[120] Laenen, R.; Simeonidis, K. and Laubereau, A. (1998): Parametric generation of synchronized, independently tunable subpicosecond pulses in the midinfrared with adjustable pulse duration, J. Opt. Soc. Am. B 15 [3], pp. 1213-1217.

[121] Müller, Andreas; Talbot, Francis and Leutwyler, Samuel (2002): Hydrogen Bond Vibrations of 2-Aminopyridine;2-Pyridone, a Watson-Crick Analogue of Adenine-Uracil, Journal of the American Chemical Society 124 [48], pp. 14486-14494.

[122] Roscioli, Joseph R. and Pratt, David W. (2003): Base pair analogs in the gas phase, Proceedings of the National Academy of Sciences of the United States of America 100 [24], pp. 13752-13754.

[123] Beak, Peter and Fry Jr., Fred S. (1973): Equilibrium between 2-hydroxypyridine and 2-pyridone in the gas phase, Journal of the American Chemical Society 95 [5], pp. 1700-1702.

[124] Beak, Peter; Fry Jr., Fred S.; Lee, Jaekeun and Steele, Frank (1976): Equilibration studies. Protomeric equilibria of 2- and 4-hydroxypyridines, 2- and 4-hydroxypyrimidines, 2- and 4-mercaptopyridines, and structurally related compounds in the gas phase, Journal of the American Chemical Society 98 [1], pp. 171-179.

[125] Brown, R. S.; Tse, A. and Vederas, J. C. (1980): Photoelectron-determined core binding energies and predicted gas-phase basicities for the 2-hydroxypyridine .dblarw. 2-pyridone system, Journal of the American Chemical Society 102 [3], pp. 1174-1176.

[126] Nimlos, M. R.; Kelley, D. F. and Bernstein, E. R. (1989): Spectroscopy, structure, and proton dynamics of 2-hydroxypyridine and its clusters with water and ammonia, Journal of Physical Chemistry 93 [2], pp. 643-651.

[127] Matsuda, Yoshiyuki; Ebata, Takayuki and Mikami, Naohiko (1999): Vibrational spectroscopy of 2-pyridone and its clusters in supersonic jets: Structures of the clusters as revealed by characteristic shifts of the NH and C=O bands, Journal of Chemical Physics 110 [17], pp. 8397-8407.

[128] Matsuda, Yoshiyuki; Ebata, Takayuki and Mikami, Naohiko (2000): Population labeling spectroscopy for the electronic and the vibrational transitions of 2-pyridone and its hydrogen-bonded clusters, Journal of Chemical Physics 113 [2], pp. 573-580.

[129] Florio, Gina M.; Gruenloh, Christopher J.; Quimpo, Robert C. and Zwier, Timothy S. (2000): The infrared spectroscopy of hydrogen-bonded bridges: 2-pyridone-(water)$_n$ and 2-hydroxypyridine-(water)$_n$ clusters, n = 1,2, Journal of Chemical Physics 113 [24], pp. 11143-11153.

[130] Sakota, Kenji; Tokuhara, Shihomi and Sekiya, Hiroshi (2007): Dispersed fluorescence spectroscopy of 2-hydroxypyridine and its cyclically hydrogen-bonded water clusters in the gas phase: An examination of occurrence of excited-state proton transfer, Chemical Physics Letters 448 [4-6], pp. 159-163.

[131] Hazra, M.K. and Chakraborty, T. (2008): Impact of Methyl Rotor in the Excited State Level Mixing of Doubly Hydrogen-Bonded Complexes of 2-Pyridone, Journal of Physical Chemistry A 112 [6], pp. 1100-1104.

[132] Hazra, Montu K.; Samanta, Amit K. and Chakraborty, Tapas (2006): Hydrogen-bond vibrations in the S_1 <-> S_0 spectra of a nucleobase pair analog: A mixed dimer between 2-pyridone and formamide, Journal of Chemical Physics 125 [21], p. 214302.

[133] Penfold, B. R. (1953): The electron distribution in crystalline α-pyridone, Acta Crystallographica 6 [7], pp. 591-600.

[134] Yang, H. W. and Craven, B. M. (1998): Charge Density Study of 2-Pyridone, Acta Crystallographica B 54 [6], pp. 912-920.

[135] Arman, H. D.; Poplaukhin, P. and Tiekink, E. R. T. (2009): 2-Pyridone: monoclinic polymorph, Acta Crystallogr., Sect. E 65, p. o3187.

[136] Müller, Andreas; Talbot, Francis and Leutwyler, Samuel (2000): Intermolecular vibrations of jet-cooled (2-pyridone)$_2$: A model for the uracil dimer, Journal of Chemical Physics 112 [8], pp. 3717-3725.

[137] Müller, Andreas; Talbot, Francis and Leutwyler, Samuel (2001): Intermolecular vibrations of the jet-cooled 2-pyridone · 2-hydroxypyridine mixed dimer, a model for tautomeric nucleic acid base pairs, Journal of Chemical Physics 115 [11], pp. 5192-5202.

[138] Müller, Andreas; Talbot, Francis and Leutwyler, Samuel (2002): S_1/S_2 exciton splitting in the (2-pyridone)$_2$ dimer, Journal of Chemical Physics 116 [7], pp. 2836-2847.

[139] Frey, Jann A.; Leist, Roman; Tanner, Christian; Frey, Hans-Martin and Leutwyler, Samuel (2006): 2-pyridone: The role of out-of-plane vibrations on the S_1 <-> S_0 spectra and S_1 state reactivity, Journal of Chemical Physics 125 [11], p. 114308.

[140] Hammes, Gordon G. and Spivey, H. Olin (1966): A Kinetic Study of the Hydrogen-Bond Dimerization of 2-Pyridone, Journal of the American Chemical Society 88 [8], pp. 1621-1625.

[141] Hammes, Gordon G. and Lillford, P. J. (1970): Kinetic and equilibrium study of the hydrogen bond dimerization of 2-pyridone in hydrogen bonding solvents, Journal of the American Chemical Society 92 [26], pp. 7578-7585.

[142] Beak, Peter (1977): Energies and alkylations of tautomeric heterocyclic compounds: old problems - new answers, Accounts of Chemical Research 10 [5], pp. 186-192.

[143] Bensaude, O.; Chevrier, M. and Dubois, J. E. (1978): Lactim-lactam tautomeric equilibriums of 2-hydroxypyridines. 1. Cation binding, dimerization, and interconversion mechanism in aprotic solvents. A spectroscopic and temperature-jump kinetic study, Journal of the American Chemical Society 100 [22], pp. 7055-7060.

[144] Rawson, Jeremy M. and Winpenny, Richard E. P. (1995): The coordination chemistry of 2-pyridone and its derivatives, Coordination Chemistry Reviews 139, pp. 313-374.

[145] Chou, Pi-Tai; Wei, Ching-Yen and Hung, Fa-Tsai (1997): Conjugated Dual Hydrogen Bonds Mediating 2-Pyridone/2-Hydroxypyridine Tautomerism, Journal of Physical Chemistry B 101 [44], pp. 9119-9126.

[146] Frank, J. and Katritzky, A.R. (1976): Tautomeric pyridines. 15. Pyridone-hydroxypyridine equilibria in solvents of differing polarity, Journal of the Chemical Society - Perkin Transactions 2 [12], pp. 1428-1431.

[147] Bensaude, Olivier; Chevrier, Marianne and Dubois, Jacques-Emile (1978): Influence of hydration upon tautomeric equilibria, Tetrahedron Letters 19 [25], pp. 2221-2224.

[148] Forlani, L.; Cristoni, G.; Boga, C.; Todesco, P. E.; Del Vecchio, E.; Selva, S. and Monari, M. (2002): Reinvestigation of tautomerism of some substituted 2-hydroxypyridines, ARKIVOC XI, pp. 198-215.

[149] Smets, J. and Maes, G. (1991): Matrix-isolation FT-IR study on the protomeric tautomerism 2-hydroxypyridine[right harpoon over left]2-pyridone, Chemical Physics Letters 187 [5], pp. 532-536.

[150] Nowak, Maciej J.; Lapinski, Leszek; Fulara, Jan; Les, Andrzej and Adamowicz, Ludwik (1992): Matrix isolation IR spectroscopy of tautomeric systems and its theoretical interpretation: 2-hydroxypyridine/2(1H)-pyridinone, The Journal of Physical Chemistry 96 [4], pp. 1562-1569.

[151] Dkhissi, A.; Houben, L.; Smets, J.; Adamowicz, L. and Maes, G. (1999): Density functional theory and ab-initio computational study of the 2-hydroxypyridine/2-pyridone system: a comparison with FT-IR data from matrix isolation experiments, Journal of Molecular Structure 484 [1-3], pp. 215-227.

[152] Abdulla, Hussain I. and El-Bermani, Muhsin F. (2001): Infrared studies of tautomerism in 2-hydroxypyridine 2-thiopyridine and 2-aminopyridine, Spectrochimica Acta Part A: Molecular Spectroscopy 57 [13], pp. 2659-2671.

[153] De Kowalewski, Dora G.; Contreras, Rub\'en H.; D\'iez, Ernesto and Esteban, Angel (2004): NMR J(C,C) scalar coupling analysis of the effects of substituents on the keto–enol tautomeric equilibrium in 2-OH-<i>n</i>-X-pyridines. An experimental and DFT study, Molecular Physics: An International Journal at the Interface Between Chemistry and Physics 102 [23], pp. 2607-2615.

[154] Moreno, Miquel and Miller, William H. (1990): On the tautomerization reaction 2-pyridone [right harpoon over left] 2-hydroxypyridine: an ab initio study, Chemical Physics Letters 171 [5-6], pp. 475-479.

[155] Wang, J. and Boyd, R.J. (1996): Tautomeric Equilibria of Hydroxypyridines in Different Solvents: An ab Initio Study, Journal of Physical Chemistry 100 [40], pp. 16141-16146.

[156] Alkorta, Ibon and Elguero, Jose (2002): Influence of Intermolecular Hydrogen Bonds on the Tautomerism of Pyridine Derivatives, The Journal of Organic Chemistry 67 [5], pp. 1515-1519.

[157] Wolfe, Saul; Weinberg, Noham and Hsieh, Yihhuang (2007): The constitution of 2-hydroxypyridine in aqueous solution, Theoretical Chemistry Accounts: Theory, Computation, and Modeling (Theoretica Chimica Acta) 118 [1], pp. 265-269.

[158] Beak, Peter; Covington, Johnny B. and Smith, Stanley G. (1976): Structural studies of tautomeric systems: the importance of association for 2-hydroxypyridine-2-pyridone and 2-mercaptopyridine-2-thiopyridone, Journal of the American Chemical Society 98 [25], pp. 8284-8286.

[159] Coburn, Robert A. and Dudek, Gerald O. (1968): Spectroscopic studies of isotopically substituted 2-pyridones, Journal of Physical Chemistry 72 [4], pp. 1177-1181.

[160] Borst, David R.; Roscioli, Joseph R.; Pratt, David W.; Florio, Gina M.; Zwier, Timothy S.; Müller, Andreas and Leutwyler, Samuel (2002): Hydrogen bonding and tunneling in the 2-pyridone·2-hydroxypyridine dimer. Effect of electronic excitation, Chemical Physics 283 [1-2], pp. 341-354.

[161] Meuwly, Markus; Müller, Andreas and Leutwyler, Samuel (2003): Energetics, dynamics and infrared spectra of the DNA base-pair analogue 2-pyridone · 2-hydroxypyridine, Physical Chemistry Chemical Physics 5 [12], pp. 2663-2672.

[162] Kwiatkowski, Józef S. and Leszczynski, Jerzy (1996): Molecular structure and vibrational IR spectra of the 2-hydroxypyridine/2(1H)-pyridinone system and its thio and seleno analogs: density functional theory versus conventional ab initio calculations, Journal of Molecular Structure 376 [1-3], pp. 325-342.

[163] Kwiatkowski, Józef S. and Leszczyniski, Jerzy (1994): Ab initio post-Hartree-Fock calculations of the 2-hydroxypyridine/2(1H)-pyridinone system: molecular structures, vibrational IR spectra and tautomeric stability, Journal of Molecular Structure: THEOCHEM 312 [2], pp. 201-213.

[164] Müller, Andreas; Losada, Martin and Leutwyler, Samuel (2004): Ab Initio Benchmark Study of (2-Pyridone)$_2$, a Strongly Bound Doubly Hydrogen-Bonded Dimer, Journal of Physical Chemistry A 108 [1], pp. 157-165.

[165] Motley, Tanieka L. and Korter, Timothy M. (2008): Terahertz spectroscopy and molecular modeling of 2-pyridone clusters, Chemical Physics Letters 464 [4-6], pp. 171-176.

[166] Wójcik, Marek J.; Tatara, Wiktor; Boczar, Marek; Apola, Anna and Ikeda, Susumu (2001): Spectroscopic and theoretical study of vibrational spectra of hydrogen-bonded 2-pyridone, Journal of Molecular Structure 596 [1-3], pp. 207-214.

[167] Thanopulos, I. and Shapiro, M. (2005): Detection and Automatic Repair of Nucleotide Base-Pair Mutations by Coherent Light, Journal of the American Chemical Society 127 [41], pp. 14434-14438.

[168] Tolstoy, P. M.; Schah-Mohammedi, P.; Smirnov, S. N.; Golubev, N. S.; Denisov, G. S. and Limbach, H.-H. (2004): Characterization of fluxional hydrogen-bonded complexes of acetic acid and acetate by NMR: Geometries and isotope and solvent effects, Journal of the American Chemical Society 126 [17], pp. 5621-5634.

[169] Meschede, Ludger and Limbach, Hans Heinrich (1991): Dynamic NMR study of the kinetic HH/HD/DD isotope effects on the double proton transfer in cyclic bis(p-fluorophenyl)formamidine dimers, The Journal of Physical Chemistry 95 [25], pp. 10267-10280.

[170] Limbach, Hans-Heinrich; Männle, Ferdinand; Detering, Carsten and Denisov, Gleb S. (2005): Dynamic NMR studies of base-catalyzed intramolecular single vs. intermolecular double proton transfer of 1,3-bis(4-fluorophenyl)triazene, Chemical Physics 319 [1-3], pp. 69-92.

[171] Nakahara, Masaru and Wakai, Chihiro (1992): Monomeric and Cluster States of Water Molecules in Organic Solvent, Chemistry Letters 21 [5], pp. 809-812.

[172] Rüterjans, H.; Kaun, E.; Hull, W.E. and Limbach, H.H. (1982): Evidence for tautornerisrn in nucleic acid base pairs.1H NMR study of 15N labeled tRNA, Nucleic Acids Research 10 [21], pp. 7027-7039.

[173] Limbach, H. H.; Pietrzak, M.; Sharif, S.; Tolstoy, P. M.; Shenderovich, I. G.; Smirnov, S. N.; Golubev, N. S. and Denisov, G. S. (2004): NMR Parameters and Geometries of OHN and ODN Hydrogen Bonds of Pyridine–Acid Complexes, Chemistry – A European Journal 10 [20], pp. 5195-5204.

[174] Frisch, M. J. ; Trucks, G. W. ; Schlegel, H. B. ; Scuseria, G. E. ; Robb, M. A. ; Cheeseman, J. R. ; Zakrzewski, V. G. ; Montgomery, J. A. ; Stratmann, R. E. ; Burant, J. C. ; Dapprich, S. ; Millam, J. M. ; Daniels, A. D. ; Kudin, K. N. ; Strain, M. C. ; Farkas, O. ; Tomasi, J. ; Barone, V. ; Cossi, M. ; Cammi, R. ; Mennucci, B. ; Pomelli, C. ; Adamo, C. ; Clifford, S. ; Ochterski, J. ; Petersson, G. A. ; Ayala, P. Y. ; Cui, Q. ; Morokuma, K. ; Malick, D. K. ; Rabuck, A. D. ; Raghavachari, K. ; Foresman, J. B. ; Cioslowski, J. ; Ortiz, J. V. ; Stefanov, B. B. ; Liu, G. ; Liashenko, A. ; Piskorz, P. ; Komaromi, I. ; Gomperts, R. ; Martin, R. L. ; Fox, D. J. ; Keith, T. ; Al-Laham, M. A. ; Peng, C. Y. ; Nanayakkara, A. ; Gonzalez, C.; Challacombe, M.; Gill, P. M. W.; G. Johnson, B.; Chen, W. ; Wong, M. W. ; Andres, J. L. ; Head-Gordon, M.; Replogle, E. S. and Pople, J. A. (2003): Gaussian 03 (Revision C.02), Gaussian, Inc., Pittsburgh PA.

[175] Florio, G. M.; Sibert, E. L. and Zwier, T. S. (2001): Fluorescence-dip IR spectra of jet-cooled benzoic acid dimer in its ground and first excited singlet states, Faraday Discussions 118, pp. 315-330.

[176] Häber, T.; Schmitt, U.; Emmeluth, C. and Suhm, M. A. (2001): Ragout-jet FTIR spectroscopy of cluster isomerism and cluster dynamics: from carboxylic acid dimers to N2O nanoparticles, Faraday Discussions 118, pp. 331-359.

[177] Florio, Gina M. ; Zwier, Timothy S. ; Myshakin, Evgeniy M. ; Jordan, Kenneth D. and Sibert III, Edwin L. (2003): Theoretical modeling of the OH stretch infrared spectrum of carboxylic acid dimers based on first-principles anharmonic couplings, Journal of Chemical Physics 118 [4], pp. 1735-1746.

[178] Emmeluth, C. and Suhm, M. A. (2003): A chemical approach towards the spectroscopy of carboxylic acid dimer isomerism, Physical Chemistry Chemical Physics 5 [15], pp. 3094-3099.

[179] Emmeluth, Corinna; Suhm, Martin A. and Luckhaus, David (2003): A monomers-in-dimers model for carboxylic acid dimers, Journal of Chemical Physics 118 [5], pp. 2242-2255.

[180] Antony, Jens; von Helden, Gert; Meijer, Gerard and Schmidt, Burkhard (2005): Anharmonic midinfrared vibrational spectra of benzoic acid monomer and dimer, Journal of Chemical Physics 123 [1], p. 014305.

[181] Dreyer, J. (2005): Hydrogen-bonded acetic acid dimers: Anharmonic coupling and linear infrared spectra studied with density-functional theory, Journal of Chemical Physics 122 [18], p. 184306.

[182] Dreyer, J. (2007): Unraveling the structure of hydrogen bond stretching mode infrared absorption bands: An anharmonic density functional theory study on 7-azaindole dimers, Journal of Chemical Physics 127 [5].

[183] Motley, T. L.; Allis, D. G. and Korter, T. M. (2009): Investigation of crystalline 2-pyridone using terahertz spectroscopy and solid-state density functional theory, Chemical Physics Letters 478 [4-6], pp. 166-171.

[184] Jackson, J. E. (1991): A User's Guide to Principal Components, John Wiley & Sons, New York.

[185] Savitzky, Abraham and Golay, M. J. E. (1964): Smoothing and Differentiation of Data by Simplified Least Squares Procedures, Analytical Chemistry 36 [8], pp. 1627-1639.

[186] Dreyer, J. (2005): Density functional theory simulations of two-dimensional infrared spectra for hydrogen-bonded acetic acid dimers, International Journal of Quantum Chemistry 104 [5], pp. 782-793.

[187] Heyne, K.; Huse, N.; Nibbering, E. T. J. and Elsaesser, T. (2003): Ultrafast coherent nuclear motions of hydrogen bonded carboxylic acid dimers, Chemical Physics Letters 369 [5-6], pp. 591-596.

[188] Dwyer, J. R.; Dreyer, J.; Nibbering, E. T. J. and Elsaesser, T. (2006): Ultrafast dynamics of vibrational N-H stretching excitations in the 7-azaindole dimer, Chemical Physics Letters 432 [1-3], pp. 146-151.

[189] Nienhuys, H.-K.; Woutersen, S.; van Santen, R. A. and Bakker, H. J. (1999): Mechanism for vibrational relaxation in water investigated by femtosecond infrared spectroscopy, Journal of Chemical Physics 111 [4], pp. 1494-1500.

[190] Woutersen, S. and Cristalli, G. (2004): Strong enhancement of vibrational relaxation by Watson-Crick base pairing, Journal of Chemical Physics 121 [11], pp. 5381-5386.

[191] Hamm, P.; Ohline, S. M. and Zinth, W. (1997): Vibrational cooling after ultrafast photoisomerization of azobenzene measured by femtosecond infrared spectroscopy, Journal of Chemical Physics 106 [2], pp. 519-529.

[192] Nibbering, E. T. J.; Fidder, H. and Pines, E. (2005): Ultrafast chemistry: Using time-resolved vibrational spectroscopy for interrogation of structural dynamics., Annual Review of Physical Chemistry 56, pp. 337-367.

[193] Huse, N.; Heyne, K.; Dreyer, J.; Nibbering, E. T. J. and Elsaesser, T. (2003): Vibrational multi-level quantum beats due to anharmonic couplings in intermolecular hydrogen bonds, Physical Review Letters 91 [19], p. 197401.

[194] Heyne, Karsten; Huse, Nils ; Dreyer, Jens ; Nibbering, Erik T. J.; Elsaesser, Thomas and Mukamel, Shaul (2004): Coherent low-frequency motions of hydrogen bonded acetic acid dimers in the liquid phase, Journal of Chemical Physics 121 [2], pp. 902-913.

[195] Shipman, S. T.; Douglass, P. C.; Yoo, H. S.; Hinkle, C. E.; Mierzejewski, E. L. and Pate, B. H. (2007): Vibrational dynamics of carboxylic acid dimers in gas and dilute solution, Physical Chemistry Chemical Physics 9 [32], pp. 4572-4586.

[196] Koller, F. O.; Huber, M.; Schrader, T. E.; Schreier, W. J. and Zinth, W. (2007): Ultrafast vibrational excitation transfer and vibrational cooling of propionic acid dimers investigated with IR-pump IR-probe spectroscopy, Chemical Physics 341 [1-3], pp. 200-206.

[197] Gundogdu, K.; Bandaria, J.; Nydegger, M.; Rock, W. and Cheatum, C. M. (2007): Relaxation and anharmonic couplings of the O-H stretching vibration of asymmetric strongly hydrogen-bonded complexes, Journal of Chemical Physics 127 [4].

[198] Yamaguchi, S.; Banno, M.; Ohta, K.; Tominaga, K. and Hayashi, T. (2008): Vibrational dynamics of benzoic acid in nonpolar solvents studied by subpicosecond infrared pump-probe spectroscopy, Chemical Physics Letters 462 [4-6], pp. 238-242.

[199] Petersen, P. B.; Roberts, S. T.; Ramasesha, K.; Nocera, D. G. and Tokmakoff, A. (2008): Ultrafast N-H Vibrational Dynamics of Cyclic Doubly Hydrogen-Bonded Homo- and Heterodimers, Journal of Physical Chemistry B 112 [42], pp. 13167-13171.

[200] Pollard, W. T. and Mathies, R. A. (1992): Analysis of femtosecond dynamic absorption spectra of nonstationary states, Annual Review of Physical Chemistry 43, pp. 497-523.

[201] Wang, Q.; Schoenlein, R. W.; Peteanu, L. A.; Mathies, R. A. and Shank, C. V. (1994): Vibrationally coherent photochemistry in the femtosecond primary event of vision, Science 266, pp. 422-424.

[202] Zhu, Leyun; Sage, J. T. and Champion, P. M. (1994): Observation of coherent reaction dynamics in heme proteins, Science 266 [5185], pp. 629-632.

[203] Kumar, A. T. N.; Rosca, F.; Widom, A. and Champion, P. M. (2001): Investigations of amplitude and phase excitation profiles in femtosecond coherence spectroscopy, Journal of Chemical Physics 114 [2], pp. 701-24.

[204] Madsen, D.; Stenger, J.; Dreyer, J.; Hamm, P.; Nibbering, E. T. J. and Elsaesser, T. (2002): Femtosecond mid-infrared pump-probe study of wave packet motion in a me-

dium-strong intramolecular hydrogen bond, Bulletin of the Chemical Society of Japan 75 [5], pp. 909-917.

[205] Saenger, Wolfram (1984): Principles of Nucleic Acid Structure, Springer-Verlag, New York.

[206] Alberts Bruce; Johnson Alexander; Lewis Julian; Raff Martin; Roberts Keith and Peter, Walters (2002): Molecular Biology of the Cell, Garland Science, New York and London.

[207] Butler, John M. (2001): Forensic DNA Typing, Elsevier, Ed.

[208] DNA chemical structure, 27.03.2011, 28.03.2007, Online image

[209] Stryer, Lubert (1981): Biochemistry, W. H. Freeman and Company, San Francisco.

[210] Watson, J.D. and Crick, F.H.C. (1953): Molecular Structure of Nucleic Acids, Nature 171, pp. 737-738.

[211] Wheeler, Richard, 29.03.2011, 27.03.2011, Online image

[212] Lavery, Richard and Zakrzewska, Krystyna (1999): Base and base pair morphologies, helical parameters, and definitions., Neidle, Stephen, Nucleic Acid Structure pp. 39-77, Oxford University Press, New York.

[213] Rippe, K. and Jovin, T.M. (1992): Parallel-stranded duplex DNA., Methods in Enzymology 211, pp. 199-220.

[214] Wing, Richard; Drew, Horace; Takano, Tsunehiro; Broka, Chris; Tanaka, Shoji; Itakura, Keiichi and Dickerson, Richard E. (1980): Crystal structure analysis of a complete turn of B-DNA, Nature 287 [5784], pp. 755-758.

[215] Pabo, C O and Sauer, R T (1984): Protein-DNA Recognition, Annual Review of Biochemistry 53 [1], pp. 293-321.

[216] Liepinsh, Edvards; Otting, Gottfried and Wüthrich, Kurt (1992): NMR observation of individual molecules of hydration water bound to DNA duplexes: direct evidence for a spine of hydration water present in aqueous solution, Nucleic Acids Research 20 [24], pp. 6549-6553.

[217] Arnott, S.; Smith, P.J.C. and Chandrasekaran, R. (1976), Fasman, Gerald D., CRC Handbook of Biochemistry and Molecular Biology 2, CRC, Cleveland.

[218] Wang, Andrew H.-J.; Quigley, Gary J.; Kolpak, Francis J.; Crawford, James L.; Boom, Jacques H. van; Marel, Gijs van der and Rich, Alexander (1979): Molecular structure of a left-handed double helical DNA fragment at atomic resolution, Nature 282, pp. 680-686.

[219] Ghosh, A. and Bansal, M. (2003): A glossary of DNA structures from A to Z, Acta Crystallographica D: Biological Crystallography 59, pp. 620-626.

[220] Haniford, David B. and Pulleyblank, David E. (1983): Facile transition of poly[d(TG)[middot]d(CA)] into a left-handed helix in physiological conditions, Nature 302 [5909], pp. 632-634.

[221] Bram, Stanley and Baudy, Pierre (1974): X-ray diffraction studies of DNA at reduced water contents, Nature 250, pp. 414-416.

[222] Corongiu, Giorgina and Clementi, Enrico (1981): Simulations of the solvent structure for macromolecules. II. Structure of water solvating Na+-B-DNA at 300 K and a model for conformational transitions induced by solvent variations, Biopolymers 20 [11], pp. 2427-2483.

[223] Franklin, R. F. and Gossling, R. G. (1953): The structure of sodium thymonucleate fibres. I. The influence of water content, Acta Crystallographica 6, pp. 673-677.

[224] Hamilton, L. D.; Barclay, R. K.; Wilkins, M. H. F.; Brown, G. L.; Wilson, H. R.; Marvin, D. A.; Ephrussi-Taylor, H. and Simmons, and N. S. (1959): Similarity of the Structure of DNA from a Variety of Sources, Journal of Biophysical and Biochemical Cytology 5, pp. 397-404.

[225] Pilet, J. and Brahms, J. (1972): Dependence of B-A Conformational Change in DNA on Base Composition, Nature New Biology 236, pp. 99-100.

[226] Pilet, J. and Brahms, J. (1973): Investigation of DNA Structural Changes by Infrared Spectroscopy, Biopolymers 12, pp. 387-403.

[227] Falk, Michael; Hartman, Karl A. and Lord, R. C. (1962): Hydration of Deoxyribonucleic Acid. I. a Gravimetric Study, Journal of the American Chemical Society 84 [20], pp. 3843-3846.

[228] Edwards, G. S.; Davis, C. C.; Saffer, J. D. and Swicord, M. L. (1984): Resonant Microwave Absorption of Selected DNA Molecules, Physical Review Letters 53 [13], p. 1284.

[229] Milton, John G. and Galley, William C. (1986): Evidence for heterogeneity in DNA-associated solvent mobility from acridine phosphorescence spectra, Biopolymers 25 [9], pp. 1673-1684.

[230] Schreiner, L. J.; Pintar, M. M.; Dianoux, A. J.; Volino, F. and Rupprecht, A. (1988): Hydration of NaDNA by neutron quasi-elastic scattering, Biophysical journal 53 [1], pp. 119-122.

[231] Mahendrasingam, A.; Rhodes, N. J.; Goodwin, D. C.; Nave, C.; Pigram, W. J.; Fuller, W.; Brahms, J. and Vergne, J. (1983): Conformational transitions in oriented fibres of the synthetic polynucleotide poly[d(AT)] · poly[d(AT)] double helix, Nature 301 [5900], pp. 535-537.

[232] Yang, C. Y.; Moses, D. and Heeger, A.J. (2003): Base-pair stacking in oriented films of DNA-surfactant complex, Advanced Materials 15, pp. 1364-1367.

[233] Dwyer, Jason R.; Szyc, Łukasz; Nibbering, Erik T. J. and Elsaesser, Thomas (2008): Ultrafast Vibrational Dynamics of Adenine-Thymine Base Pairs in DNA Oligomers, The Journal of Physical Chemistry B 112 [36], pp. 11194-11197.

[234] Tanaka, Kentaro and Okahata, Yoshio (1996): A DNA-Lipid Complex in Organic Media and Formation of an Aligned Cast Film, Journal of the American Chemical Society 118 [44], pp. 10679-10683.

[235] Yang, C.Y.; Yang, W.J.; Moses, D.; Morse, D. and Heeger, A.J. (2003): DNA alignment and characterisation, Synthetic Metals 137, pp. 1459-1460.

[236] Pohle, W. (1990): The PO_2^- moiety - a hydrogen bonding acceptor in biological molecules., Journal of Molecular Structure 219, pp. 281-286.

[237] Pohle, W.; Zhurkin, V.B. and Fritzsche, and H. (1984): The DNA phosphate orientation. Infrared data and energetically favourable structures., Biopolymers 23, pp. 2603-2622.

[238] Schneider, Bohdan; Patel, Ketan and Berman, Helen M. (1998): Hydration of the Phosphate Group in Double-Helical DNA, Biophysical journal 75 [5], pp. 2422-2434.

[239] Brunauer, Stephen; Emmett, P. H. and Teller, Edward (1938): Adsorption of Gases in Multimolecular Layers, Journal of the American Chemical Society 60 [2], pp. 309-319.

[240] Hill, Terrell L. (1946): Theory of Multimolecular Adsorption from a Mixture of Gases, The Journal of Chemical Physics 14 [4], pp. 268-275.

[241] Bonvin, Alexandre M. J. J.; Sunnerhagen, Maria; Otting, Gottfried and van Gunsteren, Wilfred F. (1998): Water molecules in DNA recognition II: a molecular dynamics view of the structure and hydration of the trp operator, Journal of Molecular Biology 282 [4], pp. 859-873.

[242] Halle, Bertil and Denisov, Vladimir P. (1998): Water and monovalent ions in the minor groove of B-DNA oligonucleotides as seen by NMR, Biopolymers 48 [4], pp. 210-233.

[243] Korolev, Nikolay; Lyubartsev, Alexander P.; Laaksonen, Aatto and Nordenskiöld, Lars (2002): On the Competition between Water, Sodium Ions, and Spermine in Binding to DNA: A Molecular Dynamics Computer Simulation Study, Biophysical journal 82 [6], pp. 2860-2875.

[244] Pal, Subrata; Maiti, Prabal K. and Bagchi, Biman (2006): Exploring DNA groove water dynamics through hydrogen bond lifetime and orientational relaxation, The Journal of Chemical Physics 125 [23], pp. 234903-11.

[245] Phan, Anh Tuân; Leroy, Jean-Louis and Guéron, Maurice (1999): Determination of the residence time of water molecules hydrating B ' -DNA and B -DNA, by one-dimensional zero-enhancement nuclear overhauser effect spectroscopy, Journal of Molecular Biology 286 [2], pp. 505-519.

[246] Sunnerhagen, Maria; Denisov, Vladimir P.; Venu, Kandadai; Bonvin, Alexandre M. J. J.; Carey, Jannette; Halle, Bertil and Otting, Gottfried (1998): Water molecules in DNA recognition I: hydration lifetimes of trp operator DNA in solution measured by NMR spectroscopy, Journal of Molecular Biology 282 [4], pp. 847-858.

[247] Pal, Samir Kumar; Zhao, Liang; Xia, Tianbing and Zewail, Ahmed H. (2003): Site- and sequence-selective ultrafast hydration of DNA, Proceedings of the National Academy of Sciences of the United States of America 100 [24], pp. 13746-13751.

[248] Chalikian, Tigran V.; Plum, G. Eric; Sarvazyan, Armen P. and Breslaver, Kenneth J. (1994): Influence of Drug Binding on DNA Hydration: Acoustic and Densimetric Characterizations of Netropsin Binding to the Poly(dAdT).cntdot.Poly(dAdT) and Poly(dA).cntdot.Poly(dT) Duplexes and the Poly(dT).cntdot.Poly(dA).cntdot.Poly(dT) Triplex at 25 .degree.C, Biochemistry 33 [29], pp. 8629-8640.

[249] Billeter, Martin; Güntert, Peter; Luginbühl, Peter and Wüthrich, Kurt (1996): Hydration and DNA Recognition by Homeodomains, Cell 85 [7], pp. 1057-1065.

[250] Laage, Damien and Hynes, James T. (2006): A Molecular Jump Mechanism of Water Reorientation, Science 311 [5762], pp. 832-835.

[251] Pecourt, Jean-Marc L.; Peon, Jorge and Kohler, Bern (2001): Ultrafast Internal Conversion of Electronically Excited RNA and DNA Nucleosides in Water Journal of the American Chemical Society 123 [21], pp. 5166-5166.

[252] Crespo-Hernandez, Carlos E.; Cohen, Boiko; Hare, Patrick M. and Kohler, Bern (2004): Ultrafast Excited-State Dynamics in Nucleic Acids, Chemical Reviews 104 [4], pp. 1977-2020.

[253] Schwalb, Nina K. and Temps, Friedrich (2008): Base Sequence and Higher-Order Structure Induce the Complex Excited-State Dynamics in DNA, Science 322 [5899], pp. 243-245.

[254] Elber, R. and Karplus, M. (1990): Enhanced sampling in molecular dynamics: use of the time-dependent Hartree approximation for a simulation of carbon monoxide diffusion through myoglobin, Journal of the American Chemical Society 112 [25], pp. 9161-9175.

[255] Karplus, Martin and Petsko, Gregory A. (1990): Molecular dynamics simulations in biology, Nature 347 [6294], pp. 631-639.

[256] Zhou, Huan-Xiang; Wlodek, Stanislaw T. and McCammon, J. Andrew (1998): Conformation gating as a mechanism for enzyme specificity, Proceedings of the National Academy of Sciences of the United States of America 95 [16], pp. 9280-9283.

[257] Daggett, Valerie and Levitt, Michael (1992): Molecular dynamics simulations of helix denaturation, Journal of Molecular Biology 223 [4], pp. 1121-1138.

[258] Soman, Kizhake V.; Karimi, Afshin and Case, David A. (1991): Unfolding of an α-helix in water, Biopolymers 31 [12], pp. 1351-1361.

[259] Sung, Shen-Shu and Wu, Xiong-Wu (1996): Molecular dynamics simulations of synthetic peptide folding, Proteins: Structure, Function, and Bioinformatics 25 [2], pp. 202-214.

[260] Eaton, William A.; Henry, Eric R. and Hofrichter, James (1996): Protein Structure: Nanosecond Crystallographic Snapshots of Protein Structural Changes, Science 274 [5293], p. 1631.

[261] Helliwell, J.R. and Rentzepis, P.M. (1997): Time-resolved diffraction, Oxford Series on Synchrotron Radiation, Clarendon Press Oxford.

[262] Bagchi, Biman (2005): Water Dynamics in the Hydration Layer around Proteins and Micelles, Chemical Reviews 105 [9], pp. 3197-3219.

[263] Lock, A. J. and Bakker, H. J. (2002): Temperature dependence of vibrational relaxation in liquid H2O, Journal of Chemical Physics 117 [4], pp. 1708-1713.

[264] Fecko, C. J.; Eaves, J. D.; Loparo, J. J.; Tokmakoff, A. and Geissler, P. L. (2003): Ultrafast hydrogen-bond dynamics in the infrared spectroscopy of water, Science 301 [5640], pp. 1698-1702.

[265] Asbury, J. B.; Steinel, T.; Kwak, K.; Corcelli, S. A.; Lawrence, C. P.; Skinner, J. L. and Fayer, M. D. (2004): Dynamics of water probed with vibrational echo correlation spectroscopy, Journal of Chemical Physics 121 [24], pp. 12431-12446.

[266] Ashihara, S.; Huse, N.; Espagne, A.; Nibbering, E. T. J. and Elsaesser, T. (2006): Vibrational couplings and ultrafast relaxation of the O-H bending mode in liquid H2O, Chemical Physics Letters 424 [1-3], pp. 66-70.

[267] Piryatinski, A.; Lawrence, C. P. and Skinner, J. L. (2003): Vibrational spectroscopy of HOD in liquid D2O. IV. Infrared two-pulse photon echoes, Journal of Chemical Physics 118 [21], pp. 9664-9671.

[268] Ingrosso, Francesca; Rey, Rossend; Elsaesser, Thomas and Hynes, James T. (2009): Ultrafast Energy Transfer from the Intramolecular Bending Vibration to Librations in Liquid Water, The Journal of Physical Chemistry A 113 [24], pp. 6657-6665.

[269] Cringus, Dan; Bakulin, Artem; Lindner, Jörg; Vöhringer, Peter; Pshenichnikov, Maxim S. and Wiersma, Douwe A. (2007): Ultrafast Energy Transfer in Water-AOT Reverse Micelles, The Journal of Physical Chemistry B 111 [51], pp. 14193-14207.

[270] Tan, H. S.; Piletic, I. R.; Riter, R. E.; Levinger, N. E. and Fayer, M. D. (2005): Dynamics of water confined on a nanometer length scale in reverse micelles: Ultrafast infrared vibrational echo spectroscopy, Physical Review Letters 94 [5], p. 057405.

[271] Volkov, Victor V.; Nuti, Francesca; Takaoka, Yuji; Chelli, Riccardo; Papini, Anna Maria and Righini, Roberto (2006): Hydration and Hydrogen Bonding of Carbonyls in Dimyristoyl-Phosphatidylcholine Bilayer, Journal of the American Chemical Society 128 [29], pp. 9466-9471.

[272] Eaves, J. D.; Tokmakoff, A. and Geissler, P. L. (2005): Electric field fluctuations drive vibrational dephasing in water, Journal of Physical Chemistry A 109 [42], pp. 9424-9436.

[273] Møller, Klaus B.; Rey, Rossend and Hynes, James T. (2004): Hydrogen bond dynamics in water and ultrafast infrared spectroscopy: A theoretical study, Journal of Physical Chemistry A 108 [7], pp. 1275 -1289.

[274] Huse, N.; Ashihara, S.; Nibbering, E. T. J. and Elsaesser, T. (2005): Ultrafast vibrational relaxation of O-H bending and librational excitations in liquid H2O, Chemical Physics Letters 404 [4-6], pp. 389-393.

[275] Brown, Ellen B. and Peticolas, Warner L. (1975): Conformational geometry and vibrational frequencies of nucleic acid chains, Biopolymers 14 [6], pp. 1259-1271.

[276] Erfurth, Stephen C.; Kiser, Ernest J. and Peticolas, Warner L. (1972): Determination of the Backbone Structure of Nucleic Acids and Nucleic Acid Oligomers by Laser Raman Scattering, Proceedings of the National Academy of Sciences of the United States of America 69 [4], pp. 938-941.

[277] Falk, Michael; Hartman, Karl A. and Lord, R. C. (1963): Hydration of Deoxyribonucleic Acid. II. An Infrared Study, Journal of the American Chemical Society 85 [4], pp. 387-391.

[278] Nishimura, Yoshifumi; Morikawa, Kosuke and Tsuboi, Masamichi (1974): Spectral Difference of the A and B Forms of Deoxyribonucleic Acid, Bulletin of the Chemical Society of Japan 47, pp. 1043-1044.

[279] Plützer, C.; Hünig, I.; Kleinermanns, K.; Nir, E. and de Vries, M. S. (2003): Pairing of isolated nucleobases: Double resonance laser spectroscopy of adenine-thymine, ChemPhysChem 4 [8], pp. 838-842.

[280] Prescott, B.; Steinmetz, W. and Thomas, G. J. (1984): Characterization of DNA structures by laser Raman spectroscopy, Biopolymers 23 [2], pp. 235-256.

[281] Tsuboi, Masamichi (1957): Vibrational Spectra of Phosphite and Hypophosphite Anions, and the Characteristic Frequencies of PO3-- and PO2- Groups, Journal of the American Chemical Society 79 [6], pp. 1351-1354.

[282] Heyne, K.; Krishnan, G. M. and Kühn, O. (2008): Revealing Anharmonic Couplings and Energy Relaxation in DNA Oligomers by Ultrafast Infrared Spectroscopy, The Journal of Physical Chemistry B 112 [26], pp. 7909-7915.

[283] Krishnan, G. M. and Kühn, O. (2007): Identifying adenine-thymine base pairing by anharmonic analysis of the hydrogen-bonded NH stretching vibrations, Chemical Physics Letters 435 [1-3], pp. 132-135.

[284] Ouali, Mohammed; Gousset, HervĂ©; Geinguenaud, FrĂ©dĂ©ric; Liquier, Jean; Gabarro-Arpa, Jacques; Le Bret, Marc and Taillandier, Eliane (1997): Hydration of the $dT_n \cdot dA_n \times dT_n$ parallel triple helix: A Fourier transform infrared and gravimetric study correlated with molecular dynamics simulations, Nucleic Acids Research 25 [23], pp. 4816-4824.

[285] Keller, P. B., and K. A. Hartman (1986): The effect of ionic environment and mercury (II) binding on the alternative structure of DNA, Spectrochimica Acta 42A, pp. 299-306.

[286] Szyc, Łukasz; Yang, Ming and Elsaesser, Thomas (2010): Ultrafast Energy Exchange via Water-Phosphate Interactions in Hydrated DNA, The Journal of Physical Chemistry B 114 [23], pp. 7951-7957.

[287] Bradbury, E. M.; Price, W. C. and Wilkinson, G. R. (1961): Infrared studies of molecular configurations of DNA, Journal of Molecular Biology 3 [3], pp. 301-317.

[288] Sutherland, G. B. B. M. and Tsuboi, M. (1957): The Infra-Red Spectrum and Molecular Configuration of Sodium Deoxyribonucleate, Proceedings of the Royal Society of London. Series A. Mathematical and Physical Sciences 239 [1219], pp. 446-463.

[289] Parker, Frank S. and Bhaskar, K. R. (1970): Infrared Studies of Hydrogen-Deuterium Exchange in Biological Molecules, Applied Spectroscopy Reviews 3 [1], pp. 91-142.

[290] Krummel, A. T.; Mukherjee, P. and Zanni, M. T. (2003): Inter and intrastrand vibrational coupling in DNA studied with heterodyned 2D-IR spectroscopy, Journal of Physical Chemistry B 107 [35], pp. 9165-9169.

[291] Krummel, Amber T. and Zanni, Martin T. (2006): DNA Vibrational Coupling Revealed with Two-Dimensional Infrared Spectroscopy: Insight into Why Vibrational Spectroscopy Is Sensitive to DNA Structure, The Journal of Physical Chemistry B 110 [28], pp. 13991-14000.

[292] Andreatta, Daniele; PĂ©rez Lustres, J. Louis; Kovalenko, Sergey A.; Ernsting, Nikolaus P.; Murphy, Catherine J.; Coleman, Robert S. and Berg, Mark A. (2005): Power-Law Solvation Dynamics in DNA over Six Decades in Time, Journal of the American Chemical Society 127 [20], pp. 7270-7271.

[293] Sen, Sobhan; Andreatta, Daniele; Ponomarev, Sergei Y.; Beveridge, David L. and Berg, Mark A. (2009): Dynamics of Water and Ions Near DNA: Comparison of Simulation to Time-Resolved Stokes-Shift Experiments, Journal of the American Chemical Society 131 [5], pp. 1724-1735.

[294] Urabe, Hisako; Hayashi, Hideyuki; Tominaga, Yasunori; Nishimura, Yoshifumi; Kubota, Kenji and Tsuboi, Masamichi (1985): Collective vibrational modes in molecular assembly of DNA and its application to biological systems. Low frequency Raman spectroscopy, The Journal of Chemical Physics 82 [1], pp. 531-535.

[295] Choi, Myong Yong; Dong, Feng; Han, Sang Woo and Miller, Roger E. (2008): Non-planarity of Adenine: Vibrational Transition Moment Angle Studies in Helium Nanodroplets, The Journal of Physical Chemistry A 112 [31], pp. 7185-7190.

[296] Zierkiewicz, Wiktor; Komorowski, Ludwik; Michalska, Danuta; Cerny, Jiri and Hobza, Pavel (2008): The Amino Group in Adenine: MP2 and CCSD(T) Complete Basis Set Limit Calculations of the Planarization Barrier and DFT/B3LYP Study of the Anharmonic Frequencies of Adenine, The Journal of Physical Chemistry B 112 [51], pp. 16734-16740.

[297] Wang, Gui Xiu; Ma, Xiao Yan and Wang, Jian Ping (2009): Anharmonic Vibrational Signatures of DNA Bases and Watson–Crick Base Pairs Chinese Journal of Chemical Physics 22 [6], pp. 563-568.

[298] Colarusso, Pina; Zhang, KeQing; Guo, Bujin and Bernath, Peter F. (1997): The infrared spectra of uracil, thymine, and adenine in the gas phase, Chemical Physics Letters 269 [1-2], pp. 39-48.

[299] Choi, Myong Yong and Miller, Roger E. (2007): Infrared Laser Spectroscopy of Uracil and Thymine in Helium Nanodroplets: Vibrational Transition Moment Angle Study, The Journal of Physical Chemistry A 111 [13], pp. 2475-2479.

[300] Dong, F. and Miller, R. E. (2002): Vibrational Transition Moment Angles in Isolated Biomolecules: A Structural Tool, Science 298 [5596], pp. 1227-1230.

[301] Nir, E.; Kleinermanns, K. and de Vries, M. S. (2000): Pairing of isolated nucleic-acid bases in the absence of the DNA backbone, Nature 408 [6815], pp. 949-951.

[302] Förster, Th (1948): Zwischenmolekulare Energiewanderung und Fluoreszenz, Annalen der Physik 437 [1-2], pp. 55-75.

[303] Matousek, P.; Parker, A. W.; Toner, W. T.; Towrie, M.; de Faria, D. L. A.; Hester, R. E. and Moore, J. N. (1995): The anti-Stokes resonance Raman spectrum of photoexcited S1 trans-stilbene, Chemical Physics Letters 237 [3-4], pp. 373-379.

[304] Qian, Jun; Schultz, Sandra L. and Jean, John M. (1995): Observation of intramolecular vibrational redistribution and vibrational cooling in S1 trans-stilbene and 2-phenylindene in solution, Chemical Physics Letters 233 [1-2], pp. 9-15.

[305] Kozich, V.; Dreyer, J.; Ashihara, S.; Werncke, W. and Elsaesser, T. (2006): Mode-selective O-H stretching relaxation in a hydrogen bond studied by ultrafast vibrational spectroscopy, Journal of Chemical Physics 125 [7].

[306] Kozich, V.; Dreyer, J. and Werncke, W. (2009): Mode-selective vibrational redistribution after spectrally selective N-H stretching mode excitation in intermolecular hydrogen bonds, Journal of Chemical Physics 130 [3].

[307] Kozich, V.; Szyc, L.; Nibbering, E. T. J.; Werncke, W. and Elsaesser, T. (2009): Ultrafast redistribution of vibrational energy after excitation of NH stretching modes in DNA oligomers, Chemical Physics Letters 473 [1-3], pp. 171-175.

[308] Szyc, Łukasz; Dwyer, Jason R.; Nibbering, Erik T. J. and Elsaesser, Thomas (2009): Ultrafast dynamics of N-H and O-H stretching excitations in hydrated DNA oligomers, Chemical Physics 357 [1-3], pp. 36-44.

[309] Cringus, D.; Lindner, J.; Milder, M. T. W.; Pshenichnikov, M. S.; Vöhringer, P. and Wiersma, D. A. (2005): Femtosecond water dynamics in reverse-micellar nanodroplets, Chemical Physics Letters 408 [1-3], pp. 162-168.

[310] Paarmann, A.; Hayashi, T.; Mukamel, S. and Miller, R. J. D. (2008): Probing intermolecular couplings in liquid water with two-dimensional infrared photon echo spectroscopy, The Journal of Chemical Physics 128 [19], pp. 191103-5.

[311] Klähn, Marco; Mathias, Gerald; Kötting, Carsten; Nonella, Marco; Schlitter, Jürgen; Gerwert, Klaus and Tavan, Paul (2004): IR Spectra of Phosphate Ions in Aqueous Solution: Predictions of a DFT/MM Approach Compared with Observations, The Journal of Physical Chemistry A 108 [29], pp. 6186-6194.

[312] Guan, Yifu; Wurrey, Charles J. and Thomas, George J. (1994): Vibrational Analysis of Nucleic Acids. 1. The Phosphodiester Group in Dimethyl Phosphate Model Com-

pounds: $(CH_3O)_2PO_2^-$, $(CD_3O)_2PO_2^-$, and $(^{13}CH_3O)_2PO_2^-$, Biophysical journal 66, pp. 225-235.

[313] Binder, H. and Pohle, W. (2000): Structural Aspects of Lyotropic Solvation-Induced Transitions in Phosphatidylcholine and Phosphatidylethanolamine Assemblies Revealed by Infrared Spectroscopy, The Journal of Physical Chemistry B 104 [50], pp. 12039-12048.

[314] Costard, Rene (2011): Private communcation.

[315] Asplund, M. C. ; Zanni, M. T. and Hochstrasser, R. M. (2000): Two-dimensional infrared spectroscopy of peptides by phase-controlled femtosecond vibrational photon echoes, Proceedings of the National Academy of Sciences of the United States of America 97 [15], pp. 8219-8224.

[316] Jonas, D. M. (2003): Two-dimensional femtosecond spectroscopy, Annual Review of Physical Chemistry 54, pp. 425-463.

[317] Mukamel, Shaul (2000): Multidimensional femtosecond correlation spectroscopies of electronic and vibrational excitations, Annual Review of Physical Chemistry 51, pp. 691-729.

Publications

Journal Articles:

1. Yang, M.; Szyc, Ł.; Elsaesser, T., Vibrational Dynamics of the Water Shell of DNA Studied by Femtosecond Two-Dimensional Infrared Spectroscopy. *Journal of Photochemistry and Photobiology A*, **accepted**.

2. Yang, M.; Szyc, Ł.; Elsaesser, T., Decelerated water dynamics and vibrational couplings of hydrated DNA mapped by two-dimensional infrared spectroscopy. *The Journal of Physical Chemistry B* **2011**, 13093-13100.

3. Yang, M.; Szyc, Ł.; Röttger, K.; Fidder, H.; Nibbering, E. T. J.; Elsaesser, T.; Temps, F., Dynamics and Couplings of N-H Stretching Excitations of Guanosine-Cytidine Base Pairs in Solution. *The Journal of Physical Chemistry B* **2011**, 5484-5492.

4. Yang, M.; Szyc, Ł.; Elsaesser, T., Femtosecond Two-Dimensional Infrared Spectroscopy of Adenine-Thymine Base Pairs in DNA Oligomers. *The Journal of Physical Chemistry B* **2011,** *115* (5), 1262-1267.

5. Szyc, Ł.; Yang, M.; Elsaesser, T., Ultrafast Energy Exchange via Water-Phosphate Interactions in Hydrated DNA. *The Journal of Physical Chemistry B* **2010,** *114* (23), 7951-7957.

6. Szyc, Ł.; Yang, M.; Nibbering, E. T. J.; Elsaesser, T., Ultrafast Vibrational Dynamics and Local Interactions of Hydrated DNA. *Angewandte Chemie International Edition* **2010,** *49* (21), 3598-3610.

7. Yang, M.; Szyc, Ł.; Dreyer, J.; Nibbering, E. T. J.; Elsaesser, T., The Hydrogen-Bonded 2-Pyridone Dimer Model System. 2. Femtosecond Mid-Infrared Pump-Probe Study. *The Journal of Physical Chemistry A* **2010,** *114* (46), 12195–12201.

8. Szyc, Ł.; Guo, J.; Yang, M.; Dreyer, J.; Tolstoy, P. M.; Nibbering, E. T. J.; Czarnik-Matusewicz, B.; Elsaesser, T.; Limbach, H.-H., The Hydrogen-Bonded 2-Pyridone Dimer Model System. 1. Combined NMR and FT-IR Spectroscopy Study. *The Journal of Physical Chemistry A* **2010,** *114* (29), 7749-7760.

9. Kozich, V.; Szyc, Ł.; Nibbering, E. T. J.; Werncke, W.; Elsaesser, T., Ultrafast redistribution of vibrational energy after excitation of NH stretching modes in DNA oligomers. *Chemical Physics Letters* **2009,** *473* (1-3), 171-175.

10. Szyc, Ł.; Dwyer, J. R.; Nibbering, E. T. J.; Elsaesser, T., Ultrafast dynamics of N-H and O-H stretching excitations in hydrated DNA oligomers. *Chemical Physics* **2009,** *357* (1-3), 36-44.

11. Dwyer, J. R.; Szyc, Ł.; Nibbering, E. T. J.; Elsaesser, T., Ultrafast Vibrational Dynamics of Adenine-Thymine Base Pairs in DNA Oligomers. *The Journal of Physical Chemistry B* **2008,** *112* (36), 11194-11197.

Conference proceedings:

1. Szyc, Ł.; Yang, M.; Elsaesser, T. In *Ultrafast Phenomena XVII*, Ultrafast dynamics of phosphate-water interactions in hydrated DNA, M. Chergui; D. M. Jonas; E. Riedle; R. W. Schoenlein; Taylor, A. J., Eds. Oxford University Press: 2010; pp 493-495.

2. Yang, M.; Szyc, Ł.; Elsaesser, T. In *Ultrafast Phenomena XVII*, Ultrafast vibrational dynamics of hydrated DNA studied by 2D infrared spectroscopy, M. Chergui; D. M. Jonas; E. Riedle; R. W. Schoenlein; Taylor, A. J., Eds. Oxford University Press: 2010; pp 472-474.

3. Dwyer, J.; Szyc, Ł.; Elsaesser, T. In *Ultrafast Phenomena XVI*, Ultrafast vibrational dynamics of adenine-thymine base pairs in hydrated DNA, P. Corkum; de Silvestri, S.; K. A. Nelson; E. Riedle; Schoenlein, R. W., Eds. Springer: 2008; pp 535-537.

Other publications:

1. Szyc, Ł.; Pilorz, S.; Czarnik-Matusewicz, B., FTIR-ATR investigations of an [alpha]-helix to [beta]-sheet conformational transition in poly(l-lysine). *Journal of Molecular Liquids* **2008,** *141* (3), 155-159.

Acknowledgments

I would like to express my deep and sincere gratitude to my supervisor, Professor Thomas Elsaesser, Head of the Max-Born-Institute for Nonlinear Optics and Short Pulse Spectroscopy in Berlin for inviting me to join his group, where in a good scientific atmosphere I could explore a fascinating field of science. Numerous discussions with Prof. Elsaesser, his wide knowledge and commitment to the highest standards helped me in all the time of research and writing of this thesis.

I gratefully acknowledge Dr. Erik Nibbering for his advice, supervision, and crucial contribution, which made him a backbone of this research and so to this thesis. I owe special thanks to Erik for our interesting discussions in a very broad spectrum of subjects: starting from physics and chemistry, up to politics, history and culture.

It gives me great pleasure in acknowledging the support and help of my Masters supervisor, Professor Bogusława Czarnik-Matusewicz. Her unending enthusiasm for work and her singular ability to pass that energy on her students, is certainly the greatest quality that supervisor can have. I am indebted to Professor Czarnik-Matusewicz for many advice, not only those related to the professional career.

During this work I have collaborated with many colleagues for whom I have great regard. Many thanks go in particular to René Costard and Ming Yang for their help in understanding the physicist language and way of thinking. Long hours in the lab taking data for this thesis were much nicer because of your presence there.

I was fortunate to work with Dr. Jens Dreyer, Dr. Henk Fidder and Mirabelle Prémont-Schwarz. Solving the problems of quantum chemistry and statistical physics was much easier and nicer with help of all of you.

For the valuable discussion and fruitful collaboration, I feel grateful to Dr. Wolfgang Werncke and Dr. Valeri Kozich.

I wish to offer my special thanks to Prof. Jason Dwyer and his wife, Dr. Shahla Yekta, who are not only a couple of great chemist but are also a blast to hang around with. Thank you for your help and friendship.

Many thanks go to the staff of the institute. Regina Goleschny, Brigitte Steinert and Regina Lendt not only supported me in the chemistry lab, but also in learning German language and culture. I also thank Peter Scholze and Wolfgang Goleschny for their support in the mechanics shop and Helmut Walz for his help with computers and electronics.

I am heartily thankful to Margaret Lehmann for offering me a kind help with solving numerous problems in complex life of PhD student.

I would like to thank also Prof. Jerzy P. Hawranek, Prof. Halina Abramczyk and Prof. Lucjan Sobczyk whose professional careers were a source of an inspiration for me during my work in the field of physical chemistry. I am indebted to them more than they know.

For interesting discussions and comradeship, I would like to thank Dr. Zunaira Ansari, Dr. Clemens von Korff Schmising, Dr. Nils Huse, Dr. Katrin Adamczyk, Markus Breusing, Christian Greve, Dr. Peter Tolstoy, Dr. Wilhelm Kühn, Dr. Gianina Gavrila, Dr. Hirendra N. Ghosh, Dr. Cynthia Aku-Leh and Dr. Claus Ropers.

I thank my friends for their support, respect and encouragement.
Above all, my best friend Konrad, who was patient enough to listen to me, complaining continuously about instable lasers. Many thanks to my old friend, Dr. Agnieszka Sikorska for sharing the good and bad sides of being a PhD student. I would like to also thank Dr. Andreas Wagner for many interesting discussions, not only about chemistry.

My parents as well as my brother and his wife and daughter I would like to thank for their continuous support and understanding.

Selbständigkeitserklärung

Hiermit erkläre ich, dass ich die vorliegende Disseration, *Ultrafast Vibrational Dynamics of Hydrogen-Bonded Base Pairs and Hydrated DNA*, selbständig erarbeitet und verfasst habe und alle Hilfsmittel und Hilfen angegeben habe.

Ich habe mich anderweitig nicht um einen Doktorgrad beworben und besitze keinen entsprechenden Doktorgrad.

Ich erkläre die Kenntnisnahme der dem Verfahren zugrunde liegenden Promotionsordnung der Mathematisch-Naturwissenschaftlichen Fakultät I der Humboldt-Universität zu Berlin.

Berlin, den _ _ . _ _ . _ _ _ _ Łukasz Szyc